

**OPTO-ELASTIC PROPERTIES OF FBG BASED FABRY-  
PEROT RESONATOR: FABRICATION,  
CHARACTERIZATION, AND APPLICATIONS**

**MD. RAJIBUL ISLAM**

**INSTITUTE FOR GRADUATE STUDIES  
UNIVERSITY OF MALAYA  
KUALA LUMPUR**

**2017**

**OPTO-ELASTIC PROPERTIES OF FBG BASED  
FABRY-PEROT RESONATOR: FABRICATION,  
CHARACTERIZATION, AND APPLICATIONS**

**MD. RAJIBUL ISLAM**

**THESIS SUBMITTED IN FULFILMENT OF THE  
REQUIREMENTS FOR THE DEGREE OF DOCTOR OF  
PHILOSOPHY**

**INSTITUTE OF GRADUATE STUDIES  
UNIVERSITY OF MALAYA  
KUALA LUMPUR**

**2017**

**UNIVERSITY OF MALAYA**  
**ORIGINAL LITERARY WORK DECLARATION**

Name of Candidate: **MD. RAJIBUL ISLAM**

Registration/Matric No: **HHE130006**

Name of Degree: **DOCTOR OF PHILOSOPHY (PHOTONICS)**

Title of Project Paper/Research Report/Dissertation/Thesis (“this Work”):

**OPTO-ELASTIC PROPERTIES OF FBG BASED FABRY-PEROT  
RESONATOR: FABRICATION, CHARACTERIZATION, AND  
APPLICATIONS**

Field of Study: **PHYSICS (PHOTONICS ENGINEERING)**

I do solemnly and sincerely declare that:

- (1) I am the sole author/writer of this Work;
- (2) This Work is original;
- (3) Any use of any work in which copyright exists was done by way of fair dealing and for permitted purposes and any excerpt or extract from, or reference to or reproduction of any copyright work has been disclosed expressly and sufficiently and the title of the Work and its authorship have been acknowledged in this Work;
- (4) I do not have any actual knowledge nor do I ought reasonably to know that the making of this work constitutes an infringement of any copyright work;
- (5) I hereby assign all and every rights in the copyright to this Work to the University of Malaya (“UM”), who henceforth shall be owner of the copyright in this Work and that any reproduction or use in any form or by any means whatsoever is prohibited without the written consent of UM having been first had and obtained;
- (6) I am fully aware that if in the course of making this Work I have infringed any copyright whether intentionally or otherwise, I may be subject to legal action or any other action as may be determined by UM.

Candidate’s Signature

Date:

Subscribed and solemnly declared before,

Witness’s Signature

Date:

Name:

Designation:

## ABSTRACT

Fiber Bragg Gratings (FBGs) are highly sensitive to acousto-optic wave, temperature, pressure wave, and etc. FBGs are used in our study to manufacture all-fiber Fabry-Perot resonator (FPR) in different optical fibers. The variations in grating pitch and refractive index of the fiber device are the key contributors to its output spectral response and sensitivity. Opto-elastic properties of FPR play an important role in output spectral response. FBG based all-fiber FPR has been comprehensively studied in this thesis for effective, inexpensive and simple manufacture aspects. The background of FBGs, Fabry-Perot resonators, their fabrication procedures, applications, and operational principles are comprehensively discussed. Moreover, the background study on the widespread theory of opto-elasticity, the correlation of refractive index and stress, in silica based optical fiber is presented.

In this thesis, the fabrication and characterization of FBG based short cavity FPR and PCF cavity FPR are demonstrated. In addition, opto-elastic properties of FBG based FPR in various fibers are studied under the influence of longitudinal waves, pressure and temperature through simulation and experimental investigation.

Additionally,  $LP_{01}$ - $LP_{11}$  cross mode interference is observed in a single chirped grating (CG) inscribed in a two-mode fiber (TMF). Both spatial modes can be concurrently excited using a phase plate at different intensity ratio of  $LP_{01}:LP_{11}$  in the TMF. Diverse interference patterns are formed in the output spectra by the excited input beams. These findings are significant steps in the advancement and characterization of more sophisticated grating structures on single mode and few mode optical fibers. This study will contribute to the understanding and designing of efficient FBG based Fabry-Perot resonators as well.

## ABSTRAK

Fiber Bragg Gratings (FBGs) amat peka kepada gelombang acousto-optik, suhu, gelombang tekanan, dan lain-lain. FBGs telah digunakan dalam kajian kami untuk menghasilkan kesemua gentian Salun Fabry-Perot (FPR) dalam gentian optik yang berbeza. Kepelbagaian nilai di dalam jarak parutan dan indeks biasan peranti gentian adalah penyumbang utama kepada tindak balas keluaran spektrum dan sensitiviti. Sifat-sifat Opto-kenyal FPR memainkan peranan penting dalam tindak balas keluaran spektrum. FBG berdasarkan kesemua gentian FPR telah dikaji secara komprehensif di dalam tesis ini dari aspek keberkesanannya, kos perbelanjaan yang murah serta pembuatannya yang mudah. Latar belakang FBGs, FPR, prosedur pembuatannya, aplikasi, dan prinsip-prinsip operasi turut dibincangkan secara menyeluruh. Selain itu, kajian latar belakang terhadap teori yang meluas tentang opto-keanjalan, perhubungan di antara indeks biasan dan tekanan, di dalam gentian optik berasaskan silika telah dibentangkan.

Di dalam tesis ini, pembuatan dan penyifatan FPR berdasarkan FBG yang berongga pendek dan berongga PCF telah ditunjukkan. Di samping itu, sifat-sifat opto-kenyal FPR berdasarkan FBG di dalam pelbagai gentian telah dikaji di bawah pengaruh gelombang membujur, tekanan dan suhu melalui simulasi dan ujikaji eksperimen.

Selain itu, mod interferens silang  $LP_{01}$ - $LP_{11}$  juga diperhatikan dalam parutan chirped tunggal (CG) yang tertulis di dalam gentian dua mod (TMF). Kedua-dua mod spasial dalam TMF boleh teruja secara serentak dengan menggunakan plat fasa pada nisbah keamatan mod  $LP_{01}$ :  $LP_{11}$  yang berbeza. Corak interferens yang berlainan dalam spektrum output telah terbentuk oleh alur input ujaan. Penemuan ini adalah langkah-langkah penting dalam kemajuan dan pencirian lagi struktur parutan yang lebih moden pada gentian optik mod tunggal dan beberapa mod. Kajian ini akan memberi sumbangan dalam pemahaman dan reka bentuk cekap FPR yang berdasarkan FBG.

## ACKNOWLEDGEMENTS

I would first like to thank Distinguished Prof. Dr. Harith Ahmad for giving me the opportunity to conduct my research at the Optical Fiber Sensors and Laser Laboratory Photonic Research Centre, University of Malaya, Kuala Lumpur, Malaysia. Moreover, I would also thank Dr. Lim Kok Sing and Dr. Chai Hwa Kian, my thesis supervisors, for their continuous guidance, support, patience and encouragement throughout my Ph.D. program. Especially, Dr. Lim has always helped me through several difficult problems of the research and always suggested to me ideas concerning the technical aspects of work. He showed me different ways to approach a research problem and the need to be persistent to accomplish any goal. I have gained much in terms of knowledge and experience in experimental and theoretical research while working with him. Not only scientific works, but he also taught me to broaden my vision when living (studying, culture, and community) in foreign countries. Without his support, patience, and guidance, this research would not have been completed. Also, his openness and willingness motivated me to execute and finish my thesis. Thank you.

I would also like to thank Dr. Chai for his suggestion and allowing me to set a part of my experiment in the Concrete Laboratory, Department of Civil Engineering, University of Malaya, Kuala Lumpur, Malaysia. Without his suggestion, the acoustic emission measurements using Fabry-Perot resonator in the concrete beam would not have been measured.

I acknowledge my collaborators, Dr. Hang Zhou Yang, Dr. Yongmin Jung, Dr. Shaif-Ul Alam, Prof. David J. Richardson, and Prof. Venkata Rajanikanth Machavaram, who give so freely of their time and their talents.

I would also like to express my thanks for Prof. Tong Sun and Prof. Azizur Rahman for reviewing my thesis and also thanks to Prof. Dr. Abrizah Abdullah, Prof. Dr. Rosli

Bin Hashim, and Prof. Dr. Sulaiman Wadi Harun for participating in my viva and giving me for future work.

I would also like to express my deepest gratitude to people who work in PRC, UM (Haniza Anuar, Ili Hanis Alias, Leonard Bayang, and Mohammad Faizal Ismail) for administration help and technical support, and also my colleagues (M. Mahmood Ali, Man Hong Lai, Marya Bagherifaez, Dinusha S. Gunawardena, Yen Sian Lee, Nurul Asha bt. Mohd Nazal, and Muhammad Khairol Annuar Bin Zaini) for their friendship and help.

Due acknowledgment is also given to the Malaysian Government and the University of Malaya for the financial support in the form of a Research Assistantship and Ph.D. research grant (PPP-PG006-2014A). Without those grant, this thesis would not have been realized.

Last but not least, I have to thank my parents for their love and support throughout my life. Thank you both for giving me strength to reach for the stars and chase my dreams. My sister deserves my wholehearted thanks as well. And thank you to all the wonderful people who have helped me enormously and who I did not mention here.

## TABLE OF CONTENTS

Abstract .....	iii
Abstrak .....	iv
Acknowledgements .....	v
Table of Contents .....	vii
List of Figures .....	xii
List of Tables .....	xvi
List of Symbols and Abbreviations .....	xvii
List of Appendices .....	xxi
<b>CHAPTER 1: INTRODUCTION.....</b>	<b>1</b>
1.1 Overview of Fabry–Perot resonator.....	1
1.2 Fiber Bragg Grating and Opto-elastic properties.....	2
1.3 Problem Statement.....	3
1.4 Thesis Motivations.....	3
1.5 Thesis Objective .....	5
1.6 Thesis Outline.....	6
<b>CHAPTER 2: REVIEW OF ALL-FIBER FABRY–PEROT RESONATOR.....</b>	<b>9</b>
2.1 Introduction.....	9
2.2 Operating Principles .....	14
2.3 Fabrication Methods of All-fiber Fabry–Perot Resonators (FPR) .....	17
2.3.1 Optic Fiber FPI using Unspliced Method.....	17
2.3.1.1 Coherence Multiplexing Technique for Remote Sensing Based on FPI .....	17



2.3.1.2	Micromachining Technique .....	19
2.3.1.3	EFPI Ultrasound Sensor Using a Thin Polymer Film .....	21
2.3.1.4	Ionic Self-Assembly Monolayer (ISAM) Technique .....	22
2.3.1.5	Langmuir–Blodgett Technique .....	24
2.3.1.6	Focused Ion Beam (FIB) Milling Technique .....	26
2.3.2	Optic Fiber FPI using Spliced Method .....	27
2.3.2.1	FPI with Dielectric Mirrors by Standard Fusion Splicing Techniques .....	27
2.3.2.2	Semi-Reflective Fusion Splice Technique .....	27
2.3.2.3	Miniature Fiber-Optic Fabry–Perot Interferometric Modulation Technique .....	28
2.3.2.4	Microscopic Air Bubble FPI by Simple Splicing Technique ....	29
2.3.2.5	Two-Mode Interferometric Sensor by Fusion Splice Technique .. .....	30
2.3.2.6	MEFPI Sensor by Chemical Etching Technique.....	31
2.3.2.7	Chitosan-based Fabry–Perot Interferometry .....	31
2.3.2.8	Femtosecond Laser Micromachining and Fusion Splicing .....	33
2.4	Characteristics of Fabry–Perot resonators .....	34
2.4.1	Thermo-optic Effect .....	34
2.4.2	Opto-elastic Effect.....	35
2.4.3	Electro-optic Effect .....	37
2.4.4	Acousto-optic Effect.....	37
2.5	Theory of the Fabry–Perot Resonator.....	38
2.5.1	FBG-based Fabry–Perot Resonator .....	40
2.5.2	Dispersive Bulk Fabry–Perot .....	44
2.6	Applications of All-fiber Fabry–Perot Interferometers .....	45

2.7	Chronology of FP Interferometers.....	55
2.8	Summary.....	67

**CHAPTER 3: THEORIES OF FIBER BRAGG GRATING AND FP  
RESONATOR.....68**

3.1	Introduction.....	68
3.2	Theory of light propagation in optical fiber .....	68
3.2.1	Maxwell's Equations .....	68
3.2.2	Propagation modes in optical fibers .....	72
3.2.3	LP modes and cut off.....	74
3.2.4	Dispersion of light in propagation.....	75
3.3	Fundamentals of Fiber Bragg Gratings.....	76
3.3.1	Phase matching and Bragg condition .....	77
3.3.2	FBG parameters.....	79
3.3.3	Chirped FBG and the grating phase shift .....	81
3.4	Mode Coupling Theory (CMT) for Grating .....	83
3.4.1	Coupling Coefficient for Single Mode grating.....	83
3.4.2	Coupling Coefficient for Few Mode grating.....	86
3.5	Theory of Proposed FBG based FPR .....	90
3.5.1.1	Uniform Period Short-cavity Fiber Bragg Grating Fabry-Perot... .....	91
3.5.1.2	PCF-cavity FBG Fabry-Perot.....	91
3.5.1.3	Chirped Fiber Bragg Grating Fabry-Perot .....	93
3.6	Opto-elasticity and the Characteristics of FBGs .....	96
3.6.1	Effect of Glass Composition on Opto-elasticity.....	98
3.7	Summary.....	100

<b>CHAPTER 4: MODE INTERFERENCE IN CHIRPED FBG .....</b>	<b>102</b>
4.1 Introduction.....	102
4.2 Fabrication of Chirped FBG in TMF .....	104
4.3 Characterization of Mode Interference Characteristics in Chirped FBG .....	105
4.3.1 Experimental Setup .....	105
4.3.2 Phase Plates .....	107
4.3.3 Beam Splitter .....	109
4.3.4 Modelling of LP <sub>01</sub> and LP <sub>11</sub> modes of Two-mode Step Index Fiber.....	111
4.3.5 Modelling the spectral characteristics of CG in TMF.....	112
4.3.6 Spectral response of the CG in TMF under different mode excitations.	113
4.4 Summary.....	117
<b>CHAPTER 5: APPLICATIONS OF FABRY-PEROT RESONATOR.....</b>	<b>118</b>
5.1 Introduction.....	118
5.2 Fabrication of Short-cavity Fabry-Perot Resonator (FPR).....	122
5.3 Fabrication of PCF-cavity FBG Fabry-Perot Resonator .....	124
5.4 Experimental setup for Acousto-optic and Pressure Sensing.....	126
5.5 Acousto-optic sensitivity of Short-cavity FP Resonator .....	130
5.6 Pressure sensitivity of PCF-cavity FBG Fabry-Perot Resonator.....	133
5.7 Von Mises Stress .....	136
5.8 Opto-elastic Response to Acousto-optic of Short-cavity FP Resonator.....	137
5.9 Opto-elastic Response of PCF-cavity FBG Fabry-Perot Resonator to Pressure .	141
5.10 Thermo-optic Response of PCF-cavity FBG Fabry-Perot Resonator to Temperature.....	147
5.11 Summary.....	149

<b>CHAPTER 6: CONCLUSION AND FUTURE WORKS .....</b>	<b>151</b>
6.1 Conclusion .....	151
6.2 Future works .....	152
References .....	155
List of Publications .....	178
Appendix A .....	185
Appendix B .....	187
Appendix C .....	190
Appendix D .....	192
Appendix E .....	194

University of Malaya

## LIST OF FIGURES

Figure 2.1: Experimental arrangement of coherence multiplexing technique for remote sensing based on Fabry–Perot interferometers (Farahi et al., 1988). The abbreviations used in the figure are light emitting diode (LED), fiber directional coupler (DC(f)), fiber Fabry–Perot (FFP), beam splitter (BSD), photodiode (PD), integrator (I), and piezoelectric transducer (PZT).....	19
Figure 2.2: Schematic of a sensor structure. The light is sent and received through the 100- $\mu\text{m}$ core fiber. The cavity length is approximately 7 $\mu\text{m}$ , and the thickness of the membrane is 8 $\mu\text{m}$ (Lee et al., 1994). .....	20
Figure 2.3: Schematic diagram of an EFPI ultrasound sensor (Beard & Mills, 1996). ...	22
Figure 2.4: Experimental humidity sensor system design (Arregui et al., 1999). .....	24
Figure 2.5: Illustration of Langmuir–Blodgett method. (a) Formation of a monolayer film of aliphatic molecules on the water surface represented by hydrophilic circles and hydrophobic rods; (b) deposition of one layer on the optical fiber by passing through the film; (c) after depositing six layers on the fiber end through the film, deposition 7th layer occurred; (d) formation of cavity at the fiber end with patterned refractive indices (Rees et al., 2001).....	25
Figure 2.6: Detail of a Fabry–Perot strain gauge placed on the cantilever beam surface (Valis et al., 1990).....	28
Figure 2.7: Model diagram for the chitosan-coated FPI, RH sensor (Chen et al., 2012). .....	32
Figure 2.8: Illustration of fabrication of an FPI cavity inside the fiber (Liao et al., 2012). (a) Creation of microholes, on the order of $\sim 1$ $\mu\text{m}$ using a femtosecond laser, through the centre of the fiber core. (b) Splicing of the two fiber ends with microholes. (c) Formation of the FP cavity. (d) Introducing the vertical cross-through microcavity for the fabrication of microchannels.....	33
Figure 2.9: FP cavity created between a fiber end and a mirror (Cheung, 2004). .....	39
Figure 2.10: FP cavity created between two fiber ends with supporting members (e.g. capillary tube) (Cheung, 2004) .....	39
Figure 2.11: FP cavity generated by fusion splicing portion of fibers together with a reflective surface to form reflective mirrors (Cheung, 2004) .....	40

Figure 2.12: schematic demonstrating a fiber FP cavity comprising an area of an optical fiber producing a cavity with its ends cleaved such that R is $\sim 4\%$ . b) transmission reaction with a slight visibility yet high intensity throughput through in c) the reflection reaction has a high visibility however a low intensity throughput (Cheung, 2004) .....	43
Figure 2.13: Percentages of the FPI fabrication studies in two categories are presented through some considered time ranges. ....	56
Figure 2.14: Percentage of sensing applications studied through some given time ranges. T = Temperature, Vi = Vibration, A = Acoustic, U = Ultrasound, Vo = Voltage, M = Magnetic, P = Pressure, S = Strain, FV = Flow velocity, H = Humidity, G = Gas, Ll = Liquid level, RI = Refractive index. ....	57
Figure 2.15: Illustration of FPI sensor categories on the basis of their fabrication. ....	64
Figure 3.1: Illustration of light in beam graph experiencing inside reflection while the incident angle to the cladding/core surface is more noteworthy than the critical angle $\phi_c$ (Cheung, 2004).....	73
Figure 3.2: Schematic illustration of structure and spectral response of fiber Bragg grating .....	76
Figure 3.3: Schematic representation of the modes existing in uncoated single mode fibers and the matching condition for the core mode reflection (Cheung, 2004). ....	79
Figure 3.4: schematic of the grating with the boundary conditions in order of appearance (Kashyap, 1999). ....	80
Figure 3.5: Forward and backward modes in FBG (Erdogan, 1997).....	84
Figure 3.6: Illustrative diagram of CG with two spatial modes in TMF .....	87
Figure 3.7: uniform FBG grating FP .....	91
Figure 3.8: Simplified illustrative diagram of the Fabry Perot resonance in the CG-TMF formed by two grating reflectors with linearly varying Bragg wavelengths of $\lambda_{01 \leftrightarrow 01}(z)$ and $\lambda_{11 \leftrightarrow 11}(z)$ respectively .....	93
Figure 3.9: Index of refraction ellipsoid .....	99
Figure 3.10: Variation of opto-elastic constant with lead oxide content (Waxler, 1907) .....	100
Figure 3.11: Variation of photoelastic constant with CaO concentration (Balmforth & Holland, 1945) .....	100

Figure 4.1: Experimental setup for characterization of beam and spectra of CG-TMF. .....	106
Figure 4.2: (a) Phase pattern for LP <sub>01</sub> -LP <sub>11</sub> mode conversion. (b) A cross-sectional view of an LP <sub>11</sub> phase plate with a protruded area that will provide a phase jump of $\pi$ to light passing through that area, where $d$ = phase pattern thickness and $s$ = slope width of the edge (Lee et al., 2016). .....	107
Figure 4.3: Fabrication of phase plate by photolithography and ICP dry etching .....	108
Figure 4.4: Two indistinguishable light beams impinging on the two sides of a beam splitter. .....	110
Figure 4.5: (a) LP <sub>01</sub> mode and (b) line intensity profile of LP <sub>01</sub> .....	111
Figure 4.6: (a) LP <sub>11</sub> mode and (b) line intensity profile of LP <sub>11</sub> .....	112
Figure 4.7: Reflection and transmission spectra of the CG written on two-mode graded index fiber. The dotted grey curves denote the simulated result ( $n_{01}-n_{11}=2.934\times 10^{-3}$ , $\Delta n=5\times 10^{-4}$ , $\eta_{01}=1.00$ , $\eta_{11}=0.9\eta_{01}$ , $\eta_c=0.2\eta_{01}$ , $r=5$ nm/cm, $\lambda_0=530.52$ nm, $L_g=6.9$ mm, (a) Intensity ratio $P_{LP01}:P_{LP11}=1:0$ , (b) Intensity ratio $P_{LP01}:P_{LP11}=0:1$ ). .....	113
Figure 4.8: (a) The figure illustrates the positions of the $0-\pi$ division line (red dotted line) of the phase plate with respect to the input LP <sub>01</sub> beam profile. The blue arrows mark different positions of the $0-\pi$ division line (b) Input mode profiles (Reference) and their corresponding transmitted mode profiles. (c) The corresponding reflection spectrum (experiment) to the mode excitation. .....	114
Figure 4.9: Reflection spectrum of CG inscribed on two-mode graded index fiber. ( $n_{01}-n_{11}=2.934\times 10^{-3}$ , $\eta_{01}=1.00$ , $\eta_{11}=0.9\eta_{01}$ , $\eta_c=0.2\eta_{01}$ , $L_g=6.9$ mm, $\lambda_0=530.52$ nm, $\Delta n=5\times 10^{-4}$ , $P_{LP01}:P_{LP11}=0.5:0.5$ , measured spectral spacing = 0.36 nm). .....	114
Figure 4.10: Reflection spectrum of a CG inscribed on a two-mode step index fiber. ( $n_{01}-n_{11}=1.4715\times 10^{-3}$ , $\eta_{01}=1.00$ , $\eta_{11}=0.9\eta_{01}$ , $\eta_c=0.2\eta_{01}$ , $L_g=8.9$ mm, $\lambda_0=530.52$ nm, $\Delta n=6.5\times 10^{-4}$ , $P_{LP01}:P_{LP11}=0.5:0.5$ , measured spectral spacing = 0.72 nm). .....	115
Figure 4.11: Calculated transmission and reflection spectra of CG-TMF with different $\eta_c$ (assume $\eta_{01}=1$ , $P_{LP01}:P_{LP11}=0.5:0.5$ ). .....	116
Figure 5.1: Transmission and reflection spectrum of the short cavity Fabry-Perot resonator (FPR). .....	123
Figure 5.2: (a) Cross-sectional image of PCF and (b) reflection spectrum of the proposed device. .....	125
Figure 5.3: Experiment setup for the ultrasonic test. .....	128

Figure 5.4: Reflectivity of (a) FBG and (b) FPR, reveal optical resonant that provide the maximum signal. ....	129
Figure 5.5: Experimental setup for characterization of the proposed pressure sensor..	130
Figure 5.6: (a) Frequency response of the PZT–B and FPR sensors while impinging a constant sinusoidal acoustic ultrasonic wave in a frequency range as 0.001-10 MHz (b) Demonstration of single frequency response of each sensor at 6.0 MHz frequency (c) Time domain signal obtained from FPR and PZT–B in case of ~ 6.0 MHz input ultrasonic signal. ....	131
Figure 5.7: Single pulse temporal and spectral responses attained by the FPR and PZT–B, respectively, while the similar spectral responses are shown in the frequency range of 110 kHz to 160 kHz. ....	132
Figure 5.8: Single pulse temporal and spectral responses attained by the FPR and PZT–B, respectively, while the similar spectral responses are shown in the frequency range of 10 kHz to 20 kHz. ....	132
Figure 5.9: (a) Reflection spectra of the proposed sensor at different temperatures, (b) the relationship between wavelength shift and temperature change. ....	134
Figure 5.10: (a) Reflection spectra of the proposed sensor at different pressures, (b) the relationship between wavelength shift and applied pressure. ....	135
Figure 5.11: Axial component of FBG (modulated grating period and grating index) by a sinusoidal wave. Parameters utilized for this modelling are: $p_{11} = 0.121$ ; $p_{12} = 0.27$ ; $v = 5760\text{m/s}$ ; $E = 70\text{GPa}$ . ....	140
Figure 5.12: Radial component (modulated grating period and grating index) of FBG based FPR by a sinusoidal wave. Parameters utilized for this modelling are: $p_{11} = 0.121$ ; $p_{12} = 0.27$ ; $v = 5760\text{m/s}$ ; $E = 70\text{GPa}$ . ....	140
Figure 5.13: The computed wavelength shift brought on by longitudinal wave (black line – Bragg wavelength, red line – modulated Bragg wavelength) ....	141
Figure 5.14: Axial and radial components contributed to refractive index changes.....	142
Figure 5.15: Von Mises stress profile affected by thermal and pressure stress for (a) 6-holes grapefruit PCF microstructured fiber, (b) SMF solid fiber.....	144
Figure 5.16: Simulation profile of radial pressure induced refractive index change for (a) 6-holes grapefruit PCF microstructured fiber, (b) zoom view of (a), (c) SMF solid fiber, when radial pressure is, $P=17.9\text{MPa}$ . ....	146



## LIST OF TABLES

Table 2.1: A brief presentation of the fabrication methods studied above with sensing applications based on the given time slots. ....	61
Table 2.2: Advantages of FPI explored in the literature are presented over given time range.....	64

University of Malaya

## LIST OF SYMBOLS AND ABBREVIATIONS

°C	:	Degree centigrade
2GIF	:	Two-mode graded index fiber
2SIF	:	Two-mode step index fiber
Al	:	Aluminum
ArF	:	Argon Fluoride
ASE	:	Amplified spontaneous emission
BHF	:	Buffered hydrogen fluoride
BPD	:	Balanced photo-detector
BSD	:	Beam Splitter
CCFOFP	:	Cavitybased fiber optic Fabry-Perot
CG	:	Chirped grating
CME	:	Coupled mode equation
CMT	:	Coupled mode theory
dB	:	Decibel
dBm	:	Decibel with reference power as 1 milli Watt (mW)
DC(f)	:	Fiber directional coupler
DC	:	Direct current
DO	:	Digital oscilloscope
EDFA	:	Erbium doped fiber amplifier
EFPI	:	Extrinsic Fabry-Perot interometer
EMI	:	Immunity to magnetic interference
ER	:	Extinction ratio
FBG	:	Fiber Bragg grating

FDM	:	Frequency division multiplexing
FFP	:	Fiber Fabry-Perot
FG	:	Function generator
FIB	:	Focused ion beam
FMF	:	Few-mode fiber
FMF	:	Few-mode fiber
FM-FBG	:	Few-mode fiber Bragg grating
FP	:	Fabry-Perot
FPI	:	Fabry-Perot interferometer
FPMI	:	Fabry-Perot modal interferometer
FPR	:	Fabry-Perot resonator
FSR	:	Free spectral range
FWHM	:	Full width at half maximum
HCl	:	Hydrochloric acid
HOF	:	Hollow optical fiber
ICP	:	Inductively-coupled plasma
ILSCT-ASFP	:	In-line silica capillary tube all-silica fiber-optic Fabry-Perot
ISAM	:	Ionic self-assembly monolayer
ISAM	:	Ionic self-assembly monolayer
ISO	:	Isolator
KrF	:	Krypton Fluoride
LB	:	Langmuir-Blodgett
LED	:	Light emitting diode
LP	:	Linearly polarized
MDM	:	Mode division multiplexing
MEFPI	:	Micro-extrinsic Fabry-Perot interferometer

MEMS	:	Micro electro-mechanical systems
$M\epsilon$	:	Micro strain
NA	:	Numerical aperture
OFLC	:	Optical fiber liquid crystal
OH	:	Hydroxyl
OPL	:	Optical path length
OSA	:	Optical spectrum analyser
PAM	:	Polyacrylamide
PCF	:	Photonic crystal fiber
PD	:	Photodiode
PDDA	:	Poly diallyldimethyl ammonium chloride
PR	:	Positive photoresist
PS-FBG	:	Phase-shifted fiber Bragg grating
PVA	:	Polyvinyl alcohol
PZT	:	Piezoelectric transducer
RH	:	Relative humidity
RI	:	Refractive index
RIU	:	Refractive index unit
$\int$	:	Integrator
SDM	:	Space division multiplexing
SHM	:	Structural health monitoring
SMF	:	Single-mode fiber
TDM	:	Time division multiplexing
TLS	:	Tunable laser source
TMF	:	Two-mode fiber
TMM	:	Transfer matrix method

UV : Ultraviolet

WDM : Wavelength division multiplexing

University of Malaya

## LIST OF APPENDICES

<b>Appendix A:</b>	Matlab code to show modulated grating period and grating index of FBG by a sinusoidal wave	185
<b>Appendix B:</b>	Matlab code to show modulated grating period and grating index of FBG based FPR by a sinusoidal wave:	187
<b>Appendix C:</b>	Matlab code to show LP <sub>01</sub> and LP <sub>11</sub> mode profile:	190
<b>Appendix D:</b>	Matlab code to show line intensity profile of LP <sub>01</sub> and LP <sub>11</sub> :	192
<b>Appendix E:</b>	Matlab code to show LP <sub>01</sub> - LP <sub>11</sub> cross mode interference in CG produced in TMF	194

## CHAPTER 1: INTRODUCTION

### 1.1 Overview of Fabry–Perot resonator

Fabry–Perot (FP) resonators function as fundamental parts of lasers and high-resolution optical spectrum analysers; thus, their functions depend on the superposition or interference of light. Jamin (Jamin, 1856) first assembled an interference device in 1856. They exhibited an exact estimation of the relative refractive index of optical media with this device. Their research shaped the premise on which Mach and Zehnder built up an interferometer of remarkable implication in 1892 (Mach, 1892), now known as the Mach–Zehnder interferometer, which became significant in laser measuring strategies (e.g., laser vibrometers). The most prominent interferometer, which is called a two-beam interferometer, was created by Michelson in 1887 (Michelson, 1887). In the interferometers or resonators technologically advanced later by FP, two (or numerous beams) were made to interfere. This kind of interferometer is consequently known as a multibeam interferometer. In the interferometer developed by Fabry and Perot (1897), the approaching light beam is split into numerous individual components, which all interfere with one another.

The fiber optic FP interferometer exhibit a wide range of structures. The resonating cavity can be intrinsic or extrinsic, implying that the space, in which the light is in part reflected forward and backward by two reflectors, can be inside or outside the optical fiber. For intrinsic cavities, semiconductor reflectors can be developed on the fiber ends. The fiber ends are then grafted together to make an internal mirror. Fiber optic loop mirrors may likewise be utilized. The FP interferometer has a sensitive advantage (of around the cavity finesse) over the Michelson and Mach–Zehnder interferometers. The most significant advantage of optical fiber FP is the solid reliance of the resonant cavity's optical length on natural parameters, such as, temperature, strain, and bending.

The optical path length changes decipher into a phase shift, which is ambiguous from the phase shift brought on by the measurand. Thus, studies on the opto-elastic behaviour of cavity are important to overcome such weaknesses. The accompanying chapter will clarify the sequence of a wide range of FP resonator/interferometer development and their manufacture, principles, and applications.

## **1.2 Fiber Bragg Grating and Opto-elastic properties**

The historical backdrop of optical fibers dated back to the 1960s. In 1969, the first gradient index fibers were manufactured by the collaboration of Nippon Sheet Glass Co. and Nippon Electric Co. for telecommunications applications (Mitschke, 2010). Nevertheless, these fibers experience a high damping of 100 dB/km mostly because of the chemical contamination of the glass. Remarkable advancement was made in the next years; in 1976, enhanced fibers were produced with  $< 1$  dB/km, which were accessible in Great Britain, USA, and Japan. Infrared was utilized then rather than visible light. Today, optical silica ( $\text{SiO}_2$ ) fibers with an attenuation coefficient of  $< 0.2$  dB/km are widely used as standard telecommunications fibers.

In 1978, Ken O. Hill revealed the effect of photosensitivity on germanium-doped fibers. Exposure to ultraviolet light incites a lasting change of the fiber refractive index. The following stride was to utilize this effect and imprint Bragg gratings into fibers, which can reflect very narrow wavelength peaks. The wavelengths of these reflections differ with temperature or when such fibers are strained. The first commercial fiber Bragg grating sensors were available in 1995 from 3M and Photonetics. Since 2000, more than 20 organizations offer Fiber Bragg gratings (FBG) (Mitschke, 2005). Like strain gauges, FBG can be utilized to construct transducers for measuring a wide range of physical quantities.



Understanding the opto-elastic conduct of optical fiber is essential while considering fiber optic devices for applications in mechanical estimations. At the point when the optical fiber core conveying the light experiences mechanical perturbations, which modify the material properties of the optical fiber – an adjustment in the yield optical signal can be observed. The optical response of the optical fiber device can be corresponded with the applied mechanical perturbations, such as stress and strain, on the optical fiber. In this research, several different FBG-based FPR structures are investigated. The optical properties and high sensitivity of the FPRs are directly related to the opto-elastic properties of FBGs and resonator cavity. Therefore, the study of the opto-elastic behaviours of FBGs is very significant in the understanding and design of complex FPR structures.

### **1.3 Problem Statement**

In spite of all the remarkable features of FBG, several challenges in its use in industrial sensing applications still exist. One of the limitations is the low sensitivity of a uniform FBG for acoustic–ultrasonic wave detection. FBG-based FPR can be useful in such application. FBG-based FPR offers advantages in terms of high sensitivity for acoustic–ultrasonic wave detection and wide frequency detection range.

Unlike the standard FBG, the optical structure of FBG-based FPR is more complex, and the opto-elastic properties of FBG-based FPR fabricated from different optical fibers are sophisticated.

### **1.4 Thesis Motivations**

The advancement in laser and fiber optic technology has greatly accelerated the progress in the development and improvement of optical instrumentation frameworks for sensor and telecommunications applications. Fiber optic devices offer great advantages over the conventional electrical counterpart in terms of robustness, compact

size, chemically latent, resistant to the electromagnetic interference (EMI), nonconductive, and simplicity in the integrated system because they do not require extensive electrical wiring for integration. FBG is among the greatest achievements in the development of optical fiber technology. FBGs are fabricated by imprinting a periodic optical structure into a silica fiber by UV laser irradiation, realizing periodic modulation of refractive index specifically into the core of fiber, producing an exceptionally resonant sensing device. Due to the intrinsic fiber properties of these optical devices, FBGs are compatible with most fiber components as well as sophisticated optical structures, such as telecommunications and optoelectronics system. These characteristics support the extensive acceptance of fiber-based components and the advancement of new optoelectronic devices. FBG-based devices offer outright information of wavelength, and the execution of these FBG devices might be designed to make the general system light levels autonomous. Due to these attractive advantages, FBG has been utilized as a part of our research study to fabricate FBG-based FB resonators. Interferometric optical fiber sensors taking into account the optical phase change offer considerably higher resolution for high sensitivity estimation. Fiber-based interferometers, such as FP interferometer, have been produced in this thesis study by utilizing FBGs performing as reflective mirrors. This thesis focuses on the study of the performance of the FBG-based FPR, particularly in acousto-ultrasonic wave detection, simultaneous temperature, and pressure detection. In order to understand the opto-elastic behaviour of FBGs and FPRs and design highly sensitive and robust FBG-based FPRs, the opto-elastic properties of FBGs and FBG-based FPRs have been extensively studied.

The FP resonator utilizing FBGs should be developed in such a way that they can achieve enhanced sensitivity to acousto-ultrasonic wave as well as to temperature and pressure, in which most FPR devices are incapable due to the unresolved cross-

sensitivity issue. The design of such FBG-based FPR requires a thorough study of opto-elastic behaviour of the proposed FBG-based FPR. Information was assembled to provide a foundation for the fabrication and operation of FBG-based FPR devices in general. In addition, in the wake of breaking down in points of interest how acousto-ultrasonic, thermal- and pressure-induced stress could influence the index of refraction (and resultant abnormalities in the FBG readings) of glass fiber. Theoretical investigation was directed to different conditions in glass fiber, causing a change in the index of refraction. Moreover, experimental work was performed to validate the theoretical analysis. The created stress fields can be converted to a change in refractive index, and these non-homogenous indexes of refraction changes are then exhibited to their effect on the FBG signal. The FPR have been characterized based on the responses in applications.  $LP_{01}$ – $LP_{11}$  cross mode interference seen in single-chirped grating (CG) inscribed in two-mode fiber is studied as a part of this thesis. The aim of this mode interference study is to develop and characterize more complex grating structures on few mode fibers. This is probably the first report on experimental and theoretical investigation of non-uniform grating structure in few mode fibers.

## **1.5 Thesis Objective**

FBGs and FPRs have engaged growing consideration regarding its gigantic potential in building photonics parts and coordinated photonic frameworks. This thesis is mainly concerned with the manufacture, characterization, and uses of FBG-based FPRs. The primary focus of this research is to investigate the opto-elastic properties of the cavity of FPR where the FPR is made utilizing FBG.

Various stages associated with the fabrication strategy are acknowledged and completed correctly to protect the manufacture of good quality FBG-based FPR. Some theoretical models are introduced to complement the test information to provide more

top to bottom understanding of the opto-elastic properties of FBG-based FPR and clarification with respect to the characteristics of these FBG-based FPR devices affected by temperature, pressure, and acoustic-ultrasonic impelled stress. Quantitative investigation of the experimental data is conducted using various software, such as Matlab, COMSOL Multiphysics, and Microsoft Excel, in the analytical and characterization investigation of this study. Finally, the uses of FBG-based FPR devices are investigated and illustrated. The demonstration of  $LP_{01}$ – $LP_{11}$  cross mode interference in a single chirped grating (CG) inscribed in two-mode fiber has increased the significance of this study. The key objectives of this thesis are the following:

1. To fabricate a short cavity FBG-based FPR in SMF and a PCF cavity FBG-based FPR.
2. To evaluate the opto-elastic properties of FBG-based FPR in various fibers and the effect of strain-optic tensor and strain vectors of different types to acoustic waves and pressures.
3. To characterize FBG-based FPR under the influence of longitudinal waves, pressure, and temperature through experimental investigation.
4. To demonstrate  $LP_{01}$ – $LP_{11}$  cross mode interference in chirped grating (CG) by both the simulation and experimental analysis along with the characteristics of CG in two-mode fiber (TMF).

## **1.6 Thesis Outline**

In this thesis, theoretical and experimental investigations on opto-elastic properties of FBG-based all-fiber FPR in various optical fibers are exhibited and trailed by an investigation of  $LP_{01}$ – $LP_{11}$  cross mode interference in chirped grating inscribed in TMF.

The first chapter provides a brief overview of the cutting edge of FPR, including the authentic perspective of FBG, the significance of study the opto-elastic properties, thesis objectives, motivations, and outlines.

Chapter 2 incorporates the writing survey of all-fiber FPR. Fabrication strategies are sorted into two groups: based on spliced techniques and based on unspliced techniques. The operating principles of a few FPRs alongside various applications, numerous physical effects on optical fibers, and statistical analysis on the sequence of FPRs advancement are discussed.

Chapter 3 covers the theories alongside opto-elasticity and characteristics of FBG-based FPR in optical fibers. This chapter incorporates the theories of light propagation in the optical fiber (e.g., Maxwell's equation, propagation modes, LP modes, dispersion of light), fundamentals of FBGs with phase matching, Bragg conditions and FBG parameters, mode coupling theories for grating, and theories of FPR.

Chapter 4 shows  $LP_{01}$ – $LP_{11}$  cross mode interference in a solitary chirped grating (CG) inscribed in TMF. Moreover, the creation of CG in TMF and the experimental setup are illustrated. The modal excitation is selectively performed with the aid of a binary phase mask in the investigation and the arrangement of various interference patterns in the output spectra are verified with the simulation results.

Chapter 5 presents the demonstration and characterization of an all-fiber short cavity FPR manufactured in SMF and a PCF-cavity FBG FPR. The discriminative sensing property if there should be an occurrence of cross-sensitivity has been researched. The manufacture of these FPR, experimental setup, and opto-elastic responses from both FPR are likewise contemplated.

The last chapter, Chapter 6, outlines the significant contributions and provides a few proposals for future improvement of the FPR devices.

University of Malaya

## CHAPTER 2: REVIEW OF ALL-FIBER FABRY–PEROT RESONATOR

### 2.1 Introduction

Optical fiber sensors made their first debut over four decades ago since the first photonic sensor had been patented in mid-1960s (U.S. 03327584 granted June 27, 1967). Several techniques are used for functionalizing the optical fiber device in industrial sensing, such as interferometric system, Bragg grating, and resonator. Among them, interferometric based optical fiber sensors have attracted considerable attention because of their prospective applications in sensing temperature, refractive index, strain measurement, pressure, acoustic wave, vibration, magnetic field, and voltage. During this time, numerous types of interferometers have been developed such as FP, Michelson, Mach–Zehnder, Sagnac Fiber, and common-path interferometers. FP interferometer (FPI) fiber-optic sensors have been extensively investigated for their exceedingly effective and simple fabrication as well as low-cost aspects. In this study, a wide variety of FPI sensors is reviewed in terms of fabrication methods, the principle of operation, and their sensing applications. The chronology of the development of FPI sensors and their implementation in various applications are discussed.

The construction of photoinduced gratings in glass optical fibers was first introduced by Hill et al. (1978). A Bragg grating structure is produced in the core of a germanosilicate-made optical fiber by inducing a periodic index change by an Ar ion laser (Wosinski et al., 1994). Optical-fiber sensors are being significantly advanced as they have numerous advantages over conventional sensors, such as the ability to function in hostile environments, high sensitivity, resistance to EMI, and perspectives for multiplexing. In recent times, growing attention has been paid to the embedding of optical fiber sensors in composite materials for the measurement of strain, temperature, and vibration in structures such as spacecraft and airplane wings (Lee et al., 1989).

Interferometer-based fiber optic sensors have been implemented in a wide range of applications since 1980 (Farahi et al., 1988). The FP interferometer (FPI) was invented by physicists Charles Fabry and Alfred Perot who published their most significant article in 1897 (Fabry & Perot, 1897). FP interferometric sensors are very promising among numerous optical fiber sensors proposed in recent times, as they are precise, simple, versatile, responsive, and immune to environmental noise. Optical sensor-based FPIs have been extensively studied because of their tunability and potentiality for signal “amplification” (i.e., resonance). However, the difficulties in device fabrication have limited their commercial growth (Han & Neikirk, 1996). The FP type sensors can be fabricated using air-glass reflectors, in-fiber Bragg gratings, or through semi-reflective splices. Two broad types of FPI fiber sensors are identified in the literature: intrinsic and extrinsic. The following sections aim to introduce some significant developments in all types of FPI fiber sensors. FPI optical fiber sensors have been used in several applications in different fields, such as aircraft jet engine monitoring where inflammable materials and high voltage electricity exists, smart structure monitoring, seismic and sonar applications, the oil industry, downhole measurement in oil wells, fiber optic gyroscopes for navigation purposes, acquiring information from small complex structures, biomechanics and rehabilitation engineering, and biological and chemical sensing.

Fiber-optic interferometer sensors have been developed in several ways by numerous researchers to improve the functionality, efficiency, and potential applications. For example, an intrinsic FP fiber sensor with an optical path length considerably greater than the coherence length of the LED light source was demonstrated, in which low coherence light emitting diode (LED) had been used and modulated by two FPIs to measure temperature (Lee & Taylor, 1991). A fiber-optic FP temperature sensor developed by Tseng and Chen can distinguish between temperature increment and falls



as well as the direction of temperature difference (Tseng & Chen, 1988). Some FPI fiber-optic sensors have been fabricated/improved through the following processes: by embedding in epoxy and also submerging in water for evaluating the ultrasonic sensing performances (John et al., 1997), by micromachining technology with a  $\text{Si}_3\text{N}_4/\text{SiO}_2/\text{Si}_3\text{N}_4(\text{N/O/N})$  diaphragm for pressure sensing (Kim et al., 1997) with a vortex-shedding flowmeter for the measurement of liquid flow velocities in a pipe (Fang et al., 1998), by creating a low-finesse FP cavity between the end of a polished fiber tip for displacement sensing (Pepe et al., 1998), by low-finesse FPI for generating fringes with good visibility (Wang et al., 1998), with a patch-type extrinsic FP interferometer (EFPI) in order to conquer interferometric non-linearity, applied to the active suppression of flutter to reduce the amplitude of the flutter mode as well as increase the speed (Kim et al., 2005), based on a nano-interferometric optical cavity by the novel ionic self-assembly monolayer (ISAM) technique for humidity sensing (Arregui et al., 1999), by a three-wavelength passive quadrature digital phase-demodulation scheme with low-coherence (Schmidt & Furstenau, 1999), by fusing several fibers with different core diameters for use in harsh gamma-radiation environments (Lai et al., 2003), by depositing a partly reflective dielectric or metallic coating on the tip of a fiber-optic, or a glass or polymer planar substrate, and a close to entirely reflective coating on a polymer film spacer to create the mirrors of the FPI sensor (Cox et al., 2004), and by bonding the silica fiber, with the ferrule, the tube, and the diaphragm together to form an interferometer with a sealed cavity for detecting acoustic emissions (Deng, 2004), using a technique silicon-to-silicon anodic bonding or a polymer structure with SU-8 on silicon wafer (Peng et al., 2013) a micro electro-mechanical systems (MEMS) structure for pressure sensing (Saran, 2004), by depositing polyaniline and Nafion layers on the face of sensor head for ammonia gas sensing (Opilski et al., 2005), by cascading a single-mode fiber (SMF), a photonic

crystal fiber (PCF), and a hollow optical fiber (HOF) for high-temperature sensing (Choi et al., 2008), by a suspended core between two single mode fibers for a FP refractive index (RI) sensor for low temperature sensitivity (Frazao et al., 2009), by using a diaphragm based on a polymer material for acoustic sensing Wang & Yu, 2010, by the measured sample and the exteriors of a sensing fiber end for optical glass RI measurement (Chen et al., 2010), by a miniature all-silica fiber optic EFPI sensor with an embedded Fiber Bragg grating (FBG) reference sensor element to determine temperature and pressure (Reinsch et al., 2012), by a thin film polyvinyl alcohol (PVA)-coated SMF tip for extreme temperature sensing (Rong et al., 2012), by an SMF with a Metglas ( $\text{Fe}_{77.5}\text{B}_{15}\text{Si}_{7.5}$ ) wire-based magnetostrictive transducer (Oh et al., 1997; 2004) or, a magnetic fluid (Lv et al., 2014; Zhao et al., 2012) to measure magnetic fields, and by coating it with a thin film of SU-8 photoresist and dipping it into a nano-magnetic fluid for measuring magnetic fields (Jin et al., 2013).

In addition, a number of FPI fiber-optic sensors and their performance have also been reviewed in this chapter, such as an FP cavity constructed by aligning two fiber endfaces in a hollow-core fiber in an EFPI fabrication (De Vries et al., 1997). Multiple path-match techniques are used for absolute phase measurement in an EFPI sensor (Chang & Sirkis, 1997). Tiny sensor heads for point measurement is significant in many applications. An FPI with a low-finesse and tiny cavity is a smart option for the fundamental sensing component. From an application point of view, it is very useful because of its compactness and straightforwardness (Kim et al., 2005). Several fiber-optic sensors derived from the MEMS technology have been proposed earlier (Wang et al., 2005; Lai et al., 2011). The use of MEMS technology is preferable due to its possible vast economical manufacturing and inexpensive products. A composite cavity-based fiber optic FP (CCFOFP) strain sensor can be fabricated using an electrical scanning mirror and a fiber optic Michelson interferometer in which the improvement

of the dynamic measurement range and multiplexing capability are observed concurrently when evaluating with the extrinsic fiber optic FP (EFOFP) strain sensor (Zhang et al., 2008). A two-mode interferometric sensor is manufactured from photonic crystal fiber (PCF) for ultra-high temperature measurement ( $\leq 1,000$  °C) (Coviello et al., 2009). A hybrid fiber-optic sensor is constructed by combining FPI and MI sensors (Jedrzejewska-Szczerska et al., 2011) with an asymmetric dual core micro-structured fiber (Frazao et al., 2010). A dual-core microstructured fiber is used to form two parallel FP cavities with low finesse between its endface and region of splicing (Lai et al., 2011). A PDMS-based polymer-based in-plane silicon FP interferometer was constructed for chemical sensing (St-Gelais et al., 2013). A non-contact vibration sensor is fabricated from an SMF extrinsic FP interferometer (EFPI) and the extracted wavelet transform optical data is used for developing a novel signal decoding technique to overcome the limitations of demodulated signals caused by complex fringe and phase ambiguity (Gangopadhyay et al., 2005). Coviello et al. (2009) reported that the two-mode interferometer sensor head requires an extended burn in terms of thermal annealing to attain its steady state and a sufficient level of functionality regardless of being robust and compact.

Few review articles have partly discussed common fabrication, sensing technologies, and measurands of FP interferometric fiber-optic sensors, including (Vahala, 2003), which only covers microcavities that play a significant role in forming FPI, vibration sensing in (Zhang et al., 2013), strain measurement in (Zhou & Sim, 2002), acousto-ultrasonic sensing in (Wild & Hinckley, 2008), and also a number of recent reviews given in (Lee et al., 2012) where the recent trends of FPI fabrication, methods, and application were reported. Reference (Jorge et al., 2012) explains RI sensing, and in-line fiber optic FPI formed by using SMF is covered in (Zhu et al., 2012), nevertheless, they did not completely cover all the latest and promising as well as previously reported

applications of FPI sensors, their remarkable fabrication processes and operating principles, which provides a reason to conduct a comprehensive study on FPI sensors. Although some books (Yin et al., 2008; Kashyap, 2009) on fiber optic sensors which detailed a general study of fiber Bragg gratings and fiber optic sensors, including some applications of FPI sensors, have been published, this chapter intends to offer a complete summary of the fabrication methods, sensing applications, and operation principles of FPI sensors in terms of the advances carried out up to recent days as well as the current status of progress in related research from all over the world. This chapter is intended for enhancing readers' understanding of the state of the art of FPI optical sensors and their applications, as well as offering better ideas for conducting further research in this exciting area.

## 2.2 Operating Principles

The FPI sensor consists of a cavity between two semi-reflective surfaces or one that is semi-reflective and the other is a full-reflective surface; thus, the total reflection will be the result of two reflective powers, i.e.,  $R_1$  and  $R_2$ , which can be expressed as (Xie, 2006):

$$P_r = P_i \left( R_1 + R_2 - 2\sqrt{R_1 R_2} \cos \varphi \right) \quad (2.1)$$

where  $P_i$  and  $P_r$  are the incident and reflected optical powers, respectively,  $R_1$  and  $R_2$  are the reflections from reflective surfaces ( $R_1$  and  $R_2$ )  $\ll 1$ , and  $\varphi$  is the phase shift of complete cycle from one reflective surface to another reflective surface, which can be written as:

$$\varphi = \frac{4\pi nL}{\lambda} = \frac{4\pi n f L}{c} \quad (2.2)$$

where  $n$  is the RI,  $L$  is the total cavity length of FPI,  $\lambda$  is the optical wavelength,  $f$  is the optical frequency, and  $c$  is the velocity of light.

From Equation (2.1), the reflected power  $P_r$  can be varied by varying the phase shift, which depends on the different physical parameters described as:

$$\varphi = \varphi_{initial} + \Delta\varphi_L + \Delta\varphi_f + \Delta\varphi_\tau \quad (2.3)$$

with:

$$\Delta\varphi_L = \frac{4\pi}{\lambda}(n\Delta L + L\Delta n) \quad (2.4)$$

$$\Delta\varphi_f = \frac{4\pi L}{c}\left(n + f \frac{\Delta n}{\Delta f}\right) \quad (2.5)$$

$$\Delta\varphi_\tau = \frac{4\pi}{\lambda}\left(L \frac{\Delta f}{\Delta T} + n \frac{\Delta L}{\Delta T}\right) \quad (2.6)$$

where  $\varphi_{initial}$  is the initial phase shift and  $\Delta L$ ,  $\Delta n$ ,  $\Delta f$ , and  $\Delta T$  are the changes in length, RI, frequency, and temperature, respectively.

Equation (2.2) is the FPI principle equation used by many researchers for different types of applications, i.e., strain, temperature, pressure, magnetic field, voltage, humidity, and vibration sensing. A variety of hypotheses concerning FPI fabrication and characterization are presented in the literature. For the reader's better understanding, some examples of the working principle equations of different sensors are given in this study. For magnetic field sensing, the RI of the cavity can be related to the magnetic field by (Zhao et al., 2012):

$$n = (n_s - n_0) \left\{ \coth\left(\alpha \frac{H - H_c}{T}\right) - \frac{T}{\alpha(H - H_c)} \right\} + n_0 \quad \text{for } H > H_c \quad (2.7)$$

where  $H_c$  is the critical value of the magnetic field,  $n_0$  is the RI of the magnetic fluid under the critical magnetic field,  $n_s$  is the saturation value of the RI of magnetic fluid, and  $\alpha$  is the fitting coefficient. For a certain kind of magnetic fluid film,  $n_s$ ,  $n_0$ ,  $\alpha$ , and  $H_c$  are constants. For a given temperature  $T$ ,  $n$  can be easily determined by  $H$ .

The humidity sensor based on RI change is also reported in (Yao et al., 2012). In this configuration, an FPI with an open interferometric cavity is coated with polyacrylamide (PAM), which is a humidity sensitive material. The RI of PAM varies when it absorbs water vapour. This induces a spectral shift  $\Delta\lambda_v$ , and the relationship is given by:

$$\frac{\Delta\lambda_v}{\Delta n} = \frac{\lambda_v}{n_{PAM}} \quad (2.8)$$

where  $\lambda_v$  is the centre wavelength of reflection,  $n_{PAM}$  is the RI of PAM, and  $\Delta n$  is the PAM RI change. The distance between two interference peaks is given by:

$$\lambda_2 - \lambda_1 = \frac{\lambda_1 \lambda_2}{2n_{PAM}L} \quad (2.9)$$

where  $\lambda_1$  and  $\lambda_2$  are the wavelengths of consecutive FPI reflection peaks, and  $L$  is the cavity length. The RI of PAM will be changed when humidity changes, which can be used as a principle for humidity sensing. An FPI is sensitive to variation in gas RI, and gas RI is a function of pressure. Based on this principle, an FPI can also serve as a pressure sensor as reported in (St-Gelais et al., 2013).

The cavity length of an FPI is sensitive to vibration, and this has been investigated in detail by Jia et al. (2012). A microelectromechanical system (MEMS)-based ultra-sensitive FPI sensor has been developed for acoustic wave sensing (Wang et al., 2005), and it has been demonstrated for partial discharge detection inside high voltage transformers. In this sensor, the FPI cavity length is modeled as:

$$\Delta L = \frac{Pa^4(1-\nu^2)}{4.2Eh^3} \quad (2.10)$$

where  $P$  is the ambient pressure related to cavity pressure,  $\Delta L$  is the cavity length, which actually is the deflection of the membrane,  $a$  is the half side length and  $h$  is the thickness of the membrane, and  $E$  and  $\nu$  are the Young modulus and Poisson ratio of the membrane material, respectively.

### **2.3 Fabrication Methods of All-fiber Fabry–Perot Resonators (FPR)**

Several varieties of optical fiber have been used for the development of the FPI sensors. Yoshino et al. fabricated an FPI sensor using SMFs by optically polishing and coating the two end faces with a multilayer of dielectric films based on a method called vacuum evaporation (Yoshino et al., 1982). A single two-core fiber has been used to develop FP interferometric sensors for concurrent comprehensive measurement of temperature and strain. This FPI is made of a pair of low reflection Bragg gratings that are holographically written with a time-division multiplexing (TDM) technique (Yoshino et al., 1982). Various interesting and challenging FPI fabrication methods can be found in the literature. The authors managed to categorize some of the significant methods into two groups: fabrication of FBI sensors with and without splicing methods. Some selected methods are presented in the following subsection.

#### **2.3.1 Optic Fiber FPI using Unspliced Method**

##### **2.3.1.1 Coherence Multiplexing Technique for Remote Sensing Based on FPI**

The unbalanced FPI using frequency division multiplexing (FDM) technique is illuminated by modulating the frequency, and appropriate amplitude is selected to force all the interferometer over an integral and a dissimilar number of fringes. Then, for every sensing component a pseudoheterodyne carrier is developed that involves crosstalk. Furthermore, utilizing FPIs, as proposed by Dakin et al. (Dakin & Wade, 1984), leads to the same problem. A coherent signal is generated in the image plane due

to highly scattering objects and shows similarity with that of sample depth within the length of coherence is referred to as “crosstalk”, which is critical for the lengths for several sensors and limits the number of sensors used. Consequently, a FP fiber-optic sensor with coherence multiplexing is constructed to overcome this drawback (Farahi et al., 1988). A super-luminescent diode source is used for illuminating two FP sensors. These FP sensors are created inside a compact fitting capillary tube by cleaving a single-mode optical fiber as shown in Figure 2.1. Each path length of the FP sensors, as well as the difference between the paths length, are larger than the length of the source’s coherence. A bulk optic Michelson interferometer is used to detect the interferometric fringes by sequentially matching the difference of path length for each FP fiber. The coherence length of the light source can be estimated by considering the visibilities of the fringes, and the translation stage at a stable velocity over the zero path length mismatches (Farahi et al., 1988). Another low-coherence technique for multiplexed measurements on a fiber sensor array was proposed by Sorin and Baney (Sorin & Baney, 1995).



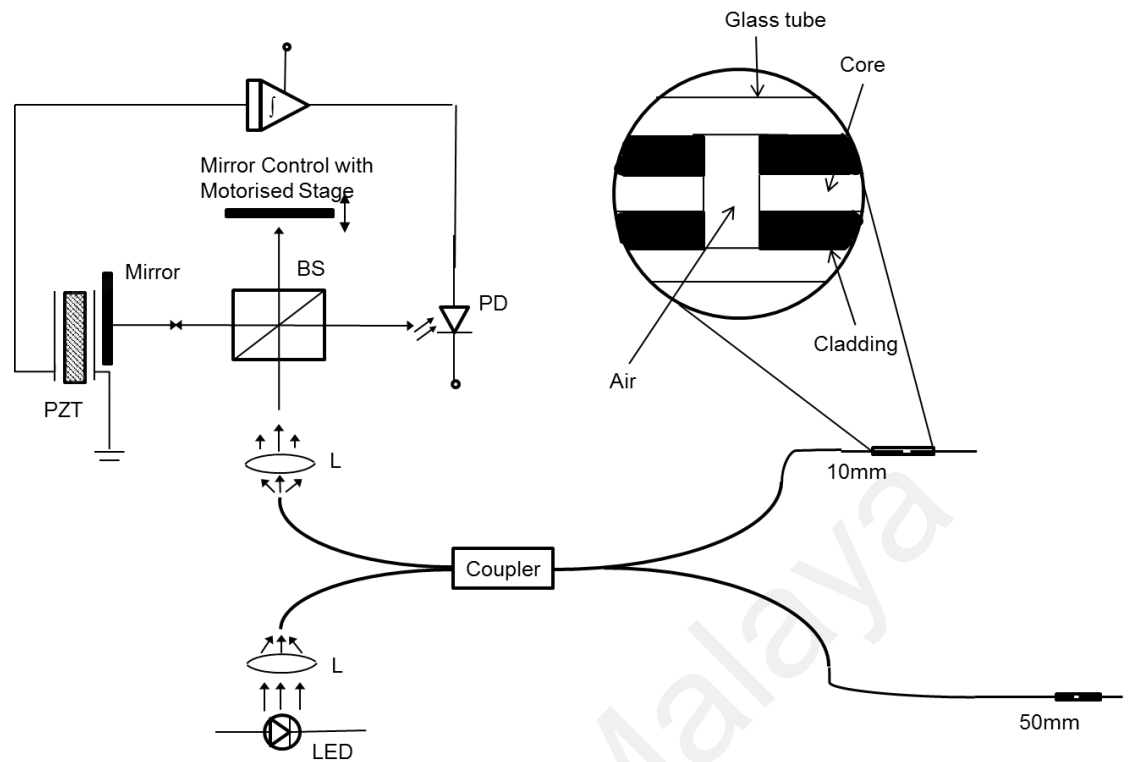


**Figure 2.1: Experimental arrangement of coherence multiplexing technique for remote sensing based on Fabry-Perot interferometers (Farahi et al., 1988). The abbreviations used in the figure are light emitting diode (LED), fiber directional coupler (DC(f)), fiber Fabry-Perot (FFP), beam splitter (BS), photodiode (PD), integrator (J), and piezoelectric transducer (PZT).**

### 2.3.1.2 Micromachining Technique

A FP cavity is formed by two light-reflecting surfaces. The amount of light passing through the cavity depends on the partition between the two reflecting surfaces. Accordingly, if one of the surfaces is made of a membrane that deflects with pressure, the light output changes according to the magnitude of the membrane deflection. Such a strategy has been found in an FPI sensor that was fabricated on a 200  $\mu\text{m}$  thick-silicon wafer using the micromachining techniques (Lee et al., 1994). The overall view of the sensor is drawn in Figure 2.2.

The sensor is attached to the end of a Corning Pyrex tube with 1 mm inner diameter (ID). A 6.8  $\mu\text{m}$ -deep etching on one side is used as a separation between the two surfaces. This separation gap is used for the convenience of using an LED light source

that is more economical, but on the other hand, the limitations of utilizing LEDs should be considered as well, such as their considerably larger spectral bandwidth and considerably shorter length of coherence, which is much shorter than that of a laser (Lee et al., 1994). A miniature based mechanical membrane structure is fabricated on silicon wafers by anisotropic etching in potassium hydroxide. First, a photolithographically structured window is etched to a depth of  $178\ \mu\text{m}$  on one side after the specific alignment of the masking patterns equally on each side of the silicon wafer. Then, both sides are etched to a depth of  $7\ \mu\text{m}$ , which yields the required cavity depth and membrane thickness of  $8\ \mu\text{m}$ .

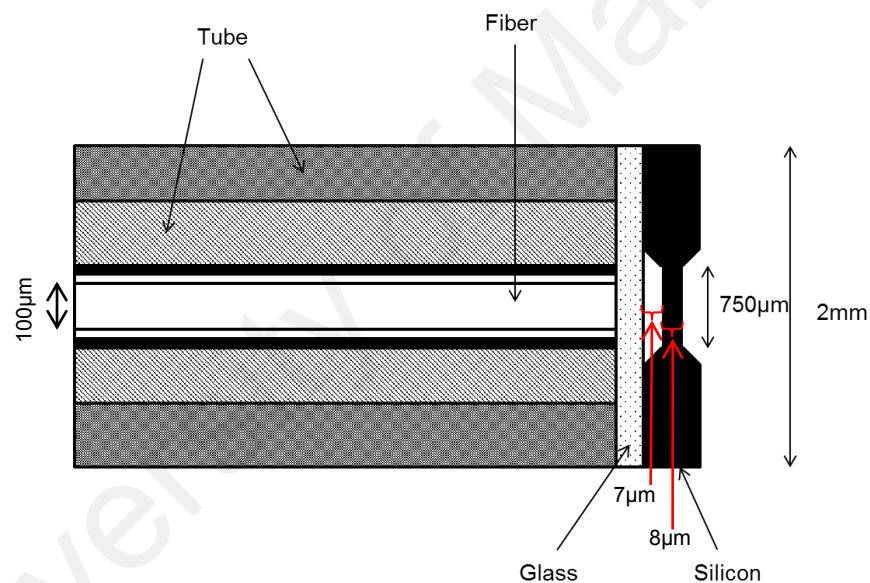


**Figure 2.2: Schematic of a sensor structure. The light is sent and received through the  $100\text{-}\mu\text{m}$  core fiber. The cavity length is approximately  $7\ \mu\text{m}$ , and the thickness of the membrane is  $8\ \mu\text{m}$  (Lee et al., 1994).**

The upper side of the membrane in a (100) crystal plane is polished to optical quality to enable reflection. Finally, a vent hole is created in the micromachined cavity to avoid any obstruction at a higher pressure caused by any resistance from the compressed air that is otherwise trapped in the cavity (Lee et al., 1994).

A micromachined FP interference based microcavity structure for pressure sensing was studied in (Lee & Taylor, 1988) as well. Based on the same technique, Boyd et al. developed a fiber optic sensor based on FPI, and it has been patented (Boyd et al., 2005).

### **2.3.1.3 EFPI Ultrasound Sensor Using a Thin Polymer Film**

An FPI is fabricated using a slim transparent polymer film that acts as a low-finesse FPI for ultrasound sensing. For the reason that the polymer film itself is an interferometer, shorter path length, low sensitivity to pressure, and thermal differences result from the use of a slim polymer film as an FPI sensing component. As a result, phase-bias-control and complicated polarization systems are not essential. A wavelength-tunable laser diode is used as a laser light source, and the laser light is launched into a multimode optical-fiber down-lead (see Figure 2.3). Fresnel reflection coefficient is a significant parameter for interferometric mirrors, is related with mismatching between the refractive indices of the surrounding media and both sides of the sensing film, no additional reflective coating is required. When the acoustic waves are applied to the sensor, the optical phase mismatch between two reflections is induced due to modulation of the film and consequently, an optical intensity modulation is induced, which is then reflected back through the fiber for detection by a photodiode (PD). The sensor is controlled and maintained at quadrature by tuning the laser diode wavelength for the best possible linearity and sensitivity. The cavity, which is the gap between the fiber end and the sensing film, is filled with water due to a couple of reasons: first, it gives the best possible fringe visibility of unity, the reflection coefficients on each side of the film will be the same, and second, it gives more acoustic-impedance matching between the fiber end and the sensing film. On the other hand, it will distort the uniformity of the frequency response of the sensor (Beard & Mills, 1996). Similarly, the low-finesse FPI technique has been used for strain sensing

with some modifications (Jiang & Gerhard, 2001) and has been patented (Elster et al., 2002; Wavering et al., 2003; Sirkis, 1994).

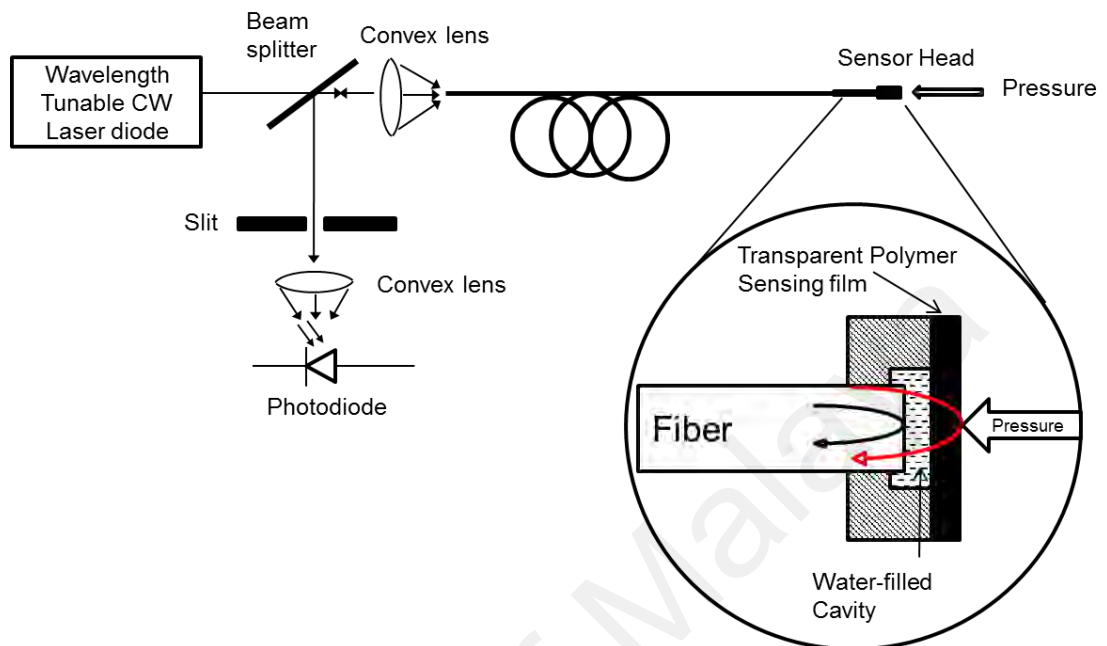


**Figure 2.3: Schematic diagram of an EFPI ultrasound sensor (Beard & Mills, 1996).**

#### 2.3.1.4 Ionic Self-Assembly Monolayer (ISAM) Technique

The ionic self-assembly method (ISAM) was first proposed by Arregui et al. (Arregui et al., 1999) for the fabrication of nano-FPI as a humidity sensor. This is a well-recognized technique and has been implemented for a long time in the fabrication of various thin film materials on substrates of numerous shapes and sizes. This method is based on the principle of the electrostatic force of attraction between the opposite charges of molecules of the thin film deposited on the substrate. In (Arregui et al., 1999), an optical fiber, treated as a substrate, is cleaned and processed to induce surface charges. Afterward, the processed substrate is dipped into the solutions of oppositely charged polymers, alternately, to produce a multilayer thin film.

Arregui et al. used a solution of sodium 4-styrenesulfonate for making the anionic electrolyte in order to fabricate a humidity sensor (Arregui et al., 1999), whereas poly

R-478 (anthrapyridone chromophore) is used in (Arregui et al., 2000) to achieve fast sensor response time. The Au:PDDA cationic electrolyte is formed by a solution of gold colloids contained by a polymer coating of poly(diallyldimethyl ammonium chloride) (PDDA). Using the aforementioned solutions, a bi-layered structure i.e.,  $[\text{Au:PDDA}^+/\text{PSS}^-]_n$ , is fabricated at the fiber end by the ISAM process, where  $n$  denotes the total number of fabricated bilayers. The humidity sensor setup is shown in Figure 4, arranged after the build-up of the coating of  $[\text{Au:PDDA}^+/\text{PSS}^-]_n$ . Two photodetectors are used to monitor the reference optical power for the incident signal at the coating, and the other measures the reflected optical power. For observing the interferometric phenomenon, a LED source is used instead of a laser source for the same reasons stated in (Lee et al., 1994). The humidity sensor is set up via a small hole through a sealed receptacle as shown in Figure 2.4 and hung in the air near above the given solutions for humidity sensing (Arregui et al., 1999).

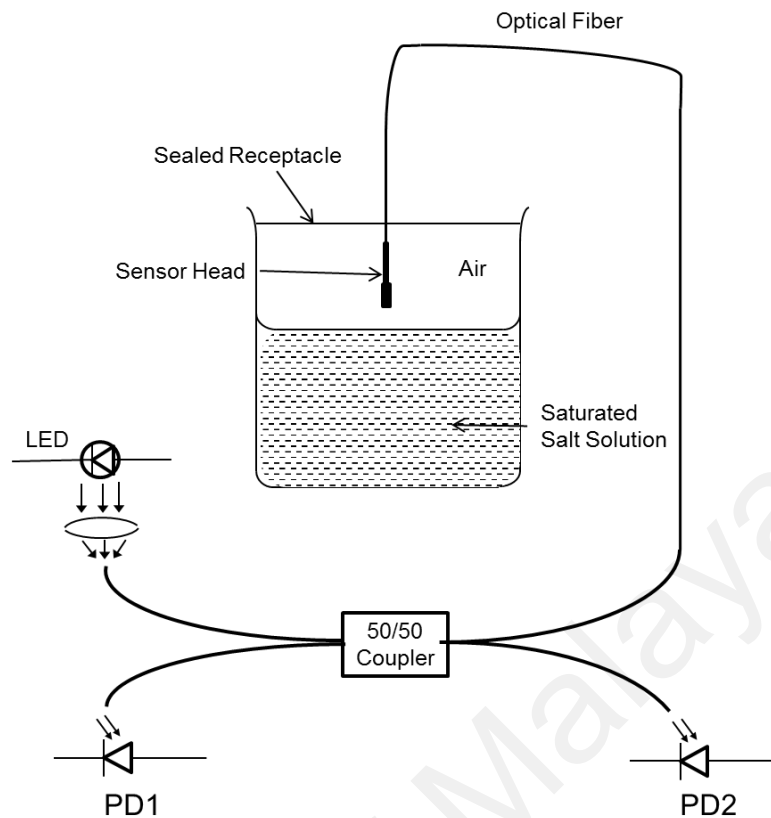


**Figure 2.4: Experimental humidity sensor system design (Arregui et al., 1999).**

### 2.3.1.5 Langmuir–Blodgett Technique

An alternative to the ISAM process, i.e., the Langmuir–Blodgett (LB) process is also presented in (Rees et al., 2001) for the synthesis of multilayer films having thicknesses in the order of nanometres. A sub-micrometer FPI is fabricated by using the LB technique, which allows the thickness management at the molecular level and the layer-by-layer deposition of multilayer structures. The FPI fiber-optic cavity can also be fabricated from a single chemical species by this technique. Such homogeneity of fabrication is unattainable with other methods, for example, the ISAM method, which requires alternate layers of materials, charged oppositely.

Tricosanoic acid [ $\text{CH}_3(\text{CH}_2)_{21}\text{CO}_2\text{H}$ ] is used as the cavity material for this technique. The acid is spread using a dilute chloroform solution with  $0.1 \text{ mg}\cdot\text{cm}^{-3}$  density, over the pure water surface that is the subphase of one compartment of a Nima Technology LB

trough, and left for approximately 10 min at  $\sim 20\text{ }^{\circ}\text{C}$ , then compressed at a rate of  $0.5\text{ cm}^2\cdot\text{s}^{-1}$ , and deposited vertically with a rate of  $1\text{ cm}/\text{min}$  onto the fiber end at a certain surface pressure, i.e.,  $30\text{ mN}\cdot\text{m}^{-1}$ . The cleaved face fiber is perpendicular to the surface plane of the film. Y-type structures are fabricated passing the fiber end through the film where the amphiphilic molecules are rearranged in head to head structures and tail to tail structures, as shown in Figure 2.5(a–c). The deposition of multilayers using the LB technique on the fiber end forms a cavity where the first mirror is formed at the optical fiber, and LB interface and the other mirror is formed at the LB film and air interface, as shown in Figure 2.5d.

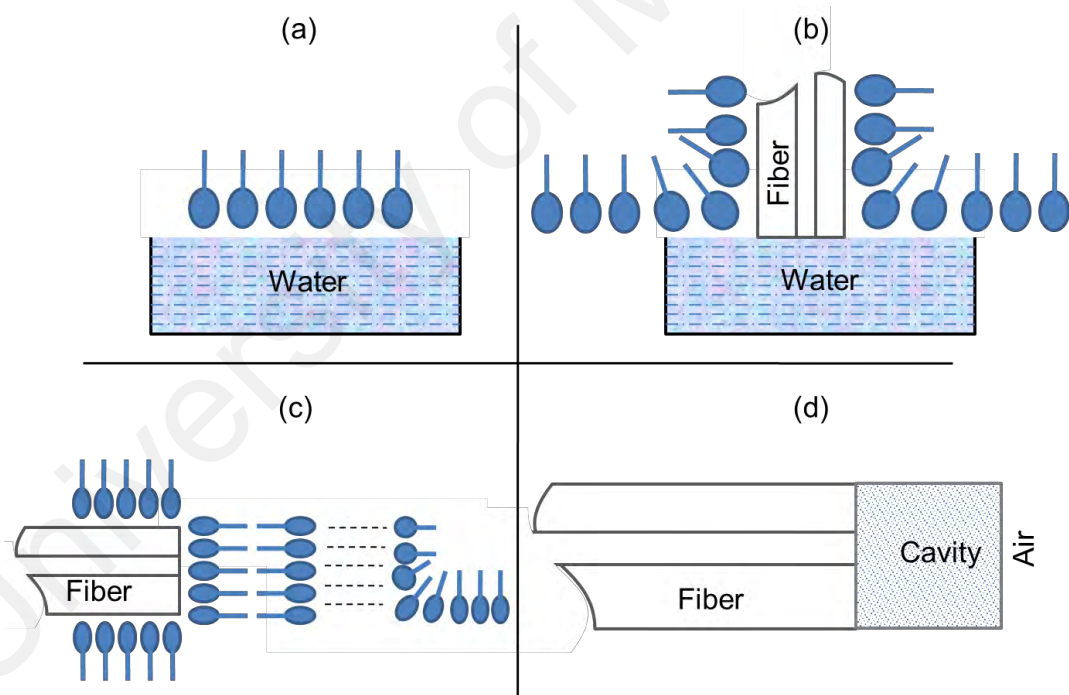


**Figure 2.5: Illustration of Langmuir–Blodgett method. (a) Formation of a monolayer film of aliphatic molecules on the water surface represented by hydrophilic circles and hydrophobic rods; (b) deposition of one layer on the optical fiber by passing through the film; (c) after depositing six layers on the fiber end through the film, deposition 7th layer occurred; (d) formation of cavity at the fiber end with patterned refractive indices (Rees et al., 2001).**

### 2.3.1.6 Focused Ion Beam (FIB) Milling Technique

FIB milling is applied on the fiber end to fabricate an all-glass FP modal interferometer (FPMI) as alternative technique for fabricating ultra-small, micro-cavity sensors with an air-gap based on FPIs for relatively higher temperature sensing (Kou et al., 2010). FIB milling is an ideal technology for nanofabrication and micromachining because of its tiny and convenient spot size (on the order of a few tens of nm). A micro-cavity can be fabricated in order of sub-wavelength fiber, while the higher current density of an electron beam is used during FIB milling. A micromachined fiber end with tapered structure can be developed by an SMF with splicing through MMF method which can be used as a highly sensitive modal interferometer. A micro-notch cavity is machined directly on an SMF tapered end to fabricate a tapered FPMI sensor. The cavity measures a few micrometres in height, width, and length. Sensing can be measured by the reflection of light from the end-faces of the cavity. The temperature sensitivity of proposed sensor is approximately 20 pm/°C.

The fabrication of an optimal fiber tapered end structure can be done by using a commercially available pipette puller with optimized pulling velocity and CO<sub>2</sub> laser power. The tapered end is coated with a 150 nm-thick aluminum (Al) layer through vacuum evaporation deposition. Accumulation of gallium ion is prevented by this Al layer in FIB micromachining process. Subsequently, the Al-coated fiber tip is positioned steadily in the FIB milling chamber using a conductive tape. In the end, the Al layer is totally removed by dipping the micro-machined tapered fiber end in hydrochloric acid (HCl) for 30 min. Then, deionized water is used to clean it properly before use.



### **2.3.2 Optic Fiber FPI using Spliced Method**

#### **2.3.2.1 FPI with Dielectric Mirrors by Standard Fusion Splicing Techniques**

Dielectric mirrors are used in continuous lengths of single mode fiber to formulate reflectively monitored FP interferometers by the fusion splicing technique for use as wavelength and temperature sensors (Lee et al., 1988). Electric arc fusion is applied for splicing two single mode fibers, one of their ends is coated with an  $\sim 1400 \text{ \AA}$   $\text{TiO}_2$  layer. Splicing is controlled at lower values of arc current and a shorter period of time than usual. Thus, several splicing pulses are required to construct each mirror. A pulsed light source is used for monitoring the reflectance throughout this process. The reflectance diminishes with every splicing pulse followed by an initial increase, and the fabrication of that mirror is completed when the required reflectance is attained. The demonstration of this sensor in the temperature and strain measurement is reported in previous studies (Lee et al., 1988; Lee et al., 1989).

#### **2.3.2.2 Semi-Reflective Fusion Splice Technique**

A 10 mm-long strain sensor was fabricated and placed on a cantilever beam surface for the formation of all-fiber FPI strain sensor using a simple semi-reflective fusion splice technique (Valis et al., 1990). Two cleaved fiber ends with York  $3.5 \mu\text{m}/125 \mu\text{m}$  specifications are coated with silver by dipping into a Rochelle solution for one hour. Then, both fiber ends are spliced with a fusion splicer by applying a sequence of fusion cycles until the desired reflectivity has been achieved.

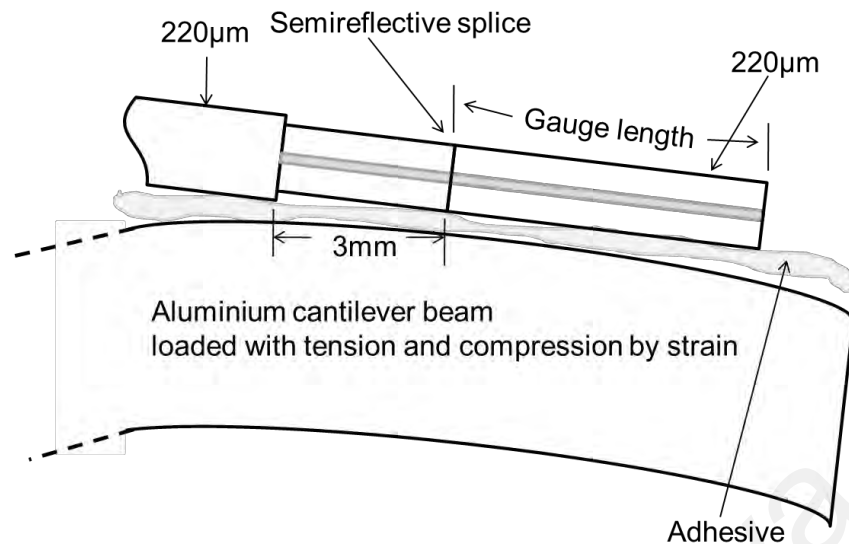


**Figure 2.6: Detail of a Fabry–Perot strain gauge placed on the cantilever beam surface (Valis et al., 1990).**

FPI cavity is fabricated by cleaving and silvering the fiber end that is 10 mm away from the splice. The other FPI mirror is made highly reflective, instead of being matched with the first. A cleaved and silvered fiber end provides a distinctive reflectivity of 0.8 that introduces the notion of semi-reflection. The FP strain sensor is attached to an aluminum beam surface by using cyanoacrylate adhesive as shown in Figure 2.6. The beam is considered as a cantilever, and it is eventually loaded with tension and compression through a strain within a range of 1000  $\mu\epsilon$ ; the phase–strain relation was linear and symmetric with respect to tension and compression (Valis et al., 1990).

### **2.3.2.3 Miniature Fiber-Optic Fabry–Perot Interferometric Modulation Technique**

Two pieces of HiBi fiber are spliced with each other and then one of the given HiBi fibers is cleaved closer to the point of splicing for fabricating a miniature FPI temperature sensor with a length of  $\sim 3$  mm. The half waveplate and the first beam splitter are positioned by a selective fiber coupler create a more practical and easy to construct system. The interferometric phase change of the carrier is measured whereby

the fiber sensing generates a gradual shift in temperature ranging from  $\sim 23$  °C to  $\sim 32$  °C (Farahi, 1991).

The cavity of a low-finesse FPI sensor is fabricated by two parallel mirrors with less reflectivity and a fixed separation distance (Ezbiri & Tatam, 1996; Perennes et al., 1999). A number of signal processing techniques are proposed to support sensing measurements. However, all these techniques suffer from phase mismatch because of multiple reflections which occur at the boundaries of two reflecting surfaces. To overcome this problem, a passive signal processing technique has been proposed for miniature FPI sensors as in a previous study (Ezbiri & Tatam, 1996), which is based on phase stepping methods, and the adjacent axial modes are used by the multimode laser diode to achieve four outputs with phase shifted intensities.

A high-temperature sensor using a miniature FPI is constructed with short hollow-core fiber (HCF) with a piece of SMF by fusion splicing. The lengths of HCF and SMF used in the reported work are 70  $\mu\text{m}$  and 510  $\mu\text{m}$ , respectively, which are indeed tiny (Choi et al., 2008). A micro-cavity FPI and a Mach–Zehnder interferometer are constructed by splicing two SMFs to both ends of a PCF fiber to form a strain sensor (Peng et al., 2013).

#### **2.3.2.4 Microscopic Air Bubble FPI by Simple Splicing Technique**

A monolithic FPI consists of a microscopic air bubble and is constructed by splicing SMF-28 with the index-guiding PCF using arc-discharge splicing technique. A non-commercial PCF with an air hole diameter of 2.3  $\mu\text{m}$  arranged around the core in a hexagonal-like pattern with PCF outer diameter of 125  $\mu\text{m}$  is used making its alignment with SMF easy (Villatoro et al., 2009).

Arc-discharge is used to heat the fiber ends above the softening point for a short interval during the splicing. Afterward, the fibers are pushed collectively to form an enduring joint. The softening point of PCFs is normally lower than that of all-solid SMFs because they have many microscopic holes in the cladding. Hence, the temperature reached through the arc discharge will be highly adequate to exceed the PCF softening point when the default splicing parameters are set. Under these conditions, the PCF holes will diffuse completely with each other. Consequently, some amount of air remain inside the space which produces the microbubble and its position can be set at the centre of the fiber if the holes inside the PCF are completely symmetric (Villatoro et al., 2009). A similar micro air bubble is formed with an SMF and a silica tube by fusion splice method to fabricate an ultrahigh sensitivity FPI pressure sensor (Wang et al., 2013).

#### **2.3.2.5 Two-Mode Interferometric Sensor by Fusion Splice Technique**

A conventional program for splicing with an arc-discharge machine considered fabricating a two-mode interferometric sensor based on a short piece of a home-produced PCF. PCF is fusion spliced on both sides to standard optical fiber (Corning SMF-28e). During splicing, part of the holey structure of PCF collapsed (for a length of approximately 300  $\mu\text{m}$ ) due to the heat required to fuse the two fibers. The guiding structure of PCF no longer exists in this collapsed region and it is replaced with an all-silica rod. The first collapsed region is utilized to excite two modes in the PCF. The fundamental SMF mode has diffracted in the pure-silica region, and as a result, the mode broadens. This result allows the excitation of two modes inside the PCF because of the mismatch between the broadened Gaussian mode and that in the PCF. An interferometric pattern is created while such modes propagated with diverse effectual indices and accordingly with diverse phase velocities through the uncollapsed PCF

region, until they recombine with the fundamental Gaussian mode of the second piece of SMF through the second PCF collapsed zone (Covielli et al., 2009).

#### **2.3.2.6 MEFPI Sensor by Chemical Etching Technique**

A micro-extrinsic FP interferometer (MEFPI) sensor with a cavity length of  $\sim 9 \mu\text{m}$  can be fabricated by chemical etching of commercially available erbium (Er)- and boron (B)-doped fibers and then splicing with an SMF. The etching procedure is performed for approximately 40 to 45 min using a mixture of 20 mg of  $\text{NH}_4\text{F}$ , 30 mL of buffered hydrogen fluoride (BHF), 40 wt% HF, and 54 mL of deionized water. Then, simple splicing method is applied between the etched EDF and BDF to an SMF (Corning, SMF-28) to fabricate a microsensor based on FPI. This type of sensor is fabricated for the measurement of strain or temperature but not both simultaneously (Rao et al., 2010).

#### **2.3.2.7 Chitosan-based Fabry–Perot Interferometry**

This miniature FPI humidity sensor is constructed by using SMF in which a hollow core fiber with a physical length of  $50 \mu\text{m}$  is used, and a thin layer of natural polymer, i.e., chitosan, sensitive to moisture (humidity) is coated over the end of the hollow fiber as shown in Figure 2.7.

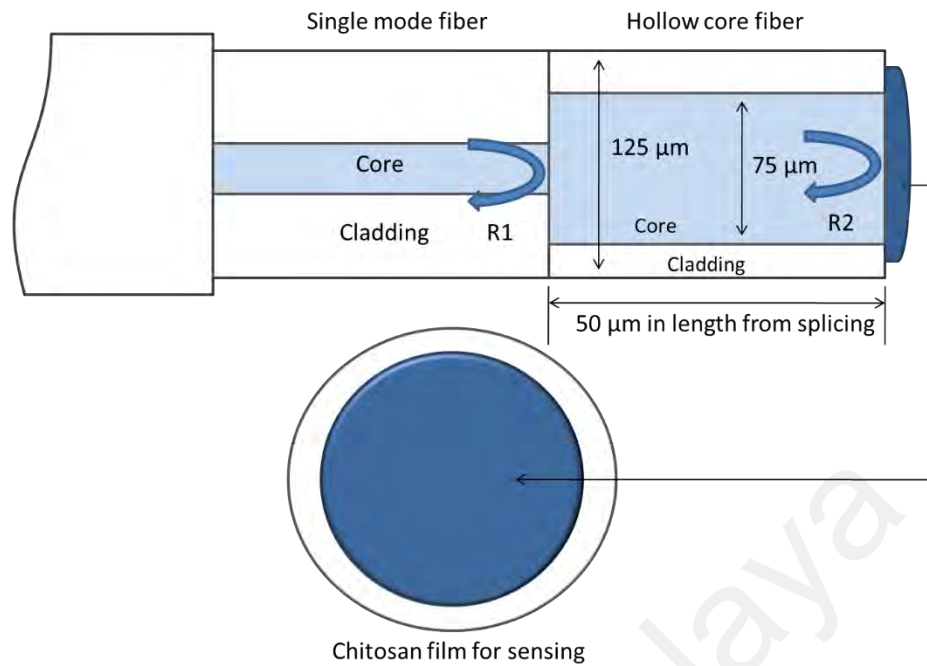


**Figure 2.7: Model diagram for the chitosan-coated FPI, RH sensor (Chen et al., 2012).**

For this fabrication process, 1% conc. of chitosan is selected to synthesize the chitosan film because such quantity of chitosan produced a perfect diaphragm by forming a thin and flat coating on the fiber end which provides an increased permeability because of the reduction in crystallinity. Before splicing, SMF-28 is first cleaved by a cleaver with high accuracy to achieve the best quality of the fiber end that provides reflectivity of ~4% for fabrication of the sensor. To form a micro gap, a hollow core fiber (Polymicro TSP050150, outer diameter-OD: 125  $\mu\text{m}$ , inner diameter-ID: 75  $\mu\text{m}$ ) is then spliced with the well-cleaved SMF end using a conventional fiber splicing device with an arc power of 8 bits, gap of 23  $\mu\text{m}$ , and arc duration of 300 ms. Then, cleavage of hollow core fiber is performed under the microscope to achieve the desired cavity length. Finally, SMFs with microcavity and 1% chitosan solution are located inside a drying chamber with 9% RH and temperature of 25  $^{\circ}\text{C}$  to perform the dip coating procedure, which provides a sensing diaphragm of thin chitosan over the HCF (Chen et al., 2012). Suspended chitosan substrate film was used in a recent study on FPI fabrication to form an immunosensor (Chen et al., 2013).

### 2.3.2.8 Femtosecond Laser Micromachining and Fusion Splicing

Easy fabrication of an FPI cavity sensor for RI measurement is presented previously (Liao et al., 2012). Microholes with  $\sim 1 \mu\text{m}$  in diameter are created using femtosecond (fs) laser through the centre of the fiber core and then splicing of the two fiber ends with micro-holes is performed to create an FP cavity, where fusion current is fixed at 16.3 mA for a duration of 2.0 s. Then, a hollow sphere with a diameter of  $\sim 60 \mu\text{m}$  is formed. In the end, FP cavity is micromachined by fs laser to create a micro-channel with a gap of  $\sim 38 \mu\text{m}$ , which can be used for RI sensing of the given liquid interacting inside or outside of the cavity as shown in Figure 2.8 (Liao et al., 2012). In another work, fs laser is used to fabricate an FPI sensor by producing a diaphragm-like thin fiber piece at the end of a fiber (Zhang et al., 2013).

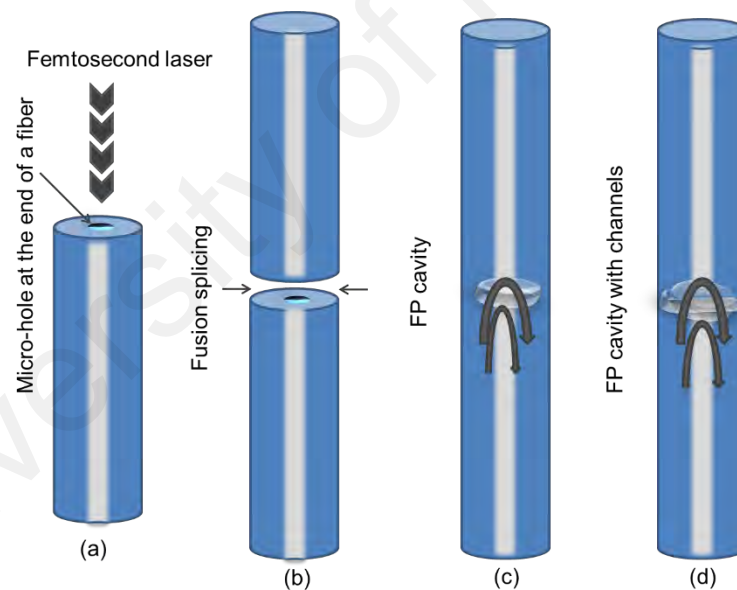


**Figure 2.8: Illustration of fabrication of an FPI cavity inside the fiber (Liao et al., 2012). (a) Creation of microholes, on the order of  $\sim 1 \mu\text{m}$  using a femtosecond laser, through the centre of the fiber core. (b) Splicing of the two fiber ends with microholes. (c) Formation of the FP cavity. (d) Introducing the vertical cross-through microcavity for the fabrication of microchannels.**

A micromachining technology is also used in the previous study (Kim et al., 1997) to develop an FPI pressure sensor with high sensitivity by using a  $\text{Si}_3\text{N}_4/\text{SiO}_2/\text{Si}_3\text{N}_4(\text{N/O/N})$  diaphragm with anisotropic etchant solution, that is,

KOH(aq). A pair of SMFs with ends coated by  $\text{TiO}_2$  film is used to fabricate an FPI based on the fusion splicing technique. Typically, 10 to 20 splicing pulses with low arc current are used until the desired value of the mirror reflectance is achieved. Splicing to the next fiber optic mirror is conducted with the first fiber after cleaving with the desired cavity length to create the FPI sensor (Kim et al., 1997).

## **2.4 Characteristics of Fabry–Perot resonators**

The refractive index of silica is a function of the induced temperature, pressure, and strain. Acoustic wave, temperature, pressure, and strain induce changes in the fiber glass refractive index due to opto-elastic and thermo-optic effects (Nye, 1985). In this section, the effects of thermo-optic, opto-elastic, electro-optics, and acousto-optic in optical fibers are reviewed.

### **2.4.1 Thermo-optic Effect**

FBGs exhibited great superiority in terms of high sensitivity to temperature and pressure as well as multiplexing capability, yet they suffer from the weakness of cross sensitivity due to the thermo-optic effect. The thermo-optic effect in FBGs is a recognized phenomenon which affects the performance of fiber devices that includes the proposed FPRs. Subsequently, this effect had been broadly utilized and considered as a part of the properties of many optical fiber devices. The thermo-optic effect is the thermal modulation of the refractive index of a material. The refractive index of a material can be controlled as an element of its thermo-optic coefficient  $\alpha$ . Recently, Zhou et al. (2006) demonstrated the responsivity of FBGs with huge tilted structures to the cross sensitivity of refractive index with temperature. In addition, such works effectively remunerate the effect of temperature in the measurement of refractive index.

The thermo-optic effect of fluids is a different intriguing impression that was contemplated with FBG refractometer. Etched FBG was utilized to investigate the



thermo-optic effect of the media because it is sensitive to both surrounding refractive index and temperature. The thermal sensitivity of the device will be diversely influenced by the surrounding media with various refractive indices considering that RIs exhibit a nonlinear behaviour (Cusano et al., 2005). Moreover, different substances have distinct thermo-optic coefficients, and the modifications in the refractive index will not be similar within a specific temperature range. In any case, the cross-sensitivity can be overcome if the sensitivity of grating is already characterized in neighbouring media with certainly known optical properties.

#### 2.4.2 Opto-elastic Effect

A transparent vitreous elastic glass-like medium becomes birefringent similar to few crystals when an exterior force is applied. Optical anisotropy is formed when the outer force is adapted to an optically isotropic medium. For example, optical fiber and this phenomenon are understood as the opto-elastic (photo-elastic) effect. The connection between the refractive index and the stress component can be expressed by the opto-elastic constant, which can decide the polarization properties of the single-mode optical fibers.

The strain-optic effect is industrially exploited in both optical physical sensors and telecommunications apparatuses. Silica-based platforms are widely extolled for such applications, because silica shows mechanical strength and a low thermal sensitivity compared with other optical platforms, for example, polymers.

Notwithstanding mechanical strain-induced phase shift, acousto-ultrasonic strain prompts different changes to the fiber Bragg grating and optical fiber. Because of the change of propagation constant  $\beta$ , the strain-induced phase shift can be composed as (Hocker, 1979)

$$L\Delta\beta = L\frac{d\beta}{dn}\Delta n + L\frac{d\beta}{dD}\Delta D \quad (2.11)$$

where  $D$  denotes the diameter of the fiber. The primary term of Equation 2.11 considers the refractive index change caused by ultrasonic waves and is consequently called strain-optic effect or elasto-optic effect. It is known that  $\beta = n_{\text{eff}}k_0$ ,  $n_{\text{cladding}} < n_{\text{eff}} < n_{\text{core}}$  and the difference between  $n_{\text{cladding}}$  and  $n_{\text{core}}$  is small, thus  $\frac{d\beta}{dn} = k_0$ . In the rest of the thesis,  $n$  represented the effective refractive index. The second term of Equation 2.11 is related to the waveguide mode dispersion due to the variation in fiber diameter induced by the acousto-ultrasonic impelled strain. This waveguide mode dispersion effect is minor compared with the other two effects.

From the elasto-optic effect, the change in optical indices is given by (Hocker, 1979):

$$\Delta\left(\frac{1}{n^2}\right)_i = \sum_{j=1}^6 p_{ij}\varepsilon_j \quad (2.12)$$

The shear strain components  $\varepsilon_4 = \varepsilon_5 = \varepsilon_6 = 0$  because the ultrasonic wave propagates longitudinally along the fiber axis. The strain-optic tensor for a homogeneous isotropic material can be rewritten as (Hocker, 1979)

$$p_{ij} = \begin{bmatrix} p_{11} & p_{12} & p_{12} \\ p_{12} & p_{11} & p_{12} \\ p_{12} & p_{12} & p_{11} \end{bmatrix} \quad (2.13)$$

where  $p_{11}$  and  $p_{12}$  are the mechanisms of the strain-optic tensor of the optical fiber material.

$$\Delta\left(\frac{1}{n^2}\right)_{x,y,z} = -\frac{P(1-2\nu)}{E}(p_{11} + 2p_{12}) \quad (2.14)$$

In this manner, the change of the refractive index is

$$\Delta n_x = \Delta n_y = \Delta n_z = \Delta n = \frac{n^3 P}{2E} (1 - 2\nu)(p_{11} + 2p_{12}) \quad (2.15)$$

This refractive index changes correspond to the x-, y-, and z-axes as presented in Figure 3.13.

### 2.4.3 Electro-optic Effect

Similar to opto-elastic effect, the changes in the refractive index due to an applied electric field is identified as the electro-optic effect. The impact of changing the index of refraction proportionally with the enforced field is known as Pockels effect. If the index change is quadratically-dependent on the applied field, then the effect is known as Kerr effect. Interestingly, the Pockels effect is missing in shapeless materials, for example, liquids and glasses but can exist just in crystalline materials, where all classes of materials have the Kerr effect.

The electro-optical effect can modify the phase of an optical wave. To retain the polarization state during propagation, the optical wave is linearly polarized in a direction that is parallel to one of the principal axes of the crystal in the presence of the exterior field for this type of application. Phase adjustment can be transformed into amplitude regulation by utilizing an interferometric strategy or birefringence difference.

A quadratic electro-optic effect might occur in centrosymmetric materials, that is, a change in the index of refraction is relative to the square of the enforced electric field (Degiorgio et al., 2014).

### 2.4.4 Acousto-optic Effect

If an elastic wave is propagating in a medium, then the index of refraction will change occasionally considering the photoelastic effect. The phenomenon is known as the acousto-optical effect. The acousto-optical interaction was initially examined in 1922 by Brillouin with a specific end goal to diffract an optical beam (Brillouin, 1922).

The acousto-optic effect is the variation of the refractive index of a medium due to the mechanical strains accompanying with the propagating acoustic wave in the medium. Refractive index modifications are induced by the photoelastic effect which occurs in all materials under mechanical stress. The treatment of the acousto-optic interaction progresses also to that of the electro-optic effect (Degiorgio et al., 2014).

## **2.5 Theory of the Fabry–Perot Resonator**

The all-fiber optical FP cavity, which comprises a couple of exceedingly reflective optically-flat surfaces, sets to produce a resonance device as discussed in Chapter 2. When the light propagates into an FP resonator, it encounters multiple reflections between the exceptionally reflective surfaces. Once the multiple reflections are united by a focusing lens, they interfere consistently, and narrow fringes are observed.

FP can be built from numerous perspectives. For instance, a bulk optical FP is a free space optical device. A type of fiber FP etalon was showed by Cheung (2004) whereby one of the reflective surfaces is produced by the cut end of a fiber coated with an exceptionally reflective material. The cavity is produced between the cut fiber end and a mirror as illustrated in Figure 2.9. In this arrangement, positioning is challenging for the light to couple again into the fiber from the mirror, making this setup incompetent (Cheung, 2004).

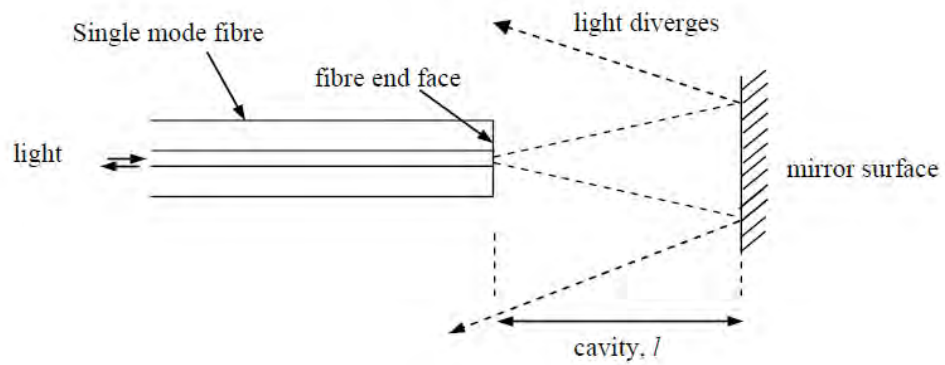


**Figure 2.9: FP cavity created between a fiber end and a mirror (Cheung, 2004).**

An expansion of this type of FP comprises the arrangement of an air cavity between two fiber ends, which necessitate supporting members (e.g. capillary tube) to retain the two fibers set up as illustrated in Figure 2.10.

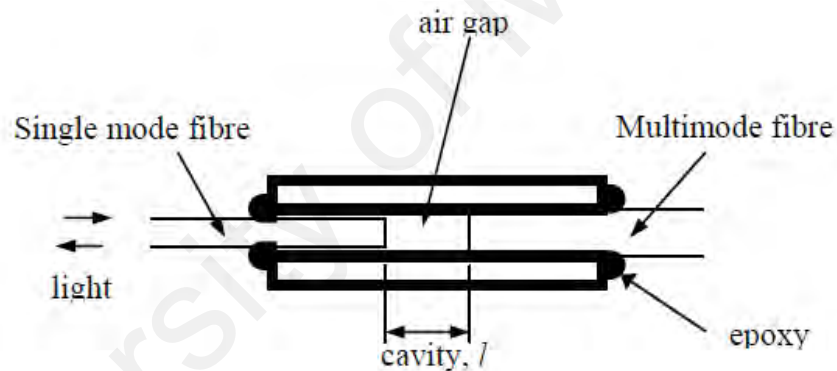


**Figure 2.10: FP cavity created between two fiber ends with supporting members (e.g. capillary tube) (Cheung, 2004)**

The arrangement and quality of the device can be enhanced by creating mirrors inside the fiber using a method for fusion splicing fiber ends together according to Figure 2.11. This method forms mirrors inside the fiber and offers benefits for all fiber frameworks. However, the reliability of physical quality and optical properties of the fiber can be traded off by interruption at the point of fusion.

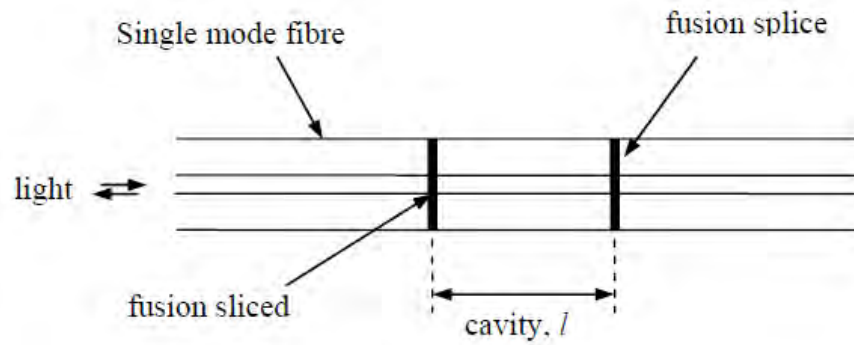


**Figure 2.11: FP cavity generated by fusion splicing portion of fibers together with a reflective surface to form reflective mirrors (Cheung, 2004)**

An approach to defeating this issue is to print a couple of indistinguishable FBGs inside the fiber with a proper physical partition. FBGs function as the reflectors forming cavity inside the fiber core with little interruption to both the physical quality and guiding properties of the fiber. The flexibility of inscribing strategy permits a progression of such FBG-based FP resonator to be printed in the same fiber with every fiber possessing an alternate wavelength bandwidth taking advantage of mode interference ability of FBGs.

### 2.5.1 FBG-based Fabry-Perot Resonator

Utilizing FBGs as partial reflectors, FP can be produced by printing two FBGs isolated by a cavity length possessing identical wavelength and bandwidth. Uniform FBG or uniform saturated FBG can be utilized to produce FP using the same approach to offer the FP a larger operating bandwidth. Considering typical prevalence case for an FP resonator at which  $\phi$  is zero, at the point when the incident light goes in the cavity, it will be reflected both forward and backward inside the cavity. The reflected waves at the two mirror surfaces will have a phase delay proportionate to double the optical path length,  $nl$ . For a monochromatic wave of a single polarization wavelength,  $\lambda$ , the round trip phase shift (RTPS) of the cavity is expressed by:  $\theta = \frac{4\pi nl}{\lambda}$ , where  $n$  is the refractive index of the medium in the cavity. Accumulations of wavelets will interfere

when united. When the phase delay is an integer product of  $2\pi$ , the reflected waves interfere productively. When they are of odd products of  $2\pi$ , they interfere ruinously. Consequently, the cavity shows an inclination for fields with the right wavelength in which the RTSP is of products of  $2\pi$ . Accepting a lossless cavity, the mathematical treatment of the transmitted intensity results in the following expression (Verdeyen, 1989):

$$I_t = I_0 \frac{(1 - R_1)(1 - R_2)^2}{(1 - R_1)(1 - R_2) + 4\sqrt{R_1 R_2} \sin^2\left(\frac{\theta}{2}\right)} \quad (2.16)$$

where  $R_1$  and  $R_2$  are reflectivities of the two mirrors. FP cavity acts as a multiple beam interferometer, and slender transmission fringes are found in the yield of FP. Such devices might be utilized as filters using a settled cavity length or as optical spectral analysers by tuning the cavity length for scanning spectral information in the signals.

From Equation 2.16, depicting the transmission of FP, the highest intensity occurs when RTPS,  $\theta$ , is an integer product of  $2\pi$  radian. The condition can be accomplished by changing the length of the cavity,  $l$  or through an adjustment in the illuminating wavelength.

The variation in the illuminating wavelength starting with one cavity resonant wavelength onto the next that emerges a variation of  $2\pi$  in RTSP is known as the free spectral range (FSR):

$$FSR = \Delta\nu_{FSR} = \frac{c}{2nl} \quad (2.17)$$

where  $\nu$  is the optical frequency.

FSR is used in the estimation of the device sensitivity. For highly reflective mirrors, the width of the resonant cavity mode is small, and when the reflectance diminishes, the

width of the resonance cavity mode widens. The full width at half maximum (FWHM) of the resonant frequency is expressed by (Verdeyen (1989)):

$$\Delta\nu_{1/2} = \Delta\nu \left( \frac{1 - (R_1 R_2)^2}{\pi (R_1 R_2)^{1/4}} \right) \quad (2.18)$$

Furthermore, the finesse ( $F_f$ ) of the cavity is expressed by:

$$F_f = \frac{\Delta\nu_{FSR}}{\Delta\nu_{1/2}} = \frac{2\pi}{\Delta\delta_{1/2}} = \frac{\pi (R_1 R_2)^{1/4}}{1 - (R_1 R_2)^{1/2}} \quad (2.19)$$

The estimation of  $F_f$  is a measure of the device's resolution, and it is identified by the reflectivity,  $R$ , and the losses acquired in the cavity. The wavelength resolution is specified by the result of FSR and finesse,  $F_f$ . Extensive FSR must be attained at the expense of a lower wavelength resolution and small FSR will produce higher sensitivity. A huge FSR indicates an extensive dynamic range.

Most extreme and least transmissions are specified by (Verdeyen (1989)):

$$I_{\max} = \frac{(1 - R_1)(1 - R_2)}{(1 - \sqrt{R_1 R_2})^2} \quad (2.20)$$

and

$$I_{\min} = \frac{(1 - R_1)(1 - R_2)}{(1 + \sqrt{R_1 R_2})^2} \quad (2.21)$$

Visibility,  $V$  is a critical variable and it decides how the spectral components can be determined satisfactorily. Visibility is assumed as follows:

$$V = \frac{I_{\max} - I_{\min}}{I_{\max} + I_{\min}} \quad (2.22)$$

Visibility additionally relies on both the condition of polarization and the level of coherence of the interfering light beams. When the reflectivity,  $R$ , is small, similar to the one experienced in the Fresnel reflection in glass/air interface in cut fiber ends, the



spectrum is in the sinusoidal form. Accepting  $R_1 = R_2$ , the visibility,  $V$ , in the transmission appears small. Reflected intensity is expressed as  $I_R = (1 - I_T)$  and expecting that no loss occurs in the cavity. The visibility,  $V$ , in reflection will have a value close to one, and the fringes can be determined but at the expense of having decreased intensity as shown in Figure 2.12c.

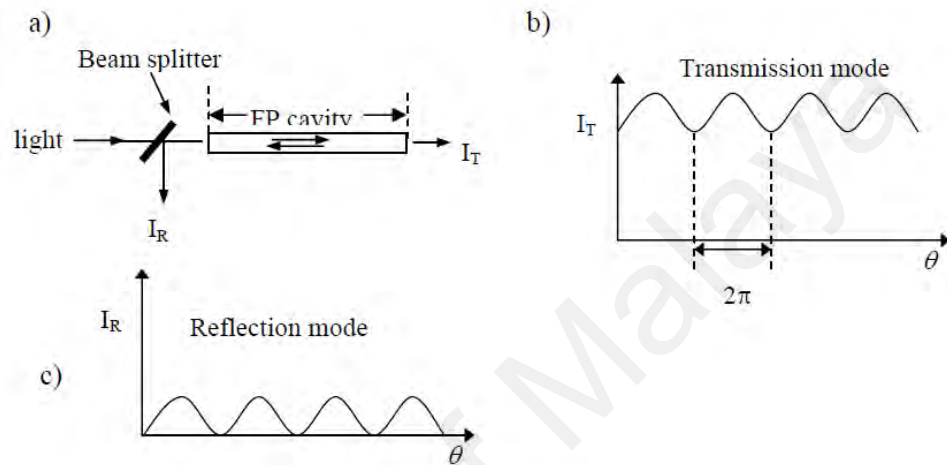


**Figure 2.12: schematic demonstrating a fiber FP cavity comprising an area of an optical fiber producing a cavity with its ends cleaved such that  $R$  is  $\sim 4\%$ . b) transmission reaction with a slight visibility yet high intensity throughput through in c) the reflection reaction has a high visibility however a low intensity throughput (Cheung, 2004)**

In the low Finesse regime, which is experienced in fiber/air interface where the reflectivity is small ( $R \sim 4\%$ ), the reflectance is achieved assuming that  $R_1 = R_2 = R$  and a lossless cavity, as indicated by Equation 2.16 (Kidd et al., 1991):

$$I_r = \lim_{R \rightarrow 0} \left( I_0 - I_0 \frac{(1-R)^2}{(1-R)^2 + 4R \sin^2\left(\frac{\theta}{2}\right)} \right) \quad (2.23)$$

$$I_r = I_0 (1 + V \cos \theta)$$

where  $V$  is given by:

$$V = \frac{2R(1-R)^2}{R + R(1-R)^2} \quad (2.24)$$

The reaction demonstrated by Equation 2.23 is compared to the co-sinusoidal transfer function of the two beam interferometer. This is the most suitable method for sensing applications through various phase measurement strategies (Giallorenzi et al., 1982) created over the years which could be utilized to demodulate low Finesse FP sensors.

### 2.5.2 Dispersive Bulk Fabry–Perot

The cavities of interest in this thesis are based on uniform FBGs, which are dispersive elements in their own rights. Parallels can be drawn from the investigation on dispersive cavity based on bulk-type FP. The impact of dispersion of the medium inside an interferometer changes the optical path length (OPL) as a component of wavelength, which thus affects the RTPS of the device. The variation of OPL,  $nl$ , with wavelength is assumed as follows (Petuchowski et al., 1981):

$$\frac{\partial(nl)}{\partial\lambda} = n \frac{dl}{d\lambda} + l \frac{dn}{d\lambda} \quad (2.25)$$

For a bulk FP etalon, the cavity length,  $l$ , is fixed and independent of wavelength. The main dispersive impact accessible is inside the material that constitutes the cavity. Suppose that the refractive index variation with wavelength is critical, then the modification in optical path with wavelength in Equation 2.25 can be reduced to  $\frac{\partial(nl)}{\partial\lambda} = l \frac{dn}{d\lambda}$ , and the detuning of the dispersive cavity's FSR can be depicted by:

$$\Delta v_{FSR} = \frac{\Delta v_0}{\left(1 - \frac{\lambda}{n} \frac{dn}{d\lambda}\right)} \quad (2.26)$$

If the material dispersion is little, then no perceptible change in FSR occurs for the device such that  $\Delta v_{FSR} \sim \Delta v_0$ . However, if a material displays dispersion, a remarkable

alteration to the FSR value in Equation 2.26 occurs. If a material, whose dispersion can be controlled or customized with a particular wavelength response, is utilized as a part of the FP cavity, the denominator in Equation 2.26 could be zero, with the outcomes that the  $\Delta\nu_{FSR}$  can be infinite. The device is then insensitive to wavelength change. The condition for this to occur is as follows:

$$\frac{n}{\lambda} = \frac{dn}{d\lambda} \quad (2.27)$$

This condition is free of cavity length,  $l$ . The condition holds if the proportion of refractive index to wavelength is equivalent to the dispersion. When the condition in the equation is not fulfilled as the wavelength is tuned away from this condition, the wavelength's insensitive condition will no longer hold and FSR will change.

Uniform FBGs are dispersive components and offer an alternate dispersive effect to be in a specific position detuning with wavelength as opposed to refractive index reliance with wavelength. This qualification has a specific influence when they create FP interferometer.

## 2.6 Applications of All-fiber Fabry–Perot Interferometers

### *Temperature Sensing*

FPI fiber-optic sensors are highly sensitive to thermal radiation. Such a property has been employed in support of the measurement of thermal variations (Yoshino et al., 1982; Jiang & Gerhard, 2001; Ezbiri & Tatam, 1996; Rao et al., 2010; Chana et al., 1992; Du et al., 2014) and direction of temperature change (Tseng & Chen, 1988) for a long time. Until recently, the widest temperature range reported is  $-200\text{ }^{\circ}\text{C}$  to  $1050\text{ }^{\circ}\text{C}$ , which is established through the characterization of a fiber FPI temperature sensor with internal mirrors (Lee & Taylor, 1991; Leilabady et al., 1985). It can be used for high-temperature sensing up to  $1000\text{ }^{\circ}\text{C}$  (Choi et al., 2008; Coviello et al., 2009). Such a

temperature sensor can also be used to detect even minute temperature differences produced by the human body (Yoshino et al., 1982). In addition, a coherent multiplexed remote FPI fiber-optic sensor is used as a point sensor (Lee et al., 1988) for remote point “temperature change” measurements (Farahi et al., 1988). FPI fiber-optic temperature sensors can be implemented for some significant applications. Such applications are transformers; cancer treatment, where the tumour is subjected to microwave radiation; and for monitoring structural materials (Lee & Taylor, 1988), where the usual sensors are not appropriate (Farahi, 1991). FP interferometers have been fabricated/modified in many approaches for temperature sensing. For instance, it can be combined with a Michelson interferometer to fabricate a hybrid temperature sensor (Frazao et al., 2010). A miniature fiber FPI (Rong et al., 2012) offers a constant temperature reading with a sensitivity up to 173.5 pm/°C at above 80 °C, whereas the temperature sensitivity was ~20 pm/°C (Kou et al., 2010) for an all-glass FP modal interferometer (FPMI). An all-silica in-line fiber FP etalon with feedback-controlled cavity length based on a piezoelectric ceramic unimorph actuator has been demonstrated for simultaneously sensing of acceleration and temperature (Jia & Wang, 2013). A thin core fiber (Zhu et al., 2010) is used to form a high-temperature FPI sensor with a sensitivity of ~18.3 pm/°C and it is capable of sensing temperature up to 850 °C (Chen et al., 2012). Other proposed FPI sensors with higher temperature sensitivities exist; for example, ~5.2 nm/°C (Zhang et al., 2013) and ~39.1 nm/°C (Xu et al., 2012). Some patents on FPI-based temperature sensors can be found in previous studies (Davis, 1986; Andrews & Pulfrey, 1999).

### *Mechanical Vibration Sensing*

FPI vibration sensors find significant applications in geological surveys, large civil structure diagnoses (<10 Hz), inertial navigation, consumer electronics, geological surveys, oil and gas field exploration, and earthquake monitoring (<20 Hz) (Zhang et

al., 2013). A low finesse FPI vibration sensor cavity with a reported sensitivity of 9 mrad Hz<sup>-1/2</sup> has also been investigated (Yoshino et al., 1982). For the measurement of periodic and non-periodic vibrations, a dual-cavity EFPI is used (Kim et al., 2005; Rees et al., 2001). Besides, a non-contact self-calibrated FPI vibration displacement sensor system (Jia & Wang, 2012), an all-fiber FPI sensor for low-frequency vibration measurements (Andrews & Pulfrey, 1999), and some other FPI vibration sensors (Pullteap, 2008; Gangopadhyay, 2004; 2006) have been developed in early studies. A method and apparatus for detecting seismic vibrations involving a micro-machined FPI sensor have been patented by Gibler et al. (Gibler & Jeffers, 2010).

#### *Acoustic Wave Sensing*

The acoustic sensitivity of an FPI varies with the fiber length. Unlike Mach–Zehnder interferometer, no reference arm is required for an FFPI as an acoustic sensor, which is significantly beneficial; hence, it is free from any spurious signals associated with the reference arm (Yoshino et al., 1982). An FPI fiber-optic sensor using a light-emitting diode (LED) temperature sensor is presented in the previous study (Lee & Taylor, 1991). Such a device is also applicable for measuring acoustic-wave pressure. A diaphragm-based optical fiber acoustic (DOFIA) sensor was developed to measure the attenuation properties of acoustic waves in water and an ~30° detection range was observed with an acoustic wave attenuation coefficient of 0.0626 cm<sup>-1</sup> (Deng, 2004). Another high sensitivity diaphragm-based interferometric fiber optical micro-electromechanical system sensor was fabricated that can detect partial discharges (PD) acoustic waves on-line that generate inside high-voltage power transformers (Wang et al., 2005). In addition, a polymer diaphragm-based EFPI fiber acoustic sensor system was proposed previously (Wang & Yu, 2010), and it had an acoustic sensitivity of 31 mV/Pa. A maximum acoustic signal with a frequency of 80 MHz and 1 pm amplitude is detected by FPI (Park et al., 2005). A high level of immunity and higher sensitivity was

achieved based on the phase-shift effect of this FPI. A multilayer graphene diaphragm is used in the formation of an FP acoustic sensor, which exhibits an acoustic pressure sensitivity of 1100 nm/kPa and a minimum detectable pressure equivalent to a noise level of  $\sim 60 \mu\text{Pa} \cdot \text{Ha}^{-1/2}$  at 10 kHz input frequency (Ma et al., 2013). Another fiber optic acoustic emission sensor has been reported in a patent, which is particularly useful for the vibration sensing under hostile conditions (Berthold & Roman, 2001).

### *Ultrasound Sensing*

Ultrasound has been widely used for the detection of a variety of material defects, structural health monitoring, and process monitoring (John et al., 1997). Piezoelectric devices are the most commonly used components for ultrasound sensing, but they suffer a common problem of non-uniform frequency response due to a poor acoustic-impedance match to liquids. The development of an extrinsic optical-fiber ultrasound sensor offers comparably better sensitivity of 61 mV/MPa (Beard & Mills, 1996). FP polymer film sensing interferometer was constructed based on an optical ultrasound sensing method that offers excellent detection sensitivities ( $< 10 \text{ kPa}$ ) (Cox et al., 2004). The development of an FPI fiber-optic ultrasound sensor offers the potential to use it in fiber optic “smart structure” applications (John et al., 1997). An in-line FPI fabricated from hollow-core PCF exhibits a wavelength pressure sensitivity twice as high as that of FBG, which is  $\sim 7.29 \times 10^{-3} \text{ nm/MPa}$  (Rao et al., 2009). In another work, an in-line silica capillary tube all-silica fiber-optic FP (ILSCT-ASFP) interferometric sensor has been demonstrated for high intensity focused ultrasound fields measurement. It has an acoustic sensitivity of 65.4 mV/MPa over a measurement bandwidth of 2.5 MHz (Wang et al., 2012).

### *Voltage Sensing*

Measuring the quality and quantity of the energy product for every power exchange point is the most significant feature of the power distribution cycle. FPI optical-fiber sensors can be a high-precision and inexpensive voltage measurement technique for high-power distribution systems. AC electric voltages can be measured optically by deducting the counted pulse number from the applied voltages with an FFPI fiber-optic sensor (Yoshino et al., 1982). A piezo-optical voltage sensor based on FPI was proposed and demonstrated for the measurement of AC voltages from 1  $V_{\text{rms}}$  to 400  $V_{\text{rms}}$ . This sensor can be used as an optical voltage transducer (Mozafari et al., 2008). A multipoint optical fiber liquid crystal (OFLC) voltage sensor was fabricated and can directly measure an electric field up to 800 kV/m at distributed points along power lines (Bal, 2011).

### *Magnetic Field Sensing*

An FPPI sensor is used for DC magnetic field measurement that is considered as a matured method. AC and DC magnetic fields are detected by pulse counting method (Yoshino et al., 1982). In general, quantization of signals creates measurement errors in a digital magnetic field sensing scheme and such errors can be decreased by FFPI. A compact fiber-optic EFPI sensor that uses a wire-based magnetostrictive transducer (Oh et al., 2004) was investigated for DC magnetic field (100–35,000 nT) sensing (Oh et al., 1997). A magnetic fluid is adopted to form an EFPI fiber-optic magnetic field sensor which produces a measurement sensitivity of 0.0431 nm/Gs (Lv et al., 2014) and 33 pm/Oe (Zhao et al., 2012). A nano-magnetic fluid-based EFPI also showed satisfactory results in magnetic field measurement (Jin et al., 2013). Another EFPI sensor is reported for DC magnetic field sensing and it has a dynamic range of 50–40,000 nT (Oh et al.,

2004). Some patents on FPI-based magnetic field sensors have been filed (Chang & Vali, 1994; Davis & Wagreeich, 1999).

### *Pressure Sensing*

Fabrication of good-performance FP pressure sensors with lower measurement errors is a challenging subject. An FPI fiber-optic sensor exhibited good response for static pressures of 15 psi to 1,000 psi by measuring the pressure-induced deflection of a membrane (Lee et al., 1994). An N/O/N diaphragm-based FPI was demonstrated (Kim et al., 1997). It possesses a pressure sensitivity of 0.11 rad/kPa and the pressure sensitivity is proportional to the area of the diaphragm. A gas pressure sensitivity of 1,526 nm/RIU was obtained by an FFPI sensor when applied to different gaseous environments (Zetterlind et al., 2003). In addition, some other FPI fiber-optic sensors were fabricated and tested (Kim et al., 1997; Reinsch et al., 2012; Lai et al., 2011; Zhang et al., 2013; Lee & Taylor, 1988; Jiang & Gerhard, 2001; Xian et al., 2005; Kao & Taylor, 1996; Dai et al., 2013) for pressure measurements. An EFPI pressure sensor showed a sensitivity of  $2.75 \times 10^{-8}$  1/kPa (Aref et al., 2007). An ultra-high FPI pressure sensor has been reported in Wang et al. (2013) that has a sensitivity of >1,000 nm/kPa. A miniature FPI fabricated at the tip of an FBG reported in Bae and Yu (2012) exhibited a sensitivity of 0.0106  $\mu\text{m}/\text{psi}$  over a range of 1.9 psi to 7.9 psi. The used FPI based on PCF was a pressure sensor with a sensitivity of  $\sim 13$  pm/ $^{\circ}\text{C}$  over a range of 0 MPa to 40 MPa (Wu et al., 2011). Some of the examples of patents on FPI-based pressure sensors can be found in Taylor et al. (2001), Schmidt (2008), Lopushansky and Berthold (2009), Bremer et al. (2011).

### *Strain Sensing*

Strain monitoring of materials for structures such as building frames, bridges, tunnels, and dams, and smart structures are essential throughout the lifetime of the



structure (Sorin & Baney, 1995). A strain range of 1,000  $\mu\epsilon$  to 12,255  $\mu\epsilon$  is reported in De Vries et al. (1997) for strain measurement by FPI fiber-optic sensors. An FPI based on a dual-cavity was used as a strain sensor (Chtcherbakov, 1997). Embedding an FPI sensor in Hercules AS4/3501-6 graphite/epoxy composite specimens is advantageous for strain measurement (Lawrence et al., 1998). Another FPI-embedded fiber-optic sensor was designed for micro-strain measurement of concrete (Quirion & Ballivy, 2000). A polymer film-based FPI strain sensor has proven to be more robust and reliable than gauges (Jiang & Gerhard, 2001). PCF-enabled micro-FPIs (Villatoro et al., 2009) and FPI–Michelson hybrid interferometer (Peng et al., 2013; Frazao et al., 2010) are more competent than resistive strain sensors in terms of reliable measurements during high-cycle, high-strain fatigue tests (Xiao et al., 2005; Hare & Moore, 2000). A temperature-insensitive FPI constructed using a chemical etching method shows a high strain sensitivity of  $\sim 3.15$  pm/ $\mu\epsilon$  (Gong et al., 2009). A GIF50 fiber with a core diameter of 50  $\mu\text{m}$  was used to form a FPI by chemical etching with HF that showed a strain sensitivity of 4.06 pm/ $\mu\epsilon$  (Tafulo et al., 2012a), whereas a graded index multimode fiber with a larger core diameter of 62.5  $\mu\text{m}$  gives a lower strain sensitivity of  $3.14 \pm 0.05$  pm/ $\mu\epsilon$  (Tafulo et al., 2012b). The FPIs constructed in Lee and Taylor (1991), Chang and Sirkis (1997), Coviello et al. (2009); Yoshino et al. (1982), Lee et al. (1988); Ezbiri (1996); Leilabady et al. (1985), and Machavaram et al. (2007) can be employed as static and mechanical strain sensors too. Some related patents on strain sensing can be found in Davis (1986), Reich (2000), (2001), and Viel (2000).

### *Flow Velocity Sensing*

A growing demand for the precise measurement of flow velocity of complex fluid flow phenomena exists. The FPI fiber-optic sensor is a potential candidate for flow velocity measurements. A vortex-shedding flowmeter with a fiber-optic FP interferometer (FFPI) was constructed for measuring the liquid flow velocity in a pipe.

A linear optical modulated frequency dependence on flow velocity is found over the range of 0.14 ms to 3.0 ms (Fang et al., 1998). A multiple measurement points-based FPI sensor was implemented for spectroscopic flow velocity measurements. The measurement uncertainty was observed to be reduced further with the assistance of a higher output power laser and higher finesse mirrors (Schlubler et al., 2012). The comparison between fiber FP interferometer and Michelson interferometer based on flow velocity measurement is presented in Leilabady et al. (1985). FPI has shown good agreement with their simulation in flow velocity sensing.

### *Humidity Sensing*

A nano-FPI humidity sensor can be fabricated using the ISAM method by achieving an operating range of 11.3% to 100% relative humidity within a very short response time; it is applicable for human breathing monitoring (Arregui et al., 1999; 2000). A slim layer of a moisture-sensitive natural polymer chitosan-assisted FPI sensor is proposed for a range of relative humidity from 20% RH to 95% RH. A sensitivity of 0.13 nm/% RH with a quick response time of 380 ms and RH uncertainty of  $\pm 1.68\%$  RH was demonstrated (Chen et al., 2012). A nanocomposite hygrometer polyacrylamide-coated low-temperature sensitivity FPI sensor was proposed and it exhibited a relative humidity sensitivity of  $\sim 0.1$  nm/(1% RH) over a range of 38% to 78% RH and  $\sim 5.868$  nm/(1% RH) over a range of 88% to 98% RH, respectively (Yao et al., 2012). In a recent publication (Xu et al., 2013), an extrinsic micro-cavity FPI with a high sensitivity of 0.307 nm/%RH over a range from 8.8% to 88.1% RH has been demonstrated. The FPI sensor mentioned in the patent (Donlagic et al., 2010) can be used as a humidity sensor.

### *Gas Sensing*

Gas sensing by optical-fiber sensors has drawn significant interest for their extensive applications in the areas of the environment, industry, healthcare, battlefield, and national security. An FPI sensor with polyaniline and Nafion layers deposited on the face of sensor head was fabricated and used as an ammonia gas sensor (Opilski et al., 2005; St-Gelais et al., 2013). A vapour-sensitive polymer layer and a silver layer are deposited in sequence on the fiber endface to construct an optical fiber FPI gas sensor. The vapour-sensitive polymer can be employed with any RIs to broaden the sensor's applications in numerous areas. The sensitivity of this FP gas sensor was reported 0.1 pm/ppm for Norland Optical Adhesive (NOA) 81 and polyethylene glycol (PEG) 400, and 3.5 pm/ppm for methanol vapour (Liu et al., 2009).

### *Liquid Level Sensing*

Liquid level measurement with high precision is a vital necessity in chemical and fuel storage processing systems. An asymmetric FPI was demonstrated for high-accuracy continuous liquid level sensing. Its calibrated sensitivity is 2.4 mV/mm, over a range of 2.3 m (water) (Tao et al., 2009). An optical fiber extrinsic FP cavity liquid-level sensor is formed with an SMF fiber and an elastic silicon layer producing an accuracy of 2 mm over a full scale of 3.5 m (water) under an ambient temperature range of 10 °C to 38 °C (Lu & Yang, 2007). In addition, various FPI liquid level sensors have been proposed in the literature, such as a double-fiber FP cavity with a diaphragm serving as a measurement component (Tong et al., 2012), a dual-optical-fiber-sensor system consisting of a FP pressure sensor and an FBG-level sensor (Lai et al., 2012), an extrinsic FP optical fiber interferometer with an all-fused-silica structure and CO<sub>2</sub> laser heating fusion bonding technology with a high sensitivity of 5.3 nm/kPa (36.6 nm/psi) (Wang & Li, 2014).

### *Refractive Index Sensing*

Refractive index (RI) measurement has gained increasing interest among industrialists due to its important role in substance detection for chemistry and biomedicine applications. As presented in Section 1, a FP RI tip sensor with an RI sensitivity of  $-11.27 \pm 0.34/\text{RIU}$  was achieved by using the FFT technique (Frazao et al., 2009). A simple FPI reported in Chen et al. (2010) can be used for RI measurement of several kinds of glasses and the accuracy of this device is found to be approximately  $10^{-3}$ . In another work, an in-line FPI sensor for RI sensing was formed by inscribing a micro-channel perpendicularly across the core axis to enable liquid flow and light-liquid interaction in the micro-channel. The sensor demonstrated a sensitivity of  $\sim 994 \text{ nm}/\text{RIU}$  and the extremely low-temperature cross sensitivity of  $\sim 4.8 \times 10^{-6} \text{ RIU}/^\circ\text{C}$  makes it a reliable sensor in a varying-temperature environment. Besides micro-channels, microstructured fiber can be used in FPI fabrication due to its micro-sized holes that enable fluid to flow in and out of the FP cavity. An RI sensitivity of  $1,051 \text{ nm}/\text{RIU}$  is reported at the wavelength of  $1,550 \text{ nm}$  (Tian et al., 2013). FPI has been used for monitoring the RI of glasses as well in Xiao et al. (2005) with a resolution greater than  $0.00001 \text{ nm}$  while monitoring changes in RI. A temperature-insensitive FPI RI sensor is reported in Zhao et al., (2010) and it is particularly suitable for circumstances where the variation of ambient temperature is large. It offers a high average RI resolution of  $5 \times 10^{-6} \text{ nm}$  in the range of  $1.314$  to  $1.365 \text{ RIU}$ . Another in-line FPI RI tip sensor was reported with a sensitivity of  $\sim 4.59/\text{RIU}$  for RI sensing (Raoa et al., 2008). FPI sensors were used for RI measurement in Jiang et al. (2013), Lee et al. (2013) as well. To date, many FPI-based RI sensors have been successfully commercialized. For example, one of the products of FISO Technologies, Inc. Quebec, Canada, is a liquid-filled FP optical cavity sensor (FISO Tech., 2014).

## 2.7 Chronology of FP Interferometers

Studying the chronology of FPI sensors is essentially important to understand the sequential development of fabrication techniques and their implementation for sensing applications, which have been discussed in detail in the earlier sections. Achieving an adequate sequential investigative structure of the literature is simply an element in presenting the research chronology. Therefore, a specific collection of diverse forms of research is required in chronological order.

All the possible literature considered for this study has been categorized into two types based on their fabrication techniques: FPI sensor fabrication with splicing and without splicing methods. The sensing applications listed here have been chosen from referred articles. To present a chronological study, we set an approximate starting point at 1981, which has been considered based on a few of the oldest related articles. Thus, we divided the whole period into four time-slots since 1981 to the current period to present the fabrication development and implementation of sensing applications for FPI sensors. Research articles, reviews, proceedings, books, technical papers, patents, dissertations are selected for this review study according to measurands, fabrication techniques, and principles applied. Articles not directly related to these areas are not included in the statistics of this section. The statistics presented below are obtained from all the papers included in the references.

In Figure 2.13, an interesting trend was investigated in terms of the percentage of the various FPI sensor fabrication techniques used over the time ranges of 1981 to 1990, 1991 to 2000, 2001 to 2010, and 2011 to 2014. The percentages are calculated over the total number of papers falling within each time range. The statistics indicate that a larger number of FPI fabrication techniques (approximately 64%) in 2011–2014 involved splicing. Nevertheless, the use of the splicing method was quite low in 1991–

2000. However, it has gained popularity and has currently become widely employed in FPI fabrication. The reason behind this fact is that the fusion splicing technology is well developed and the splicers have become more affordable. In terms of performance, the sensors fabricated based on splicing methods are more stable and compact. Higher throughput power can be attained because of the reduced fiber cavity losses.

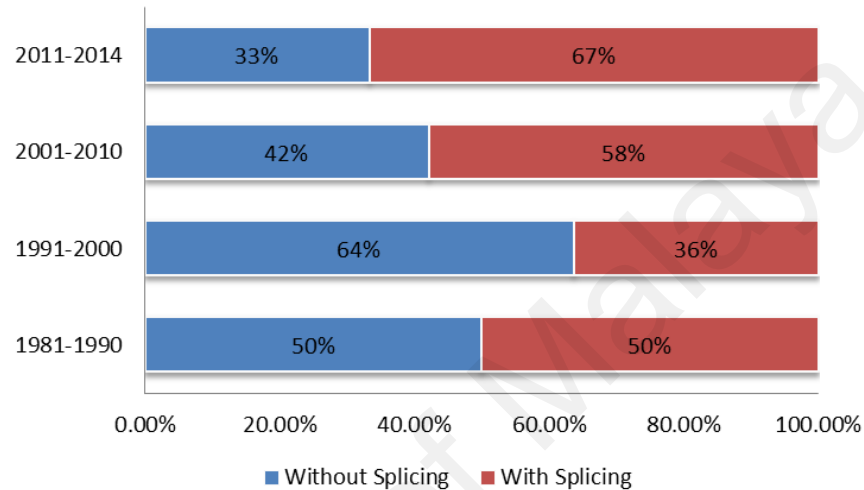


**Figure 2.13: Percentages of the FPI fabrication studies in two categories are presented through some considered time ranges.**

The percentages of sensing applications studied based on the similar strategy applied in the previous chart through the given time spans can be seen in Figure 2.14. Based on the sensing application, the researchers found it difficult to draw any conclusion because almost all the applications have been under consideration throughout the mentioned periods, except for a few sensing applications. Many studies on temperature sensing using FPI sensors followed by vibration, acoustic, strain, and magnetic sensing have been performed over all the time ranges, whereas few studies on other sensing applications have been reported because of their shortcomings such as walk-off loss, crosstalk, phase mismatch, and fragility problems in the case of the tapered fiber ends used for FPIs.

Strain sensing has also been an area of interest for many researchers until 2000, then a decline of interest occurred afterward; whereas pressure sensing by FPI has been

introduced since 1991. The most exciting statistic coming out of this chronology and review study is that a noteworthy rise in the exploration of the measurands is shown with increasing time. In recent years, an increasing number investigations were conducted for temperature, RI, vibration, magnetic, pressure, humidity, acoustic, ultrasonic, strain, velocity, and liquid level sensing using FPI sensors. These measurands have been measured with FPI sensors for many years in civil engineering and transportation, gas and oil industries, energy industries, aerospace, biology and chemical research, and other industries, etc.

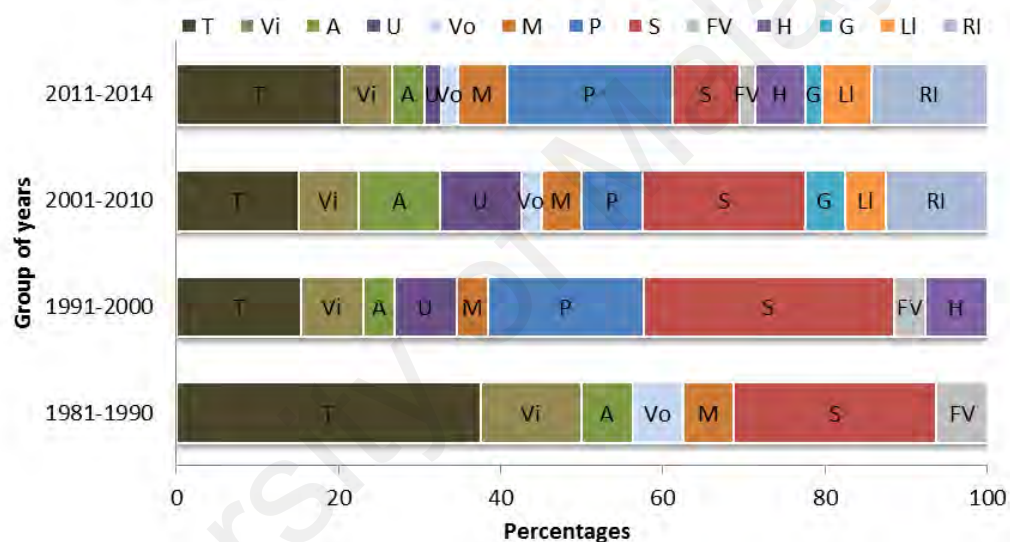


**Figure 2.14: Percentage of sensing applications studied through some given time ranges. T = Temperature, Vi = Vibration, A = Acoustic, U = Ultrasound, Vo = Voltage, M = Magnetic, P = Pressure, S = Strain, FV = Flow velocity, H = Humidity, G = Gas, LI = Liquid level, RI = Refractive index.**

On the basis of patents and studies performed by many researchers, fiber-optic-based FP interferometric sensors have several appealing applications in the industrial sector. To show its significance, some of the industrial applications are mentioned here for better understanding. As reported by Gao et al. (2007), the real-time fiber-optic sensors are used widely in structural health monitoring of large civil structures such as dams, bridges, buildings, and composite material structures because of their good sensitivity and other unique features. These sensors can be mounted on the surface of the structure or embedded into construction materials and structures for continuous monitoring of

various physical conditions, i.e., damage, strain, stress, crack formation, pore pressure, and temperature. The first cable-stayed bridge with a maximum span of 312 m carrying both railway and highway traffic constructed from 1997 to 2000, the Wuhu Yangtze River bridge (WYRB) situated in China, is an example of such an application where some spot-weldable FP fiber-optic strain sensors were installed on the bridge-deck sections as part of WYRB real-time health monitoring system in December 2003. The sensors were more stable and worked efficiently to fulfil the monitoring requirements. Basing on such efficiency, the researchers found that a similar monitoring system including FPI sensors was installed on the Zhengzhou Yellow Railway Bridge for strain monitoring as reported by Gao et al. (2007). Other examples of fiber-optic EFPI sensors are the ones embedded into the Liaohe Bridge, Liaoning, China, at the time of its construction for measuring its dynamic strain. The results obtained from the monitoring system showed the good stability and dynamic response of the sensors as reported by Zhang et al. (2008). Underground fault measurements have been performed using an EFPI displacement sensor in geomechanics (Zhnag et al., 2013). In addition, a partial discharge in transformers was detected as well by using a sulfur hexafluoride-filled FPI (Dong et al., 2008).

Kersey et al. (2007; 2005) affiliated with CiDRA Corporation and developed and patented an FPI sensing element which can sense pressure over the range of 0 MPa to 103 MPa with a resolution of 2.06 kPa and within the suitable temperature range of 25 °C to 175 °C. The borehole pressure/temperature series pressure sensor developed by Sabeus Corporation can operate up to 200 °C with a measurable pressure resolution of 0.69 kPa. Some oil-gas companies, e.g., Weatherford, Sabeus, and SENSORNET, offer similar products, including FPI pressure sensors which have been used for downhole monitoring as reported by Yu et al. (2011). Another EFPI pressure sensor used in downhole monitoring was reported as well (Aref et al., 2007). The other FP cavity



pressure sensor was constructed with the pressure sensitivity of  $-1.8 \text{ rad bar}^{-1}$  and a typical range of 0 kPa to 600 kPa in a turbine test application, using micromachining technique at the isentropic light piston facility at QinetiQ, (Pyestock, UK) (Gander et al., 2003). FPI sensors have been reported to offer promising prospects in nuclear power plant technology because of their unique signal processing techniques and their resistance to power loss (Sexton et al., 1998). One important application of such FPI sensor is temperature monitoring in harsh nuclear plant environments, using a sensor developed by Fiso Technologies in Canada (Liu et al., 2002). Similarly, Sentec Corporation has fabricated FPI temperature sensors under a NASA contract (NAS3-27202) and ground as well as flight tests were performed successfully on an OV-10D airplane (Tuma et al., 1997).

Recently, FPI sensors have been utilized in some interesting applications in biology, the environment, and even in medical sciences. Notably, one of the applications is a biosensor that is capable of producing concentration-dependent signals from antibodies or antigens employing an FPI sensor as an immunosensor. It can eliminate fluorescence labelling or chemiluminescence which requires additional budget and labour for detecting biological interactions. Such sensors have potential for monitoring environmental pollution, in food industries, and monitoring human diseases as well (Chen et al., 2013). Another layer-by-layer modified label-free FPI biosensor was fabricated to detect protein in real-time possessing a potential for immunosensing applications (Chen et al., 2012). One more exciting application is the use of a low-coherence FPI in constructing a surgical tool integrated with a force sensor, which can be used during micro-surgery (e.g., vitreoretinal surgery) (Liu et al., 2012). In addition, an intrinsic FPI sensor fabricated with a nanoporous zeolite thin film was used to detect dissolved organics in water (Liu et al., 2006).

Some of the key findings of the current review are summarized chronologically in Table 2.1. This will assist target audiences (e.g., researchers, commercial industries, users, readers) to draw a quick picture of the chronological flow of the advancement of FPI fiber-optics. With fabrication techniques categorized into with or without splicing, another feature applicable for further division such as, with or without air gap, as illustrated based on entity relationships in Figure 2.15, has been found.

For better illustration, some of the reported techniques are given in Table 2.2, which summarizes all the common advantages reported in the literature based on the given time slots. This table presents the significant features of FPI sensors that make them suitable for various applications. This table will help understand how the FPI was explored chronologically up to the present and prove the potential in several significant applications.

**Table 2.1: A brief presentation of the fabrication methods studied above with sensing applications based on the given time slots.**

Time Slots	[Ref.] /Year	Fabrication techniques	With/without Splicing	With/without Air Gap	Sensing applications
1981–1990	(Wosinski et al., 1994) (1982)	FPI is formed by two dielectric-coated high-reflectance end faces SMF	Without splicing	With air gap	Temperature, vibration, acoustic wave, voltage, magnetic field
	(Lee et al., 1989) (1985)	An SMF is stretched through a tube so that vortex shedding can induce an oscillating strain	Without splicing	Without air gap	Flow velocity
	(Farahi et al., 1988) (1988)	Coherence multiplexing remote fiber-optic FP sensing technique	Without splicing	With air gap	Temperature
	(Lee & Taylor, 1988) (1988)	FPI using dielectric mirrors by standard fusion splicing technique	With splicing	With air gap	Temperature and wavelength
	(Valis et al., 1990) (1990)	Semi-reflective fusion splice technique	With splicing	With air gap	Strain
1991–2000	(Farahi, 1991) (1991)	A miniature fiber FP interferometric modulation technique	With splicing	With air gap	Temperature
	(Lee et al., 1994) (1994)	Micromachining technique	Without splicing	Without air gap	Pressure
	(Sorin & Baney, 1995) (1995)	Low-coherence technique for multiplexed measurements	Without splicing	With air gap	Temperature and strain
	(Han & Neikirk, 1996) (1996)	Micromachined FP interference-based microcavity fabrication	Without splicing	Without air gap	Pressure
	(Beard et al., 1996) (1996)	FPI ultrasound sensing with a thin polymer film	Without splicing	With air gap but water-filled cavity	Ultrasound
	(Kim et al., 1997) (1997)	FPI with Si <sub>3</sub> N/SiO <sub>2</sub> /Si <sub>3</sub> N <sub>4</sub> diaphragm fabrication using micromachining technology	With splicing	With air gap	Pressure
	(Arregui et al., 1999) (1999)	Ionic self-assembly monolayer (ISAM) technique	Without splicing	Without air gap	Humidity
	(Perennes et al., 1999) (1999)	FPI cavity with low-finesse illuminated by a multimode optical fiber	With splicing	With air gap	Not studied

	(Arregui et al., 2000) (2000)	Nanometer-scale FP interferometer by using the ISAM method	Without splicing	Without air gap	Humidity
	(Jiang & Gerhard, 2001) (2001)	A thin transparent elastic polymer film used as a low-finesse FP interferometer	Without splicing	Without air gap	Strain
	(Rees et al., 2001) (2001)	Langmuir-Blodgett (LB) technique	Without splicing	Without air gap	Not studied
	(Oh et al., 2004) (2004)	A magnetostrictive gauge and SMF are inserted in a hollow-core borosilicate tube and an airgap between these is acting as a cavity	Without splicing	With air gap	Magnetic field
<b>2001– 2010</b>	(Liu et al., 2006) (2006)	By polishing a thin layer of zeolite film on the end face of SMF	Without splicing	Without air gap	Dissolved organic matter (DOM) in water
	(Machavaram et al., 2007) (2007)	Two SMF is etched by acid and fusion spliced to form intrinsic FP cavity	With splicing	With air gap	Strain
	(Choi et al., 2008) (2008)	A miniature FP interferometric fiber-optic sensor	With splicing	With air gap	High temperature
	(Villatoro et al., 2009) (2009)	Microscopic air bubble FPI by simple splicing technique	With splicing	With air gap	Strain
	(Coviello et al., 2009) (2009)	Two-mode interferometric sensor by fusion spliced technique	With splicing	With air gap	Temperature
<b>2001– 2010</b>	(Rao et al., 2010) (2009)	MEFPIs sensor by chemical etching technique	With splicing	With air gap	Strain and Temperature
	(Zhao et al., 2010) (2010)	FPI consisting of a segment of SMF tip coated with an SU-8 polymer thin film based on modulated Fresnel reflection	Without splicing	Without air gap	Refractive index
<b>2011– 2014</b>	(Wu et al., 2011) (2011)	Spliced a short length PCF with a standard SMF	With splicing	Without air gap	Pressure and high temperature
	(Kou et al., 2010) (2012)	Focused ion beam (FIB) machining technique	Without splicing	Without air gap	High temperature
	(Chen et al., 2012) (2012)	Chitosan-based FP interferometry	With splicing	With air gap	Humidity
	(Liao et al., 2012) (2012)	Femtosecond laser micromachining and fusion splicing	With splicing	With air gap	Refractive index
	(Zhang et al., 2013) (2013)	Thinned and roughened FPI's external surface of diaphragm by fs laser	With splicing	With air gap	High temperature

(Peng et al., 2013) (2013)	Hybrid interferometric with micro-cavity FPI and Mach-Sender	With splicing	With air gap	Strain
(Dai et al., 2013) (2013)	Tunable micro-cavity FPI by using polymer MEMS technology	Without splicing	With air gap	Pressure
(Wang et al., 2013) (2013)	Spliced SMF with a silica tube	With splicing	With air gap	Pressure
(Lv et al., 2014) (2014)	FPI cavity is filled with water-based magnetic fluid EMG507	Without splicing	Without air gap	Magnetic field
(Du et al., 2014) (2014)	Miniature FPI formed by bundle-core PCF and SMF fiber by splicing	With splicing	Without air gap	High temperature
(Silva et al., 2014) (2014)	A small segment of silica rod spliced between two SMF	With splicing	With air gap	Pressure
(Wang et al., 2014) (2014)	Fusion bonding with a fused-silica diaphragm by CO <sub>2</sub> laser	Without splicing	With air gap	Liquid level

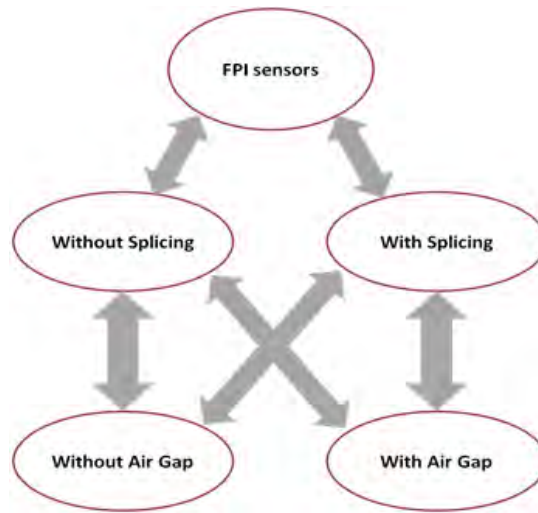


**Figure 2.15: Illustration of FPI sensor categories on the basis of their fabrication.**

**Table 2.2: Advantages of FPI explored in the literature are presented over given time range.**

Time Slots	Ref. No.	Advantages Reported in Literature	Disadvantages Reported in Literature
1981–1990	(Yoshino et al., 1982) (1982)	FPI can have high finesse; Very long distance FPI can be achieved, thus so a high spectral resolution; Walk-off loss problem has been addressed by the fabricated FPI, that involves less accuracy for the tilt angle of reflection surface than the usual form of FPI; such sensor is compatible for a scanning FPI because the optical path length in fiber can be readily modulated by appropriate external perturbations, for example, temperature and mechanical forces.	The walk-off loss of light power is a severe difficulty of FPI fabrication technique that causes by the presence of tilt of the reflection surfaces. It merely decreases the effectiveness and reflectance of the conventional FPI. An increase in interferometer length is the proportion of walk-off loss increase, so construction of long-distance FPI is hardly possible.
	(Faraht et al., 1988) (1988)	Crosstalk drawback is conquered. Requires no separate fiber reference arm.	Crosstalk is another serious drawback of FPI fiber-optic sensor with coherence multiplexing. A coherent signal is generated in the image plane due to highly scattering objects and shows similarity with that of sample depth within the length of coherence refers to “crosstalk”. This problem affects the lengths for several sensors and limits the number of sensors used.
1991–2000	(Chan et al., 1992) (1992)	FPI sensors have High spatial resolution (~20 $\mu\text{m}^2$ ), High-temperature resolution (sub mK), Intrinsic calibration, High measurement bandwidth (>100 kHz), Multiplexed arrays possible, Immunity to electro-magnetic interference.	

**Table 2.2: Cont.**

	(Lee et al., 1994) (1994)	LED is used due to gain advantages from the proposed fabrication technique.	The limitations of utilizing LED is that it has much larger spectral bandwidth and its length of coherence is the much shorter than that of a laser.
	(Ezbiroglu & Tatam, 1996) (1996)	The phase measurement inaccuracy problem has been overcome by a passive signal processing technique.	Almost all the signal processing techniques suffer from phase measurement inaccuracy problem due to the multiple reflections at the two reflective surfaces of FPI.
<b>Time Slots</b>	<b>Ref. No.</b>	<b>Advantages Reported in Literature</b>	<b>Disadvantages Reported in Literature</b>
<b>1991–2000</b>	(Beard & Mills, 1996) (1996)	Using a slim polymer film as one of the reflective surfaces of FPI has many advantages such as short path length, low sensitivity to pressure and thermal differences. As a result, phase-bias-control and complicated polarization systems are not essential. Using a cavity that filled with water other than air has merits too such as, (i) giving a best possible fringe visibility of unity the coefficients of Fresnel reflection on both sides of the film will be the same, and (ii) a possibility of degrading the sensor's consistency of frequency response.	Phase-bias-control and polarization systems are essential for FPI fabrication techniques which make the entire system more complicated.
<b>2001–2010</b>	(Jedrzejowska-Szczerska et al., 2009) (2009)	Reasonably easy fabrication, high resolution, possibly inexpensive, and low sluggishness on temperature differences.	
	(Villatoro et al., 2009) (2009)	A miniature monolithic FPI with a cavity of microbubble exhibits low-temperature sensitivity (less than 1 pm/°C) which indicates that measuring an extremely low temperature can be possible by a microcavity based FPI sensor.	
<b>2011–2014</b>	(Jedrzejowska-Szczerska et al., 2011) (2011)	Easy fabrication even a small size of sensor heads as well as low thermal indolence, and support dielectric construction.	
	(Rong et al., 2012) (2012)	FPI can be constructed as ultra-compact in size, cost effective, and easy to fabricate.	

---

**Table 2.2: Cont.**

---

(Kou et al., 2010) (2012)	It can be exceptionally tiny size, high sensitivity, all-fiber connection, and particularly exclusive structure presents huge potentials for fast-response high-temperature sensing mostly in miniature and harsh area with high temperature gradient. Fragility problem has not been addressed.	The fragility of taper fiber tip is a serious shortcoming in the implementation of such sensors to sensing applications. The sensor can be broken easily due to simple handling or to vibrations that are frequently met in actual industrial applications.
(Chen et al., 2012) (2012)	Using chitosan as reflective surfaces of FPI proposes excellent diaphragm forming capability, high-quality mechanical stiffness as well as enhanced steadiness with respect to the differences in comparative humidity.	
(Liao et al., 2012) (2012)	A fiber in-line FPI fabrication by femtosecond laser micromachining is consistent in the measurement of exceptionally low-temperature cross sensitivity.	

---

Other than the limitations presented in Table 2.2, some usual drawbacks also have been found which require further investigation to achieve handy solutions. For example, OSAs are used widely to detect the wavelength shift, but they are relatively slow. To fully take the advantage of FPI fiber-optic sensors' potential, a detector array-based spectrum analyser can be used. Given that the implementation possibilities of such sensors are endangered in some practical applications due to, for example, fragility, some useful techniques are required to encapsulate the sensor head to protect it and prevent dust particles or fluids from condensing in the cavity, as well as improving its working stability without reducing the performance. According to our knowledge and based on the literature, no work has been performed so far on this aspect. Again, the stability in terms of performance, effectiveness, and extended operation has not been investigated as well as the involved components and environmental effects, and these parameters have not been considered to conquer the risk factors of FPI fiber-optic sensors' implementation in practical applications.



## 2.8 Summary

A literature review of fiber-optic FPI sensors' fabrication methods, working principles, and sensing applications such as detecting temperature, pressure, ultrasonic, acoustic, as well as strain signals has been rigorously considered to compose an informative chapter keeping their pros and cons in mind. Two major categories of FPI optical fiber sensors are discussed, those based on the fabrication method (with splicing and without splicing) and those further interrelated with reference to the air gap present inside the FPI cavity devices. Furthermore, the analytical theory for all types of FPI fabricated sensors with their sensing applications to interferometry has been presented.

On the basis of the investigated study, FPI sensors have enormous practical applications and thus further exploration is needed to make these devices more efficient and beneficial as well as economical. In our perspective, the special optical waveguides, like photonic crystal fibers, have a chance to enable many new sensing mechanisms and configurations. Improved micro-fabrication technologies are appealing to continue the research for the enhancement of sensor performance, functionality, and reliability with operating ability in harsh environments. In addition, the advanced optical signal processing and network technology will enable high-density fiber-optic sensor networks. Unquestionably, FPI sensors will play a key role in future solutions for a widespread diversity of appliances.

Encompassing all of the fabrication technologies, principles, and applications in a limited-length thesis chapter is challenging. Nevertheless, we have included most of the research articles, reviews, proceedings, books, technical papers, patents, and dissertations that match the scope of this thesis. The chronological statistics presented in the earlier section provide an approximation of the whole picture.

## **CHAPTER 3: THEORIES OF FIBER BRAGG GRATING AND FP RESONATOR**

### **3.1 Introduction**

The fundamental theories and principles of fiber Bragg grating and FP resonator are explained in this chapter with a specific end goal to decipher the opto-elastic properties of FBG-based FPR that incorporates theories of light propagation in optical fibers, fundamentals of FBGs, mode coupling, and FP resonator.

### **3.2 Theory of light propagation in optical fiber**

To study opto-elastic properties in short cavity FBG-based FPR manufactured in SMF and PCF cavity FBG-based FPR, including LP<sub>01</sub>–LP<sub>11</sub> cross mode coupling in CG fabricated in TMF, considering the hypothesis of electromagnetic wave propagation in various optical fibers is important. A brief overview of the derivation of wave equation (i.e., Maxwell's equations), the derivation of propagation modes in optical fibers, LP modes, and cut off, and dispersion of light propagation, will be introduced in this section.

Silica-based glass fiber is a suitable transmission medium with recorded losses of less than 0.2 dB km<sup>-1</sup> by utilizing monochromatic and coherent light, laser, as the signal sources. For this, utilizing glass optical fiber to serve as transmission media has resulted in a high-potential option in optical communication frameworks.

#### **3.2.1 Maxwell's Equations**

Every electromagnetic effect is ruled by the four Maxwell equations. The differential form of these equations, should there be an occurrence of a dielectric medium without having currents or free charges in the whole domain, would be as follows (Agrawal, 2007):

$$\nabla \times E = -\frac{\partial B}{\partial t} \quad (3.1)$$

$$\nabla \times H = -\frac{\partial D}{\partial t} \quad (3.2)$$

$$\nabla \cdot B = 0 \quad (3.3)$$

$$\nabla \cdot D = 0 \quad (3.4)$$

where  $H$  and  $E$  are correspondingly the magnetic and vectorial electric fields,  $B$  and  $D$  the magnetic induction and electric displacement fields. Every one of these fields is a function of both time and space. Every case of interest for this research includes isotropic materials, and assuming propagation in the linear regime is often a decent estimate. For example, for a nonmagnetic isotropic medium of an optical fiber, the flux densities  $B$  and  $D$ , are identified by  $H$  and  $E$  through the constitutive equations:

$$D = \varepsilon E + P \quad B = \mu H. \quad (3.5)$$

where  $\varepsilon$  is the electric permittivity,  $\mu$  is the magnetic permeability, and  $P$  is the induced electric polarization. As the dielectric materials are important to us,  $\mu$  can be assumed to be a constant, equivalent to its free-space value. The electric permittivity,  $\varepsilon$ , for the most part, is a function of frequency ( $\omega$ ). The imaginary part of  $\varepsilon$  records material-related losses (absorption). However, in case of low-loss dielectrics, for example, silica in the near-infrared part of the spectrum,  $\varepsilon$  can be presumed to be real.

By applying the operator curl (rotor) on Equation 3.1, and utilizing Equation 3.2 and Equation 3.5 into the outcome, the accompanying wave condition for the electric field can be achieved:

$$\nabla \times \nabla \times E = -\frac{1}{c^2} \frac{\partial^2 E}{\partial t^2} - \mu_0 \frac{\partial^2 P}{\partial t^2} \quad (3.6)$$

where the affected electric polarization  $P$  is identified with the electric field  $E(r, t)$  (a long way from medium resonances), given by the nonlinear Equation by Agrawal (2007).

The electric field  $E(r, t)$  can be represented as far as gradually changing envelope is estimated as:

$$E(r, t) = \frac{1}{2} \hat{x} [E(r, t) \exp(-i\omega_0 t) + c.c.] \quad (3.7)$$

where  $E(r, t)$  is a gradually changing complex envelope,  $\hat{x}$  is the polarization unit vector, c.c. stands for complex conjugate, and  $\omega_0$  is an angular optical frequency.

The linearity of Maxwell's equations allows the utilization of Fourier investigation. By utilizing Fourier analysis, the wave condition Equation 3.6 communicated in the frequency domain is as follows (Agrawal, 2007):

$$\nabla^2 \tilde{E} + \varepsilon(\omega) k_0^2 \tilde{E} = 0 \quad (3.8)$$

where the free-space wavenumber is characterized as:

$$k_0 = \frac{\omega}{c} = \frac{2\pi}{\lambda} \quad (3.9)$$

and the frequency dependent dielectric constant is:

$$\varepsilon(\omega) = 1 + \tilde{\chi}^{(1)}(\omega) + \varepsilon_{NL} \quad (3.10)$$

where  $\varepsilon_{NL}$  is the nonlinear contribution to the dielectric constant (regarded as a constant amid the pulse propagation) and is characterized by:

$$\varepsilon_{NL} = \frac{3}{4} \chi_{xxxx}^{(3)} |E(r, t)|^2 \quad (3.11)$$

$\tilde{\chi}^{(1)}(\omega)$  is the Fourier transform of  $\chi^{(1)}(t)$ . Its real and imaginary parts can be identified with the refractive index  $\tilde{n}(\omega)$  and the attenuation coefficient  $\alpha(\omega)$  using the equation below:

$$\varepsilon = \left( \tilde{n} + \frac{i\alpha c}{2\omega} \right)^2 \quad (3.12)$$

From Equation 3.10, Equation 3.12 and the Equation to ascertain nonlinear refraction from the intensity reliance of refractive index displayed in Agrawal (2007)'s study, the accompanying conditions are attained:

$$n(\omega) = 1 + \frac{1}{2} \text{Re} \left[ \tilde{\chi}^{(1)}(\omega) \right] \quad (3.13)$$

$$\alpha(\omega) = \frac{\omega}{nc} \text{Im} \left[ \tilde{\chi}^{(1)}(\omega) \right] \quad (3.14)$$

where Re and Im are real and imaginary parts, respectively. Given that the imaginary part of  $\varepsilon(\omega)$  is not as important compared to the real part (because of the low losses in fibers), then  $\varepsilon(\omega)$  can be supplanted by  $\tilde{n}^2(\omega)$ .  $\tilde{n}^2(\omega)$  is frequently autonomous of the spatial directions in both the core and cladding of step-index fiber, so that Equation 3.8 arrives at:

$$\nabla^2 \tilde{E} + \tilde{n}^2(\omega) k_0^2 \tilde{E} = 0 \quad (3.15)$$

$$\tilde{E}(r, \omega) = \int_{-\infty}^{\infty} E(r, t) \exp(i\omega t) dt \quad (3.16)$$

In quest for arrangements of the optical field, utilizing the technique for partition of variables is beneficial, so that the envelope  $E(r, t)$  is in a structure as follows:

$$E(r, t) = F(x, y) A(z, t) \exp(i\beta_0 z) \quad (3.17)$$

where  $F(x, y)$  is transverse mode distribution,  $A(z, t)$  is a gradually fluctuating function of  $z$  and  $\beta_0 = \beta(\omega_0)$  is the wavenumber at the carrier frequency. Substitution of Equation

3.17 into the wave equation prompts two conditions for  $F(x, y)$  and  $A(z, t)$  (Agrawal, 2007). The wavenumber  $\beta$  is controlled by tackling the eigenvalue equation for the modes  $F(x, y)$ , while the temporal characteristics of the optical pulse are acquired by utilizing the results of  $A(z, t)$ . For step-index fiber,  $F(x, y)$  is acquired as a solution of the differential equation for Bessel functions (note that in the current practice, the fundamental fiber mode is regularly approximated using a Gaussian distribution of the structure  $F(x, y) \approx \exp[-(x^2 + y^2)/\Omega^2]$ , where  $\Omega$  is the width parameter (Agrawal, 2007)).

The propagation constant,  $\beta$  is by and large a complex number, where the imaginary part represents the losses of the mode as it propagates along the fiber. On account of a traditional optical fiber, the wave condition with suitable boundary conditions can be identified scientifically (Zolla et al., 2005).

### 3.2.2 Propagation modes in optical fibers

Numerous studies have been performed on the mode propagation properties in optical fibers (Snitzer, 1961). Maxwell's equations present the propagation of electromagnetic radiation. For example, light; as a result of which, rich information on the energy confinement, propagation, and dispersion of every mode can be achieved (Gloge, 1971). A voyaging wave is a part of the summed up result for  $E$ , which is the electric field from Maxwell's Equations, as (Snitzer, 1961);

$$E = \bar{E}e^{-i(\omega t \pm \beta z)} \quad (3.18)$$

The propagation constant,  $\beta$ , is given by  $\beta = k_0 n_{eff}$ , where  $k_0 = \frac{2\pi}{\lambda_0}$ , the angular velocity is  $\omega$ , the effective index of refraction of the mode is  $n_{eff}$  and the wavelength of the light is  $\lambda_0$ . The light guiding properties of fiber can be well understood by the fiber

geometry. The core region of the optical fiber allows the light that coupled into the core to be confined and propagate indefinitely. The zig-zag light beam in the core region describes the light propagating inside the core as outlined in Figure 3.1.

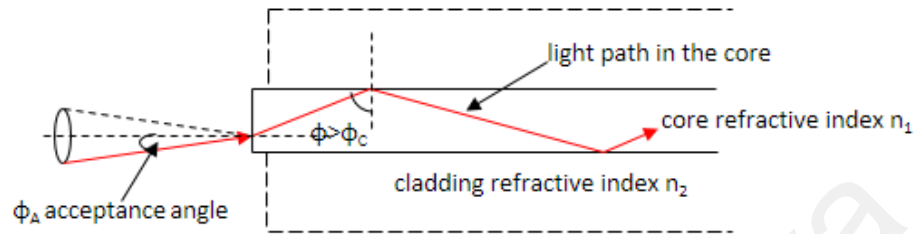


**Figure 3.1: Illustration of light in beam graph experiencing inside reflection while the incident angle to the cladding/core surface is more noteworthy than the critical angle  $\phi_c$  (Cheung, 2004).**

Beams at the core–cladding interface experience numerous reflections. Incident beams undergo total internal reflection at bigger angles than the basic angle,  $\phi_c$  upon the core–cladding interface. The loss is considered least if the light propagates in such way that no absorption transpires in a perfect fiber. By utilizing the Fresnel reflection condition relationship at boundaries, a limit has been set on the coupling angle,  $\phi_A$ . Through this angle, the cladding refractive index and mode set a limit to assure the mode propagation constant  $\beta$  is as follows;

$$n_1 k_0 < \beta < n_2 k_0 \quad (3.19)$$

where the horizontal component  $\beta = \sin \phi$ , voyages down the fiber,  $\beta$  is the propagation constant, the index of refractions of the cladding and core are  $n_2$  and  $n_1$ , respectively. Phase information is carried by light radiation, which is a direction of travel and a wave-like phenomenon. After the phase shift occurred on reflection at the boundary surfaces, productive interference that occurs will advance angles' discrete arrangement, by which propagating constants,  $\beta$  ascends in a discrete arrangement. The numerical

aperture (NA) controls the extent of the fiber's ability to accept light into its bound modes. Jeunhomme (1990) derived the NA as follows:

$$NA = \sqrt{n_1^2 - n_2^2} = n_1 \sqrt{2\Delta n} \quad (3.20)$$

To understand the behaviour of light in a perturbed situation, for example, using FBGs, which is essential to learning the modal properties.

### 3.2.3 LP modes and cut off

Including each of the six non-zero field components in the purported hybrid  $EH_{lm}$  and  $HE_{ml}$  modes causes the careful arrangement of wave condition for a step index fiber to be exceptionally complicated (Snitzer, 1961). A generalization to the arrangement can be communicated by utilizing the estimate for the purported 'Weak Guidance' (Gloge, 1971) where the fractional refractive index contrast is expected to be little.

$$\Delta = \frac{(n_1 - n_2)}{n_1} = \frac{\Delta n}{n_1} \ll 1 \quad (3.21)$$

Utilizing the normalized frequency,  $V$ , given by Gloge (1971), the following equation is obtained;

$$V^2 = (ah)^2 + (ak)^2 \quad (3.22)$$

where  $h^2 = n_1^2 k_0^2 - \beta^2$  and  $k^2 = \beta^2 - n_2^2 k_0^2$ .

The lowermost order is the LP mode, i.e. the  $LP_{01}$ , has no low-frequency cutoff in the weakly guiding estimate. This mode is observed to be indistinguishable to the precise  $HE_{11}$  mode. The  $LP_{11}$  mode, which is the onset of the following LP modes has a cutoff at  $V = 2.401$ . The fibers that support a single mode or just a couple of modes over a specific range of wavelength are essential for a few applications. The standardized



frequency,  $V$  would be less than  $< 2.405$ , for single-mode operation. The standardized frequency,  $V$  in equation (3.22), can be composed as:

$$V = \frac{2\pi a}{\lambda} \sqrt{n_1^2 - n_2^2} \quad (3.23)$$

where the free space wavelength is  $\lambda$  and the core radius is  $a$ . The fiber diameter influences the quantity of modes, i.e. the quantity of modes diminishes if the fiber diameter is diminished, or if the fiber is operated at an extended wavelength. Single-mode fibers in the infrared and visible part of the spectrum typically require a core diameter of a few microns.

#### 3.2.4 Dispersion of light in propagation

Propagation of light satisfying Maxwell's equations can be carefully considered as a superposition of numerous plane-wave solutions. In a Fourier representation, the electric field,  $E$ , can be considered to comprise frequency bandwidth,  $\Delta\omega$ , centre frequency,  $\omega_0$  (Jeunhomme, 1990);

$$E(t) = \int_{\Delta\omega} \xi(\omega) \exp(i\omega t) d\omega \quad (3.24)$$

where  $\omega$ , is the plane wave and the amplitude of its component is  $\xi(\omega)$ . As a result of voyaging a distance,  $z$ , the diverse components of the wave will have their phases changed by the quantity,  $\beta(\omega)z$ ; where,  $\beta$  can be extended utilizing the Taylor series around the central  $\beta_0$ ;

$$\beta(\omega) = \beta_0 + \frac{d\beta}{d\omega} \Delta\omega + \frac{1}{2} \frac{d^2\beta}{d^2\omega} \Delta\omega + \dots \quad (3.25)$$

where  $\beta_0$  is the propagation constant at  $\omega_0$ . Substituting equation 3.25 into equation (3.24),

$$E(z, t) = \int_{\Delta\omega} \xi(\omega) \exp i(\omega t - (\beta_0 + \frac{d\beta}{d\omega} \Delta\omega + \frac{1}{2} \frac{d^2\beta}{d^2\omega} \Delta\omega + \dots)z) d\omega \quad (3.26)$$

which can be deciphered as the propagation of a plane wave adjusted by an envelope function whose phase velocity is given by  $(\beta/\omega)^{-1}$  and group velocity is given by  $(d\beta/d\omega)^{-1}$ . The impact of dispersion (the relationship amongst  $\omega$  and  $\beta$ ) will bring about distinctive components,  $\omega$ , to reach various times. The delay per unit length is given by (Gloge, 1971);

$$\tau = \frac{1}{c} \frac{d\beta}{dk} = \frac{d\beta}{d\omega} \quad (3.27)$$

where, the speed of light is  $c$ .

### 3.3 Fundamentals of Fiber Bragg Gratings

The basic fiber Bragg grating includes a short segment of single-mode optical fiber in which the core refractive index is modulated periodically. As delineated in Figure 3.2, this structure acts as a highly-selective wavelength reflection filter with the wavelength of the peak reflectivity,  $\lambda_B$ , controlled by the phase matching condition as follows:

$$\lambda_B = 2n_{eff} \Lambda \quad (3.28)$$

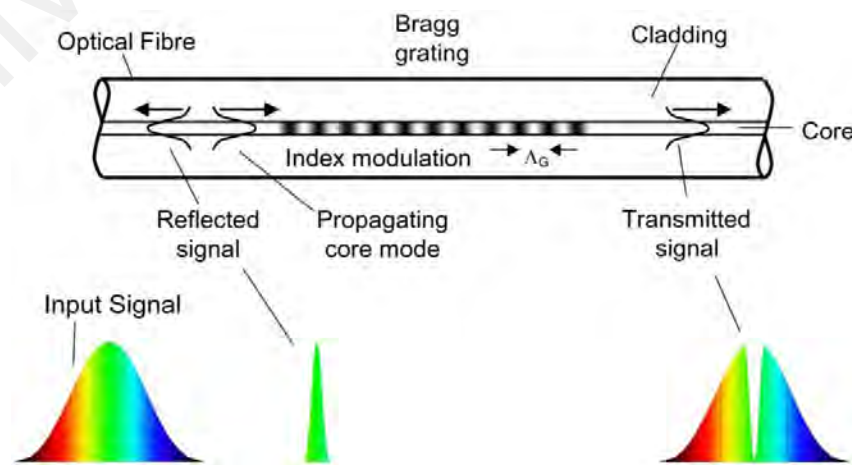


**Figure 3.2: Schematic illustration of structure and spectral response of fiber Bragg grating**

where  $n_{eff}$  is the effective refractive index of the guided mode in the fiber, and  $\Lambda$  is the period of the refractive index modulation with the following type:

$$n(z) = n_{co} + \delta n [1 + \cos(2\pi z / \Lambda)] \quad (3.29)$$

where  $n_{co}$  is the unexposed core refractive index and  $\delta n$  is the amplitude of the photo-induced index excursion. This periodical index-modulated structure enables the light to be paired from the forward-propagating core mode into the backward-propagating core mode, producing a reflection response. The refractive index modulation of the FBG is accomplished through the exposure of the core to a powerful UV interference fringe pattern produced either by free-space two-beam holographic strategy or by diffractive phase mask technique.

### 3.3.1 Phase matching and Bragg condition

Fiber gratings permit the exchange and transfer of power between modes of an optical fiber. This is accomplished by perturbing the phase of one mode such that it matches the phase of the other, which is called the “phase matching condition”. Fiber gratings are generally printed on bare fibers where the acrylate coating is removed. This implies that the optical fiber acts as a three-layer structure with various effective refractive indexes in the core,  $n_1$ , and the cladding,  $n_2$ , with the last external cladding being air,  $n_3 = 1$ . For a single mode fiber with these parameters, the core-guided mode has a propagation constant,  $\beta_{co}$ , given by Equation (3.30):

$$\frac{2\pi}{\lambda} n_2 < \beta_{co} = \frac{2\pi}{\lambda} n_{co} < \frac{2\pi}{\lambda} n_1 \quad (3.30)$$

Furthermore, the cladding modes guided by the cladding-air structure have propagation constants that fall in the range below:

$$\frac{2\pi}{\lambda} n_3 < \beta_{cl} < \frac{2\pi}{\lambda} n_2 \quad (3.31)$$

Last, radiation modes that can have propagation constants in the following limit exist:

$$0 < \beta_{rad} < \frac{2\pi}{\lambda} n_3 \quad (3.32)$$

With the introduction of the effective index's periodic variety along the fiber length, the first order phase matching between the fundamental and backward propagation fiber modes (fundamental of cladding modes) happens when (Erdogan, 1997):

$$\beta_1 - \beta_2 = \frac{2\pi}{\Lambda} \quad (3.33)$$

For example, coupling into the backward propagating fundamental mode, where  $\beta_2 = -\beta_1$ , the resonance condition yields the following equation:

$$\beta_1 = \frac{\pi}{\Lambda} \quad (3.34)$$

In expressions (3.33) and (3.34),  $\Lambda$  is the period of the effective index modulation, whereas  $\beta_1$  and  $\beta_2$ , which are the propagation constants of the fundamental mode and the mode the reflected light is coupled into, respectively. Gratings that couple to backward propagation modes are known as reflection or Bragg gratings. Characteristically, these devices depend on a coupling between the forward and backward fundamental modes.

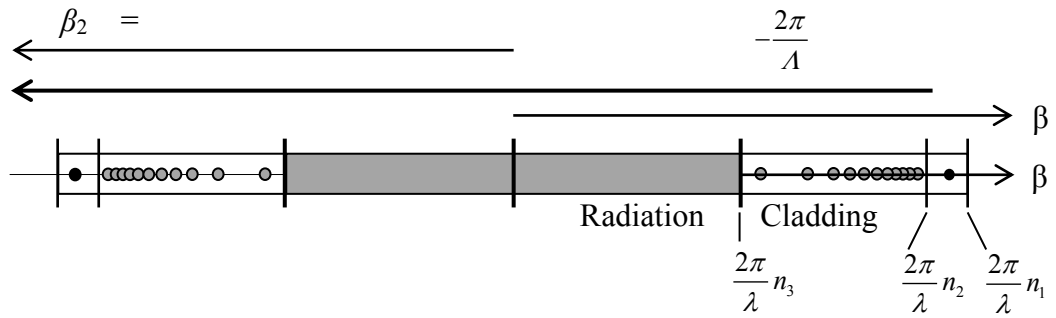


**Figure 3.3: Schematic representation of the modes existing in uncoated single mode fibers and the matching condition for the core mode reflection (Cheung, 2004).**

The phase-matched condition is given by equation (3.33) where,  $\beta_1 = \frac{2\pi n_{eff}^1}{\lambda}$

and  $\beta_2 = \frac{2\pi n_{eff}^2}{\lambda}$ ,  $n_{eff}^1$  and  $n_{eff}^2$  are the mode indices of the forward and backward propagating modes. Hence, equation (3.33) can be composed as:

$$\Lambda = \frac{\lambda}{n_{eff}^1 + n_{eff}^2} \quad (3.35)$$

Considering the preservation of energy advances the coupling of modes with the same optical frequency,  $\omega$ . For indistinguishable forward and counter-propagating modes, equation (3.35) produces the Bragg condition that can be expressed by equation (3.28) where the Bragg wavelength is reflected prevalently.

### 3.3.2 FBG parameters

The coupled-mode equations for the forward and backward propagating modes, when connected to a uniform period grating, can be resolved utilizing suitable boundary conditions. Taking Figure 3.4 as an example, the grating has a length of  $L_g$ , and the boundary conditions expect a forward propagating mode with  $F(0) = 1$  and that the backward propagating mode toward the end of the grating, will be zero,  $B(L_g) = 0$  as there are no perturbing beyond the end of the grating.

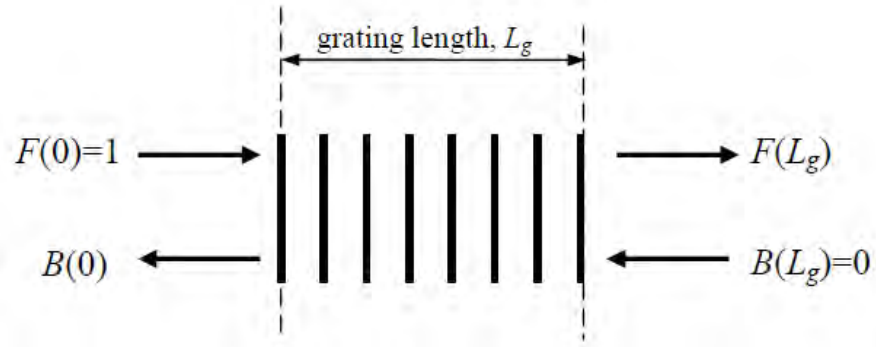


**Figure 3.4: schematic of the grating with the boundary conditions in order of appearance (Kashyap, 1999).**

For uniform grating,  $d\phi/dz = 0$ , and at the phase-matched condition,  $\Delta\beta = 0$ , it is possible to demonstrate that a closed-structure solution exists for the reflectivity,  $R(0)$ , which is given by Kashyap (1999) in Equation 3.36 below:

$$R = \frac{|K_{ac}|^2 \sinh^2(\alpha L_g)}{|K_{ac}|^2 \cosh^2(\alpha L_g) - \delta^2} \quad (3.36)$$

where  $|K_{ac}| < \delta$  and  $\alpha = \sqrt{|k_{ac}|^2 - \delta^2}$

The reflectivity in equation (3.36) has a decay nature and drops off exponentially along the perturbation region as the power is exchanged from the forward to the backward propagating mode. The maximum reflectivity,  $R_{max}$  is then acquired from equation (3.36) when  $\delta = 0$ , i.e. at the phase-matching condition in equation (3.28), yielding equation 3.37 below:

$$R_{max} = \tanh(k_{ac} L_g) \quad (3.37)$$

The initial two zeros of equation (3.36) may be utilized to estimate the full Bragg grating bandwidth given by Equation 3.38 below:

$$\Delta\lambda = \frac{\lambda^2}{2\pi n_{eff} L} \sqrt{(k_{ac} L_g)^2 + \pi^2} \quad (3.38)$$

The condition for weak grating corresponds to  $k_{ac} L_g \ll \pi$ , in which the bandwidth is an inverse function of the grating length, denoted by the following equation:

$$\Delta\lambda = \frac{\lambda^2}{2\pi n_{eff} L_g} \quad (3.39)$$

whereas for a robust grating,  $k_{ac} L_g \gg \pi$ , the bandwidth is given the following equation:

$$\Delta\lambda = \frac{\lambda^2 k_{ac}}{2n_{eff}} \quad (3.40)$$

where the bandwidth relies on the coupling constant  $k_{ac}$ .

### 3.3.3 Chirped FBG and the grating phase shift

A variety of grating periods along the length of the FBG is termed chirp. Chirp can likewise be accomplished by a variety of mode refractive indexes. These distinctive types of chirps can be denoted by an additional phase function,  $\phi(z)$ , in the perturbed polarization produced by the refractive index variation given by Kashyap (1999);

$$P_{grating} = 2n\epsilon_0 \left[ \overline{\Delta n} + \frac{\Delta n}{2} \left( e^{i((2\pi N/\Lambda)z + \phi(z))} + cc \right) \right] E \quad (3.41)$$

where  $\overline{\Delta n}$  is the refractive index change occurring over a single period of the grating,  $\nu$  is the visibility of the fringes, and the exponent term alongside the complex conjugate,  $cc$ , portrays the real periodic modulation in the complex documentation. A subjective spatially differing phase of  $\phi(z)$  has been incorporated.  $\Lambda$  is the perturbation period, while  $N$  is an integer ( $-\infty < N < +\infty$ ) that indicates harmonic order. The period-averaged change in the refractive index must be checked because it changes the effective index  $n_{eff}$  of a mode.

The chirp changes the effective detuning parameters. Therefore,  $\Delta\beta$  in the equation of detuning would be:

$$\delta = k_{dc} + \frac{1}{2} \left( \Delta\beta - \frac{d\phi(z)}{dz} \right) \quad (3.42)$$

where  $\Delta\beta = \beta_u + \beta_v - 2\pi N/\Lambda$ , is the detuning, whereas  $\beta_u$  and  $\beta_v$  are elements of wavelength. Period chirp is made by an adjustment in the phase of refractive index modulations, closely resembling a phase-modulated carrier. The index perturbation can be composed as a sinusoidal function:

$$\cos(Kz + \phi(z)), \quad (3.43)$$

which has a constant spatial frequency, given by  $K = \frac{2\pi}{\Lambda}$  with an extra position-dependent phase variation  $\phi(z)$  to signify the variation in periodicity. The chirp could be seen as a perturbation with differing spatial frequency (Koelnik, 1979):

$$\cos(K + \Delta K(z)) \quad (3.44)$$

The relationship between the period,  $\Lambda$ , and the spatial frequency can be composed as:

$$dK = -\frac{2\pi}{\Lambda^2} d\Lambda \quad (3.45)$$

The rate of phase variation with separation along the grating,  $z$ , can be determined as follows:

$$\frac{d\phi}{dz} = \Delta K \quad (3.46)$$

$$\frac{d\phi}{dz} = -\frac{2\pi}{\Lambda^2} d\Lambda \quad (3.47)$$

From the Bragg condition from equation (3.28), equation (3.47) is derived as (Erdogan, 1997)

$$\frac{d\phi}{dz} = -\frac{4\pi n}{\lambda^2} \frac{d\lambda}{dz} z \quad (3.48)$$

where  $\frac{d\lambda}{dz}$  is the chirp rate of the FBG, that is characterized by a disparity of the periodicity, difference of the mode refractive index along the grating length, a mix of the two or just an extra position-dependent phase along the grating.



### 3.4 Mode Coupling Theory (CMT) for Grating

The coupled-mode theory is a helpful tool for quantitative investigation of the spectral response of FBGs. Considering a dielectric medium with a dielectric tensor perturbation  $\Delta\varepsilon$ ; the optical waves propagate in a limitless number of modes. As indicated by the coupled-mode theory (Alemohammad, 2010), the minute disparity of amplitude  $A_m$  of the  $m^{\text{th}}$  mode signified by  $dA_m$ , due to the coupling with the  $l^{\text{th}}$  mode in the region amongst  $z$  and  $z + dz$  is as follows:

$$dA_m(z) = -i \frac{|\beta_m|}{\beta_m} \sum_l A_l(z) K_{ml} e^{i(\beta_m - \beta_l)z} \quad (3.49)$$

where  $K_{ml}$  is the coupling coefficient between the  $l^{\text{th}}$  and the  $m^{\text{th}}$  modes, demonstrated by:

$$K_{ml} = \frac{\omega}{4} \int_S E_m^*(x, y) \Delta\varepsilon(x, y, z) E_l(x, y) dx dy \quad (3.50)$$

Equation (3.49) is an arrangement of coupled differential equations portraying the coupling between a vast number of modes in the light propagation.

In view of the heading of the propagating mode, the coupling can be co-directional; where the modes propagate in the same direction, or contra-directional and where the modes propagate in inverse directions.

#### 3.4.1 Coupling Coefficient for Single Mode grating

In FBGs, the mode coupling takes place between two contra-directional core modes, as shown in Figure 3.5 (Erdogan, 1997).

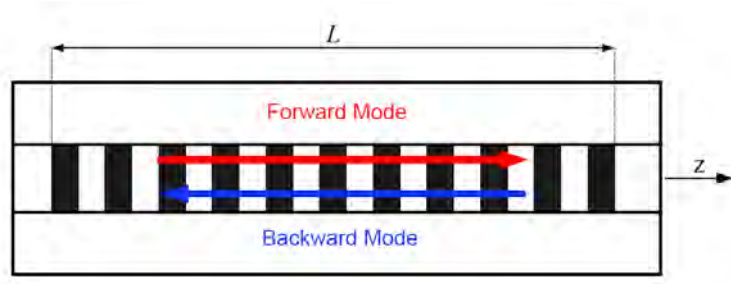


**Figure 3.5: Forward and backward modes in FBG (Erdogan, 1997).**

Thus, the coupled-mode equation (3.49) can be streamlined to the following equations:

$$\frac{dA_1(z)}{dz} = -iK_{11}A_1(z) - iK_{12}A_2(z)e^{i(\beta_1 - \beta_2)z} \quad (3.51)$$

$$\frac{dA_2(z)}{dz} = iK_{21}A_1(z)e^{i(\beta_2 - \beta_1)z} + iK_{22}A_2(z) \quad (3.52)$$

where  $A_1(z)$  and  $A_2(z)$  are the amplitudes of the forward and backward propagating modes, respectively. Since FBG is a periodic modulation of the index of refraction, the perturbation in the dielectric tensor ( $\Delta\epsilon$ ) is denoted as:

$$\Delta\epsilon(z) = \epsilon_0\Delta n^2(z) \quad (3.53)$$

By expecting little variation in the refraction index,

$$\Delta\epsilon \approx 2\epsilon_0 n \Delta n \quad (3.54)$$

where  $\Delta n$  is depicted by Equation 3.55

$$\Delta n(z) = \overline{\Delta n}(z) \left[ 1 + v \cos\left(\frac{2\pi}{\Lambda}z + \Phi(z)\right) \right] \quad (3.55)$$

In a uniform grating,  $\overline{\Delta n}(z)$  is constant and can be supplanted by  $\overline{\Delta n}$ .  $\Delta n$  can also be represented as:

$$\Delta n(z) = \overline{\Delta n} \left[ 1 + \frac{v}{2} \left( e^{i\left(\frac{2\pi}{\Lambda}z + \Phi(z)\right)} + e^{-i\left(\frac{2\pi}{\Lambda}z + \Phi(z)\right)} \right) \right] \quad (3.56)$$

By substituting Equation (3.56) into Equation (3.53),  $K_{ml}$  is modified as:

$$k_{ml} = \frac{\omega \varepsilon_0}{2} \left[ 1 + \frac{\nu}{2} \left( e^{i\left(\frac{2\pi}{\Lambda}z + \Phi(z)\right)} + e^{-i\left(\frac{2\pi}{\Lambda}z + \Phi(z)\right)} \right) \right] \int_S \overline{n \Delta n} E_m^*(x, y) E_l(x, y) dx dy \quad (3.57)$$

where  $m, l = 1, 2$

For two contra-directional modes with propagation constants,  $\beta_1$  and  $\beta_2$ , in FBG are represented by:

$$\begin{aligned} \beta_1 &= -\beta_2 > 0 \\ E_1(x, y) &= E_2(x, y) \end{aligned} \quad (3.58)$$

Equation (3.57) is utilized to get  $K_{11}$ ,  $K_{12}$ ,  $K_{21}$ , and  $K_{22}$ . By substituting them into Equation (3.51),

$$\begin{aligned} \frac{dA_1(z)}{dz} &= -i \frac{\omega \varepsilon_0 n \Delta n}{2} A_1(z) \int_S E_1^*(x, y) E_1(x, y) dx dy \\ &- i \frac{\omega \varepsilon_0 n \Delta n}{4} A_1(z) \left( e^{i\left(\frac{2\pi}{\Lambda}z + \Phi(z)\right)} + e^{-i\left(\frac{2\pi}{\Lambda}z + \Phi(z)\right)} \right) \int_S E_1^*(x, y) E_1(x, y) dx dy \\ &- i \frac{\omega \varepsilon_0 n \overline{\Delta n}}{2} A_2(z) e^{2\beta_2 z} \int_S E_1^*(x, y) E_1(x, y) dx dy \\ &- i \frac{\omega \varepsilon_0 n \overline{\Delta n}}{4} A_2(z) \left( e^{i\left(2\beta_2 z + \frac{2\pi}{\Lambda}z + \Phi(z)\right)} + e^{i\left(2\beta_2 z - \frac{2\pi}{\Lambda}z - \Phi(z)\right)} \right) \int_S E_1^*(x, y) E_1(x, y) dx dy \end{aligned} \quad (3.59)$$

From the orthogonality of the propagating modes (Yariv & Yeh, 2003), the following equation is derived:

$$\int_S E_1^*(x, y) E_1(x, y) dx dy = \frac{2\omega\mu}{\beta} \quad (3.60)$$

where  $\mu$  is magnetic permeability of the dielectric material and is presumed to be a tensor. By substituting Equation (3.60) into Equation (3.59),

$$\begin{aligned} \frac{dA_1(z)}{dz} = & -iK_{dc}A_1(z) - iK_{AC}A_1(z)e^{i\left(\frac{2\pi}{\Lambda}z + \Phi(z)\right)} - iK_{AC}A_1(z)e^{-i\left(\frac{2\pi}{\Lambda}z + \Phi(z)\right)} \\ & - iK_{dc}A_2(z)e^{i\beta z} - iK_{AC}A_2(z)e^{i\left(2\beta z + \frac{2\pi}{\Lambda}z + \Phi(z)\right)} - iK_{AC}A_2(z)e^{i\left(2\beta z - \frac{2\pi}{\Lambda}z - \Phi(z)\right)} \end{aligned} \quad (3.61)$$

where

$$K_{dc} = \frac{\omega^2 \mu \varepsilon_0 n \overline{\Delta n}}{\beta} = \frac{2\pi}{\lambda} \frac{n}{n_{eff}} \overline{\Delta n}$$

furthermore,

$$K_{AC} = \frac{v}{2} K_{dc}$$

In apodised gratings,  $\overline{\Delta n}$  is not constant along the fiber and can change (Alemohammad, 2010). Subsequently, the coupling coefficients,  $K_{dc}$  and  $K_{AC}$ , are not consistent along the grating.

For uniform gratings, ( $\Phi(z) = 0$ ), it is clear that  $2\pi / \Lambda \neq 0$  and  $\beta \neq 0$ . Along this line, phase-matching condition takes place as per Equation (3.33), portraying resonance in the propagating mode coupling (Yariv & Yeh, 2003). Furthermore, the Bragg condition in FBG is acquired specifically from Equation (3.33).

### 3.4.2 Coupling Coefficient for Few Mode grating

The derivation of CME has been extensively presented and discussed in many prior literatures (Ergogan, 1997; Okamoto, 2006; Huang, 1994). To be explained simply, the presentation of CME in this work follows the model reported in Ergogan (1997) closely. For CG inscribed in TMF, the two lowest spatial modes LP<sub>01</sub> and LP<sub>11</sub> in the TMF are being considered in the analysis illustrated in Figure 3.6.

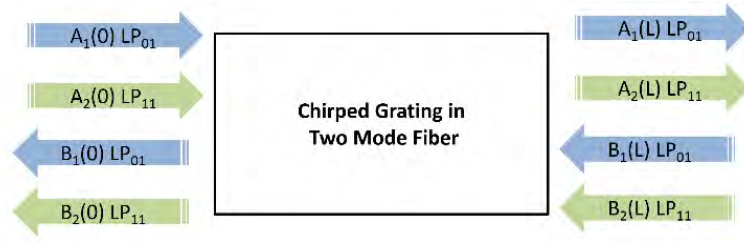


**Figure 3.6: Illustrative diagram of CG with two spatial modes in TMF**

The coupled mode equations can be expressed as follows:

$$\frac{dA_1}{dz} = -j\hat{\sigma}_{01}A_1 - jk_{01}B_1 - jk_cB_2 \quad (3.62a)$$

$$\frac{dA_2}{dz} = -j\hat{\sigma}_{11}A_2 - jk_cB_1 - jk_{11}B_2 \quad (3.62b)$$

$$\frac{dB_1}{dz} = j\hat{\sigma}_{01}B_1 + jk_{01}^*A_1 + jk_c^*A_2 \quad (3.62c)$$

$$\frac{dB_2}{dz} = j\hat{\sigma}_{11}B_2 + jk_{11}^*A_2 + jk_c^*A_1 \quad (3.62d)$$

where  $A_1(z)$  and  $A_2(z)$  denote the forward propagating field amplitudes of LP<sub>01</sub> mode of LP<sub>11</sub> mode whereas  $B_1(z)$  and  $B_2(z)$  denote the backward propagating field amplitudes of LP<sub>01</sub> mode of LP<sub>11</sub> mode, respectively.  $z$  is the position along the grating structure. The detailed relations of coupling coefficients under different mode coupling conditions are as follows:

The coupling coefficients of the two modes are given by (Ergogan, 1997; Wu et al., 2012) as

DC coupling coefficient:

$$\sigma_{\mu\nu}(z) = \frac{\omega N}{2} \iint_{core} \Delta N(x, y) E_{\mu}(x, y) E_{\nu}^*(x, y) dx dy \quad (3.63a)$$

AC coupling coefficient:

$$k_{\mu\nu}(z) = \frac{\nu}{2} \sigma_{\mu\nu}(z) \quad (3.63b)$$

where  $N$  is the refractive index of the fiber core,  $\omega$  is an angular frequency of light,  $\nu$  is the fringe visibility,  $\Delta N$  is UV-perturbed refractive index profile,  $E_\mu$  and  $E_\nu$  are the normalized electric field of associated spatial modes. Equations (3.63a) and (3.63b) can be simplified and expressed in the following form for different mode-coupling conditions.

*A. LP<sub>01</sub>↔<sub>01</sub> Self mode-coupling:*

AC coupling coefficient:

$$k_{01} = k_{01}^* = \eta_{01} \pi \Delta N / \lambda \quad (3.64a)$$

DC coupling coefficient:

$$\hat{\sigma}_{01} = \sigma_{01} + \delta_{01} \quad (3.64b)$$

where

$$\sigma_{01} = \eta_{01} 2\pi \Delta N / \lambda \quad (3.64c)$$

and detuning

$$\delta_{01} = \beta_{01} - \pi / \Lambda(z) \quad (3.64d)$$

*B. LP<sub>11</sub>↔<sub>11</sub> Self mode-coupling:*

AC coupling coefficient:

$$k_{11} = k_{11}^* = \eta_{11} \pi \Delta N / \lambda \quad (3.65a)$$

DC coupling coefficient:

$$\hat{\sigma}_{11} = \sigma_{11} + \delta_{11} \quad (3.65b)$$

where

$$\sigma_{11} = \eta_{11} 2\pi\Delta N / \lambda \quad (3.65c)$$

and

$$\delta_{11} = \beta_{11} - \pi / \Lambda(z) \quad (3.65d)$$

*C. LP<sub>01</sub>↔<sub>11</sub> cross mode-coupling:*

AC coupling coefficient:

$$k_c = k_c^* = \eta_c \pi \Delta N / \lambda \quad (3.66)$$

$\eta_v$  denotes the overlap factor of the mode-coupling,  $v = 01, 11$  (self-mode) or  $c$  (cross mode).  $\Delta N$  denotes the induced index change in the core and  $\lambda$  is the wavelength. The mode propagation constant can be expressed using Equation (3.28).

$\Lambda(z)$  represents the grating period of the chirped grating in the function of  $z$ . For a grating with linear chirp rate, the grating period can be expressed as:

$$\Lambda(z) = \Lambda(0) + rz \quad (3.67)$$

where  $r$  is the chirped rate.

Assuming that the grating length is sufficiently short, the mode coupling between core modes and cladding modes is small and therefore the cladding modes are ignored in this study.

The differential equations from Equations (3.62a)–(3.62d) can be written in matrix form, as follows:

$$\frac{d}{dz} \begin{pmatrix} A_1 \\ A_2 \\ B_1 \\ B_2 \end{pmatrix} = \begin{pmatrix} -j\hat{\sigma}_{01} & 0 & -jk_{01} & -jk_c \\ 0 & -j\hat{\sigma}_{11} & -jk_c & -jk_{11} \\ jk_{01}^* & jk_c^* & j\hat{\sigma}_{01} & 0 \\ jk_c^* & jk_{11}^* & 0 & j\hat{\sigma}_{11} \end{pmatrix} \begin{pmatrix} A_1 \\ A_2 \\ B_1 \\ B_2 \end{pmatrix} \quad (3.68)$$

The equation can be numerically solved using the fourth order Runge-Kutta (RK4) method (Sun et al., 2009).

The total input power is denoted by Equation 3.69

$$P_i = |A_1(0) + A_2(0)|^2 \quad (3.69)$$

Assuming that  $P_i = 1$ , the reflectance is denoted by Equation 3.70

$$R = |B_1(0) + B_2(0)|^2 \quad (3.70)$$

and the transmittance is denoted by

$$T = |A_1(L_g) + A_2(L_g)|^2 \quad (3.71)$$

Depending on the mode of excitations, different boundary conditions are defined as follows:

$$\text{LP}_{01} \text{ mode excitation: } A_1(0) = 1, A_2(0) = 0, B_1(L_g) = 0, B_2(L_g) = 0$$

$$\text{LP}_{11} \text{ mode excitation: } A_1(0) = 0, A_2(0) = 1, B_1(L_g) = 0, B_2(L_g) = 0$$

where  $L_g$  represents the grating length.

### 3.5 Theory of Proposed FBG based FPR

In this thesis, a short cavity FBG based FPR, PCF cavity FBG based FPR, and chirped grating FP interferences have been investigated. The following subsections demonstrate the theories of the proposed FP resonators.



### 3.5.1.1 Uniform Period Short-cavity Fiber Bragg Grating Fabry-Perot

The least difficult kind of fiber FBG is one where FP comprises two uniform FBGs isolated by a cavity printed in an optical fiber with the FBGs possessing the same wavelength. Figure (3.7) illustrated the FBG FP.

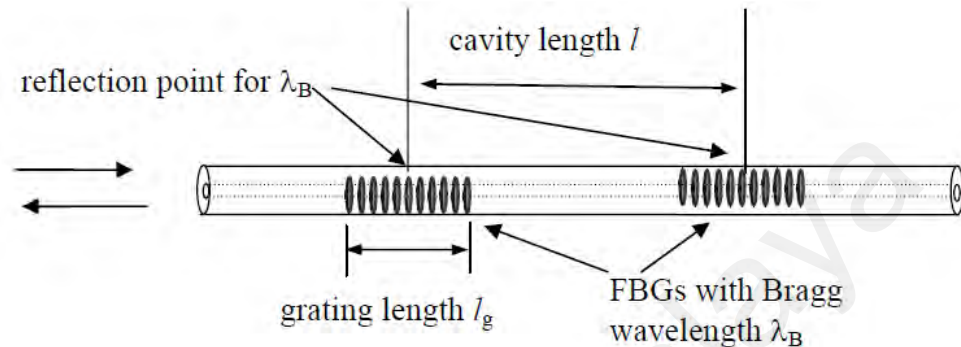


**Figure 3.7: uniform FBG grating FP**

The Bragg wavelength is given by Equation (3.28) and the usual FBG bandwidth is given by Equation (3.33) contingent upon the quality of coupling between the regressive and forward waves. At zero detuning, the peak reflectivity of the FP filter, RFP, with FBGs of undisguisable reflectivity, R, is specified by Legoubin et al. (1995).

### 3.5.1.2 PCF-cavity FBG Fabry-Perot

A mechanical cleaver equally partitioned a 2 cm long uniform FBG into two and then spliced with a ~1.5 mm long PCF using FSM-45PM, Fujikura splicer to construct an FBG-PCF-FBG structure. It is apparent that the two partitioned FBGs that originate from the same uniform grating share the same centre wavelength and the PCF segment forms a cavity between two grating reflectors. As a result, a narrow dip formed within the reflection curve of the FBG, known as resonance wavelength.

The cavity length is selected in such a way that the wavelength spacing between the adjacent resonance wavelength  $\Delta\lambda$  is approximately the same as the reflection bandwidth to facilitate single resonance wavelength accommodation within the FBG

reflection curve for easy identification. The wavelength spacing given by (Taylor, 2002):

$$\Delta\lambda = \lambda^2 / 2n_{PCF}L_{PCF} \quad (3.72)$$

where  $n_{PCF}$  is the effective index,  $L_{PCF}$  is the cavity length, and  $\lambda$  is the operating wavelength. For  $L_{PCF} = 1.5$  mm, the estimated  $\Delta\lambda$  is 0.54 nm. However, it is also possible to achieve greater  $\Delta\lambda$  by reducing the segment length of PCF. The phase difference induced by PCF is given by

$$\phi = \frac{4\pi n_p L_{PCF}}{\lambda} \quad (3.73)$$

At resonance wavelength, the phase difference is multiple of  $2\pi$ . Hence,

$$\lambda_R = \frac{2n_p L_{PCF}}{p} \quad (3.74)$$

where  $p$  is an integer.

When the PCF segment is subjected to the external perturbations,  $\lambda_R$  is shifted by

$$\Delta\lambda_R = \left( \frac{\Delta n}{n} + \frac{\Delta L_{PCF}}{L_{PCF}} \right) \lambda_p = \left( \frac{\Delta n}{n} + \varepsilon_{z,PCF} \right) \lambda_R \quad (3.75)$$

where  $\Delta n$  and  $\Delta L_{PCF}$  are the changes in  $n$  and  $L_{PCF}$ , respectively.  $\varepsilon_z$  is the axial strain in PCF, which is equal to  $\Delta L_{PCF} / L_{PCF}$ . Similarly, the Bragg wavelength shift can be formulated as

$$\Delta\lambda_B = \left( \frac{\Delta n_{eff}}{n_{eff}} + \frac{\Delta\Lambda}{\Lambda} \right) \lambda_B = \left( \frac{\Delta n_{eff}}{n_{eff}} + \varepsilon_{z,FBG} \right) \lambda_B \quad (3.76)$$

where  $\Delta n_{eff}$  and  $\Delta\Lambda$  are the changes in  $n_{eff}$  and  $\Lambda$  of FBG, respectively.

### 3.5.1.3 Chirped Fiber Bragg Grating Fabry-Perot

The chirped FBG FP offers a larger bandwidth, whereas uniform FBG FP gives a larger dynamic range. Chirped grating manufactured in this study in two-mode optical fiber (TMF) and cross-mode interference was observed. The characterization test was executed on the CG with an extended fiber length of 50 cm to both ends of TMF to change the fiber's optical path lengths. Both spatial modes in CG were simultaneously excited by LP<sub>11</sub> mode profile. The reflection spectrum demonstrates the interference between two beams from both LP<sub>01</sub> and LP<sub>11</sub>.

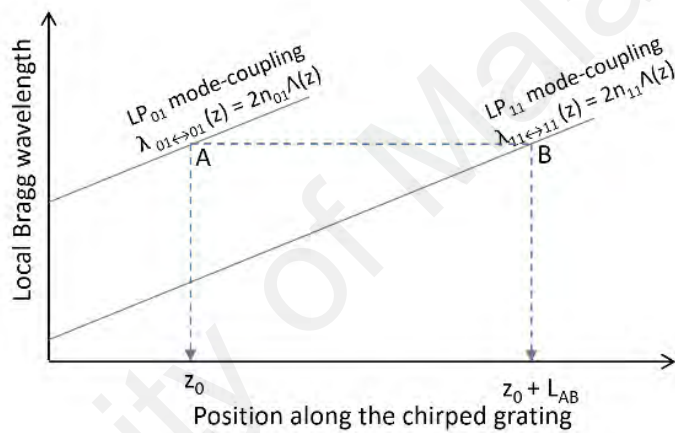


**Figure 3.8: Simplified illustrative diagram of the Fabry Perot resonance in the CG-TMF formed by two grating reflectors with linearly varying Bragg wavelengths of  $\lambda_{01 \leftrightarrow 01}(z)$  and  $\lambda_{11 \leftrightarrow 11}(z)$  respectively**

Figure 3.8 demonstrates the local Bragg wavelengths of various mode couplings along the CG. Contingent upon the types of mode coupling, the corresponding local Bragg wavelengths are as follows:

$$\text{LP}_{01 \leftrightarrow 01} \text{ mode-coupling: } \lambda_{01 \leftrightarrow 01}(z) = 2n_{01}\Lambda(z) \quad (3.77)$$

$$\text{LP}_{11 \leftrightarrow 11} \text{ mode-coupling: } \lambda_{11 \leftrightarrow 11}(z) = 2n_{11}\Lambda(z) \quad (3.78)$$

Since  $\Lambda(z)$  was linearly differing along CG, both  $\lambda_{01 \leftrightarrow 01}$  and  $\lambda_{11 \leftrightarrow 11}$  were in the same chirping direction along CG, accepting that  $n_{01} - n_{11}$  was consistent with the scope of the reflection range. It was conceivable to accomplish  $\lambda_{01 \leftrightarrow 01}(z) = \lambda_{11 \leftrightarrow 11}(z + L)$  at two

distinct positions along CG, which are indicated as A and B in Figure 3.8 and isolated by a spacing of  $L$ . The incurred interference patterns in the output spectra were the consequences of the FP resonance between these two local grating elements.

The spacing between point A and point B,  $L_{AB}$  can be determined as stated below:

The local Bragg wavelength  $\lambda_{01 \leftrightarrow 01}$  at point A coincides with the local Bragg wavelength  $\lambda_{11 \leftrightarrow 11}$  at point B as follows:

$$\lambda_{01 \leftrightarrow 01}(z) = \lambda_{11 \leftrightarrow 11}(z + L_{AB}) \quad (3.79)$$

where  $0 < z < L_g$ .

Let  $\Lambda(z) = \Lambda_0 + rz$ , the grating pitch linearly increases at the rate of  $r$  along  $z$ .  $\Lambda_0$  is the shortest pitch in CG. Equation (3.79) can be rewritten as,

$$2(n_{01} + \eta_{01}\Delta n)(\Lambda_0 + rz) = 2(n_{11} + \eta_{11}\Delta n)(\Lambda_0 + r(z + L_{AB})) \quad (3.80)$$

$\eta_{01}\Delta n$  and  $\eta_{11}\Delta n$  represent the UV-induced DC index changes for effective indices of LP<sub>01</sub> and LP<sub>11</sub> modes in the fiber. Incorporation of these index changes is essential for the precise computation of the interference pattern's wavelength spacing.

Rearranging Equation. 3.80 derives the following equation:

$$L_{AB} = \left( \frac{\Lambda_0}{r} + z \right) \left( \frac{n_{01} + \eta_{01}\Delta n}{n_{11} + \eta_{11}\Delta n} - 1 \right) \quad (3.81)$$

Since  $z \ll \frac{\Lambda_0}{r}$ , Equation. 3.81 can be simplified as:

$$L_{AB} \approx \frac{\Lambda_0}{r} \left( \frac{n_{01} + \eta_{01}\Delta n}{n_{11} + \eta_{11}\Delta n} - 1 \right) \quad (3.82)$$

The wavelength spacing of a typical FP resonator is,

$$\Delta\lambda = \frac{\lambda^2}{2n_v L} \quad (3.83)$$

The oscillating wavelength between the two grating elements at point A and point B is exchanging among LP<sub>01</sub> and LP<sub>11</sub> modes due to the presence of cross-mode coupling element in CG. Equation (3.83) is rewritten as:

$$\Delta\lambda = \frac{\lambda^2}{\left[ (n_{01} + \eta_{01} \Delta n) + (n_{11} + \eta_{11} \Delta n) \right] L_{AB}} \quad (3.84)$$

$\left[ (n_{01} + \eta_{01} \Delta n) + (n_{11} + \eta_{11} \Delta n) \right] L_{AB}$  is the resultant optical path length of a single round trip within the FP resonator.

Substituting Equation. (3.82) into Equation. (3.84), we have,

$$\Delta\lambda = \frac{r\lambda^2}{A_0} \left( \frac{n_{01} + \eta_{01} \Delta n}{n_{01} + n_{11} + (\eta_{01} + \eta_{11}) \Delta n} \right) \left( \frac{1}{n_{01} - n_{11} + (\eta_{01} - \eta_{11}) \Delta n} \right) \quad (3.85)$$

Since  $\eta_{01} \Delta n + \eta_{11} \Delta n \ll n_{01} + n_{11}$  and  $n_{01} \approx n_{11}$ , we can assume that

$\frac{n_{01} + \eta_{01} \Delta n}{n_{01} + n_{11} + (\eta_{01} + \eta_{11}) \Delta n} \approx \frac{1}{2}$  and Equation. (3.85) can be simplified as;

$$\Delta\lambda \approx \frac{r\lambda^2}{2A_0} \left( \frac{1}{n_{01} - n_{11} + (\eta_{01} - \eta_{11}) \Delta n} \right) \quad (3.86)$$

For CG inscribed in two-mode graded index fiber with  $n_{01}-n_{11}=2.934 \times 10^{-3}$  and  $\Delta n = 5 \times 10^{-4}$ , the ascertained wavelength spacing is 0.37 nm, which is consistent with the measurement,  $\sim 0.36$  nm (see Figure 4.9). For two-mode step index fiber with  $n_{01}-n_{11}=1.4715 \times 10^{-3}$  and  $\Delta n = 6.5 \times 10^{-4}$ , due to smaller mode index difference between LP<sub>01</sub> and LP<sub>11</sub>, the ascertained wavelength spacing is 0.719 nm and it is consistent with the measurement,  $\sim 0.72$  nm (see Figure 4.10).

However, there is no simple way to depict the resonance mechanism explicitly within the CG on TMF. The cross-mode coupling coefficient is the empowering element of the mode exchange amongst  $LP_{01}$  and  $LP_{11}$  modes, allowing FP resonance and interference in the CG. Numerical modelling can provide a more precise estimation of CG's spectral characteristics in TMF.

### **3.6 Opto-elasticity and the Characteristics of FBGs**

Throughout the advances of innovative fiber optic devices, issues commonly arise that require the investigation of the essential properties of glass. At present, researchers are studying the advancement and investigation of fiber optic devices that measure different properties contained in a mechanical framework. Similarly, with any sensing device, the execution and properties of fiber optic device (a mechanical and material framework itself) must be completely understood before utilizing any innovation. The accompanying information assists in understanding the FBG fiber-optic device framework by analysing the essential coherent light transmission property of glass. The optical conduct of light in glass under stress clearly influences the execution of FBGs and FBG-based FP resonators.

Generally, fiber optic devices work by relating some physical perturbation with the light being transmitted inside the optical fiber itself. Certain exterior occurrences can affect light transmission inside an optical fiber because electromagnetic and heat fields can influence current in a wire. Although the exact circumstances and end result relationship between exterior perturbations and light signal are the motivation of some in-depth research work, ultimately, it is important to examine the properties of glass fiber, initially. This investigation delves into the phenomenon of opto-elasticity.

Opto-elasticity is a sensible and noteworthy idea regarding the investigation of fiber optic devices and transmission in glass, in general. It strongly portrays the interaction of

light with the glass matter and depicts the propagation of electromagnetic radiation in glass subjected to stresses. Concerning FBG-based FPR devices, it is intriguing to study the impact of strains and stresses anywhere on the optical fiber and the FPR devices' signal. For some fiber optic devices (for example, Bragg gratings), the impact of opto-elasticity can be as critical as optical anisotropy in the fiber core, which can specifically influence the execution of the framework.

Glass, in different structures, is one of the common materials used in daily life. Glass is thought to have been made around 2500 B.C. The principal tests showing “double refraction of glass” (the way refractive index could be anisotropic inside glass) under stress were conveyed by Brewster (1816).

In these investigations, it was demonstrated that glass under pressure behaved as a uniaxial negative crystal, and as a uniaxial positive crystal under tension, with the optical axis adjusting to the direction of stress or loading. Wertheim (1854) initially measured the optical-stress coefficient of glasses and different materials, and established the idea of opto-elasticity framework in 1864. In these tests, the optical impact of pure compression and pure tension were considered. The aforementioned examinations and investigations revealed the disclosure of opto-elasticity as an influence present in glass under stress. The principal quantitative determination of a piece of glass's outright optical-stress coefficients was completed in the late 1800s (Kerr, 1888). In 1925, these examinations were rehashed (up to 10 MPa stress), and the law associating birefringence and stress was observed to be linear and same for tension and compression. This conduct is mostly seen in all glasses of different syntheses. A point-by-point examination of the pioneers' endeavours in opto-elasticity can be found in the work of Coker and Filon (1957).

### 3.6.1 Effect of Glass Composition on Opto-elasticity

The eminent scientist, Pockels, directed the primary study on how glass composition influences its opto-elastic coefficient. The stress-optic law as expressed by Maxwell in 1852 characterizes the opto-elastic coefficient that measures the distinction in stress and in refractive index (Maxwell, 1853). For a given material, in the broadest case, an index ellipsoid as illustrated in Figure 3.13 signifies the optical properties at any point. The major indices of refraction and principal stresses correspond to direction. If  $n_1$ ,  $n_2$ , and  $n_3$  denote the major refractive indices,  $n_0$  represents the unstressed material's index of refraction, and  $\sigma_1$ ,  $\sigma_2$ ,  $\sigma_3$  are the major stresses. Then, per Maxwell, the accompanying relations can be made:

$$n_1 = n_0 + C_1\sigma_1 + C_2(\sigma_2 + \sigma_3) \quad (3.87)$$

$$n_2 = n_0 + C_1\sigma_2 + C_2(\sigma_3 + \sigma_1) \quad (3.88)$$

$$n_3 = n_0 + C_1\sigma_3 + C_2(\sigma_1 + \sigma_2) \quad (3.89)$$

where  $C_1$  and  $C_2$  are constants relying upon material properties. By consolidating these equations, the accompanying relations relate to variation in stress, with variations in index of refraction as follows:

$$n_1 - n_2 = C(\sigma_1 + \sigma_2) \quad (3.90)$$

$$n_1 - n_3 = C(\sigma_1 + \sigma_3) \quad (3.91)$$

$$n_2 - n_3 = C(\sigma_2 + \sigma_3) \quad (3.92)$$

where  $C = C_1 - C_2$  and  $C$  is the stress-optic or opto-elastic constant.

Pockel demonstrated the impact of a glass material's structure on the opto-elastic constant in test outcomes as depicted in Figure 3.9. These outcomes demonstrate how opto-elastic constant changes with the lead oxide content in flint glass, alongside the consequences of comparable tests by Waxler (Waxler, 1953) and Filon (Waxler, 1907).



The curve in this figure demonstrates that  $C$  vanishes when the rate of lead oxide is roughly 75% and be negative at values higher than 75%. This implies that the law expressed by Brewster, wherein the glass acts as a negative crystal, no longer applies.

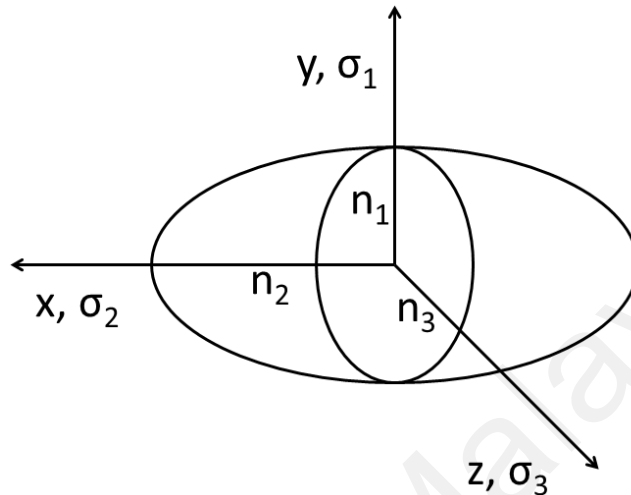


**Figure 3.9: Index of refraction ellipsoid**

Filon investigated opto-elastic behaviour of borosilicate glasses and found that  $C$  increased with  $B_2O_3$  inclusion, and diminished by  $K_2O$ . This effect, on the other hand, was slightly different than when lead oxide was changed.

In 1927, an investigation had demonstrated the opto-elastic constant of silica to be  $3.45 \text{ TPa}^{-1}$ . In 1945, Balmforth and Holland reported consequences of investigations in which  $CaO$  was gradually replacing  $Na_2O$  on a molar basis with a parent glass whose general recipe was  $6SiO_{2(2-x)}Na_2O_xCaO$  (Balmforth & Holland, 1945). This substitution brought about a little yet noteworthy rise in the opto-elastic constant as found in Figure 3.11. Schweiker similarly studied the impact of  $SiO_2$  on the opto-elastic constant of different glasses (Aben & Guillemet, 1993). The literature is brimming with such illustrations. The key component is the recognition of changing opto-elastic constant  $C$  with glass structure. The variation in modulus by the changing chemical arrangement and physical structure of glass, as well as its concentration is normally classified as the mechanisms of polarizability.

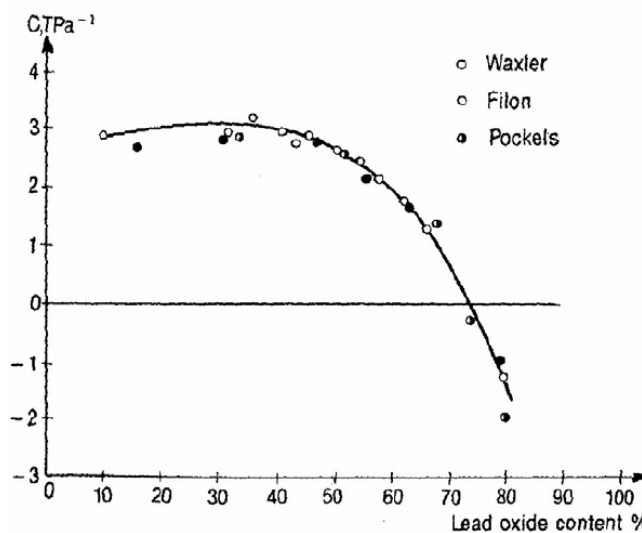


Figure 3.10: Variation of opto-elastic constant with lead oxide content (Waxler, 1907)

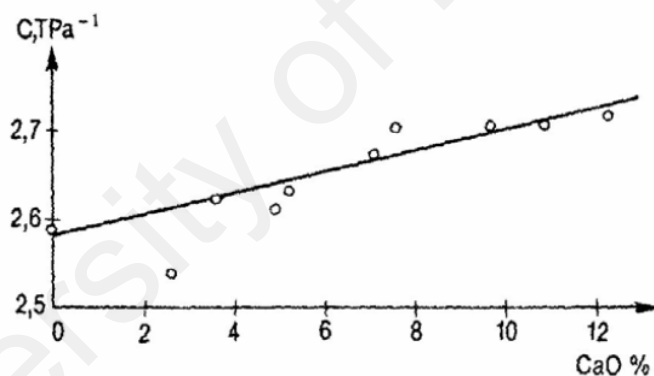


Figure 3.11: Variation of photoelastic constant with CaO concentration (Balmforth & Holland, 1945)

### 3.7 Summary

Speculations of FBGs and FPRs were explained in this chapter. The modelling and analysis of this thesis depends on opto-elastic properties of FBG-based FPR that cause variation in refraction index in this optical device exposed to acousto-ultrasonic, temperature, and pressure changes. The acquisition of FBGs considered the essential speculations of light propagation and dispersion and the general type of mode-coupling hypothesis. The FPR speculations are exhibited in view of uniform and chirped grating-based FPR. Moreover, the opto-elastic impact on glass composite alongside the general

hypothesis of opto-elasticity and its constant wavelength of transmitted light were also exhibited.

University of Malaya

## CHAPTER 4: MODE INTERFERENCE IN CHIRPED FBG

### 4.1 Introduction

We have demonstrated LP<sub>01</sub>-LP<sub>11</sub> cross mode interference in a single chirped grating (CG) inscribed in a two-mode fiber (TMF). With the aid of a binary phase plate, LP<sub>01</sub> mode and LP<sub>11</sub> mode can be selectively excited in the CG. By offsetting the position of the phase plate from the centre of the input beam, we can simultaneously excite both spatial modes at different LP<sub>01</sub>:LP<sub>11</sub> intensity ratio in the TMF. The excited modes lead to the formation of different interference patterns in the output spectra. The measured output spectra are found to be in good agreement with the simulation based on coupled mode theory (CMT).

Coupled mode theory (CMT) is an important apparatus in describing the wave properties of various gratings imprinted on waveguides and optical fibers. The coupled mode equations (CME) can be derived from the perturbation theory (Yariv, 1973) and various approaches based on numerical or analytical methods were proposed to simulate and analyse the spectra and characteristics of the gratings. Comparative analysis of several employed formulations of CMT in order to simulate fiber Bragg grating with respect the grating period, phase and amplitude discontinuities is presented in (McCall, 2000). In particular, Erdogan et al (Erdogan, 1997) presented a comprehensive study on CME and the simulation of the grating spectra mainly focus on single mode fiber (SMF). CME for uniform gratings with constant parameter along the z-axis is simple and they can be analytically solved.

However, close form solution is not possible for most non-uniform gratings with varying parameters along the fiber. The problem can be addressed by using the Transfer Matrix Method (TMM), which is a commonly used numerical method for solving the

CME of non-uniform grating such as phase-shifted grating, chirped grating (CG), apodised grating, superstructured grating and etc. Apart from the studies in fiber gratings, CME has also been studied for analysis of mode propagation in uniform and slightly non-uniform cylindrical optical-fiber (Snyder, 1972), birefringence in spun 4-lobe stress region fibers (Qian & Wang, 2007) and etc.

CME for few-mode FBG is more sophisticated due to the additional spatial variables and terms describing the cross mode-coupling between two different spatial modes in the system (Raghuwanshi & Panda, 2014). Generally, spatial modes in an FMF are orthogonal and they do not couple or interfere with each other except under the condition of inhomogeneous refractive index profile over the cross-section of the fiber. For example, optical fiber in curvature may experiences asymmetrical index profile fiber core index due to the bending stress (Marcuse, 1976), index perturbation in fiber by mechanical stress relaxation using CO<sub>2</sub> laser irradiation (Davis et al., 1998; Kim et al., 2000; Rao et al., 2003; Grubsky & Feinberg, 2006; Lee et al., 2008) and asymmetrical index change in the fiber core induced by UV laser. UV-induced asymmetrical index change is generally found in FBG written by UV-side illumination (Renner, 2001), in which the side of the fiber core that is nearer to the incoming laser beam receives higher laser intensity and yields greater index change than the far side of the fiber due to the high absorption / attenuation of UV laser in the fiber glass. As the result of inhomogeneous core index profile, the mode profiles deform and the orthogonality between the spatial modes degrades. Subsequently, this leads to the production of non-zero cross-coupling coefficients, enabling the exchange of energy among the spatial modes (Wu et al., 2012). For a uniform grating on FMF, multiple resonant wavelengths are observed in the spectrum. Each of them can be associated with the self mode-coupling of a spatial mode or cross mode-coupling between two different spatial modes in the fiber. With the aid of binary phase plates, the associated

spatial modes to each resonant wavelength can be identified. In particular, the cross-coupled wavelengths offer an attractive feature of bidirectional conversion between the associated modes (Ali et al., 2015). In the excitation of higher order modes in FMFs, there are several available techniques such as core offset technique, binary phase mask, prism mode selector (Giles et al., 2012) and etc. Among them, core offset technique is the simplest approach for the excitation of multiple higher order modes but it lacks the flexibility in terms of mode selectivity. A binary phase plate is a robust and precise approach for selective mode excitation in FMFs. Despite the high insertion loss and bulky opto-mechanical setup, phase plates are still the preferred choice for mode conversion and selective mode excitation in various Space-division multiplexing (SDM) applications (Igarashi et al., 2014a; 2014b; Randel et al., 2011).

In this work, we have fabricated and investigated the characteristics of CG on TMF. In this grating structure, the lowest two spatial modes, namely  $LP_{01}$  and  $LP_{11}$  contribute to two sets of grating elements, where each can be mathematically described as the product of local grating period and the corresponding mode propagation constant. With the assistance of a binary phase plate, each of the two lowest spatial modes, namely  $LP_{01}$  and  $LP_{11}$  are selectively excited and the corresponding output spectra are recorded. Due to the existence of cross-mode coupling element in the CG, a strong interaction and exchange of energy between  $LP_{01}$  mode and  $LP_{11}$  mode are possible within the CG. The experimental data are compared with the analytical result obtained from a simulation based on CME.

#### **4.2 Fabrication of Chirped FBG in TMF**

In the inscription of chirped grating (CG) on two-mode fibers (TMF) manufactured by OFS. In this work, two types of two-mode fibers were used, namely the two-mode step index fiber and the two-mode graded index fiber. The diameter of two-mode step

index is 125.2  $\mu\text{m}$  with an  $\text{LP}_{01}$  mode field diameter of 15.5  $\mu\text{m}$  and  $\text{LP}_{11}$  mode field diameter of 13.6  $\mu\text{m}$ . The diameter of two-mode graded index fiber is 125.1  $\mu\text{m}$  with an  $\text{LP}_{01}$  mode field diameter of 11.0  $\mu\text{m}$  and  $\text{LP}_{11}$  mode field diameter of 11  $\mu\text{m}$ . The fibers were hydrogenated in a high-pressure hydrogen chamber at 1800 psi for two weeks at a room temperature of 25°C for photosensitization. Subsequently, a chirped grating was inscribed in the hydrogenated TMF using an ArF excimer laser (193nm) based on fixed beam / phasemask lithography technique. In the UV inscription process, laser pulse energy of  $\sim 5$  mJ (single pulse fluence of 400  $\text{mJ}/\text{cm}^2$ ) at 1 Hz repetition rate was used to produce the CG and the entire inscription process takes 3-5 minutes. The phase mask has a shortest grating period of 1060nm with a chirp rate of 10nm/cm. Due to the linearly varying grating period along the grating region, the reflectivity over the wideband spectrum of the CG was generally lower than that of a grating with uniform period and narrow reflection curve. From our observation, the hydrogenated fibers freshly withdrawn from the hydrogen chamber had excellent photosensitive for the inscription process but the process slows down significantly one hour later due to the out-diffusion of hydrogen. Therefore, it is important to initiate the inscription process and complete the writing within the period of 1 hour after the withdrawal to minimize the loss of hydrogen content in the fiber. Production of CGs on TMF with high reflectivity is essentially important to acquiring reliable result from the characterization test later. After the inscription process, the written gratings were annealed in an oven at 80 °C for  $\sim 10$  hours to dehydrogenate and stabilize the gratings.

### **4.3 Characterization of Mode Interference Characteristics in Chirped FBG**

#### **4.3.1 Experimental Setup**

Figure 4.1 shows the experimental setup for the characterization of the CG written on a 1.5 m long TMF. The phase plate is vertically held by a plate holder that is mounted on a linear translation stage. The laser is launched from a TLS via an SMF. A

short focal objective lens with a focal length of 4.5 mm is used to expand and collimate the  $LP_{01}$  beam from the SMF to the phase plate. Another objective lens with the same focal length is positioned after a non-polarizing beamsplitter to converge and couple the beam into the CG-TMF. Between the two lenses, the phase plate is used to convert the beam from  $LP_{01}$  mode to  $LP_{11}$  mode. A fraction of the converted beam is tapped using the beam splitter and used as a reference for comparison against the transmitted beam from the CG-TMF. In addition, the beamsplitter is also used to tap the reflected beam from the CG and redirecting to the OSA for spectral analysis. The beam characterization is performed with the TLS at a wavelength that is out of, but not too far away from the reflection curve of any of the spatial mode to prevent the excitation of an undesired spatial mode in the TMF by the cross-coupling in the chirped grating. The CG on the TMF is located at a position  $\sim 1$  m away from the fiber input. The purpose of the long buffer fiber length before the CG is to eliminate the possible excited higher order modes other than the  $LP_{01}$  and  $LP_{11}$  modes in the fiber. The characterization test was performed in a temperature controlled environment (at a room temperature of  $25^{\circ}\text{C}$ ) because the grating period and refractive index of CG are sensitive to ambient temperature variation.

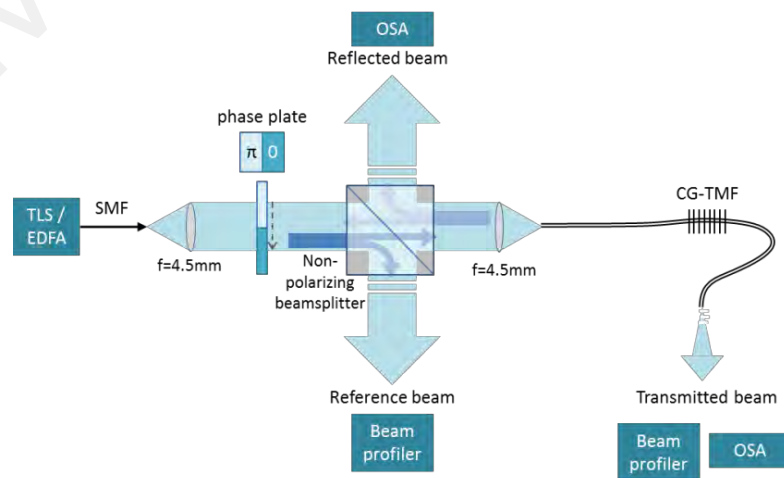


**Figure 4.1: Experimental setup for characterization of beam and spectra of CG-TMF.**



### 4.3.2 Phase Plates

A phase plate consisted of phase pattern with protruded areas that introduce a phase jump of  $\pi$  to light passing through the pattern. Depending on the spatial mode profile, a specific phase pattern is required to produce the desired mode profile. The pattern for  $LP_{01}$ - $LP_{11}$  mode conversion is shown in Figure 4.2(a). The shaded area in Figure 4.2(a) is the protruded area. Meanwhile, the cross-sectional view of the phase plate is shown in Figure 4.2(b). The edge of the protruded area might not be vertical and there is a width of the edge, which is denoted as  $s$  in the figure. Igarashi et al. have shown that phase plate with slope width less than  $0.1 \mu\text{m}$  can produce converted beam with better symmetry when compared to that with a width of around  $200 \mu\text{m}$  (Igarashi et al., 2014a).

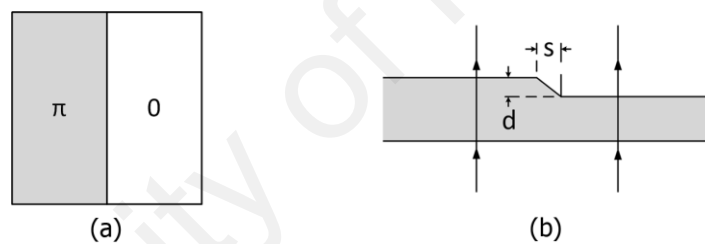


**Figure 4.2: (a) Phase pattern for  $LP_{01}$ - $LP_{11}$  mode conversion. (b) A cross-sectional view of an  $LP_{11}$  phase plate with a protruded area that will provide a phase jump of  $\pi$  to light passing through that area, where  $d$  = phase pattern thickness and  $s$  = slope width of the edge (Lee et al., 2016).**

The phase pattern thickness,  $d$ , is tailored to match the wavelength of the incident light. In order to convert the incident beam from  $LP_{01}$  mode to  $LP_{11}$  mode, the phase plate needs to be aligned in such a way that the edge of the protruded and non-protruded area falls at the centre of the  $LP_{01}$  mode profile. At the appropriate wavelength and thickness, the part of the incident light that passes through the protruded area will experience a phase shift of  $\pi$  relative to the other part that passes through the non-protruded area. The coupling of the converted beam to the FMF will lead to the excitation of  $LP_{11}$  mode. For a phase shift of  $\pi$ , the phase pattern thickness is related to the design wavelength and phase plate refractive index by the following equation:

$$d = \frac{\lambda}{2(n-1)} \quad (4.1)$$

where  $n$  = refractive index of the phase plate,  $d$  = phase pattern thickness and  $\lambda$  = design wavelength. The design wavelength is a critical parameter governing the performance of the phase plate. A deviation from the design wavelength could potentially lead to the excitation of undesired spatial modes in the fiber and low LP<sub>01</sub>-LP<sub>11</sub> conversion efficiency.

The fabrication of phase plate involves two-steps process on fused silica with a thickness of 2 mm. It started with photolithography and followed by inductively-coupled plasma (ICP) dry etching to create the protruded phase pattern on the fused silica plate.

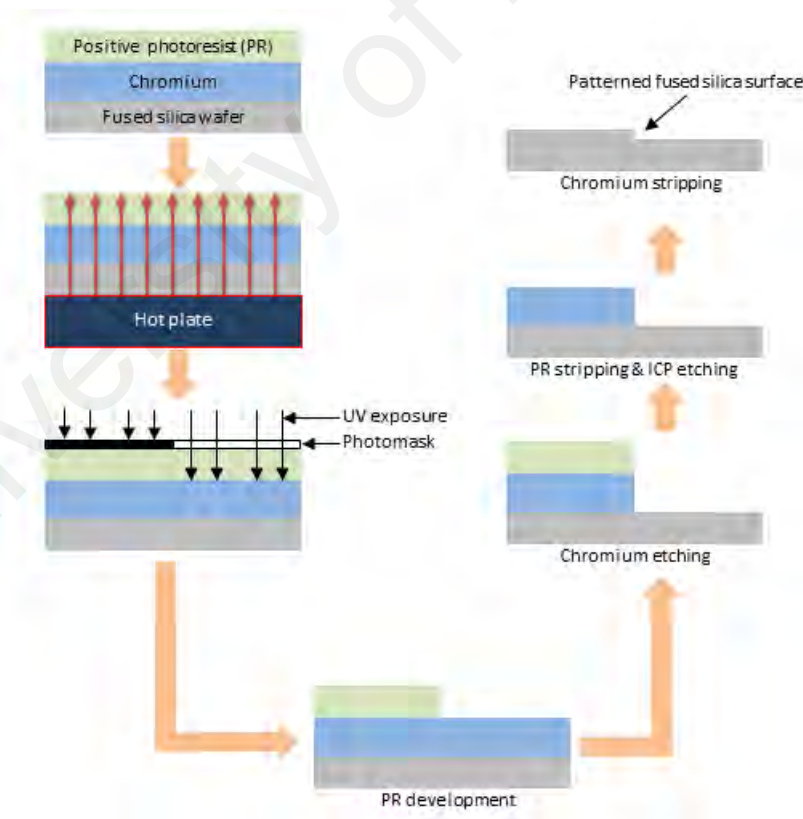


**Figure 4.3: Fabrication of phase plate by photolithography and ICP dry etching**

In the photolithography process, a fused silica plate was first coated with a layer of chromium having a thickness of about 100 nm by using direct current (DC) sputtering

method. Then, a layer of positive photoresist (PR) was deposited on top of the chromium using a spin-coating method. This is followed by soft baking of the PR. After that, the PR covered by a photomask was exposed to ultraviolet (UV) light to produce the required pattern on the PR. The PR was then developed to remove the part exposed to UV while the unexposed PR remained on the chromium. This completed the transfer of the pattern from the photomask onto the PR. Then, the coated fused silica plate was immersed into chromium etchant to remove the part of chromium that is not protected by the PR. After the chromium etching, all PR on the chromium would be stripped. At this stage, the pattern has been transferred from the photomask onto the chromium. This marks the end of the photolithography process and the fused silica plate coated with chromium pattern would be loaded into the vacuum chamber for ICP etching. The reactive ions of the ICP etched the part of fused silica plate that is unprotected by the chromium layer. By controlling the etching rate and etching period, the required etch depth was obtained. The area on the fused silica plate covered by the chromium pattern would not be etched and this led to the formation of a protruded pattern similar to that of the photomask. After the dry etching process, the fused silica plate was removed from the vacuum chamber and the chromium pattern on the plate was stripped. This completed the fabrication of the phase plate where a protruded phase pattern was formed on the fused silica plate. The thickness of the protruded pattern would be same as the etch depth after the chromium pattern on the fused silica plate was stripped.

### **4.3.3 Beam Splitter**

As pointed out in the aforementioned section 4.3.1, a beam splitter is utilized as a part of the trial that has a beam split apportion of 50:50. Beam splitters are semi-reflecting mirrors that split an optical beam into two sections propagating in various directions. Keeping in mind the end goal to comprehend the conduct of some optical

frameworks using beam splitters, it is basically vital to know the phase relation amongst reflected and transmitted fields.

Let  $\tau = \tau_0 \exp(i\varphi_\tau)$  and  $\rho = \rho_0 \exp(i\varphi_\rho)$  be, correspondingly, the transmission and reflection coefficients for the electric field. The real value taken by these coefficients relies on numerous parameters, for example, the beam-splitter structure, the wavelength of the incident beam, and the incidence angle.

The schematic graph in Figure. 4.4 demonstrates a beam-splitter is symmetrically enlightened on both sides by two indistinguishable light beams that have the same incidence angle, phase, polarization, and intensity  $I_0$ . Accepting that  $I_1$  and  $I_2$  are the intensities of the two output beams and the framework is lossless, it ought normal, for symmetry reason, that  $I_1 = I_2 = I_0$ . Since the field  $E_1$  at output 1 is the total of two contributions, one originating from reflection and the other from transmission,  $E_1 = \rho E_0 + \tau E_0$ , the intensity at output 1 is given by  $I_1 = |\rho + \tau|^2 I_0$ . The condition  $I_1 = I_0$  is fulfilled if:

$$|\rho + \tau|^2 = [\tau\tau^* + \rho\rho^* + 2\text{Re}(\tau\rho^*)] = 1. \quad (4.2)$$

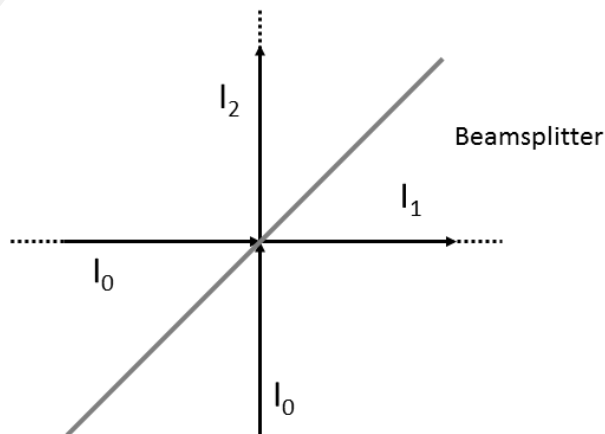


**Figure 4.4: Two indistinguishable light beams impinging on the two sides of a beam splitter**

Since  $\tau\tau^* + \rho\rho^* = 1$ , the term  $\text{Re}(\tau\rho^*) = \tau_0\rho_0\cos(\varphi_\tau - \varphi_\rho)$  must be nil, in this way:

$$\phi_r - \phi_s = \frac{\pi}{2} \quad (4.3)$$

Equation (4.3) is a general connection, effective for any lossless beam-splitter. The main impediment is that the beam-splitter ought to be symmetrical.

#### 4.3.4 Modelling of LP<sub>01</sub> and LP<sub>11</sub> modes of Two-mode Step Index Fiber

LP<sub>01</sub> and LP<sub>11</sub> modes' intensity profiles supported by two-mode step index fiber have been plotted using MATLAB are shown in Figures 4.5 and 4.6, respectively. 3-dimensional plotting were used to illustrate the LP<sub>01</sub> and LP<sub>11</sub> modes. The core and cladding refractive indices of 1.4483 and 1.4433 (index contrast of  $5 \times 10^{-3}$ ) are assumed in the modelling. In addition, the core and cladding radii are 9.25 and 125  $\mu\text{m}$ , respectively. The intensity of LP<sub>01</sub> mode is concentrated at the centre of the mode and it has a Gaussian shape beam profile. On the other hand, the LP<sub>11</sub> mode has a high intensity at the interface of core and cladding. The intensity profiles of LP<sub>01</sub> and LP<sub>11</sub> modes have been plotted in Figures 4.5 and 4.6 where  $z$  denotes the fiber axis. Furthermore, this research focuses on the LP<sub>01</sub> and LP<sub>11</sub> cross mode interference instead of the mode polarizations.

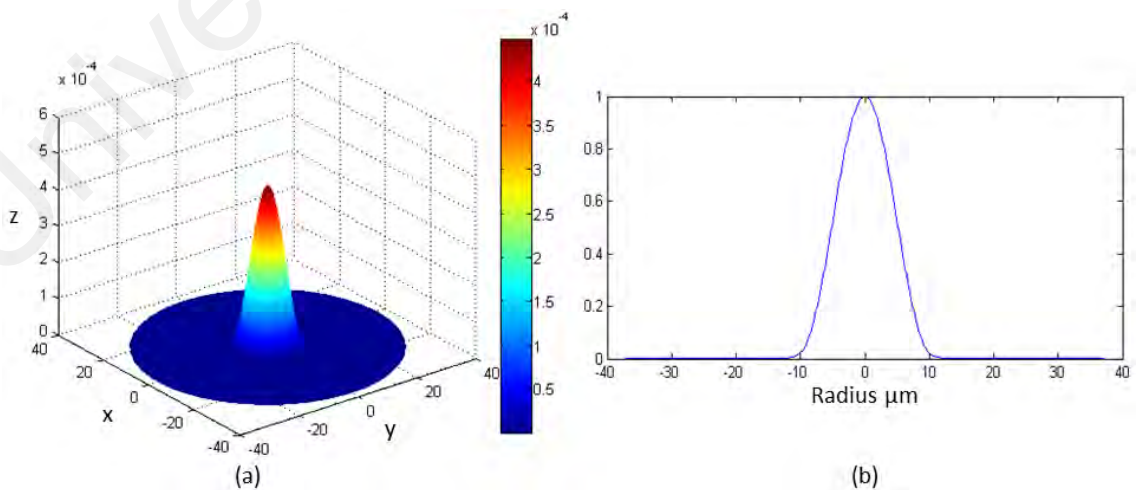
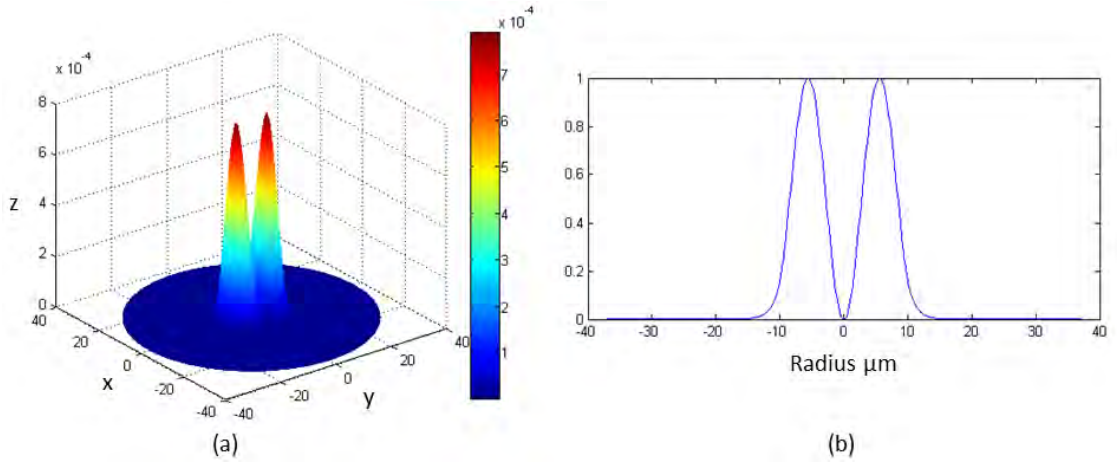


Figure 4.5: (a) LP<sub>01</sub> mode and (b) line intensity profile of LP<sub>01</sub>



**Figure 4.6: (a) LP<sub>11</sub> mode and (b) line intensity profile of LP<sub>11</sub>**

#### 4.3.5 Modelling the spectral characteristics of CG in TMF

The reflection and transmission spectra of a CG on a single mode fiber depend on the length, period, coupling coefficients, chirped rate of the grating and mode effective index of the fiber. A flat top and broadband spectrum can be acquired from the CG under the condition of single spatial mode excitation. Figures 4.7(a) and 4.7(b) show the reflection/ transmission spectra of the CG-TMF under selective mode excitation of LP<sub>01</sub> and LP<sub>11</sub> respectively. Despite the difference in mode excitations, both spectra share almost similar curve characteristics except that the LP<sub>11</sub> mode has a shorter reflection wavelength due to the lower mode effective index and lower band rejection. The band rejection and reflectivity can be associated with the overlap factor between the modes and index modulation in the core. The LP<sub>01</sub> mode has a Gaussian-like beam profile in which most of the mode intensity is concentrated at the centre of the core whereas the LP<sub>11</sub> mode has an extended profile where the mode intensity is mostly distributed within the vicinity of the core-cladding boundary but less at the core centre. Therefore, LP<sub>11</sub> self mode-coupling has lower overlap factor  $\eta_{11}$  and coupling coefficient  $k_{11}$  as compared to that of LP<sub>01</sub>,  $k_{01}$ . The experimental results are found to be in good agreement with the numerical result. The best-fit curves are attained based on the values as,  $n_{01}-n_{11}= 2.934 \times 10^{-3}$ ,  $\Delta n = 5 \times 10^{-4}$ ,  $\eta_{01} = 1.00$ ,  $\eta_{11} = 0.9\eta_{01}$ ,  $\eta_c = 0.2\eta_{01}$ . These

parameters are defined in section 3.4.2. The estimated AC coupling coefficients are  $k_{01} = 1021$ ,  $k_{11} = 919$  and  $k_c = 204$  using equation (3.64a) presented in section 3.4.2.

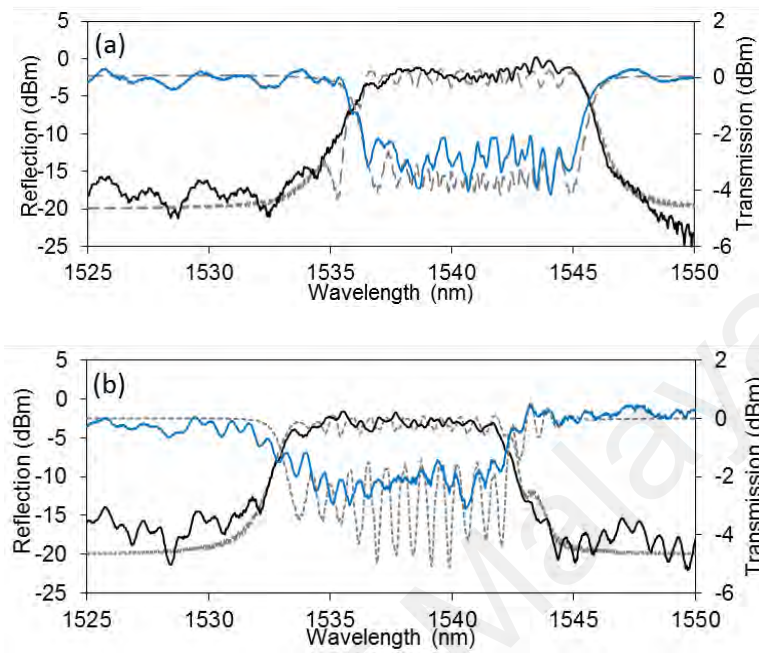


**Figure 4.7: Reflection and transmission spectra of the CG written on two-mode graded index fiber. The dotted grey curves denote the simulated result ( $n_{01}-n_{11}=2.934\times 10^{-3}$ ,  $\Delta n=5\times 10^{-4}$ ,  $\eta_{01}=1.00$ ,  $\eta_{11}=0.9\eta_{01}$ ,  $\eta_c=0.2\eta_{01}$ ,  $r=5\text{ nm/cm}$ ,  $\Lambda_0=530.52\text{ nm}$ ,  $L_g=6.9\text{ mm}$ , (a) Intensity ratio  $P_{LP01}:P_{LP11}=1:0$ , (b) Intensity ratio  $P_{LP01}:P_{LP11}=0:1$ ).**

#### 4.3.6 Spectral response of the CG in TMF under different mode excitations

In the experiment, the phase plate is gently translated in such a way that the division line (refer red dotted line in Figure 4.8(a)) between  $0$  and  $\pi$  regions of the phase plate is placed at different positions from (i) to (v) as illustrated in Figure 4.8(a). Defined by the division line, both partitions of the laser beam are subjected to a phase difference of  $\pi$  at the operating wavelength of  $1550\text{ nm}$ . At position (i), the  $0-\pi$  division line is located outside of the laser beam region hence the  $LP_{01}$  input beam is launched directly into the TMF without experiencing mode conversion. Consequently, an  $LP_{01}$  transmitted beam profile is acquired from the output of the TMF as shown in Figure 4.8(b). As the binary phase plate is sliding perpendicularly across the input laser beam, the input beam is divided into two unequal regions both subject to different phase retardation with a phase difference of  $\pi$  (See reference mode profiles (ii)-(v)). The transmission beam is



evolving from LP<sub>01</sub> mode to LP<sub>11</sub> mode as shown in the transmission mode profiles (ii)-(v). The variation in the transmitted beam profile can be interpreted as the diminishing LP<sub>01</sub> component and growing LP<sub>11</sub> component in the fiber as the 0- $\pi$  division line is being offset from position (i) to (v). At position (v), the input laser beam is equally partitioned into two by the 0- $\pi$  division line (See reference in Figure 4.8(b)(v)) and a pure LP<sub>11</sub> mode is formed at the output of the TMF (See transmission in Figure 4.8(b)).

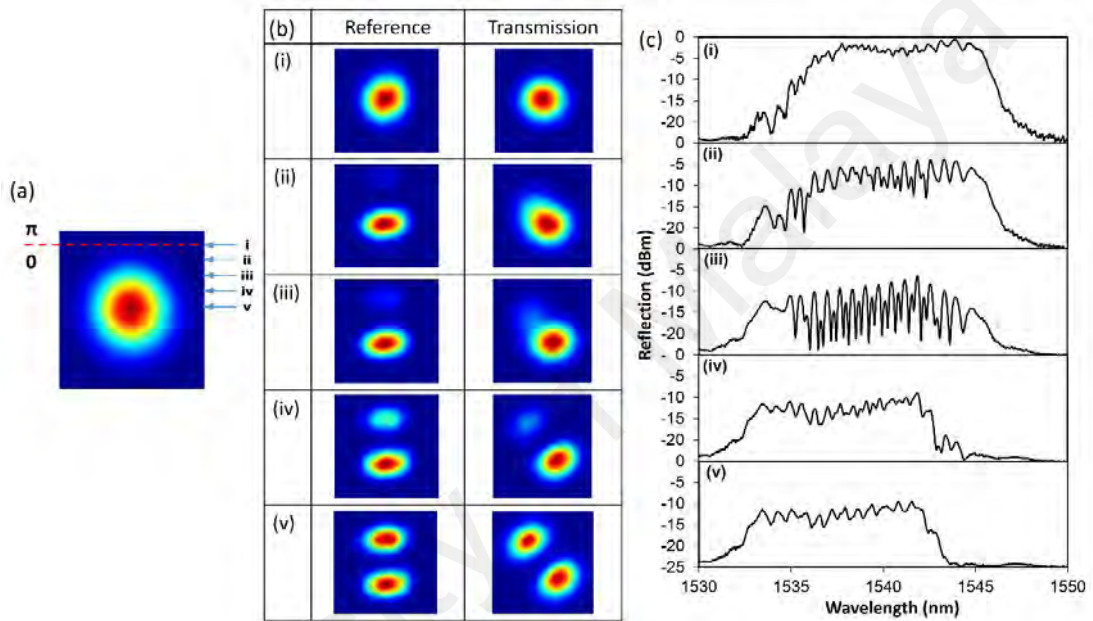


**Figure 4.8:** (a) The figure illustrates the positions of the 0- $\pi$  division line (red dotted line) of the phase plate with respect to the input LP<sub>01</sub> beam profile. The blue arrows mark different positions of the 0- $\pi$  division line (b) Input mode profiles (Reference) and their corresponding transmitted mode profiles. (c) The corresponding reflection spectrum (experiment) to the mode excitation.

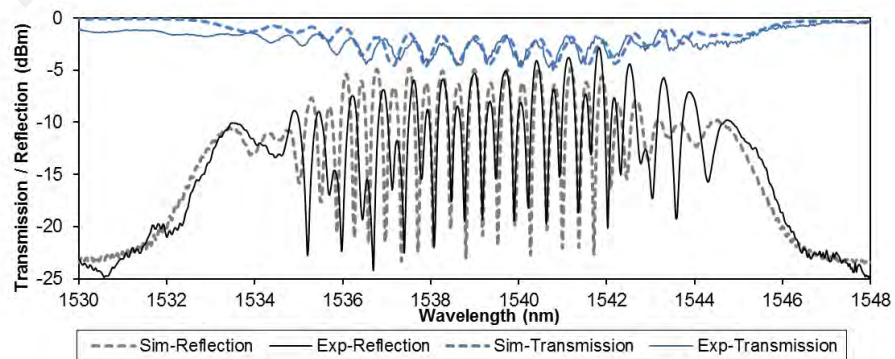


**Figure 4.9:** Reflection spectrum of CG inscribed on two-mode graded index fiber. ( $n_{01} - n_{11} = 2.934 \times 10^{-3}$ ,  $\eta_{01} = 1.00$ ,  $\eta_{11} = 0.9\eta_{01}$ ,  $\eta_c = 0.2\eta_{01}$ ,  $L_g = 6.9$  mm,  $\lambda_0 = 530.52$  nm,  $\Delta n = 5 \times 10^{-4}$ ,  $P_{LP01} : P_{LP11} = 0.5 : 0.5$ , measured spectral spacing = 0.36 nm).



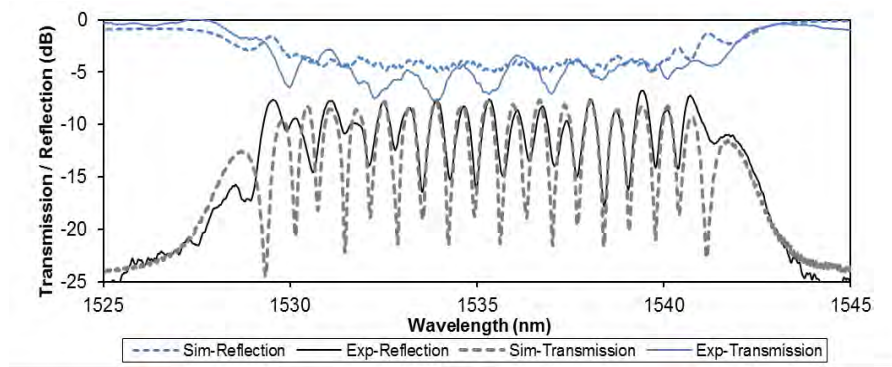


**Figure 4.10: Reflection spectrum of a CG inscribed on a two-mode step index fiber. ( $n_{01}-n_{11}=1.4715\times 10^{-3}$ ,  $\eta_{01}=1.00$ ,  $\eta_{11}=0.9\eta_{01}$ ,  $\eta_c=0.2\eta_{01}$ ,  $L_g=8.9$  mm,  $\Lambda_0=530.52$  nm,  $\Delta n=6.5\times 10^{-4}$ ,  $P_{LP01}:P_{LP11}=0.5:0.5$ , measured spectral spacing = 0.72 nm)**

In the characterization of the CG output spectrum, the TLS is replaced with an EDFA with a broad spectrum range of 1500 nm to 1600 nm. The stacked graph shows the corresponding reflection spectra from CG on two-mode graded index fiber. In the analysis, the reflection curve of the CG is blue-shifted from 1535 – 1545 nm to 1532 - 1542 nm when the phase plate is translated from position (i) to (v).

This indicates a pure  $LP_{11}$  mode excitation in the TMF and it is in agreement with the beam profiles observed in the experiment presented in Figure 4.8(b). Unlike the single mode excitation presented in the previous section, both spatial modes in the CG-TMF are simultaneously excited by the degenerated  $LP_{11}$  mode profile in this case. Notably, the reflection spectrum in Figure 4.8(c)(iii) shows the interference between two beams from both the  $LP_{01}$  and  $LP_{11}$  modes. The interference pattern only appears in the overlap region between reflection curves of  $LP_{01}$  and  $LP_{11}$  modes. The observed highest extinction ratio of 17dB in the reflection spectrum indicates good interference visibility induced by  $LP_{01}$  and  $LP_{11}$  modes with almost equivalent intensities in the fiber. This extinction ratio is denoted by the difference between the maximum and minimum optical power levels of the reflection spectrum. Figures 4.9 and 4.10 show the comparison between simulation result and the experimental data (taken from Figure 4.8(c)(iii)). The same best-fit parameters for the simulation in Figure 4.7 (except the

intensity ratio,  $P_{LP01} : P_{LP11} = 0.5 : 0.5$ ) are adopted for the simulation in Figure 4.9. Again, we observed good agreement between the simulation result and experimental result for both the transmission spectrum and reflection spectrum.

Figure 4.11 shows the calculated transmission spectra and reflection spectra of CG-TMF excited at  $P_{LP01} : P_{LP11} = 0.5 : 0.5$  but with different cross-coupling overlap factors,  $\eta_c$  ( $k_c$ ). At  $\eta_c = 0.0$ , the transmission curve can be interpreted as the superimposition of two rejection bands of  $LP_{01}$  and  $LP_{11}$  modes in which their overlap region ( $\sim 1536 - \sim 1542$  nm) has higher rejection. However, there is no interaction between the  $LP_{01}$  and  $LP_{11}$  modes due to the absence of cross-mode coupling element in the CG. Starting from  $\eta_c = 0.1$  to  $\eta_c = 0.3$ , it can be observed that the amplitude of the fringes begins to grow with increasing  $\eta_c$  in the overlap region due to the increasing interaction and interference between the two spatial modes. However, the impact of cross-mode coupling is insignificant in the reflection spectra.

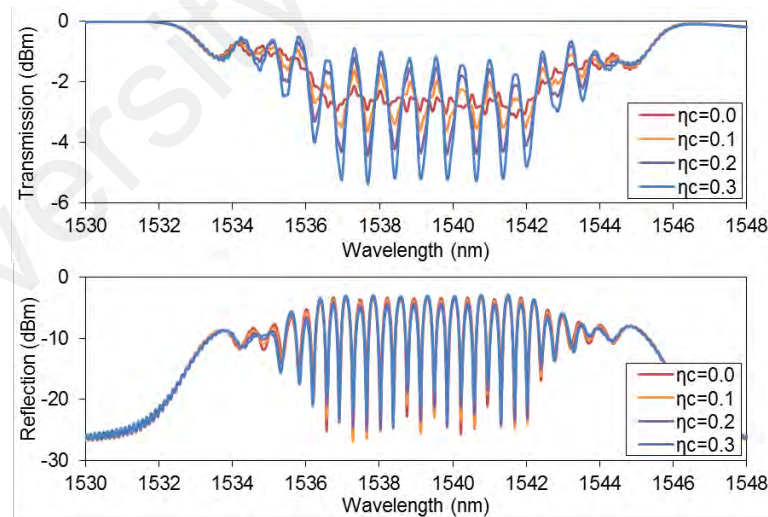


**Figure 4.11: Calculated transmission and reflection spectra of CG-TMF with different  $\eta_c$  (assume  $\eta_{01} = 1$ ,  $P_{LP01} : P_{LP11} = 0.5 : 0.5$ ).**

However, there is no easy way that can explicitly describe the mechanism of the resonance. Numerical modelling can provide a more precise estimation of the spectral characteristics of the CG in TMF. We repeated the characterization test on the CG-TMF

with an extended fiber length of 50 cm to both ends of the TMF to change the optical path lengths of the fiber. Nonetheless, the exact same output spectra were acquired. This eliminates the possibility of other effects such as intermodal interference between LP<sub>01</sub> and LP<sub>11</sub> modes in the TMF or the resonance between the CG and the fiber end surfaces.

#### 4.4 Summary

We have demonstrated the fabrication of CG in TMF. We characterized the spectra of the CG under LP<sub>01</sub> and LP<sub>11</sub> mode excitations using a binary phase plate. It is observed that at the excitations of pure LP<sub>01</sub> mode or LP<sub>11</sub> mode, flat-top reflection curves in the spectrum are attained. In comparison, the reflection curve under LP<sub>11</sub> mode excitation is located at the shorter wavelength region from that of LP<sub>01</sub> mode due to the lower LP<sub>11</sub> effective mode index. By offsetting the position of the binary phase plate from the centre of the input beam, deformed modes are produced to excite both LP<sub>01</sub> and LP<sub>11</sub> modes in the CG at different  $P_{LP01} : P_{LP11}$  mode intensity ratios. Under the condition of equivalent intensity ratio,  $P_{LP01} = P_{LP11} = 0.5$ , an interference pattern with an extinction ratio as high as 17 dB is produced. The measurements are in good agreement with the simulation calculated using CMT. The simulation result also indicates that the cross-mode coupling contributes to interaction and interference between the two spatial modes within the CG. To our best knowledge, this is probably the first report on experimental and theoretical investigation of non-uniform grating structure in few-mode fiber. This finding is an important step in the design and development of more complex grating structures on few-mode fibers. The discovery in this investigation has opened up a new perspective in intermodal interference in few-mode fiber devices and its potential applications in optical filters, multi-wavelength lasers, and fiber sensors.

## CHAPTER 5: APPLICATIONS OF FABRY-PEROT RESONATOR

### 5.1 Introduction

This chapter reports on the demonstration and characterization of a short cavity fiber Fabry-Perot resonator (FPR) for the detection of ultrasonic waves propagating through a solid medium over a frequency range of 1 kHz to 10 MHz. The proposed sensing device offers outstanding features in terms of simple fabrication technique, frequency response and high sensitivity over a wide frequency range. The response of the surface-mounted FPR sensor showed good agreement with that of a commercially available piezoelectric transducer during ultrasonic excitation.

In this chapter, we propose a PCF-cavity FBG Fabry-Perot resonator for simultaneous sensing of temperature and pressure. The proposed device is constructed by splicing a 1.5 mm long PCF segment between two identical saturated FBGs written in SMF-28 forming an FBG-PCF-FBG configuration. As a result, a resonance dip is created within the Bragg reflection curve. Taking advantage of the difference in pressure sensitivities between the two types of fiber, discriminative measurement of pressure and temperature can be achieved from the shifts of the resonance wavelength and band-edge wavelength. In addition, the same temperature sensitivity of PCF and SMF-28 provides the convenience of eliminating the temperature variable and achieving temperature insensitive pressure measurement.

Ultrasonic detection is a well-known, safe and non-destructive investigation technique in numerous elementary processes, services, manufacturing industries and also in applications concerning structural metals and aerospace composites (Betz et al., 2003; Wild & Hinckley, 2008). The design of an appropriate ultrasound detection system for any application would generally require flat frequency response over the

sensing frequency range; high sensitivity; robustness and ease of deployment. It is widely appreciated that the production and instrumentation costs involved in ultrasound sensors are high compared to other common sensor systems for strain and temperature (Betz et al., 2003). Acoustic emission sensing over few tens of kHz to several MHz serves as a means of damage detection in materials where fiber-based sensors are used extensively for a wide variety of applications due to their small size, remote monitoring capability and immunity to electromagnetic interference (Wild & Hinckley, 2008; Menadier et al., 1967). Hence, in many structural health monitoring (SHM) studies (Menadier et al., 1967; Liu & Han, 2012) based on ultrasound detection, fiber optic sensors (e.g. tapered FBGs; biconical coupler-based fiber sensor; diaphragm-based; and cantilever-based fiber sensors) (Yu & Giurgiutiu, 2008; Tsuda, 2006) are increasingly replacing conventional piezoelectric transducers (PZTs). The main drawback for PZT is that it is an electromechanical device whose performance is directly influenced by unwanted surrounding electromagnetic noise in the high-frequency region. This shortcoming can be overcome by employing optical fiber sensors such as fiber Bragg gratings (FBGs), Mach-Zehnder interferometer and Fabry-Perot sensors (Tsuda, 2006). Also due to lightweight, compactness, and easy integration, the FBGs are a preferable choice for acousto-ultrasonic emission detection in smart structures. An FBG, firstly invented by Hill et al. (1978) is very simple in-fiber structure defined as a periodic perturbation of the refractive index (RI) along the core of the fiber.

As compared to other ultrasound fiber sensors, fiber Bragg gratings (Hill et al., 1978) can be produced consistently in large numbers. The two main parameters that describe the performance of an FBG ultrasound sensor are its sensitivity and bandwidth. To improve these parameters, various techniques have been utilized for making different types of FBG sensors for detecting ultrasonic waves (Wu & Okabe, 2012; Zhou et al., 2011). Qu et al. (Wu & Okabe, 2012) studied the phase-shifted fiber Bragg grating (PS-

FBG) sensor with balanced photo-detector (BPD) which exhibits the high sensitivity and broad bandwidth with the capability to reduce laser intensity noise. The proposed FPR design aims to improve the sensitivity to ultrasound via the generation of a resonance which is much narrower than a conventional Bragg resonance.

Zhou et al. (2011) reported a modified FBG structure produced by micromachining a channel using a femtosecond laser. In their study, the micro-channel was used for enabling dynamic interaction between the liquid under test and light in the fiber where high sensitivity and large dynamic range of refractive index detection have been demonstrated. In the current work, a short cavity FPR is produced on an FBG to improve the sensitivity of the device. This is achieved by erasing a short length of the grating at its centre. This chapter describes the short cavity FPR sensor fabrication methodology and characterization of response to surface-mounted version to ultrasound as compared to a standard PZT transducer.

In recent years, fiber optic sensor technology has become the leading area of interest to many researchers and industries for several sensing applications due to their potential advantages, such as light weight, low cost, and immunity to electromagnetic interference (EMI). One of the earliest fiber based pressure sensors was proposed by Xu et al. (1993). In their sensor, the strain-optic property of FBG was exploited in the detection of hydrostatic pressure. Since then, numerous improved models have been proposed for pressure detection based on FBGs inscribed in specialty fibers (Yamate et al., 2000; Kreger et al., 2002; Chmielewska et al., 2003; Jin et al., 2013). The use of PCF in pressure sensing is particularly interesting and attractive. Taking advantages of the air-hole and small cross-sectional area of silica region, PCFs show greater pressure sensitivity than most SMFs which are solid fibers. In addition, it is possible to selectively fill specific air holes in the PCF to achieve desired optical properties such as

enhance sensitivity asymmetric coupling (Wu et al., 2009) and birefringence (Eggleton et al., 2001). Wang et al. proposed the method for selectively filling of PCF using focus ion beam milled microchannel (Wang et al., 2011). Furthermore, recent studies have demonstrated high pressure and temperature measurement using PCF along with standard SMF through the construction of a fiber-optic Fabry–Perot interferometer (Wu et al., 2011). The proposed structure has a temperature sensitivity of  $13.5 \text{ pm}/^\circ\text{C}$  and pressure sensitivity of  $-5.77 \text{ pm}/\text{MPa}$ . A considerable amount of effort has been put into the development of different techniques to distinguish the mechanical and thermal effects (Yang et al., 2015; Kanellopoulos et al., 1995; James et al., 1996; Taylor, 2002; Wu et al., 2010). However, it is necessary to investigate a cost-effective single system with ease of characterization and fabrication to fulfil this aspect. Hollow-core fiber based Fabry-Perot interferometers present rather interesting results (Jin et al., 2013). Due to the small light-glass interaction, the pressure sensitivity is mainly contributed by the pressure-induced change in fiber cavity length. Yamate et al. (2000) measured hydrostatic pressure by monitoring Bragg grating peak splitting caused by transverse strain differences in the core of a side-hole fiber which presents enhanced pressure sensitivity and reduced thermal dependence in comparison with FBG inscribed in solid fiber.

In this chapter, we also investigate a PCF-cavity FBG Fabry-Perot resonator for pressure sensing (Ali et al., 2015). The device is assembled from two segments of uniform FBG inscribed in SMF and a short length PCF based on the configuration of FBG-PCF-FBG. In other words, the short PCF cavity in FBG-PCF-FBG structure induces the phase discontinuity between the two FBGs and it presents a similar output spectrum with that of phase-shifted FBG (Liu & Han, 2012). The phase is dependent on the PCF structure and indicates much higher pressure sensitivity compared to the FBG even though both exhibit similar temperature sensitivities. Based on this observation,

the proposed device can be used for simultaneous measurement of temperature and pressure including temperature independent pressure measurement. Potential applications of the proposed device include in-situ monitoring of temperature and pressure especially in oil and gas industries as well as down-hole applications in chemical industries.

## **5.2 Fabrication of Short-cavity Fabry-Perot Resonator (FPR)**

For fabricating short cavity FPR, a uniform grating (FBG) is inscribed in a photosensitive fiber (GF1 Nufern) by using a KrF excimer laser emitting at 248 nm in conjunction with a phase mask. This produces a Bragg reflection at  $\sim 1556.52$  nm with a reflectivity of 40 dB. Photosensitive fibers are used in this work to evade the requirement for the supplementary processing stages, for example, loading hydrogen or deuterium. Besides, splice losses should be minimized by ensuring good mode matching between two of these fibers in the splicing. In addition, it helps to prevent high reflection at the splicing point. It is important to ensure that the photosensitivity of the fiber used for FBG writing so that a desired reflectivity can be achieved (Gillooly, 2011). The irradiation of UV light through the phase mask forms a periodic interference pattern. By placing the core of a photosensitive fiber within the field of interference, a periodic refractive index change can be imprinted in the fiber core. Such in-fiber Bragg gratings fabrication technique is easy to use and robust. The grating inscription rig is compact, insensitive to ambient disturbance and efficient in fabrication regardless of the coherence properties of the laser sources (Hill et al., 1993).

The normalized reflection and transmission spectrum achieved after the fabrication process is shown in Figure 5.1. Subsequently, the centre of this 20 mm long uniform grating is exposed to the focused excimer beam over a length of  $\sim 10$   $\mu\text{m}$  to erase the index modulation. This procedure splits the grating structure into two short gratings



separated by a length ( $\sim 10 \mu\text{m}$ ) which constitutes a short cavity length Fabry-Perot resonator. As a result, a phase-shift is introduced by the cavity length and a narrow notch is formed in the transmission spectrum, herewith known as resonance wavelength (Refer Figure 5.1). Complementary to the transmission curve, a narrow reflection peak is formed at the resonance wavelength. The cavity length of FPR can be controlled by varying the length of exposure at specific UV-fluence at the centre of the FBG. The narrow-band transmission peak has a full width at half maximum (FWHM) value of  $0.0304 \text{ nm}$  as shown in Figure 5.1, which shows a similar characteristic of  $\pi$ -phase-shift FBG. This structure can be considered as an in-fiber Fabry-Perot (FP) cavity between two FBG mirrors (Liu & Han, 2012). If the reflectivity of the FPR is very high, then this increases the Q-factor of the FP short cavity. The short cavity length FPR-induced spectral notch is significantly narrower than the width of uniform grating reflection. This reflection curve can be used to facilitate ultrasonic detection in a similar manner to normal FBGs by setting the laser wavelength to the steep linear region of the reflection curve and thereby enabling the detection of a change in reflectivity due to the ultrasonic wave-induced spectral shift. Hence this narrow band reflection could aid in sensitivity enhancement.

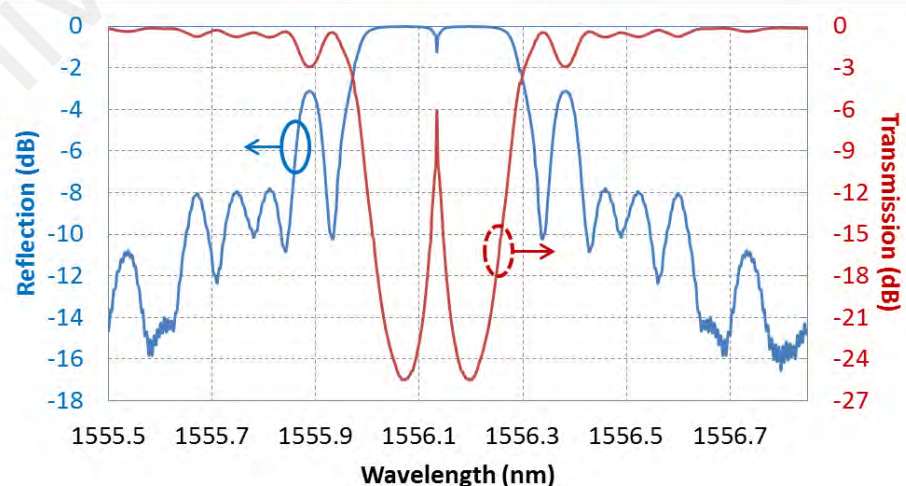


**Figure 5.1: Transmission and reflection spectrum of the short cavity Fabry-Perot resonator (FPR).**

### 5.3 Fabrication of PCF-cavity FBG Fabry-Perot Resonator

A 20 mm long uniform grating is written in a hydrogenated SMF-28 by using KrF excimer laser and a phase mask. The inscription process is carried out until a saturated grating with a transmission dip of  $\sim -45$  dB and a bandwidth of  $\sim 0.672$  nm are formed. Then, the written FBG is thermally annealed in an oven at  $80$  °C for 10 hours to out-diffuse the residue hydrogen from the fiber. After that, the FBG is equally partitioned into two by using a mechanical cleaver and then spliced with a  $\sim 1.5$  mm long PCF using FSM-45PM, Fujikura splicer to construct an FBG-PCF-FBG structure as illustrated in Figure 5.2(a). It is apparent that the two partitioned FBGs that originate from the same uniform grating share the same centre wavelength and the PCF segment forms a cavity between the two grating reflectors. As a result, a narrow dip is formed within the reflection curve of the FBG, herein known as resonance wavelength as shown in Figure 5.2(b). The Grapefruit PCF (FiberHome) used in this device is a 6-holes microstructure fiber with a pore size of  $27.5 \pm 3.0$   $\mu\text{m}$ , a Ge-doped core with a diameter of  $3.0 \pm 1.0$   $\mu\text{m}$  and effective index,  $n_{\text{eff}}$  of 1.479 (Refer micrograph in Figure 5.2(a)). Considering the mode field mismatch between PCF (MFD  $\approx 6$   $\mu\text{m}$ , NA  $\approx 0.254$ ) and SMF-28 (MFD  $\approx 10.4$   $\mu\text{m}$ , NA  $\approx 0.14$ ), offset splicing method (Xiao et al., 2007) is performed to achieve low splice loss in the fabrication of FBG-PCF-FBG structure. In our observation, the dip wavelength can be varied by re-arc-ing the PCF-FBG splicing point at low arc current. This is due to the erasure of a small portion of the grating within the vicinity of the PCF-FBG splicing point by the fusion arc. This induces a small change in the cavity length between the two FBGs and results to the variation of dip wavelength. Re-arc-ing is repeated several times until the dip is shifted to the desired position. The measured insertion loss of the produced structure is  $\sim 1.5$  dB. The measured band-edge wavelengths ( $\lambda_{B1}$ ,  $\lambda_{B2}$ ) and resonance wavelength ( $\lambda_R$ ) of the

reflection spectrum at atmospheric pressure and room temperature ( $T_0 = 22.9 \text{ }^\circ\text{C}$ ) are 1546.554, 1547.226, and 1546.931 nm, respectively.

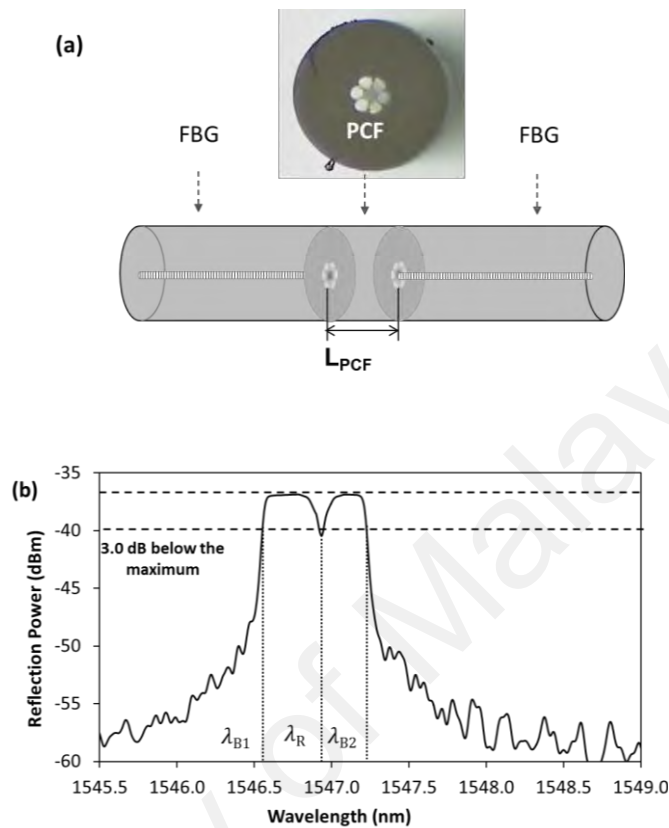


**Figure 5.2: (a) Cross-sectional image of PCF and (b) reflection spectrum of the proposed device.**

The variable  $\varepsilon_z$  in Equations. (4) and (5) can be interpreted as the sum of axial and radial strains in PCF or FBG induced by the external pressure (Wu et al., 2010). Generally, there are two constituents to the pressure sensitivity: pressure-induced changes in the effective index and the axial cavity length of the fiber. The change in the effective index can be explained by strain-optic effect contributed by the radial component and axial component of the hydrostatic pressure. Intriguingly, both components have opposite contribution to the effective index of the fiber, in which the radial component induces negative index change, whereas the axial component induces positive index change. Depending on the fiber structure, it is noted that the axial component is the dominating effect than the radial component and it is greater in PCF

than solid fiber. In the context of spectral change, the radial strain contributes to the positive change whereas the axial strain contributes to negative change in  $\Delta\lambda_R$  and  $\Delta\lambda_B$  and it is greater than that of radial strain. The sum of both strains results in blue shift in the spectrum. It is worth noting that the sensitivities are not dependent on PCF-cavity length.

For PCF, the pressure-induced axial stress in the core is given by  $\sigma_z = -(A_T / A_S) p = -\eta p$ , where  $\eta$  is the ratio of the total cross-sectional area of the fiber,  $A_T$  to the cross-sectional area of silica region,  $A_S$  in the PCF. For the FBG written in solid SMF, the axial stress is  $\sigma_z = -p$ . This indicates the strain sensitivity in PCF is  $\eta$  times greater than SMF. On the other hand,  $\lambda_R$  and  $\lambda_B$  share similar temperature sensitivity. This is partly due to the same thermal expansion coefficients of PCF and FBGs.

#### 5.4 Experimental setup for Acousto-optic and Pressure Sensing

##### *Optical setup of acousto-optic sensing*

The experimental setup for developing ultrasound detection is shown in Figure 5.3. The FBG structures on both sides of the short cavity share similar Bragg wavelength at  $\sim 1556.052$  nm separated by about 0.001 nm. The FPR which has a narrow-band transmission peak at  $\sim 1556.052$  nm with a reflectivity and bandwidth of 25.48 dB and 0.6 nm, respectively, is placed on an Aluminum (Al) plate and connected to a wavelength division multiplexing (WDM) coupler. This is a commonly used configuration to enable higher output laser emission through the FBG which has low reflectivity. The role of the WDM coupler besides coupling tunable laser source to the FPR is to collect throughput laser from the FPR to the photodetector where the optical signal is converted into electrical signal and subsequently analysed and recorded using a

digital oscilloscope. In this experiment, an InGaAs switchable amplified photodetector (PDA20CS) which offers a maximum bandwidth 10MHz at 0 dB gain is used. An optical isolator is used between the tunable laser source (TLS) and the WDM coupler to prevent unwanted reflected power to the TLS. The TLS should be tuned to a point in the spectra where the linear approximation holds true while the input wavelength is retained constant throughout the measurement process. However, in proposed study, the laser is set to the wavelength corresponding to the FWHM of the reflection curve in order to accomplish the maximum amplitude at the frequency of acoustic excitation and adequate dynamic range. So the TLS wavelength was tuned to 1556.134 nm and power were set as 2dBm. Both the transducer and the FPR are bonded onto a 12"×12"×0.008" aluminum plate using UV-curable resin and spaced 40 mm apart. The small thickness of the plate is to ensure that only the lowest order acoustic waves are excited for the frequency range used in this work. The plate serves as the ultrasonic wave transmission medium for all experiments and is therefore placed on noise isolation feet. A function generator was used to drive the ultrasound generating PZT–A whereas the aluminum plate serves as the medium of transmission to the FRP sensor. As the cavity length of the sensor is small, it is reasonable to assume that the ultrasonic waves influence both FBGs equally as they perturb the sensing length. Optical resonance of FPR reveals through the maximum sensitivity in the normalized reflection obtained via smoothed numerical derivative in Figure 5.4 (Kim et al., 2013). The absolute gradient curve shows a high sensitivity of 70.25 nm<sup>-1</sup> in FPR (see Figure 5.4(b)) whilst that of same FBG before inscribing the phase shift is 25.72 nm<sup>-1</sup> (see Figure 5.4(a)). The gradient of the curve is calculated by, (change in y-coordinate) / (change in x-coordinate). A PZT–B has been used as a sensing element as a comparison to the FPR. In addition, it should be noted that temperature variation during measurements is within ±1°C as the

experiment was carried out in a temperature-controlled room and hence the temperature influence is considered insignificant.

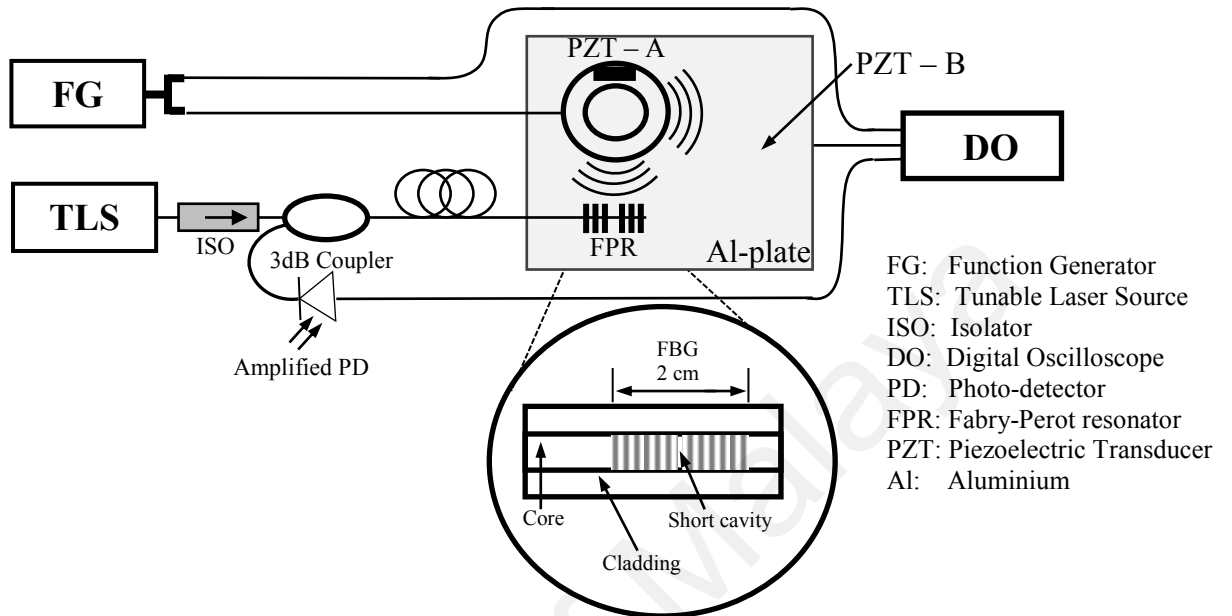
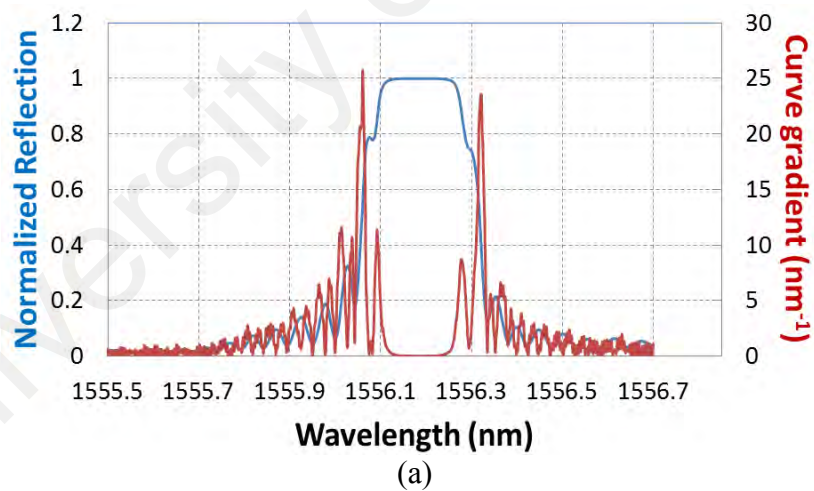
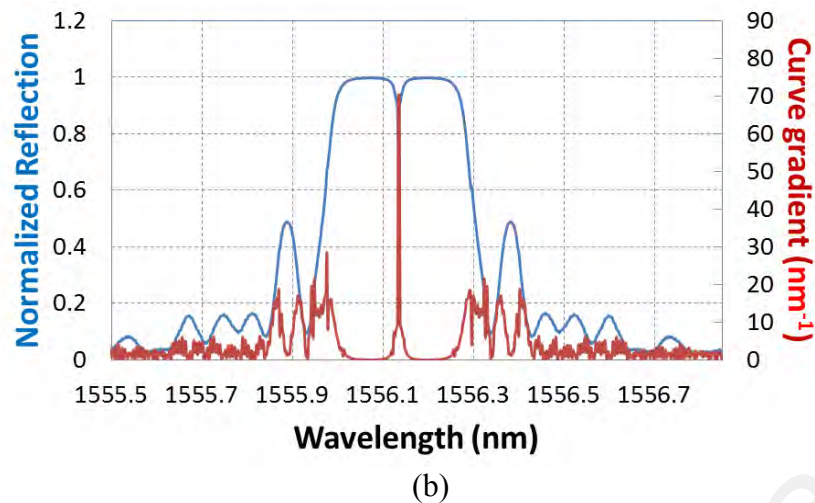


Figure 5.3: Experiment setup for the ultrasonic test.





**Figure 5.4: Reflectivity of (a) FBG and (b) FPR, reveal optical resonant that provide the maximum signal.**

#### *Optical setup of pressure sensing*

Figure 5.5 shows the experimental setup. The EDFA generates a broadband source centred at 1535 nm for illuminating the sensor in the pressure tube. The reflection from the sensor is redirected by the circulator to the OSA for analysis and record. The optical connection between the sensor inside the tube and the optical instruments outside is established via a feedthrough at one end of the tube and is sealed using epoxy to ensure no leakage of gas. Index matching gel is applied to the fiber end of the sensor to eliminate the undesired Fresnel reflection that may interfere with the reflection from the proposed device. The heat to the pressurized tube is generated from a heating tape wrapping on the tube from the outside in which the temperature is controlled in the range from room temperature to  $\sim 87$  °C under a close-loop system with an uncertainty in temperature of  $\pm 0.5$  °C. In addition, a thermocouple is positioned in proximity with the sensor inside the pressurized steel tube to measure the temperature as a reference. The pressure inside the tube can be regulated in the range of 0 - 2600 psi by using gas flow regulator. At each step point of temperature or pressure, 20 mins of settling time are applied to ensure the temperature of the entire sensor is stabilized and homogenous.

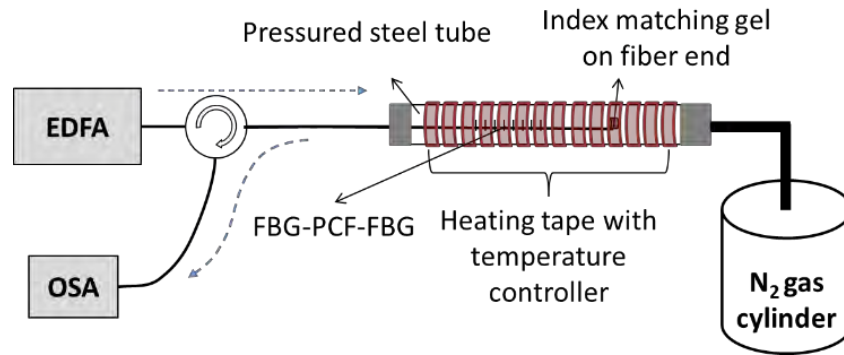


**Figure 5.5: Experimental setup for characterization of the proposed pressure sensor.**

### 5.5 Acousto-optic sensitivity of Short-cavity FP Resonator

Initially, the acoustic source was made to produce sinusoidal waveform over a frequency range of 0.001-10 MHz. Figures 5.6(a) and 5.6(c) show the temporal and spectral responses of the FPR fiber sensor and PZT-B respectively. The separation distance between the acoustic source and the centre of the FPR is approximately 40 mm. To compare the temporal and spectral waveforms measured by the FPR fiber optic sensor, a PZT-B sensor is placed on the Al-plate at an equal separation as that between the source and the FPR sensor. The acoustic waveform obtained in such a way is shown in Figure 5.3. The frequency spectra were generated by carrying out Fourier transforms on time domain signals. The ultrasonic waves are detected by both sensors; however, the FPR sensor exhibits more noise than the PZT-B sensor as in the temporal response. The spectral response of FPR is shown over a frequency range of 1 kHz – 10 MHz in Figure 5.6(a) and a single spectrum to present an enlarged response in Figure 5.6(b). The higher frequency limit is determined by the bandwidth of the photodetector; the wavelength of acoustic waves and the orientation of the proposed sensor with respect to the acoustic waves (Wu et al., 1994).

Furthermore, a continuous pulse signal is driven to PZT-A by a function generator to produce the ultrasonic wave while the input voltage is 5V with a 50 Hz pulse repetition rate. Figure 5.7 shows the temporal and spectral responses of the FPR sensor and PZT-



B. The time domain signals of both the sensors show an excellent phase correlation and correspond to the same onset time of about 119.87 ms. In addition, both signals have shown a similar high spectral response in a frequency range of 110 kHz to 160 kHz. On the contrary, noise in the signal can be reduced by using moving average filter.

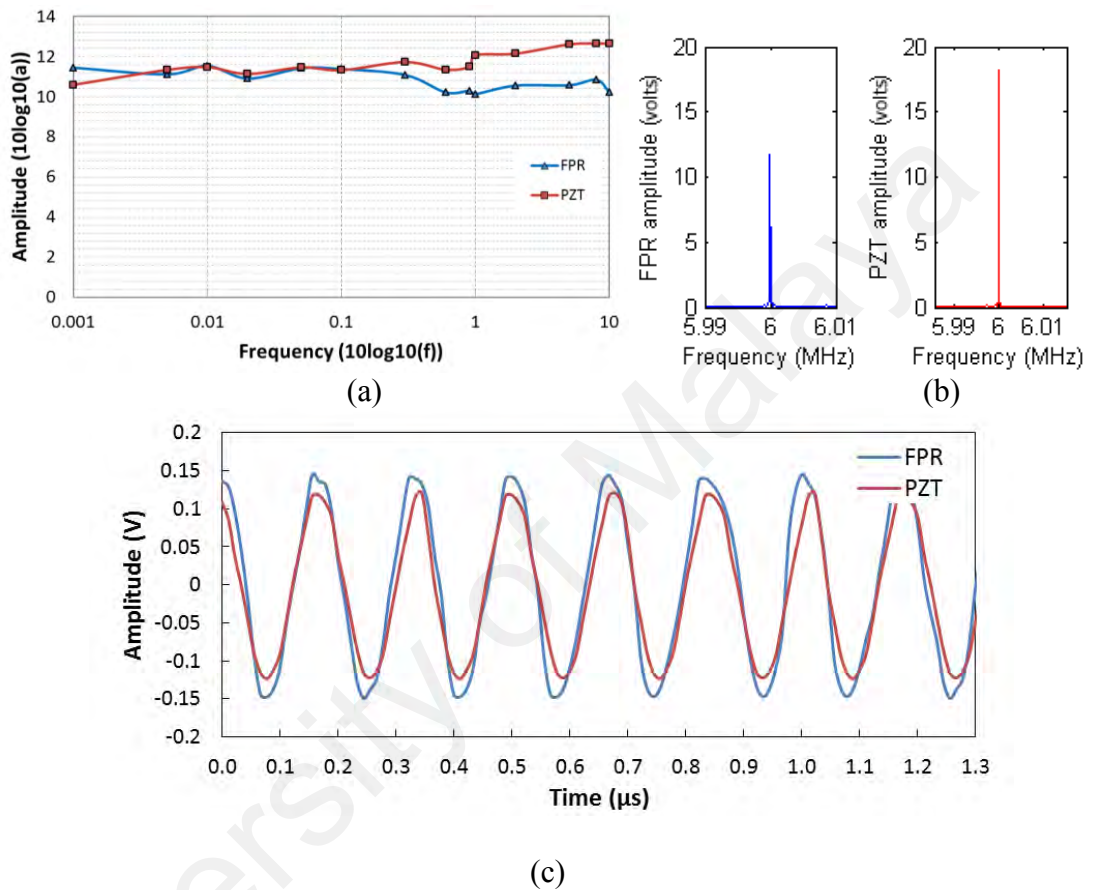


**Figure 5.6: (a) Frequency response of the PZT–B and FPR sensors while impinging a constant sinusoidal acoustic ultrasonic wave in a frequency range as 0.001-10 MHz (b) Demonstration of single frequency response of each sensor at 6.0 MHz frequency (c) Time domain signal obtained from FPR and PZT–B in case of ~ 6.0 MHz input ultrasonic signal.**

From the experiment results, it was demonstrated that the proposed sensor design is highly sensitive and it can perform as good as PZT–B in the high-frequency region. The dynamic range for the acoustic amplitude is limited due to the narrow peak of the FPR. Nevertheless, this would not be a problem as the transient strain in the application of ultrasonic detection is generally small, according to (Wu & Okabe, 2012).

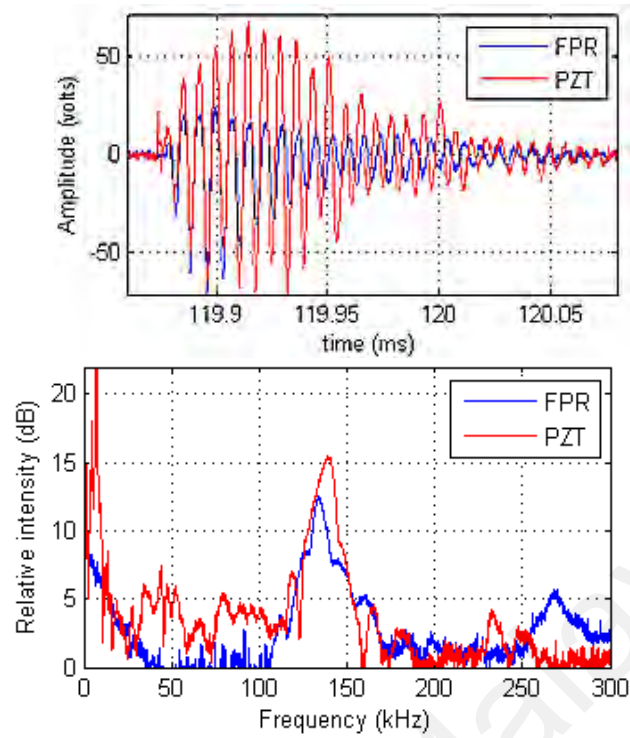


**Figure 5.7: Single pulse temporal and spectral responses attained by the FPR and PZT–B, respectively, while the similar spectral responses are shown in the frequency range of 110 kHz to 160 kHz.**

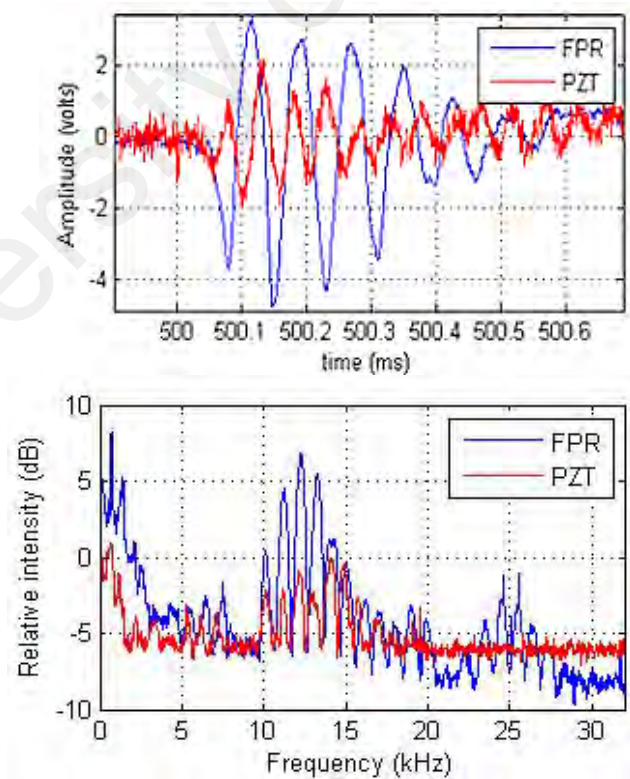


**Figure 5.8: Single pulse temporal and spectral responses attained by the FPR and PZT–B, respectively, while the similar spectral responses are shown in the frequency range of 10 kHz to 20 kHz.**

Lastly, a similar pulse signal is generated (as mentioned in the early section) to study the frequency response of FPR by replacing the PZT–A. This transducer is used for generating ultrasonic waves in a lower range of frequencies. Here, the PZT–A sensor is placed at the same position and the acoustic wave is generated while the input voltage is 10V with a 50 Hz pulse repetition rate. Figure 5.8 presents a good accordance in the temporal and spectral responses of the both FPR and PZT–B, and larger signal amplitude is achieved by the FPR than the standard PZT–B. Besides, both sensors show the same starting time. The higher frequency components of the acoustic signal are shown in the frequency range of 10 kHz to 20 kHz, though the range is very small due to same reason mentioned above. However, the spectral response of the FPR is higher than that of PZT–B at low frequencies. A minor delay of PZT in the temporal response of Figure 5.8 is observed due to the poor sensitivity of PZT in the lower frequency range (few hundreds of Hz) which has been reported in the literature (Bornand et al., 2005). Also, it can be seen that the frequency components of PZT are very close to the background noise level in the spectral response of Figure 5.8 which leads to the poor sensitivity and delay.

### **5.6 Pressure sensitivity of PCF-cavity FBG Fabry-Perot Resonator**

The thermal response of the proposed sensor is presented in Figure 5.9 (a). It is observed that the reflection spectrum is shifted to the red with increasing temperature, in which  $\lambda_{B1}$ ,  $\lambda_{B2}$ , and  $\lambda_R$  respond at the same sensitivity of  $\sim 12.1$  pm/°C in the range of 22 - 87 °C as illustrated in Figure 5.9 (b). The spectral shift with the increment in pressure at room temperature is shown in Figure 5.10 (a). The output spectrum is blue-shifted in response to increasing pressure as shown in Figure 5.10. The blue shift in resonance wavelength is greater than those in band-edge wavelengths (refer to Figure 5.10 (b)). The pressure sensitivities for both  $\lambda_{B1}$  and  $\lambda_{B2}$  are identical and measured to

be  $\sim 2.4$  pm/MPa whereas the sensitivity for  $\lambda_R$  is  $\sim 10.1$  pm/MPa which is 4.2 times higher than the former two wavelengths.

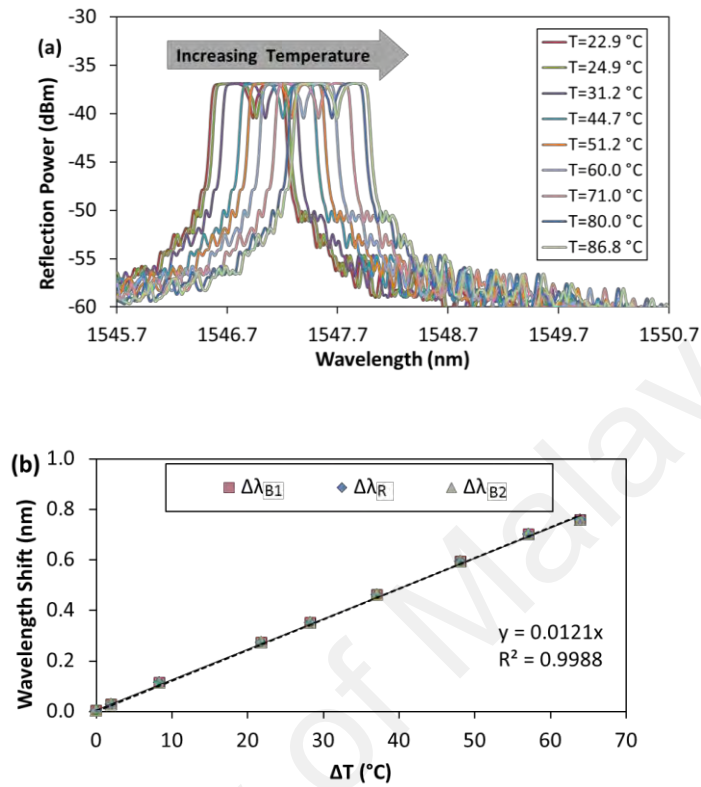


**Figure 5.9: (a) Reflection spectra of the proposed sensor at different temperatures, (b) the relationship between wavelength shift and temperature change.**

Based on the calibration results presented in Figure 5.9 and Figure 5.10, simultaneous equations can be formulated in matrix form as follows:

$$\begin{bmatrix} \Delta\lambda_B \\ \Delta\lambda_R \end{bmatrix} = \begin{bmatrix} S_{11} & S_{12} \\ S_{21} & S_{22} \end{bmatrix} \begin{bmatrix} \Delta T \\ \Delta P \end{bmatrix} \quad (5.1)$$

where  $\Delta$  denotes the change in the corresponding parameter,

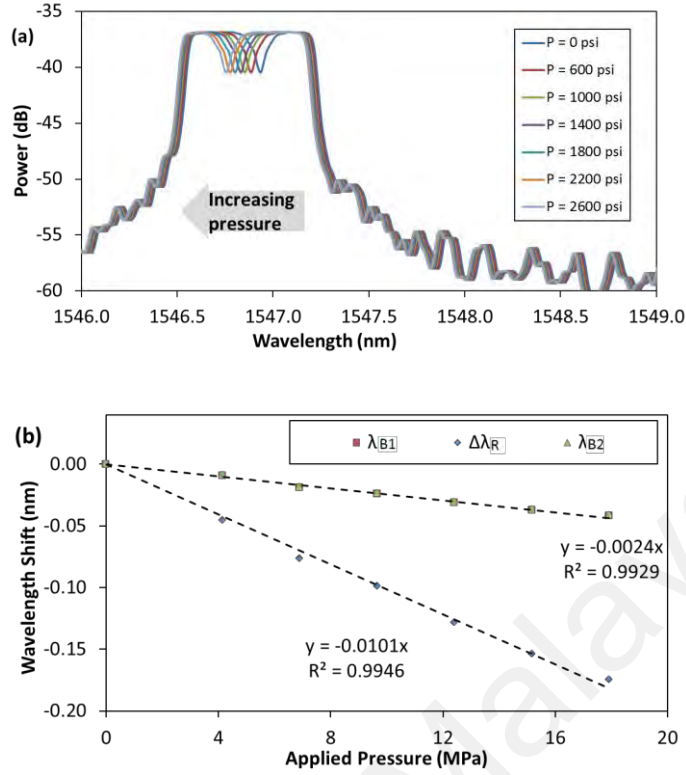


**Figure 5.10: (a) Reflection spectra of the proposed sensor at different pressures, (b) the relationship between wavelength shift and applied pressure.**

since both  $\lambda_{B1}$  and  $\lambda_{B2}$  share the same sensitivities of pressure and sensitivity, they exhibit the same wavelength shift  $\Delta\lambda_B$  to the changes of temperature and pressure.  $\Delta\lambda_B$  can be acquired from either one of them,  $s_{11}$  and  $s_{21}$  are the temperature sensitivities of  $\Delta\lambda_B$  and  $\Delta\lambda_R$  respectively whereas  $s_{12}$ , and  $s_{22}$  are the pressure sensitivities of  $\Delta\lambda_B$  and  $\Delta\lambda_R$  respectively. With reference to the data in Figure 5.9 and Figure 5.10, the measured sensitivities are

$$\begin{bmatrix} s_{11} & s_{12} \\ s_{21} & s_{22} \end{bmatrix} = \begin{bmatrix} 12.1 & -2.4 \\ 12.1 & -10.1 \end{bmatrix} \quad (5.2)$$

Based on the inverted characteristic matrix below, simultaneous measurement of  $\Delta T$  and  $\Delta P$  can be achieved.

$$\begin{bmatrix} \Delta T \\ \Delta P \end{bmatrix} = \begin{bmatrix} 12.1 & -2.4 \\ 12.1 & -10.1 \end{bmatrix}^{-1} \begin{bmatrix} \Delta\lambda_B \\ \Delta\lambda_R \end{bmatrix} \quad (5.3)$$

Considering the same temperature sensitivity of  $\lambda_B$  and  $\lambda_R$ , the measurement of pressure change can be conveniently attained by performing a simple subtraction between the linear equations of  $\Delta\lambda_B$  and  $\Delta\lambda_R$ :

$$\Delta P = (\Delta\lambda_R - \Delta\lambda_B) / (-7.7) \quad (5.4)$$

where -7.7 pm/MPa is the difference between the pressure sensitivities of  $\Delta\lambda_B$  and  $\Delta\lambda_R$ .

Discriminative measurement can be achieved with a simple calculation with the matrix equation. In the scenario where temperature cancellation is required, the measurement of pressure can be easily acquired by performing a simple subtraction using Equation (5.4).

Unlike most Fabry-Perot resonators or other similar optical structures with periodic output spectra, the proposed device has a single reflection curve with a resonance wavelength that offers multi-parametric responses to the changes of temperature and pressure. The signal processing is easy and it does not have the problem of confusion when the wavelength shift is greater than a period of the spectrum. It is reasonable to believe that the temperature range of the device can be further extended until the maximum sustainable temperature of the FBGs. However, the dynamic range for pressure sensing is limited by the bandwidth of the reflection curve ( $\lambda_{B2} - \lambda_{B1}$ ) nonetheless it can be further enhanced by using shorter grating length for both FBG segments and the PCF cavity length should be adjusted accordingly (reduced) to ensure the existence of a single resonance wavelength within the larger reflection curve.

## 5.7 Von Mises Stress

Von Mises stress is broadly utilized by designers to check whether their scheme will withstand a certain load condition. In engineering genuine designing issue with an intricate loading condition, ordinary stress hypothesis doesn't work. The material fails

when the extreme typical stress value prompted in the material is more than the yield point value. The most favoured failure hypothesis utilized in the industry is ‘Von Mises stress’ based. We will apply Von Mises stress in the simulation of the following section to compute whether the extreme estimation of Von Mises Stress prompted in PCF/SMF is not exactly the yield point estimation of PCF and SMF fiber or not.

### 5.8 Opto-elastic Response to Acousto-optic of Short-cavity FP Resonator

In this segment, we examine the inner stresses in FBG produced in hydrogenated SMF fiber furthermore investigate the FBG based FPR device and their effects on its physical properties.

Ultrasonic longitudinal waves, whose direction of vibration is parallel to the direction of propagation, differently affect both refractive index and grating period change from ultrasonic pressure waves. Expect the direction of propagation and vibration are both in the z direction, which is alongside the fiber axis. The stress along z direction can be modelled by

$$\sigma_z = -P \cos\left(\frac{2\pi}{\lambda_s} z - \omega t\right) \quad (5.5)$$

where P is the pressure delivered by the ultrasonic wave. The stress vector can be composed as

$$\sigma = \begin{bmatrix} 0 \\ 0 \\ -P \end{bmatrix} \quad (5.6)$$

For an ultrasonic longitudinal wave which has no shear mechanisms, the strain vector of optical fiber affected by the pressure wave can be composed as underneath in view of the equation of strain-stress relativity;

$$\begin{bmatrix} \varepsilon_{xx} \\ \varepsilon_{yy} \\ \varepsilon_{zz} \end{bmatrix} = \begin{bmatrix} \frac{\nu}{E} P \\ \frac{\nu}{E} P \\ -\frac{1}{E} P \end{bmatrix} \quad (5.7)$$

The adjustments in fiber length and fiber grating period are identified with  $\varepsilon_{zz}$  by (Rao, 1997)

$$\frac{\Delta\Lambda}{\Lambda} = \frac{\Delta L}{L} = \varepsilon_{zz} = -\frac{1}{E} P \quad (5.8)$$

We realize that the interaction of materials and ultrasonic waves as well causes the change of refractive index of the material, which is called strain-optic impact or elasto-optic impact. As per the elasto-optic impact discussed in section 2.4, the change in optical index matrix brought about by an enforced strain is specified by (Wild & Hinekley, 2008)

$$\Delta\left(\frac{1}{n^2}\right)_i = \sum_{j=1}^6 P_{ij} \varepsilon_j \quad (5.9)$$

where  $p_{ij}$  is the strain-optic tensor. The strain vector for a homogeneous and isotropic fiber brought about by the longitudinal wave is

$$\varepsilon = \begin{bmatrix} \varepsilon_{xx} \\ \varepsilon_{yy} \\ \varepsilon_{zz} \\ \varepsilon_{xy} \\ \varepsilon_{yz} \\ \varepsilon_{zx} \end{bmatrix} = \begin{bmatrix} \frac{\nu}{E} P \\ \frac{\nu}{E} P \\ -\frac{1}{E} P \\ 0 \\ 0 \\ 0 \end{bmatrix} \quad (5.10)$$

By solving the Equation (5.9) and Equation (5.10), and the adjustment in the index matrix is acquired as



$$\Delta\left(\frac{1}{n^2}\right)_{x,y} = [vp_{11} - (1-v)p_{12}] \frac{P}{E} \quad (5.11)$$

The refractive index identified with the change in optical index matrix is (Wild & Hinekley, 2008)

$$\begin{aligned} \Delta n_{x,y} &= -\frac{1}{2} n^3 \Delta\left(\frac{1}{n^2}\right)_{x,y} \\ &= \frac{n^3}{2E} [(1-v)p_{12} - vp_{12}] P \end{aligned} \quad (5.12)$$

We can anticipate the spectral shift concerning the ultrasonic-impelled pressure by substituting the Equation (5.8) and Equation (5.12) in the equation of wavelength shift by pressure change;

$$\Delta\lambda_B = \lambda_B \left\{ -\frac{1}{E} + \frac{n^2}{2E} [(1-v)p_{12} - vp_{12}] \right\} \Delta P \quad (5.13)$$

Figures 5.11 and 5.12 underneath demonstrate the stress profile in axial and radial components of an FBG manufactured in SMF fiber and FBG based FPR, correspondingly.

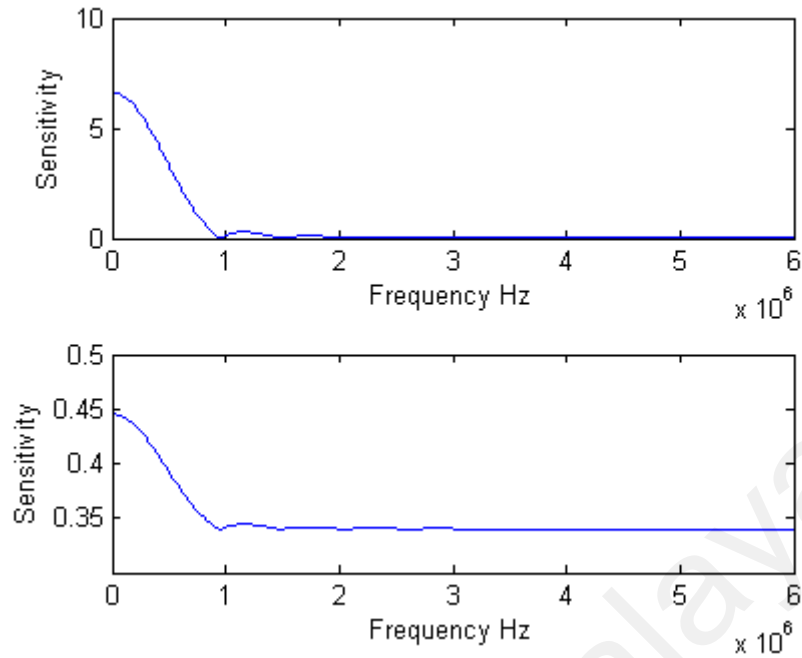


**Figure 5.11: Axial component of FBG (modulated grating period and grating index) by a sinusoidal wave. Parameters utilized for this modelling are:  $p_{11} = 0.121$ ;  $p_{12} = 0.27$ ;  $v = 5760\text{m/s}$ ;  $E = 70\text{GPa}$ .**

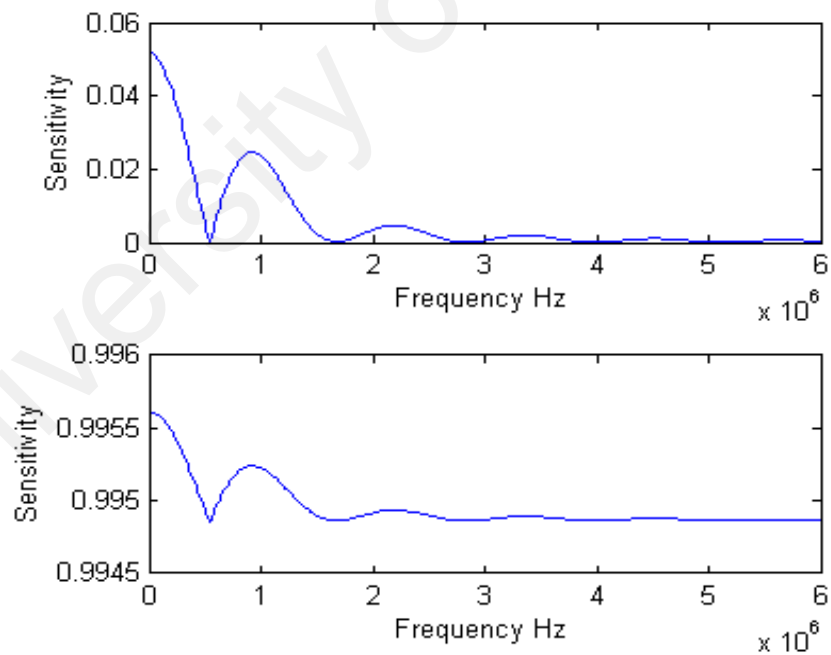


**Figure 5.12: Radial component (modulated grating period and grating index) of FBG based FPR by a sinusoidal wave. Parameters utilized for this modelling are:  $p_{11} = 0.121$ ;  $p_{12} = 0.27$ ;  $v = 5760\text{m/s}$ ;  $E = 70\text{GPa}$ .**

We have simulated the spectral shift produced by the ultrasonic wave prompted pressure utilizing the accompanying values and the resultant wavelength shift of FBG based FPR has appeared in Figure 5.13.

Symbol	Physical Quantity	Value	Unit
<b>E</b>	Young's modulus of optical fiber	70	GPa
<b>V</b>	Poisson's ratio	0.12	-
<b>p<sub>11</sub></b>	1,1 element in strain-optic tensor	0.121	-
<b>p<sub>12</sub></b>	1,2 element in strain-optic tensor	0.270	-
<b>S</b>	Ultrasound velocity in fused silica	4000	m/s
<b>P</b>	Differential pressure amplitude of ultrasonic wave	1	MPa
<b>λ<sub>B</sub></b>	Bragg wavelength	1550	Nm

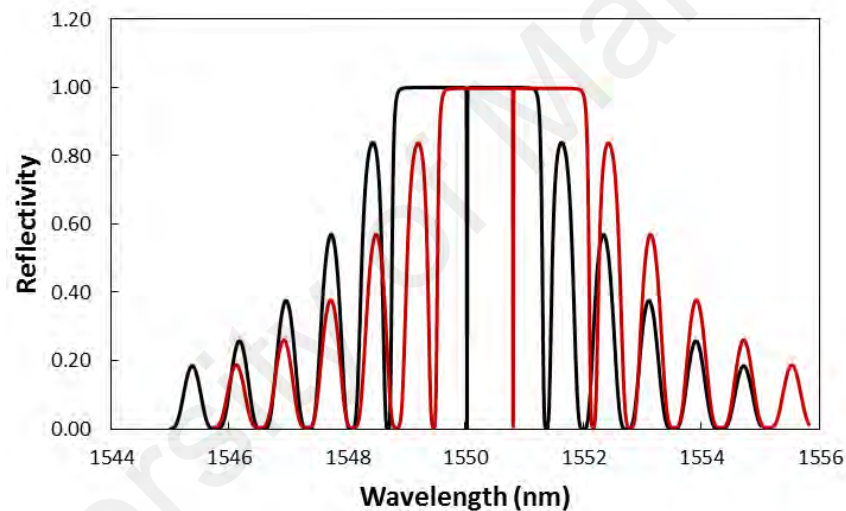


**Figure 5.13: The computed wavelength shift brought on by longitudinal wave (black line – Bragg wavelength, red line – modulated Bragg wavelength)**

## 5.9 Opto-elastic Response of PCF-cavity FBG Fabry-Perot Resonator to Pressure

PCF-cavity FBG Fabry-Perot has extraordinary potential for use in sensing applications as it has a decent temperature and pressure sensitivity. Opto-elasticity reactions of PCF and SMF fiber by the pressure-induced change in refractive index of the fiber are worth studying considering keeping in mind the end goal to understand the effectiveness of the proposed PCF-cavity FBG Fabry-Perot device. In this study, the

refractive index of the PCF-cavity FBG Fabry-Perot changes by the pressure-induced change as appeared in Figure. 5.14. This figure demonstrates the schematic outline of the PCF-cavity FBG Fabry-Perot under the influence of gas pressure. One end of the fiber is exposed to the gas tube in a manner that it encounters both radial and axial pressures. The radial and axial pressures lead to a negative and positive index change. The axial component is the commanding impact than the radial component in PCF than solid fiber. Be that as it may, the aggregate of both the radial and axial pressures contributes to a blue shift in the wavelength of PCF-cavity FBG Fabry-Perot device.

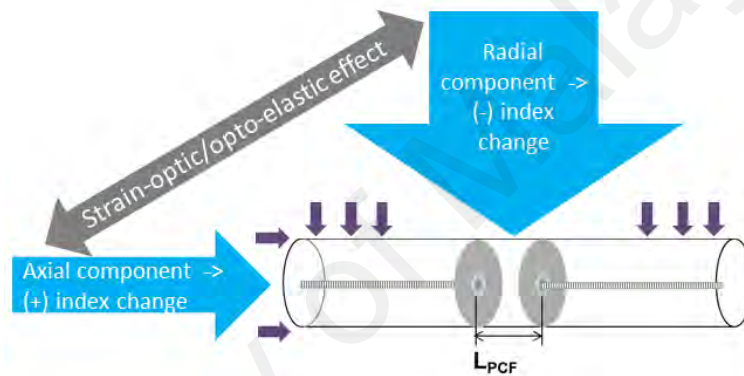


**Figure 5.14: Axial and radial components contributed to refractive index changes**

To achieve stress profile of PCF, COMSOL software is utilized to compute  $n_{eff}$  and  $\Delta n_{eff}$  of a grapefruit PCF under a state of pressure enforced stress. We simulated the stress optic impact of the PCF and SMF fibers utilizing a structural mechanics module of the COMSOL software. The parameters utilized as a part of this progression are as taking after: Poisson's ratio,  $\nu_{SiO_2}=0.42$ ; Young's modulus,  $E_{SiO_2}=7.8 \times 10^{10} Pa$ ; operating temperature,  $T_1=293.15K$ ; reference temperature,  $T_0=373.15K$ ;

In the following stride, as indicated by opto-elastic impact, we utilize the stress conveyance to acquire the refractive index profile as the accompanying formula:

$$N_x = N_0 - B_2 \sigma_x - B_1 (\sigma_y + \sigma_z) \quad (5.14)$$

$$N_y = N_0 - B_2\sigma_y - B_1(\sigma_x + \sigma_z) \quad (5.15)$$

$$N_z = N_0 - B_2\sigma_z - B_1(\sigma_x + \sigma_y) \quad (5.16)$$

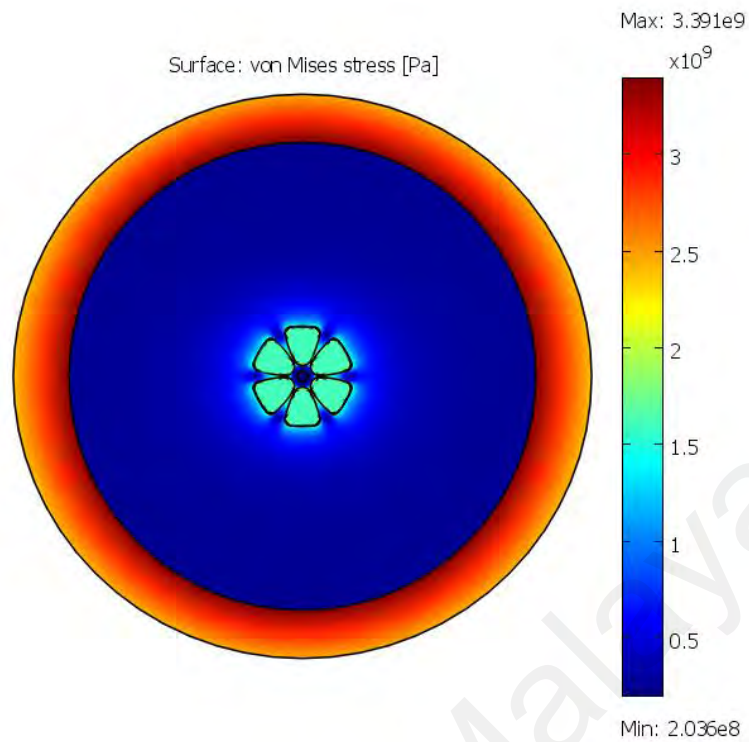
where  $\sigma_x, \sigma_y, \sigma_z$  are the stress components, and the first stress optical coefficient,

$B_1=(4.2 \times 10^{-12}) \text{ Pa}^{-1}$ ; second stress optical coefficient,  $B_2=(6.5 \times 10^{-13}) \text{ Pa}^{-1}$ .

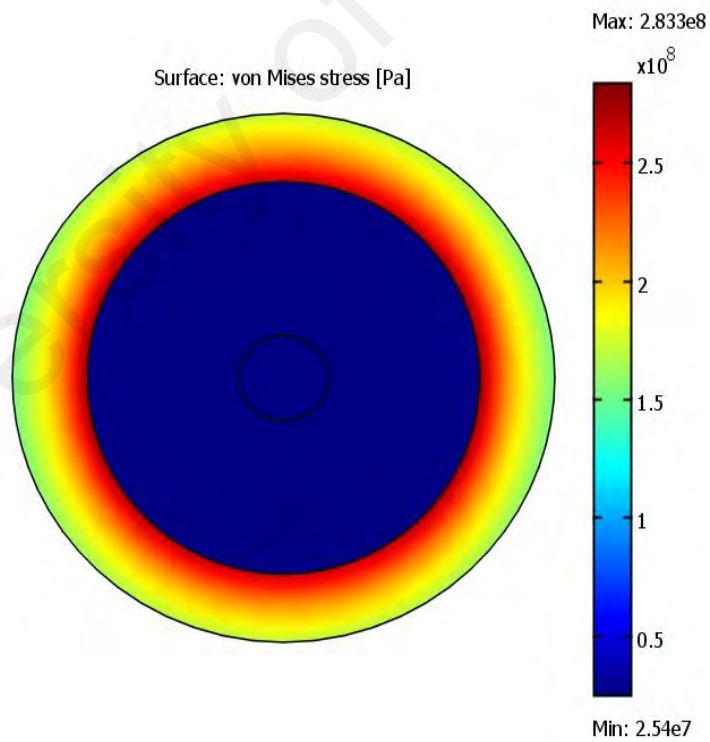
Our simulation incorporates just these two independent parameters,  $B_1$  and  $B_2$ . At that point, the stress-optical connection simplifies to

$$\begin{bmatrix} \Delta N_x \\ \Delta N_y \\ \Delta N_z \end{bmatrix} = - \begin{bmatrix} B_2 & B_1 & B_1 \\ B_1 & B_2 & B_1 \\ B_1 & B_1 & B_2 \end{bmatrix} \begin{bmatrix} \sigma_x \\ \sigma_y \\ \sigma_z \end{bmatrix} \quad (5.17)$$

where  $N_x = n_{11}$ ,  $N_y = n_{22}$ ,  $N_z = n_{33}$ ,  $\sigma_x = \sigma_{11}$ ,  $\sigma_y = \sigma_{22}$ ,  $\sigma_z = \sigma_{33}$ . This can be meant to equation (5.14-5.17). The shear stress comparing to  $\sigma_{11}, \sigma_{22}, \sigma_{33}$  are ignored in the simulation. Additionally, it is to be noticed that, the adapted strain guesstimate holds in a circumstance where the structure is free in the x and y axes but the z strain is presumed to be zero. Figure 5.15 shows Von Mises stress profile for thermal and gas pressure, correspondingly for both the PCF and SMF case. It's to be noted that the effective stress is gradually fluctuating on the x-axis which implies that the critical impact on the stress-induced index changes mostly contributed by the stress varieties in the y-axis. Von Mises stress profile has been displayed to see the material's yield point.



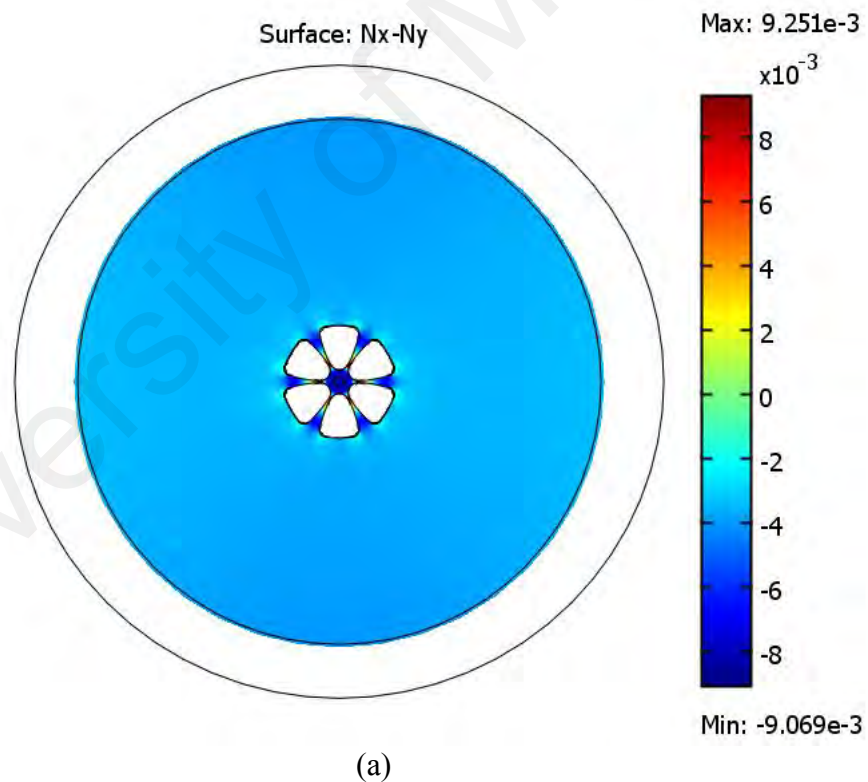
(a)

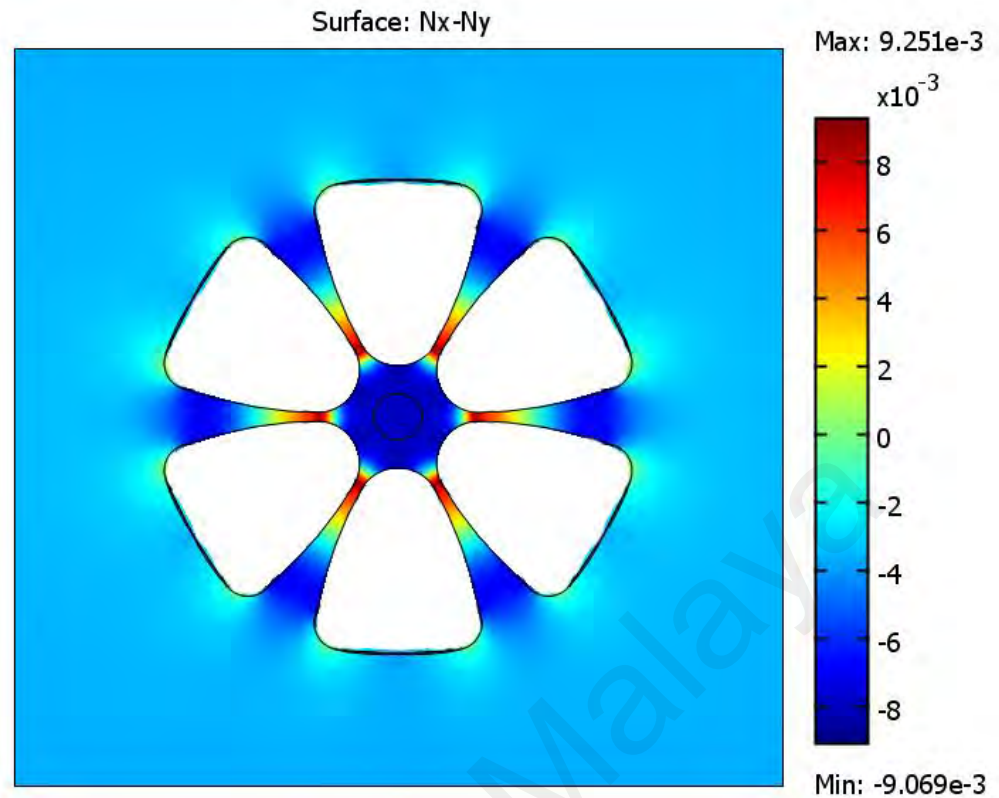


(b)

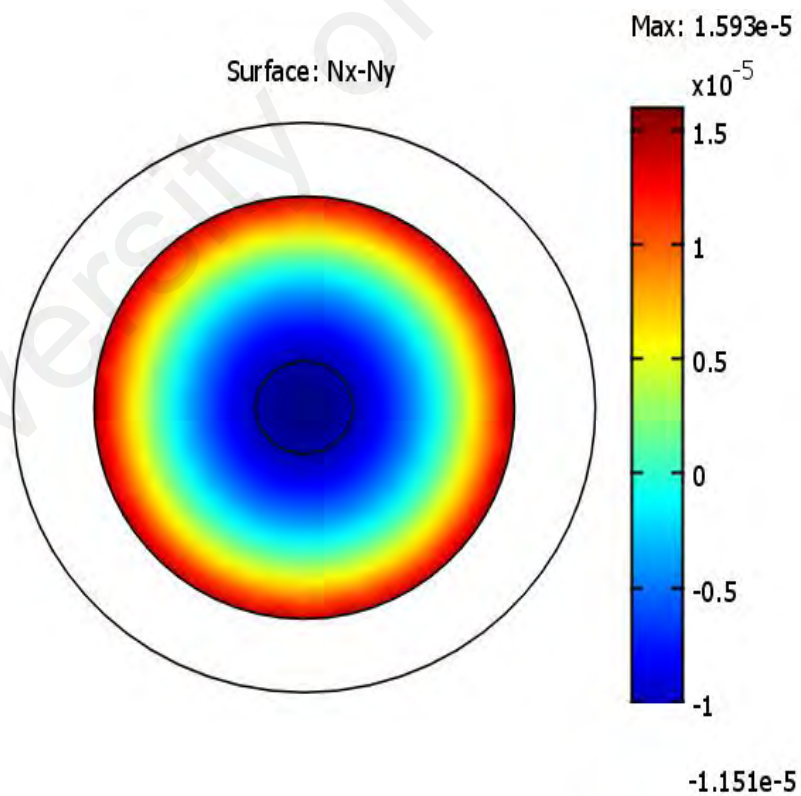
**Figure 5.15: Von Mises stress profile affected by thermal and pressure stress for (a) 6-holes grapefruit PCF microstructured fiber, (b) SMF solid fiber.**

By plotting these Von Mises stress profile it has been demonstrated that the values utilized as stress optical coefficients are appropriate. The subsequent birefringent refractive index is figured utilizing expression variables,  $N_x-N_y$ . Figure 5.16 demonstrates the radial pressure induced refractive index changes. The maximum refractive index changes are seen to have occurred close to the core of grapefruit PCF microstructured fiber than solid fiber. This radial pressure induced a change in refractive index alongside axial refractive index change contributes a blue shift in the dip wavelength within the bandwidth reflection curve of the proposed PCF-cavity FBG Fabry-Perot device. The dip is the aftereffect of short PCF segment spliced between two saturated FBG inscribed in SMF.





(b)



(c)

**Figure 5.16: Simulation profile of radial pressure induced refractive index change for (a) 6-holes grapefruit PCF microstructured fiber, (b) zoom view of (a), (c) SMF solid fiber, when radial pressure is,  $P=17.9\text{MPa}$ .**



## 5.10 Thermo-optic Response of PCF-cavity FBG Fabry-Perot Resonator to Temperature

FBGs have been broadly utilized as a part of fiber sensor applications owing to its compactness in structures, straightforwardness in manufactures and wavelength coding in measurements. In any case, in temperature and pressure sensor applications, it is hard to discriminate between the temperature and the pressure impacts from the spectral response, as FBG is sensitive to both. Hence, it merits examining the thermo-optic impact in FBG based sensors which will add to the understanding and designing of effective FBG. The temperature reliance of the refractive index is characterized by the thermo-optic coefficient, which depends on the change of refractive index emerging from a tiny change of the temperature as shown in Figure 5.9. This figure shows the thermo-optic response of the proposed PCF-cavity FBG based Fabry-Perot resonator where a red shift of the reflection spectrum has been observed with increasing temperature.

By the coupled-mode hypothesis, the centre wavelength of reflected light from FBG can be depicted by the Bragg equation (3.28) where  $n_{eff}$ ,  $\Lambda$  and  $\lambda_B$  are the effective index, period and centre wavelength of FBG correspondingly, and are connected with temperature and strain. Strain impacts  $\lambda_B$  because of grating's period change and elastic-optic effect, and temperature impacts  $\lambda_B$  because of thermal expansion and thermo-optic impact, so the temperature or strain measurement can be acknowledged by recognizing the centre wavelength or reflection spectrum (Jhang & Yongqian, 2009).

$$\frac{\Delta\lambda_B}{\lambda_B} = \frac{\Delta\Lambda}{\Lambda} + \frac{\Delta n_{eff}}{n_{eff}} \quad (5.18)$$

Given that no strain is adapted, yet the temperature changes  $\Delta T$ , then Bragg grating's period change because of thermal expansion can be composed as

$$\Delta L = \alpha \cdot L \cdot \Delta T \quad (5.19)$$

The effective refractive index change  $n_{eff}$  because of thermo-optic impact can be communicated as

$$n_{eff} = \xi \cdot n_{eff} \cdot \Delta T \quad (5.20)$$

where  $\alpha$  is the thermal expansion coefficient,  $\xi$  is the thermo-optic coefficient. Substituting equations (5.19) and (5.20) into (5.18), the centre wavelength of FBG change because of temperature can be composed as

$$\frac{\Delta \lambda_B}{\lambda_B} = (\alpha + \xi) \cdot \Delta T = K_T \cdot \Delta T \quad (5.21)$$

in which  $K_T = \alpha + \xi$  is the temperature sensitivity of FBG.

Thermal expansion and thermo-optic coefficient would vary when consistency germanium and the temperature sensitivity differs. At the point when the temperature does not change significantly or exactness is low, we consider the temperature sensitivity to be a constant. Indeed, thermal expansion and thermo-optic coefficients fluctuate with temperature change. At the point when the required exactness is high or the temperature change is extensive, these coefficients have a nonlinear impact on temperature sensitivity.

To ascertain the change of Bragg grating period because of temperature change, it is important to know the thermal expansion coefficient of fiber material. Solid length changes when the temperature changes. Accepting that solid length raises  $dL$  when temperature raises  $dT$ , then thermal expansion coefficient can be communicated as

$$\alpha = \frac{1}{L_0} \frac{dL}{dT} \quad (5.22)$$

where  $L_0$  is the solid length at 0°C. The trial has demonstrated that  $\alpha$  is not constant. In light of the table of expansion coefficient of vitreous silica in the temperature range from (0-100)°C displayed by Jing Zhang (Zhang & Yongqian, 2009) the thermal expansion coefficient  $\alpha$  of the proposed PCF-cavity FBG Fabry-Perot resonator differ within the range of  $(0.40 \times 10^{-6}/\text{C}) - (0.47 \times 10^{-6}/\text{C})$  for 22-87°C temperature. It is observed in our experiment that PCF cavity and FBGs exhibits the comparable wavelength shift because of the same thermal expansion coefficient of comparative material structures.

### 5.11 Summary

The sensitivity of the proposed short cavity FBG based FPR inscribed in SMF is three times higher than an uniform FBG based on the obtained curve gradient presented in Figure 5.4. This design of the sensor is simple and the fabrication is easy. This sensor has the promising device for acoustic and ultrasonic sensing applications particularly in lower to the higher frequency range of 1 kHz -10 MHz. Experimental results show that the performance of short cavity FPR is comparable to that of a commercial PZT and can be used in applications where the use of PZT is not viable. The conventional ultrasonic sensors can be replaced by the proposed sensor because of its high sensitivity, narrow bandwidth, as well as all its advantages explained in the early section of this chapter. However, it is presumed that the broad frequency response and high sensitivity can be further improved by adopting suitable modifications to the sensor design and instrumentation. The reduction of hydroxyl (OH) content and stress alteration in the fiber during UV erasure process may contribute to the uncertainty.

A PCF-cavity FBG Fabry-Perot resonator based on FBG-PCF-FBG configuration has been fabricated and investigated for simultaneous measurement of pressure and temperature. The characterized pressure sensitivities for band-edge wavelengths and

resonance wavelength are found to be  $-2.4 \text{ pm/MPa}$  and  $-10.1 \text{ pm/MPa}$  in the range of  $0 - 18 \text{ MPa}$  whereas the temperature sensitivities for all three wavelengths are the same,  $12.1 \text{ pm/}^\circ\text{C}$  in the range of  $22 - 87 \text{ }^\circ\text{C}$ . The investigation result also suggested that the device can be used for simultaneous sensing of temperature and pressure. The same temperature sensitivity of resonance wavelength and band-edge wavelength provides the convenience of simple pressure measurement. The characterized model of the linear system of equations has also been presented. The proposed sensing device has potential applications in chemical industries for in situ monitoring of temperature and pressure.

University of Malaya

## CHAPTER 6: CONCLUSION AND FUTURE WORKS

### 6.1 Conclusion

In this thesis, a short cavity length FP resonator has been produced through a simple fabrication technique. Analytical and experimental studies on the stress and opto-elastic properties of FBG based FPR have been conducted. The short cavity FBG based FPR showed a wide range of frequency response and high sensitivity to acousto-ultrasonic excitation. Such device can be utilized in applications where the utilization of traditional PZT is not suitable.

A PCF-cavity FBG FP resonator based on FBG-PCF-FBG design has been manufactured and characterized by simultaneous sensitivity to pressure and temperature. The configuration of the FBG based FPR device proved to produce a synchronous measuring optical device and analysis of its opto-elastic behaviour validated the fabrication design of the device and in addition, advanced the understanding of its operational principle. The proposed sensing device has potential applications in chemical industries for in situ observation of temperature and pressure.

The  $LP_{01}$ - $LP_{11}$  cross mode interference in chirped grating (CG) is examined by both simulation and experimental investigation alongside the attributes of CG in two-mode fiber (TMF). We characterized the spectra of the CG under  $LP_{01}$  and  $LP_{11}$  mode excitations utilizing a binary phase plate. By balancing the position of the binary phase plate from the focal point of the input beam, distorted modes were created to energize both  $LP_{01}$  and  $LP_{11}$  modes in the CG at various  $P_{LP_{01}}:P_{LP_{11}}$  mode intensity proportions. To the best of our knowledge, this work is the first to report on experimental and theoretical examination of non-uniform grating structure in few-mode fibers. The discovery in this examination has opened up another viewpoint in intermodal

interference in few-mode fiber devices and its potential applications in optical filters, multi-wavelength lasers, and sensors.

These discoveries are noteworthy steps in the advancement and characterization of more intricate grating structures on single mode and few-mode fibers. This study will add to the understanding and design of complex FBG-based FP resonator structures.

This work has taken a far-reaching novel approach (i.e. opto-elastic properties) to the characterization of FBG based FPR under embedded conditions concentrating on acousto-ultrasonic-, temperature-, and pressure-induced stress in both simulation and experiment. In particular, relating analytical and numerical examinations to analyse the change in material properties inside the fiber core, and the subsequent change in the FBG signal. In addition, LP<sub>01</sub>–LP<sub>11</sub> cross mode interference in a solitary chirped grating (CG) manufactured in few-mode fiber was studied and shown by both the simulation and experiment. Specific contributions were unremarkable but notable changes in the index of refraction from the centre to the edge of the optical fiber core, and the visualization of property changes throughout the optical fiber framework.

## **6.2 Future works**

We have fabricated a few FBG-based FPR optical devices that are exceptionally sensitive to pressure, acoustics, and temperature with preferences in simple creation process conditions, minute cavity size, and higher simultaneous sensitivity. Future studies are necessary to establish the difference between experimental and theoretical study for the concluding FBG-based FPR, which probably is in the frame of theoretical study and an experimental probe. A few suggestions for future probe are provided.

The wide frequency response and high sensitivity of short cavity FPR produced in SMF stands a chance to be enhanced further by developing suitable modifications in

sensor design and instrumentation. The reduction of hydroxyl (OH) content and stress modification in the fiber throughout the ultraviolet illumination erasure method, which may contribute to the ambiguity. The opto-elastic properties of the proposed device can be theoretically investigated by using numerical method. The study of opto-elastic properties of the PCF-cavity FBG FP resonator can provide more insight in the design of complex FPR structures.

In future, the simulation of the opto-elastic properties of FBG-based FPR cavities can be enhanced with the goal that it will verify and support the theories on the cavity responses of FBG-based FPRs to wavelength, acousto-ultrasonic, temperature, and pressure. This would include the incorporation of the distinctive FBG length and cavity size used to produce the FPRs. Particularly, to anticipate and confirm the cavity response to the reported acousto-ultrasonic, temperature, and pressure amplification of the individual FBG based FPR. The realization of the opto-elastic model may encourage the prediction of the specification of the FBG-based FPR's cavity prerequisite for various sensitivities. As such, the performance of FBG-based FPR's cavity and the result of future experiments may be improved.

Latest methods including multi-level modulation, mode-division multiplexing, and space-division multiplexing have attracted expanding research enthusiasm to accomplish vast optical communication limit, because of the constantly increasing demand for high-speed optical fiber communications. In contrast with the ordinary single-mode fiber, FMF bolsters multiplexing transmission of spatial modes. To our knowledge, taking into account the literature, no work has been done on  $LP_{01}$ – $LP_{11}$  cross-mode interference saw in a solitary CG imprinted in few-mode fiber, to date.  $LP_{01}$ – $LP_{11}$  cross-mode interference phenomenon has been witnessed and shown by both simulation and experiment in this thesis. However, there may be no simple approach,

which can unequivocally portray the cross-mode coupling component in CG resonance. Numerical simulation can furnish an additional exact estimation of the spectral characteristics of the CG made in TMF. A distinctive numerical model can be used to clarify this phenomenon. Another recommendation is to study mode coupling among  $LP_{01}$  and other higher-order modes, for example,  $LP_{21}$  and  $LP_{02}$  modes.

University of Malaya



## REFERENCES

- Aben, H., & Guillemet, C. (1993). *Photoelasticity of Glass*. Berlin: Springer-Verlag.
- Agrawal, G. (2007). *Nonlinear Fiber Optics*. Fourth Edition, San Francisco: Academic Press.
- Alemohammad, S. H. (2010). Development of optical fiber-based sensing devices using laser microfabrication methods (Doctoral dissertation). Retrieved from <https://uwspace.uwaterloo.ca/handle/10012/5091>
- Ali, M. M., Jung, Y., Lim, K.S., Islam, M.R., Alam, S.U., Richardson, D.J., & Ahmad, H. (2015a). Characterization of mode coupling in few-mode FBG with selective mode excitation. *IEEE Photon. Technol. Lett.*, 27(16), 1713-1716.
- Ali, M. M., Islam, M. R., Lim, K-S., Gunawardena, D. S., Yang, H-Z., & Ahmad, H. (2015b). PCF-cavity FBG Fabry-Perot resonator for simultaneous measurement of pressure and temperature. *IEEE Sensors Journal*, 15(12), 6921-6925.
- Andrews, J.P., & Pulfrey, R.E. (1999). US Patent No.5907403, Washington, DC: U.S. Patent and Trademark Office.
- Aref, S.H., Latifi, H., Zibaii, M.I., & Afshari, M. (2007). Fiber optic Fabry-Perot pressure sensor with low sensitivity to temperature changes for downhole application. *Opt. Commun.*, 269, 322–330.
- Arregui, F.J., Cooper, K.L., Liu, Y., Matias, I.R., & Claus, R.O. (2000). Optical fiber humidity sensor with a fast response time using the ionic self-assembly method. *IEICE T. Electron.*, E83-C, 360–365.
- Arregui, F.J., Liu, Y., Matias, I.R., & Claus, R.O. (1999). Optical fiber humidity sensor using a nano Fabry-Perot cavity formed by the ionic self-assembly method. *Sens. Actuat. B Chem.*, 59, 54–59.
- Bae, H., & Yu, M. (2012). Miniature Fabry-Perot pressure sensor created by using UV-molding process with an optical fiber based mold. *Opt. Express*, 20, 14573–14583.
- Bal, H.K. (2011). Optical Fiber Refractive Index, Voltage and Strain Sensors: Fabrication and Applications (Doctoral dissertation). Retrieved from [http://vuir.vu.edu.au/18968/1/Harpreet\\_Kaur\\_Bal.pdf](http://vuir.vu.edu.au/18968/1/Harpreet_Kaur_Bal.pdf)

- Balmforth, W., & Holland, A.J., (1945). The stress optical coefficient of glasses. *J. Soc. Glass Technology*, 29.
- Banerjee, K.R. (1927). Theory of Photoelasticity. *Indian J. Physics*, 2.
- Beard, P.C., & Mills, T.N. (1996). Extrinsic optical-fiber ultrasound sensor using a thin polymer film as a low-finesse Fabry-Perot interferometer. *Appl. Opt.*, 35, 663–675.
- Berezina, E.E., & Golynja, V.S. (1972). Dispersion in optical stress coefficients. *Sov. Journal of Optical Technology*, 40.
- Berthold, J.W., & Roman, G.W. (2001). US 6289143 B1, Washington, DC: U.S. Patent and Trademark Office.
- Betz, D. C., Thursby, G., Culshaw, B., & Staszewski, W. J. (2003). Acousto-ultrasonic sensing using fiber Bragg gratings. *Smart Mater. Struct.*, 12, 122–128.
- Bornand, C., Yang, M., Wang, Z., Ji, Z., & Al-Kutubi, M. (2005). *Hardware structure of tangible acoustic interface systems*. In Pham, D. T., Eklukhri, E. E., Soroka, A. J. (Eds.), *Intellegent Production Machines and Systems*. Elsevier Science Press, 493-496.
- Boyd, J.T., Abeysinghe, D., Dasgupta, S., & Jackson, H. (2005). U.S. Patent No. 6925213 B2. Washington, DC: U.S. Patent and Trademark Office.
- Bremer, K., Leen, G., Lewis, E., Moss, B.J., Lochmann, S., & Mueller, I. (2011). US Patent No. 20110190640, Washington, DC: U.S. Patent and Trademark Office.
- Brewster, D. (1816). On the Communication of the Structure of Doubly Refracting Crystals to Glass, Muriate of Soda, Fluor Spar, and Other Substances, by Mechanical Compression and Dilatation. *Philosophical Transactions of the Royal Society of London*, 106(0), 156-178.
- Brillouin, L. (1922). Diffusion de la lumiere et des rayons X par un corps transparent homogene, influence de l'agitation thermique. *Ann. Phys.*, 17, 88-122.
- Chana, K.S., Kidd, S.R., Matthews, I.W., Barton, J.S., & Jones, J.D.C. (1992). Optical fibre Fabry-Perot interferometers for calorimetric heat transfer gauges. In *proceedings of the 11th International Symposium on Measuring Techniques for*

*Transonic and Supersonic Flows in Cascades and Turbomachines*, Munich, Germany, 1–13.

- Chang, C.-C., & Sirkis, J. (1997). Absolute phase measurement in extrinsic Fabry-Perot optical fiber sensors using multiple path-match conditions. *Exp. Mech.*, *37*, 26–32.
- Chang, D.B., & Vali, V. US Patent No. 5361383, Washington, DC: U.S. Patent and Trademark Office.
- Chen, J.-H., Zhao, J.-R., Huang, X.-G., & Huang, Z.-J. (2010). Extrinsic fiber-optic Fabry-Perot interferometer sensor for refractive index measurement of optical glass. *Appl. Opt.*, *49*, 5592–5596.
- Chen, L.H., Ang, X.M., Chan, C.C., Shaillender, M., Neu, B., Wong, W.C., Zu, P., & Leong, K.C. (2012). Layer-by-layer (Chitosan/Polystyrene Sulfonate) membrane-based Fabry-Perot interferometric fiber optic biosensor. *IEEE J. Sel. Top. Quantum Electron.*, *18*, 1457–1464.
- Chen, L.H., Chan, C.C., Menon, R., Balamurali, P., Wong, W.C., Ang, X.M., Hua, P.B., Shaillendere, M., Neu, B.,...Zu, P. (2013). Fabry-Perot fiber-optic immunosensor based on suspended layer-by-layer (chitosan/polystyrene sulfonate) membrane. *Sens. Actuats B Chem.*, *188*, 185–192.
- Chen, L.H., Li, T., Chan, C.C., Menon, R., Balamurali, P., Shaillender, M., Neu, B., Ang, X.M., Zu, P.,...Wong, W.C. (2012). Chitosan based fiber-optic Fabry-Perot humidity sensor. *Sens. Actuats B Chem.*, *169*, 167–172.
- Chmielewska, E., Urbańczyk, W., & Bock, W. J. (2003). Measurement of pressure and temperature sensitivities of a Bragg grating imprinted in a highly birefringent side-hole fiber. *Appl. Opt.*, *42*(31), 6284–6291.
- Choi, H.Y., Park, K.S., Park, S.J., Paek, U.-C., Lee, B.H., & Choi, E.S. (2008). Miniature fiber-optic high temperature sensor based on a hybrid structured Fabry-Perot interferometer. *Opt. Lett.*, *33*, 2455–2457.
- Chitchebakov, A.A. (1997). Reflective Interferometric Fibre Optic Sensors (Doctoral dissertation). Retrieved from [http://ujdigispace.uj.ac.za/bitstream/handle/10210/5707/A.A.%20CHTCHERBAKOV\\_1997\\_PHD.pdf?sequence=3](http://ujdigispace.uj.ac.za/bitstream/handle/10210/5707/A.A.%20CHTCHERBAKOV_1997_PHD.pdf?sequence=3)
- Coker, E.G., & Filon, L.N.G., (1957). *A Treatise on Photoelasticity*. 2nd eds.

- Coviello, G., Finazzi, V., Villatoro, J., & Pruneri, V. (2009). Thermally stabilized PCF-based sensor for temperature measurements up to 1000 °C. *Opt. Exp.*, *17*, 21551–21559.
- Cox, B.T., Zhang, E.Z., Laufer, J.G., & Beard, P.C. (2004). Fabry Perot polymer film fibre-optic hydrophones and arrays for ultrasound field characterisation. *J. Phys.: Conf. Ser.*, *1*, 32–37.
- Cusano, A., Iadicicco, S., Campopiano, M., Giordano, A., & Cutolo, A. (2005). Thinned and micro-structured fibre Bragg gratings: Towards new all-fibre high-sensitivity chemical sensors. *J. Opt. A: Pure Appl. Opt.*, *7*(12), 734-741.
- Dai, L., Wang, M., Cai, D., Rong, H., Zhu, J., Jia, S., & You, J. (2013). Optical fiber Fabry-Pérot pressure sensor based on a polymer structure. *IEEE Photon. Tech. Lett.*, *25*, 2505–2508.
- Dakin, P., Wade, C.A., & Henning, M. (1984). Novel optical fiber hydrophone array using a single laser source and detector. *Electron. Lett.*, *20*, 53–54.
- Davis, C.C., & Wagreich, R.B. (1999). US Patent No. 5982174, Washington, DC: U.S. Patent and Trademark Office.
- Davis, C.M. (1986). US Patent No. 4755668, Washington, DC: U.S. Patent and Trademark Office.
- Davis, D. D., Gaylord, T. K., Glytsis, E. N., Kosinski, S. G., Mettler, S. C., & Vengsarkar, A. M. (1998). Long-period fibre grating fabrication with focused CO<sub>2</sub> laser beams. *Electron. Lett.*, *34*(3), 302-303.
- De Vries, M., Arya, V., Meller, S., Masri, S.F., & Claus, R.O. (1997). Implementation of EFPI-based optical-fiber sensor instrumentation for the NDE of concrete structures. *Cement. Concrete Commun.*, *19*, 69–79.
- Degiorgio, V., & Cristiani, I. (2014). *Photonics: A Short Course*. 2nd edition. Undergraduate Lecture Notes in Physics (p.244). Switzerland: Springer International Publishing AG.
- Deng, J. (2004). Development of Novel Optical Fiber interferometric Sensors with High Sensitivity for Acoustic Emission Detection (Doctoral dissertation). Retrived from <https://theses.lib.vt.edu/theses/available/etd-10162004-233005/unrestricted/ETD-final-re01.pdf>

- Dong, B., Han, M., Sun, L., Wang, J., Wang, Y., & Wang, A. (2008). Sulfur hexafluoride-filled extrinsic Fabry-Pérot interferometric fiber-optic sensors for partial discharge detection in transformers. *IEEE Photon. Tech. Lett.*, *20*, 1566–1568.
- Donlagic, D., Cibula, E., & Pinet, É. (2010). US Patent No. 7684657, Washington, DC: U.S. Patent and Trademark Office.
- Du, Y., Qiao, X., Rong, Q., Yang, H., Feng, D., Wang, R., Hu, M., & Feng, Z. (2014). A miniature Fabry-Pérot interferometer for high temperature measurement using a double-core photonic crystal fiber. *IEEE Sens. J.*, *14*, 1069–1073.
- Eggleton, B., Kerbage, C., Westbrook, P., Windeler, R., & Hale, A. (2001). Microstructured optical fiber devices. *Opt. Express*, *9*(13), 698–713.
- Elster, J.L., Davis, R.M., & Jones, M.E. (2002). US Patent No. 6341185 B1. Washington, DC: U.S. Patent and Trademark Office.
- Erdogan, T. (1997a). Cladding-mode resonances in short- and long-period fiber grating filters. *Journal of the Optical Society of America A*, *14*, 1760-1773.
- Erdogan, T. (1997b). Fiber grating spectra. *J. Lightwave Technol.*, *15*(8), 1277-1294.
- Ezbiri, A., & Tatam, R.P. (1996). Interrogation of low finesse optical fibre Fabry-Pérot interferometers using a four wavelength technique. *Measur. Sci. Technol.*, *7*, 117–120.
- Fabry, C., & Pérot, A. (1897). Sur les franges des lames minces argentées et leur application à la mesure de petites épaisseurs d'air. *Ann. Chim. Phys.*, *12*, 459–501.
- Fang, J.X., Taylor, H.F., & Choi, H.S. (1998). Fiber-optic Fabry-Perot flow sensor. *Microw. Opt. Techn. Lett.*, *18*, 209–211.
- Farahi, F. (1991). Fiber-optic interferometric point thermometer. *Fiber Integr. Opt.*, *10*, 205–212.
- Farahi, F., Newson, T.P., Jones, J.D.C., & Jackson, D.A. (1988). Coherence multiplexing of remote fibre Fabry-Perot sensing system. *Opt. Commun.*, *65*, 319–331.

Filon, F.N.G. (1907). On the Dispersion in Artificial Double Refraction. *Phil. Trans.*, *A207*.

FISO Technologies Inc. (2014 March 25) Retrieved from <http://www.fiso.com/>

Foote, P. D. (1995). Optical fibre Bragg grating sensors for aerospace smart structure. In *proceedings of Optical Fibre Gratings and Their Applications*, London, UK: IEE Colloquium (Digest), (17), 14/1-14/6.

Frazaõ, O., Baptista, J.M., Santos, J.L., Kobelke, J., & Schuster, K. (2009). Refractive index tip sensor based on Fabry-Perot cavities formed by a suspended core fibre. *J. Eur. Opt. Soc. Rapid*, *4*, 09041.

Frazaõ, O., Silva, S.F., Viegas, J., Baptista, J.M., Santos, J.L., & Roy, P. (2010). A hybrid Fabry-Perot/Michelson interferometer sensor using a dual asymmetric core microstructured fiber. *Measur. Sci. Technol.*, *21*, 025205:1–025205:5.

Gander, M.J., MacPherson, W.N., Barton, J.S., Reuben, R.L., Jones, J.D.C., Stevens, R., Chana, K.S., Anderson, S.J., & Jones, T.V. (2003). Embedded micromachined fibre-optic Fabry-Perot pressure sensors in aerodynamics applications. *IEEE Sens. J.*, *3*, 102–107.

Gangopadhyay, T.K. (2004). Prospects for Fibre Bragg Gratings and Fabry-Perot Interferometers in fibre-optic vibration sensing. *Sens. Actuats A Phys.*, *113*, 20–38.

Gangopadhyay, T.K., Chakravorti, S., Bhattacharya, K., & Chatterjee, S. (2005). Wavelet analysis of optical signal extracted from a non-contact fibre-optic vibration sensor using an extrinsic Fabry-Perot interferometer. *Measur. Sci. Technol.*, *16*, 1075–1082.

Gangopadhyay, T.K., Chakravorti, S., Chatterjee, S., & Bhattacharya, K. (2006). Time-frequency analysis of multiple fringe and nonsinusoidal signals obtained from a fiber-optic vibration sensor using an extrinsic Fabry-Pérot interferometer. *J. Lightw. Technol.*, *24*, 2122–2131.

Gao, Z.-f., Yan-liang, D., Bao-chen, S., & Xiu-mei, J. (2007). Strain monitoring of railway bridges using optic fiber sensors. *J. Qual. Mainten. Eng.*, *13*, 186–197.

Giallorenzi, T. G., Bucaro, J. A., Dandridge, A., Siegel Jr. G. H., Cole, J. H., Rashleigh, S. C., & Priest, R. G. (1982). Optical fiber sensor technology. *IEEE Journ. of Quant. Elect.*, *18*, 625-665.

- Gibler, W.N., Jeffers, L.A., Lopushansky, R.L., & Gillham, F.J. (2010). US Patent No. 7,782,465 B2, Washington, DC: U.S. Patent and Trademark Office.
- Giles, I., Obeysekara, A., Poletti, F., & Richardson, D. (2012). Method to visualise and measure individual modes in a few moded fibre. In *proceedings of European Conference and Exhibition on Optical Communication*.
- Gillooly, A. (2011). Photosensitive fibers: growing gratings. *Nat. Photonics*, 5, 468–469.
- Gloge, D. (1971). Weakly Guiding fibers. *Applied Optics*, 10, 2252-2258.
- Gong, Y., Rao, Y.-J., Guo, Y., Ran, Z.-L., & Wu, Y. (2009). Temperature-insensitive micro Fabry–Pérot strain sensor fabricated by chemically etching er-doped fiber. *IEEE Photon. Tech. Lett.*, 21, 1725–1727.
- Grubsky, V., & Feinberg, J. (2006). Fabrication of axially symmetric long-period fiber gratings with a carbon dioxide laser. *IEEE Photon. Technol. Lett.*, 18(21), 2299-2298.
- Han, J., & Neikirk, D.P. (1996). Deflection behavior of Fabry-Perot pressure sensors having planar and corrugated membrane. In *proceedings of the SPIE 2882, Micromachined Devices and Components II*, 79–90.
- Hare, D.A., Moore, T.C., Sr. (2000). Characteristics of Extrinsic Fabry-Perot Interferometric (EFPI) Fiber-Optic Strain Gages (Technical Report: NASA Langley Technical Report Server). Retrieved from <http://dl.acm.org/citation.cfm?id=886160>
- Herzfeld, K.J. (1928). Theory of forced double refraction. *Journal of the Optical Society of America*, 17.
- Hill, K. O., Fujii, Y., Johnson, D. C., & Kawasaki, B. S. (1978). Photosensitivity in optical fiber waveguides: Application to reflection filter fabrication. *Appl. Phys. Lett.*, 32, 64–649.
- Hill, KO., Bilodeau, MF., Johnson, DC., & Albert, J. (1993). Bragg gratings fabricated in monomode photosensitive optical fiber by UV exposure through a phase mask. *Appl. Phys. Lett.*, 62, 1035-1037.

- Hocker, G. B. (1979). Fiber-optic sensing of pressure and temperature. *Applied Optics*, 18, 1445–1448.
- Hogg, W. D., Janzen, D., Valis, T. & Measures, R. M. (1991). Development of a fiber Fabry-Perot strain gauge. In *proceedings of SPIE 1588, Fiber Optic Smart Structures and Skins IV*, 300-307.
- Huang, W. P. (1994). Coupled-mode theory for optical waveguides: an overview. *J. Opt. Soc. Am. A*, 11(3), 963-983.
- Igarashi, K., Souma, D., Tsuritani, T. (2014b). Selective mode conversion using phase plates for 10-mode fiber. In *proceedings of 2014 European Conference on Optical Communication (ECOC)*, 1-3.
- Igarashi, K., Souma, D., Tsuritani, T., & Morita, I. (2014a). Performance evaluation of selective mode conversion based on phase plates for a 10-mode fiber. *Opt. Express*, 22(7), 20881-20893.
- James, S. W., Dockney, M. L., & Tatam, R. P. (1996). Simultaneous independent temperature and strain measurement using in-fibre Bragg grating sensors. *Elect. Lett.*, 32, 1133-1134.
- J. Jamin. (1856). *Pogg. Ann.*, 98, P.345
- Jedrzejewska-Szczerska, M., Gnyba, M., & Kosmowski, B. (2011). Low-coherence fiber-optic interferometric sensors. *Acta Phys. Pol. A*, 120, 621–662.
- Jędrzejewska-Szczerska, M., Kosmowski, B.B., & Hyspser, R. (2009). The optimal construction of a fiber-optic Fabry-Perot interferometer. *Photon. Lett. Pol.*, 1, 61–63.
- Jeunhomme, L. B. (1989). *Single-mode fibre optics: principles and applications*. CRC Press.
- Jia, P., & Wang, D. (2013). Temperature-compensated fiber optic Fabry-Perot accelerometer based on the feedback control of the Fabry-Perot cavity length. *Chin. Opt. Lett.*, 11, 040601–040605.
- Jia, P.G., & Wang, D.H. (2012). Self-calibrated non-contact fibre-optic Fabry-Perot interferometric vibration displacement sensor system using laser emission



frequency modulated phase generated carrier demodulation scheme. *Measur. Sci. Technol.*, *23*, 115201:1–115201:9.

Jiang, M., & Gerhard, E. (2001). A simple strain sensor using a thin film as a low-finesse fiber-optic Fabry-Perot interferometer. *Sens. Actuat. A Phys.*, *88*, 41–46.

Jiang, M., Li, Q.-S., Wang, J.-N., Yao, W.-G., Jin, Z., Sui, Q., Shi, J., Zhang, F., Jia, L., & Dong, W.-F. (2013). Optical response of fiber-optic Fabry-Perot refractive-index tip sensor coated with polyelectrolyte multilayer ultra-thin films. *J. Lightw. Technol.*, *31*, 2321–2326.

Jin, L., Guan, B., & Wei, H. (2013). Sensitivity characteristics of Fabry-Perot pressure sensors based on hollow-core microstructured fibers. *J. Lightwave Technol.*, *31*(15), 2526–2532.

Jin, X., Huang, X., & Chen, L. (2013). An extrinsic fabry-perot optical fiber sensor based on nano-magnetic fluid. *Fiber Integr. Opt.*, *32*, 233–241.

John, D., Sridhar, K., & Achenbach, J.D. (1997). Response of an embedded fiber optic ultrasound sensor. *J. Acoust. Soc. Am.*, *101*, 257–263.

Jorge, P. A., Silva, S. O., Gouveia, C., Tafulo, P., Coelho, L., Caldas, P., . . . Frazão, O. (2012). Fiber Optic-Based Refractive Index Sensing at INESC Porto. *Sensors*, *12*(12), 8371–8389.

Jules Célestin, J. (1856). Neuer Interferential-Refractor. *Ann. Phys. Chem.*, *174*(6): 345–349.

Kanellopoulos, S. E., Handerek, V. A., & Rogers, A. J. (1995). Simultaneous strain and temperature sensing with photogenerated in-fiber gratings. *Opt. Lett.*, *20*(3), 333–335.

Kao, T.W., & Taylor, H.F. (1996). High-sensitivity intrinsic fiber-optic Fabry-Perot pressure sensor. *Opt. Lett.*, *21*, 615–617.

Kashyap, R. (1999). *Fiber Bragg Gratings*. San Diego: Academic Press.

Kashyap, R. (2009). *Fiber Bragg Gratings*, 2nd ed., Amsterdam, the Netherlands: Academic Press: Elsevier.

- Kerr, J., (1888). Experiments of the birefringent action of strained glass. *Phil. Mag.*, 26.
- Kersey, A.D., Putnam, M.A., Fernald, M.R., Brucato, R.N., & Sirkis, J.S. (2007). U.S. Patent 7209606, Washington, DC: U.S. Patent and Trademark Office.
- Kersey, A.D., Putnam, M.A., Fernald, M.R., Brucato, R.N., & Sirkis, J.S. (2005). U.S. Patent 6898338, Washington, DC: U.S. Patent and Trademark Office.
- Kidd, S. R., Sinha, P. G., Barton, J. S., & Jones, J. D. C. (1991). Fibre optic Fabry-Perot sensors for high speed heat transfer measurements. In *Proceedings of SPIE, 1504*, 180-190.
- Kim, C. S., Han, Y., Lee, B. H., Han, W. T., Paek, U. C., & Chung, Y. (2000). Induction of the refractive index changes in B-doped optical fibers through relaxation of the mechanical stress. *Opt. Commun.*, 185(4-6), 337-342.
- Kim, D.-H., Han, J.-H., & Lee, I. (2005). Vibration measurement and flutter suppression using patch-type EFPI sensor system. *Int. J. Aeronaut. Space Sci.*, 6, 17-26.
- Kim, M.G., Park, J., Kang, S.-W., & Sohn, B.-K. (1997). Fiber optic Fabry-Perot pressure sensor with the Si<sub>3</sub>N<sub>4</sub>/SiO<sub>2</sub>/Si<sub>3</sub>N<sub>4</sub> diaphragm fabricated using micromachining technology. In *proceedings of the SPIE 3242, Smart Electronics and MEMS*, 347-353.
- Kim, P. H., Doolin, C., Hauer, B. D., MacDonald, A.J.R., Freeman, M. R., Barclay, P. E., & Davis, J.P. (2013). Nanoscale torsional optomechanics', *Applied Physics Letters*, 102(5), 053102-0531105.
- Kogelnik, H. (1979). Filter response of nonuniform almost-periodic structures. *The Bell System Technical Journal*, 55, 109-125.
- Kou, J.-L., Feng, J., Ye, L., Xu, F., & Lu, Y.-Q. (2010). Miniaturized fiber taper reflective interferometer for high temperature measurement. *Opt. Express*, 18, 14245-14250.
- Kreger, S., Calvert, S., & Udd, E. (2002). High pressure sensing using fiber Bragg gratings written in birefringent side hole fiber. In *Proceedings of 15th Int. Conf. Opt. Fiber Sens., Proc. SPIE.*, 1, 355-358.

- Lai, C.-C., Lee, W.-Y., & Wang, W.-S. (2003). Gamma radiation effect on the FiberFabry-Perot interference sensor. *IEEE Photon. Tech. Lett.*, *15*, 1132–1134.
- Lai, C.W., Lo, Y.L., Yur, J.P., & Chuang, C.H. (2012). Application of fiber Bragg grating level sensor and Fabry-Perot pressure sensor to simultaneous measurement of liquid level and specific gravity. *IEEE Sens. J.*, *12*, 827–831.
- Lai, C.-W., Yur, J.-P., Liao, C.-C., & Lo, Y.-L. (2011). Study on optical fiber pressure sensors with temperature-insensitivity based on Fabry-Pérot interferometry. *Recent Pat. Signal Process.*, *1*, 48–54.
- Lawrence, C.M., Nelson, D.V., Bennett, T.E., & Spingarn, J.R. (1998). An embedded fiber optic sensor method for determining residual stresses in fiber-reinforced composite materials. *J. Int. Mat. Syst. Str.*, *9*, 788–799.
- Lee, B.H., Kim, Y.H., Park, K.S., Eom, J.B., Kim, M.J., Rho, B.S., & Choi, H.Y. (2012). Interferometric fiber optic sensors. *Sensors*, *12*, 2467–2486.
- Lee, C.E., & Taylor, H.F. (1988). Interferometric optical fiber sensors using internal mirrors. *Electron. Lett.*, *24*, 193–195.
- Lee, C.E., & Taylor, H.F. (1991). Fiber-optic Fabry-Pérot temperature sensor using a low-coherence source. *J. Lightw. Technol.*, *9*, 129–134.
- Lee, C.E., Atkins, R.A., & Taylor, H.F. (1988). Performance of a fiber-optic temperature sensor from –200 to 1050 °C. *Opt. Lett.*, *13*, 1038–1040.
- Lee, C.E., Taylor, H.F., Markus, A.M., & Udd, E. (1989). Optical-fiber Fabry-Perot embedded sensor. *Opt. Lett.*, *14*(21): 1225–1227.
- Lee, C.-L., Hsu, J.-M., Horng, J.-S., Sung, W.-Y., & Li, C.-M. (2013). Microcavity Fiber Fabry-Pérot interferometer with an embedded golden thin film. *IEEE Photon. Tech. Lett.*, *25*, 833–836.
- Lee, H. W., Liu, Y., & Chiang, K. S. (2008). Writing of long-period gratings in conventional and photonic-crystal polarization-maintaining fibers by CO<sub>2</sub>-laser pulses. *IEEE Photon. Technol. Lett.*, *20*(2), 132-134.
- Lee, S.B., Yu, C.M., Ciarlo, D.R., & Sheem, S.K. (1994). Micromachined Fabry-Perot interferometric pressure sensor for automotive combustion engine. In *proceedings of the Sensors Expo 94*, Cleveland, OH, USA, 1–6.

- Lee, Y.-S., Lim, K.-S., Islam, M. R., Lai, M.-H. & Ahmad, H. (2016). Dynamic LP<sub>01</sub>-LP<sub>11</sub> Mode Conversion by a Tilted Binary Phase Plate. *IEEE/OSA Journal of Lightwave Technology*, PP (99): 1-7.
- Legoubin, S., Boj, S., Delevaque, E., Douay, M., Bernage, P., & Niay, P. (1995). Free spectral range variations of grating-based Fabry–Perot filters photowritten in optical fibers. *J. Opt. Soc. Am. A*, 12(8), 1687.
- Legoubin, S., Boj, S., Delevaque, E., Douay, M., Bernage, P., & Niay, P. (1995). Free spectral range variations of grating-based Fabry–Perot filters photowritten in optical fibers. *J. Opt. Soc. Am. A*, 12(8), 1687-1694.
- Leilabady, P.A., Jones, J.D. C., & Jackson, D.A. (1985). Monomode fibre optic interferometric techniques in flow velocity measurement. *Opt. Acta Int. J. Opt.*, 32, 233–240.
- Liao, C.R., Hu, T.Y., & Wang, D.N. (2012). Optical fiber Fabry-Perot interferometer cavity fabricated by femtosecond laser micromachining and fusion splicing for refractive index sensing. *Opt. Express*, 20, 22813–22818.
- Lim, K. S., Yang, H.Z., Becir, A., Lai, M. H., Ali, M. M., Qiao, X. & Ahmad, H. (2013). Spectral analysis of bent fiber Bragg gratings: theory and experiment. *Opt. Lett.*, 38(21), 4409-4412.
- Lim, K-S., Islam, M. R., Lee, Y-S., Yang, H-Z., & Ahmad, H. (2016). LP<sub>01</sub>-LP<sub>11</sub> cross mode interference in a chirped grating inscribed in two-mode fiber. *IEEE Journal of Quantum Electronics*, 52(6), 6600206.
- Liu, H., Miller, D.W., & Talnagi, J. (2002). Gamma radiation resistant Fabry–Perot fiber optic sensors. *Rev. Sci. Instrum.*, 73, 3112.
- Liu, J., Sun, Y., & Fan, X. (2009). Highly versatile fiber-based optical Fabry-Pérot gas sensor. *Opt. Express*, 17, 2731–2738.
- Liu, N., Hui, J., Sun, C., Dong, J., Zhang, L., & Xiao, H. (2006). Nanoporous zeolite thin film-based fiber intrinsic Fabry-Perot interferometric sensor for detection of dissolved organics in water. *Sensors-Basel*, 6, 835–847.
- Liu, T., & Han, M. (2012). Analysis of  $\pi$ -Phase-Shifted Fiber Bragg Gratings for Ultrasonic Detection. *IEEE Sensors Journal*, 12(7), 2368-2373.

- Liu, X., Iordachita, I.I., He, X., Taylor, R.H., & Kang, J.U. (2012). Miniature fiber-optic force sensor based on low-coherence Fabry-Pérot interferometry for vitreoretinal microsurgery. *Biomed. Opt. Express*, 3, 1062–1076.
- Lopushansky, R.L., & Berthold, J.W. (2009). US Patent No. 7492463, Washington, DC: U.S. Patent and Trademark Office.
- Lü, T., & Yang, S. (2007). Extrinsic Fabry-Perot cavity optical fiber liquid-level sensor. *Appl. Opt.*, 46, 3682–3687.
- Ludwig, M. (1892). Ueber einen Interferenzrefraktor. *Zeitschrift für Instrumentenkunde*, 12, 89–93.
- Lv, R.-q., Zhao, Y., Wang, D., & Wang, Q. (2014). Magnetic fluid-filled optical fiber Fabry-Perot sensor for magnetic field measurement. *IEEE Photon. Tech. Lett.*, 26, 217–219.
- Ma, J., Xuan, H., Ho, H.L., Jin, W., Yang, Y., & Fan, S. (2013). Fiber-optic Fabry-Pérotacoustic sensor with multilayer grapheme diaphragm. *IEEE Photonic Tech. Lett.*, 25, 932–935.
- Machavaram, V.R., Badcock, R.A., & Fernando, G.F. (2007). Fabrication of intrinsic fibre Fabry-Perot sensors in silica fibres using hydrofluoric acid etching. *Sens. Actuat. A-Phys.*, 138, 248–260.
- Marcuse, D. (1976). Field deformation and loss caused by curvature of optical fibers. *J. Opt. Soc. Am.*, 66(4), 311–320.
- Maxwell, J.C., (1853). On the equilibrium of elastic solids. *Trans. Roy. Soc. Edinb.*, 20.
- Mach Z. E. (1892). *Building instruments*, 12, P.89
- McCall, M. (2000). On the application of coupled mode theory for modelling fiber bragg gratings. *J. Lightwave Technol.*, 18(2), 236-242.
- Meltz, G., Morey, W. W., & Glen, W. H. (1989). Formation of Bragg gratings in optical fibers by a transverse holographic method, *Opt. Lett.* 14, 823-825.
- Menadier, C., Kissenger, C., & Adkins, H. (1967). The fotonic sensor. *I&CS Control Tech. Eng.*, 40, 114–114.

- Michelson, A. A., & Morley, E. W. (1887). On the relative motion of the earth and the luminiferous ether. *American Journal of Science*, 34(203): 333–345.
- Mitschke, F. M. (2005). *Glasfasern: Physik und Technologie*. Heidelberg: Elsevier, Spectrum, Akad. Verl.
- Morey, W.W., Bailey, T. J., Glenn, W. H., & Meltz, G. (1992). Fiber Fabry-Perot interferometer using side exposed fiber Bragg Gratings. In *proceedings of OFC, WA2*, 96.
- Mozafari, M., Sanjabi, Z., & Granpayeh, N. (2008). Design and fabrication of piezo-optical Fabry-Perot voltage sensor. In *proceedings of the Avionics, Fiber-Optics and Photonics Technology*, 39–40.
- Mueller, H. (1938). The Theory of Photoelasticity. *J. Am. Ceramics*, 21.
- Mitschke, F. (2010). *Fiber Optics: Physics and Technology*. Heidelberg, Springer.
- Nye, J. F., (1985). *Physical Properties of Crystals*. New York: Oxford University Press, 1985.
- Oh, K.D., Ranade, J., Arya, V., Wang, A., & Claus, R.O. (1997). Optical fiber Fabry-Perot interferometric sensor for magnetic field measurement. *IEEE Photon. Tech. Lett.*, 9, 797–799.
- Oh, K.D., Wang, A., & Claus, R.O. (2004). Fiber-optic extrinsic Fabry-Perot dc magnetic field sensor. *Opt. Lett.*, 29, 2115–2117.
- Okamoto, K. (2006). *Chapter 4 - Coupled mode theory*. In K. Okamoto (Eds.), *Fundamentals of optical waveguides*. Amsterdam: Elsevier, Academic Press.
- Opilski, Z., Pustelny, T., Maciak, E., Bednorz, & M., Stolarczyk, A. Jadamiec. (2005). Investigations of optical interferometric structures applied in toxic gas sensors. *Bull. Pol. Ac.: Tech.*, 53, 151–156.
- Park, H.S., Thursby, G., & Culshaw, B. (2005). Detection of laser-generated ultrasound based on phase demodulation technique using a fibre Fabry-Perot interferometer. *Measur. Sci. Technol.*, 16, 1261–1266.

- Peng, W., Zhang, X., Gong, Z., & Liu, Y. (2013). Miniature fiber-optic strain sensor based on a hybrid interferometric structure. *IEEE Photon. Tech. Lett.*, 25, 2385–2388.
- Pepe, G. Davis, Bush, J., & Gregory, S. Maurer. (1998). Fiber optic displacement sensor. In *proceedings of the SPIE 3489, Fourth Pacific Northwest Fiber Optic Sensor Workshop*, 1–5.
- Pérennès, F., Beard, P.C., & Mills, T.N. (1999). Analysis of a low-finesse Fabry-Perot sensing interferometer illuminated by a multimode optical fiber. *Appl. Opt.*, 38, 7026–7034.
- Petuchowski, S., Giallorenzi, T., & Sheem, S. (1981). A sensitive fiber-optic Fabry-Perot interferometer. *J. Quantum Electron.*, 17(11), 2168-2170.
- Pullteap, S. (2008). Development of an extrinsic dual-cavity fiber Fabry-Perot interferometer: applications to periodic and non-periodic vibration measurements (Doctoral dissertation). Retrieved from <http://ethesis.inp-toulouse.fr/archive/00000706/01/pullteap.pdf>
- Qian, J. (2007). Coupled-mode theory for spun four-lobe stress region fibers. *Microwave and Opt. Technol. Lett.*, 49(11), 2814–2817.
- Quirion, M., & Ballivy, G. (2000). Concrete strain monitoring with Fabry-Perot fibre-optic sensor. *J. Mater. Civil. Eng.*, 12, 254–261.
- Raghuwanshi, S. K. & Panda, D. P. (2014). A complete analytical analysis and modeling of few mode non-uniform fiber Bragg grating assisted sensing waveguide devices. *Progress in Electromagnetics Research M*, 36, 23-37.
- Randel, S., Ryf, R., Sierra, A., Winzer, P. J., Gnauck, A. H., Bolle, C. A., Essiambre, R. J., Peckham, D. W., McCurdy, A., & Lingle, R. (2011). 6×56-Gb/s mode-division multiplexed transmission over 33-km few-mode fiber enabled by 6×6 MIMO equalization. *Opt. Express*, 19(17), 16697-16707.
- Rao, Y. J., Cooper, M. R., Jackson, D. A., Pannell, C. N., & Reekie, L. (2000). Absolute strain measurement using an in-fibre-Bragg-grating-based Fabry-Perot sensor. *Elect. Lett.*, 36, 708-709.
- Rao, Y. J., Wang, Y. P., Ran, Z. L., & Zhu, T. (2003). Novel fiber-optic sensors based on the long-period fiber grating written by high-frequency CO<sub>2</sub> laser pulses. *J. Lightwave Technol.*, 21(5), 1320-1327.

- Rao, Y.-J. (1997). In-fibre Bragg grating sensors. *Measurement science and technology*, 8, 355–375.
- Rao, Y.-J., Wang, W., Zhu, T., & Duan, D. (2009). In-line fiber-optic Fabry-Perot ultrasound sensor formed by hollowcore photonic-crystal fiber. In *proceedings of the IEEE Sensors 2009*, Christchurch, New Zealand, 858–860.
- Rao, Y.J., Xu, B., Ran, Z.L., & Gong, Y. (2010). Micro extrinsic fiber-optic Fabry-Perot interferometric sensor based on Erbium and Boron doped fibers. *Chinese Phys. Lett.*, 27, 024208.
- Rao, Y.-J., Denga, M., Duana, D.-W., & Zhu, T. (2008). In-line fiber Fabry-Perot refractive-index tip sensor based on endlessly photonic crystal fiber. *Sens. Actuats A Phys.*, 148, 33–38.
- Rees, N.D., James, S.W., Staines, S.E., Tatam, R.P., & Ashwell, G.J. (2001). Submicrometer fiber-optic Fabry-Perot interferometer formed by use of the Langmuir-Blodgett technique. *Opt. Lett.*, 26, 1840–1842.
- Reich, S.M. (2000). US Patent No. 6057911, Washington, DC: U.S. Patent and Trademark Office.
- Reich, S.M. (2001). US Patent No. 6173091, Washington, DC: U.S. Patent and Trademark Office.
- Reinsch, T., Blöcher, G., Milsch, H., Bremer, K., Lewis, E., Leen, G., & Lochmann, S. (2012). A fibre optic sensor for the in situ determination of rock physical properties. *Int. J. Rock Mech. Min.*, 55, 55–62.
- Renner, H. (2001). Effective-index increase, form birefringence and transition losses in UV-side-illuminated photosensitive fibers. *Opt. Express*, 9(11), 546–560.
- Rong, Q., Sun, H., Qiao, X., Zhang, J., Hu, M., & Feng, Z. (2012). Corrigendum: A miniature fiber-optic temperature sensor based on a Fabry-Perot interferometer. *J. Opt.*, 14, 059501:1–059501:5.
- Saran, A. (2004). MEMS based fabry perot pressure sensor and non-adhesive integration on optical fiber by anodic bonding (Electronic Thesis or Dissertation). Retrieved from <https://etd.ohiolink.edu/>



- Schlüßler, R., Fischer, A., Büttner, L., & Czarske, J. (2012). Application of a Fabry-Pérot Interferometer for Multi-Point Flow Measurements. In *proceedings of the DGaO Proceedings*, Cologne, Germany, 1–2.
- Schmidt, M., & Fürstenau, N. (1999). Fiber-optic extrinsic Fabry-Perot interferometer sensors with three-wavelength digital phase demodulation. *Opt. Lett.*, *24*, 599–601.
- Schmidt, S. (2008). US Patent No. 7423762, Washington, DC: U.S. Patent and Trademark Office.
- Sexton, C.D., Beverly, D.D., Mitchell, D.W., Riggsbee, E.T., Morton, G.W., Hashemian, H.M. (1998). Advanced Instrumentation and Maintenance Technologies for Nuclear Power Plants (Technical Report. NUREG/CR-5501). Retrieved from <https://ntrl.ntis.gov/NTRL/dashboard/searchResults/titleDetail/NUREGCR5501.xhtml>
- Shing, C. C. (2004). An investigation of chirped fiber Bragg gratings Fabry-Perot interferometer for sensing applications (Doctoral dissertation). Retrieved from <https://core.ac.uk/download/files/23/137894.pdf>
- Silva, S., Coelho, L., & Frazão, O. (2014). An all-fiber Fabry-Pérot interferometer for pressure sensing in different gaseous environments. *Measurement*, *47*, 418–421.
- Sirkis, J.S. (1994). US Patent No. 5367583 A, Washington, DC: U.S. Patent and Trademark Office.
- Snitzer, E. (1961). Cylindrical Dielectric Waveguide Modes. *J. Opt. Soc. Am.* *51*, 491-498.
- Snyder, A. W. (1972). Coupled-mode theory for optical fibers. *J. Opt. Soc. Am.*, *62*(11), 1267-1277.
- Sorin, W.V., & Baney, D.M. (1995). Multiplexed sensing using optical low-coherence reflectometry. *IEEE Photon. Tech. Lett.*, *7*, 917–919.
- St-Gelais, R., Mackey, G., Saunders, J., Zhou, J., Leblanc-Hotte, A., Poulin, A., Barnes, J.A., Loock, H.-P., Brown, R.S., & Peter, Y.-A. (2013). Gas sensing using polymer-functionalized deformable Fabry-Perot interferometers. *Sens. Actuat. B Chem.*, *182*, 45–52.

- Sun, N.-H., Liao, J.-J., Kiang, Y.-W., Lin, S.-C., Ro, R.-Y., Chiang, J.-S., & Chang, H.-W. (2009). Numerical analysis of apodized fiber bragg gratings using coupled mode theory. *Prog. Electromagn. Res.*, *99*, 289–306.
- Tafulo, P.A.R., Jorge, P.A.S., Santos, J.L., & Frazão, O. (2012b). Fabry-Pérot cavities based on chemical etching for high temperature and strain measurement. *Opt. Commun.*, *285*, 1159–1162.
- Tafulo, P.A.R., Jorge, P.A.S., Santos, J.L., Araújo, F.M., & Frazão, O. (2012a). Intrinsic Fabry-Pérot cavity sensor based on etched multimode graded index fiber for strain and temperature measurement. *IEEE Sens. J.*, *12*, 8–12.
- Tao, L., Zhengjia, L., Xia, D., He, K., & Zhang, G. (2009). Asymmetric Fabry-Pérot fiber-optic pressure sensor for liquid-level measurement. *Rev. Sci. Instrum.*, *80*, 033104.
- Taylor, H. F. (2002). In Yu, F. T., & Yin, S., (Eds.), *Fiber Optic Sensors*. New York: Marcel Dekker. 41–74.
- Taylor, H.F., Kao, T.-W., Gardner, J., Gibler, W.N., Atkins, R.A., Lee, C.E., Swenson, V.P., Spears, M., & Perez, R.X. (2001). US Patent No. 6281976, Washington, DC: U.S. Patent and Trademark Office.
- Tian, J., Lu, Y., Zhang, Q., & Han, M. (2013). Microfluidic refractive index sensor based on an all-silica in-line Fabry-Pérot interferometer fabricated with microstructured fibers. *Opt. Express*, *21*, 6633–6639.
- Tong, B., Li, M., & Li, Y. (2012). Double-fiber Fabry-Perot Interferometry optical fiber liquid level sensor. In *proceedings of the SPIE 8351, Third Asia Pacific Optical Sensors Conference*, Sydney, Australia, 83510T:1–83510T:6.
- Tseng, S.-M., & Chen, C.-L. (1988). Optical fiber Fabry-Perot sensors. *Appl. Opt.*, *27*, 547–551.
- Tsuda, H. (2006). Ultrasound and damage detection in CFRP using fiber Bragg grating sensors. *Compos. Sci. Technol.*, *66*, 676–683.
- Tuma, M.L., Elam, K.A., Sawatari, T., Gaubis, P., & Lin, Y. (1997). Fabry-Perot photonic temperature sensor system. In *proceedings of the international congress on instrumentation in aerospace simulation facilities*, ICIASF '97 Record, Pacific Grove, CA, USA, 369–377.

- Vahala, K.J. (2003) Optical microcavities. *Nature*, 424, 839–846.
- Valis, T., Hogg, D., & Measures, R.M. (1990). Fiber optic Fabry-Perot strain gauge. *IEEE Photon. Tech. Lett.*, 2, 227–228.
- Verdeyen, J. T. (1989). *Laser Electronics* (2nd edit). London: Prentice-Hall International Inc., p.131.
- Viel, T.E. (2000). US Patent No. 6141087, Washington, DC: U.S. Patent and Trademark Office.
- Villatoro, J., Finazzi, V., Coviello, G., & Pruneri, V. (2009). Photonic-crystal-fiber-enabled micro-Fabry-Perot interferometer. *Opt. Lett.*, 34, 2441–2443.
- Wang, D.H., Wang, S.J., & Jia, P.G. (2012). In-line silica capillary tube all-silica fiber-optic Fabry-Perot interferometric sensor for detecting high intensity focused ultrasound fields. *Opt. Lett.*, 37, 2046–2048.
- Wang, F., Yuan, W., Hansen, O., & Bang, O. (2011). Selective filling of photonic crystal fibers using focused ion beam milled microchannels. *Opt. Express*, 19(18), 17585-17590.
- Wang, Q., & Yu, Q. (2010). Polymer diaphragm based sensitive fiber optic Fabry-Perot acoustic sensor. *Chin. Opt. Lett.*, 8, 266–269.
- Wang, T., Zheng, S., & Yang, Z. (1998). A high precision displacement sensor using a low-finesse fiber-optic Fabry-Pérot interferometer. *Sens. Actuat. A Phys.*, 69, 134–138.
- Wang, W., & Li, F. (2014). Large-range liquid level sensor based on an optical fibre extrinsic Fabry-Perot interferometer. *Opt. Laser. Eng.*, 52, 201–205.
- Wang, X., Li, B., Xiao, Z., Lee, S.H., Roman, H., Russo, O.L., Chin, K.K., & Farmer, K.R. (2005). An ultra-sensitive optical MEMS sensor for partial discharge detection. *J. Micromech. Microeng.*, 15, 521–527.
- Wang, Y., Wang, D.N., Wang, C., & Hu, T. (2013). Compressible fiber optic micro-Fabry-Pérot cavity with ultra-high pressure sensitivity. *Opt. Express*, 21, 14084–14089.

- Wavering, T.A., Meller, S.A., Borinski, J.W., Pulliam, W.J., & Russler, P.M. (2003). US Patent No. 6671055 B1, Washington, DC: U.S. Patent and Trademark Office.
- Waxler, R.M. (1953). The stress-optical coefficient of plate glass. *Glass Industry*, 34.
- Wertheim, G. (1854). Temporary double refraction of glass. *Ann. Chim. Phys. Serr III*.
- Wild, G., & Hinckley, S. (2008). Acousto-ultrasonic optical fiber sensors: overview and state-of-the-art. *IEEE Sens. J.*, 8, 1184–1193.
- Wosinski, L., Sahlgren, B., Breidne, M., Stubbe, R., & Betend-Bon, J.-P. (1994). Fiber gratings for distributed sensors. In *proceedings of the SPIE, Interferometry '94: Interferometric Fiber Sensing*, 2341, 14–20.
- Wu, C., Fu, H. Y., Qureshi, K. K., Guan, B., & Tam, H. Y. (2011). High-pressure and high-temperature characteristics of a Fabry–Perot interferometer based on photonic crystal fiber. *Opt. Lett.*, 36(3), 412-414.
- Wu, C., Guan, B., Wang, Z., & Feng, X. (2010). Characterization of pressure response of Bragg gratings in grapefruit microstructured fibers. *J. Lightwave Technol.*, 28(9), 1392-1397.
- Wu, C., Liu, Z., Chung, K. M., Tse, M. L.V., Chan, F.Y.M., Lau, A.P.T., Lu, C., & Tam, H.Y. (2012). Strong LP<sub>01</sub> and LP<sub>11</sub> mutual coupling conversion in a two-mode fiber Bragg grating. *IEEE Photon. J.*, 4(4), 1080-1086.
- Wu, D. K., Kuhlmeier, B. T., & Eggleton, B. J. (2009). Ultrasensitive photonic crystal fiber refractive index sensor. *Opt. Lett.*, 34(3), 322-324.
- Wu, Q., & Okabe, Y. (2012). High-sensitivity ultrasonic phase-shifted fiber Bragg grating balanced sensing system. *Opt. Express*, 20(27), 28353–28362.
- Wu, Q., & Okabe, Y. (2012). Ultrasonic sensor employing two cascaded phase-shifted fiber Bragg gratings suitable for multiplexing. *Opt. Lett.*, 37, 3336-3338.
- Wu, Y., Shankar, P. M., & Lewin, P. A. (1994). Fiber optic ultrasonic sensor using Raman-Nath light diffraction. *IEEE Trans. Ultrason., Ferroelect., Freq. Contr.*, 41, 166–171.

- Xiao, G.Z., Adnet, A., Zhang, Z., Sun, F.G., & Grover, C.P. (2005). Monitoring changes in the refractive index of gases by means of a fiber optic Fabry-Perot interferometer sensor. *Sens. Actuats A Phys.*, 118, 177–182.
- Xiao, L., Demokan, M. S., Jin, W., Wang, Y., & Zhao, C. (2007). Fusion splicing photonic crystal fibers and conventional single-mode fibers: microhole collapse effect. *J. Lightwave Technol. Journal of Lightwave Technology*, 25(11), 3563-3574.
- Xie, Z. (2006). Two Applications of the Fabry-Perot Interferometric Sensor (Doctoral dissertation). Retrieved from <http://oaktrust.library.tamu.edu/bitstream/handle/1969.1/ETD-TAMU-1019/XIE-DISSERTATION.pdf?sequence=1&isAllowed=y>
- Xu, L.-C., Deng, M., Duan, D.-W., Wen, W.-P., & Han, M. (2012). High-temperature measurement by using a PCF-based Fabry-Perot interferometer. *Opt. Lasers Eng.*, 50, 1391–1396.
- Xu, M. G., Reekie, L., Chow, Y. T. & Dakin, J. P. (1993). Optical in-fiber grating high pressure sensor. *Electron. Lett.*, 29(4), 398–399.
- Xu, W., Huang, W.-B., Huang, X.-G., & Yu, C.-Y. (2013). A simple fiber-optic humidity sensor based on extrinsic Fabry-Perot cavity constructed by cellulose acetate butyrate film. *Opt. Fiber Technol.*, 19, 583–586.
- Yamate, T., Ramos, R. T., Schroeder, R. J., & Udd, E. (2000). Thermally insensitive pressure measurements up to 300 degrees C using fiber Bragg gratings written onto side-hole single mode fiber. In *proceedings of 14th International Conference on Optical Fiber Sensors*, Proc. SPIE., 4185, 628–631.
- Yang, H. Z., Qiao, X. G., Wang, Y. P., Ali, M. M., Lai, M. H., Lim, K. S., & Ahmad, H. (2015). In-fiber gratings for simultaneous monitoring temperature and strain in ultra-high temperature. *IEEE Photonics Technology Letters*, 27(1), 58-61.
- Yao, J., Zhu, T., Duan, D.-W., & Deng, M. (2012). Nanocomposite polyacrylamide based open cavity fiber Fabry-Perot humidity sensor. *Appl. Opt.*, 51, 7643–7647.
- Yariv, A. & Yeh, P. (2003). *Optical Waves in Crystals*. Hoboken: John Wiley & Sons.
- Yariv, A. (1973). Coupled-mode theory for guided-wave optics. *IEEE J. Quantum Electron.* 9(9), 919–933.

- Yin, S., Ruffin, P.B., & Yu, F.T.S. (2008). *Fiber Optic Sensors*, 2nd ed., Boca Raton, FL, USA: CRC Press: Taylor & Francis.
- Yoshino, T., Kurasawa, K., & Katsuji, I. (1982). Fiber-optic Fabry-Perot interferometer and its sensor applications. *IEEE J. Quantum Elect.*, 18, 1624–1633.
- Yu, L., & Giurgiutiu, V. (2008). In situ 2-D piezoelectric wafer active sensors arrays for guided wave damage detection. *Ultrasonics*, 48, 117-134.
- Yu, Q., & Zhou, X. (2011). Pressure sensor based on the fiber optic extrinsic Fabry-Perot interferometer. *Photon. Sens.*, 1, 72–83.
- Zetterlind, V.E., Watkins, S.E., & Spoltman, M. (2003). Fatigue testing of a composite propeller blade using fiber-optic strain sensors. *IEEE Sens. J.*, 3, 393–399.
- Zhang, G., Yang, M., & Wang, M. (2013). Large temperature sensitivity of fiber-optic extrinsic Fabry-Perot interferometer based on polymer-filled glass capillary. *Opt. Fiber Technol.*, 19, 618–622.
- Zhang, J., & Li, Y. (2009). Calibration Method for Fiber Bragg Grating Temperature Sensor. In *proceedings of the Ninth International Conference on Electronic Measurement & Instruments (ICEMI'2009)*, Beijing, China.
- Zhang, J.Z., Yang, J., Sun, W.M., Jin, W.C., Yuan, L.B., & Peng, G.D. (2008). Composite cavity based fiber optic Fabry-Perot strain sensors demodulated by an unbalanced fiber optic Michelson interferometer with an electrical scanning mirror. *Measur. Sci. Technol.*, 19, 085305.
- Zhang, Q., Zhu, T., Hou, Y., & Chiang, K.S. (2013). All-fiber vibration sensor based on a Fabry-Perot interferometer and a microstructure beam. *J. Opt. Soc. Am. B*, 30, 1211–1215.
- Zhang, W., Dai, J., Sun, B., & Du, Y. (2008). *Experiment on dynamic response of fiber optic Fabry-Perot sensors and its application in structural health monitoring*. In Tomizuka, M., Chen, R.W., Yun, C.B., Spencer, B.F., Chen, W.M., (Eds.), *World Forum on Smart Materials and Smart Structures Technology* (pp. 504). Boca Raton, FL, USA: CRC Press, Taylor & Francis.
- Zhang, Y., Yuan, L., Lan, X., Kaur, A., Huang, J., & Xiao, H. (2013). High-temperature fiber-optic Fabry-Perot interferometric pressure sensor fabricated by femtosecond laser. *Opt. Lett.*, 38, 4609–4612.

- Zhao, J.-R., Huang, X.-G., He, W.-X., & Chen, J.-H. (2010). High-resolution and temperature-insensitive fiber optic refractive index sensor based on fresnel reflection modulated by Fabry-Perot interference. *J. Lightw. Technol.*, *28*, 2799–2803.
- Zhao, Y., Lv, R.-Q., Ying, Y., & Wang, Q. (2012). Hollow-core photonic crystal fiber Fabry-Perot sensor for magnetic field measurement based on magnetic fluid. *Opt. Laser Technol.*, *44*, 899–902.
- Zhou, G., & Sim, L.M. (2002). Damage detection and assessment in fibre-reinforced composite structures with embedded fibre optic sensors - Review. *Smart Mater. Struct.*, *11*, 925–939.
- Zhou, K., Yan, Z., Zhang, L., & Bennion, I. (2011). Refractometer based on fiber Bragg grating Fabry-Pérot cavity embedded with a narrow microchannel. *Opt. Express*, *19*(12), 11769–11779.
- Zhou, K., Zhang, L., Chen, X., & Bennion, I. (2006). Optic sensors of high refractive-index responsivity and low thermal cross sensitivity that use fiber Bragg gratings of 80° tilted structures. *Opt. Lett.*, *31*, 1193-1195.
- Zhu, J.-J., Zhang, A.P., Xia, T.-H., He, S., & Xue, W. (2010). Fiber-optic high-temperature sensor based on thin-core fiber modal interferometer. *IEEE Sens. J.*, *10*, 1415–1418.
- Zhu, T., Wu, D., Liu, M., & Duan, D.-W. (2012). In-line fiber optic interferometric sensors in single-mode fibers. *Sensors*, *12*, 10430–10449.
- Zolla, F., Renversez, G., Nicolet, A., Kuhlmeiy, B., Guenneau, S., & Felbacq, D. (2005). *Photonic Crystal Fibres*. London: Imperial College Press.

## LIST OF PUBLICATIONS

### **(a). Candidate's Journal Publications directly related to this thesis work:**

1. **Md. Rajibul Islam**, Muhammad Mahmood Ali, Man-Hong Lai, Kok-Sing Lim, Harith Ahmad: Chronology of fabry-perot interferometer fiber-optic sensors and their applications: a review. *Sensors* 04/2014; 14(4):7451-88. DOI: 10.3390/s140407451
2. **Md. Rajibul Islam**, muhammad mahmood ali, Man-Hong Lai, Kok-Sing Lim, Dinusha Serandi Gunawardena, Venkata Rajanikanth Machavaram, Harith Ahmad: Wide-range in-fiber Fabry-Perot resonator for ultrasonic sensing. *IET Optoelectronics* 06/2015; 9(3):136-140. DOI: 10.1049/iet-opt.2014.0056
3. Kok-Sing Lim, **Md. Rajibul Islam**, Yen-Sian Lee, Hang-Zhou Yang, Harith Ahmad: LP<sub>01</sub>-LP<sub>11</sub> cross mode interference in a chirped grating inscribed in two-mode fiber. *IEEE Journal of Quantum Electronics* 06/2016; 52(6): 6600206. DOI: 10.1109/JQE.2016.2564679.
4. Muhammad M. Ali, **Md. Rajibul Islam**, Kok-Sing Lim, Dinusha S. Gunawardena, Hang-Zhou Yang, Harith Ahmad. PCF-cavity FBG Fabry-Perot resonator for simultaneous measurement of pressure and temperature. *IEEE Sensors Journal* 08/2015; 15(12): 6921-6925. DOI: 10.1109/JSEN.2015.2468065



**(b). Patents on Fabricated Devices (partially related to this thesis work)**

1. Few-Mode Fibre Grating Sensor, Patent filed no. PI 2014703282, Filing date: 5 NOVEMBER 2014. (National, Malaysia)
2. A Fiber-Based System as a Spatial Mode Converter, A Method for Forming Few Mode Fiber Bragg Gratings and Use Therefor, Patent filed no. PI 2015701694, Filing date: 26 MAY 2015. (National, Malaysia)

**(c). Candidate's work presented in Conferences/Colloquium/Seminar:**

1. **Md. Rajibul Islam**, Kok Sing Lim, M. Mahmood Ali, Hwa Kian Chai, Harith Ahmad: Opto-elastic properties of FBG based Fabry-Perot resonator: fabrication, characterization, and applications. The MMRRC and OFSRC annual colloquium 2016, Analog Devices building, University of Limerick, Limerick, Ireland, 16 Dec 2016.
2. Muhammad Mahmood Ali, Yongmin Jung, Kok-Sing Lim, **Md. Rajibul Islam**, Shaif-ul Alam, David J. Richardson, Harith Ahmad: Optical Mode-converters based on Few Mode Fiber for Mode Division Multiplexing. The 5th International Conference on Solid State Science and Technology 2015 (ICSSST2015), Bayview Hotel, Langkawi, Kedah, Malaysia. 13-15 December 2015.
3. **Md. Rajibul Islam**, Kok Sing Lim, Harith Ahmad: Fabrication and Characterization of Fiber Bragg Grating. The Colloquia @ The Advanced School/Workshop on Fiber Optics: Light in action from science to technology program at the University of Fort Hare, Alice, Eastern Cape - South Africa, 01 October, 2015.

4. **Md. Rajibul Islam**, Marya Bagherifaez, M. Mahmood Ali, Hwa Kian Chai, Kok Sing Lim, Harith Ahmad: Optical Fiber Sensors for Reinforcement Corrosion Monitoring in Marine Concrete Structure. The 7th Asia and Pacific Young Researchers and Graduates Symposium (YRGS 2015), University of Malaya, Malaysia. August, 2015.
5. **Md. Rajibul Islam**, Kok Sing Lim, Hwa Kian Chai, Harith Ahmad: Fabry-Perot Resonator for Acoustic-ultrasonic Sensing. Physics Colloquium 2015, Department of Physics, Faculty of Science, University of Malaya, Malaysia. June, 2015.
6. **Md. Rajibul Islam**, Muhammad Mahmood Ali, Kok Sing Lim, Harith Ahmad: Characterization of acousto-optic effect on in-fiber fabry-perot resonator. The LAMP (Laser, Atomic and Molecular Physics) program, Winter College on Optics and Light: a Bridge between Earth and Space (preparatory school) program at The Abdus Salam International Centre for Theoretical Physics (ICTP), Trieste, Italy, 16 February 2015.
7. **Md. Rajibul Islam**, Muhammad Mahmood Ali, Kok Sing Lim, Harith Ahmad: Characterization of acousto-optic effect of in-fiber fabry-perot resonator”, Poster Presentation @ The LAMP (Laser, Atomic and Molecular Physics) program, Winter College on Optics and Light: a Bridge between Earth and Space (preparatory school) program at The Abdus Salam International Centre for Theoretical Physics (ICTP), Trieste, Italy, 11 February 2015.
8. **Md. Rajibul Islam**, “Opto-elastic properties of FBG based Fabry-Perot resonator: fabrication, characterization and applications”, presented in Institute of Graduate Studies, University of Malaya, Postgraduate Research Findings Seminar for the partial fulfilment of Ph.D Candidature, 12<sup>st</sup> April 2016.

9. **Md. Rajibul Islam**, “Opto-elastic properties of FBG based Fabry-Perot resonator: fabrication, characterization and applications”, presented in Institute of Graduate Studies, University of Malaya, Postgraduate Candidature Defence for the partial fulfilment of Ph.D Candidature, 22<sup>nd</sup> March 2016.
10. **Md. Rajibul Islam**, “Opto-elastic properties of FBG based Fabry-Perot resonator: fabrication, characterization and applications”, presented in Institute of Graduate Studies, University of Malaya, Postgraduate Proposal Defence Seminar for the partial fulfilment of Ph.D Candidature, 02<sup>nd</sup> July 2015.

**(d).Candidate’s additional Publications during candidature (partially related to this thesis work):**

1. Omar Almubaied, Hwa Kian Chai, **Md. Rajibul Islam**, Kok Sing Lim, Chee Ghuan Tan: Monitoring Corrosion Process of Reinforced Concrete Structure using FBG Strain Sensor. *IEEE transaction on instrumentation and measurement*. vol. x(x), pp. xx-xx. (Feb 2017). [In press].
2. Man-Hong Lai, **Md. Rajibul Islam**, Kok-Sing Lim, Shirley Diong-Chea Fang, Hang-Zhou Yang, Xueguang Qiao, Harith Ahmad: Nonlinear output response of acousto-optic modulated distributed Bragg reflector (DBR) fiber laser. *Optoelectronics and Advanced Materials – Rapid Communications*. vol. 10(9-10), pp. 611-615. (Sep-Oct 2016).
3. Yen-Sian Lee, Kok-Sing Lim, **Md. Rajibul Islam**, Man-Hong Lai, Harith Ahmad: Dynamic LP<sub>01</sub>-LP<sub>11</sub> Mode Conversion by a Tilted Binary Phase Plate. *IEEE/OSA Journal of Lightwave Technology* 08/2016; PP (99): 1-7. DOI: 10.1109/JLT.2016.2599179.
4. **Md. Rajibul Islam**, Dinusha Serandi Gunawardena, Yen-Sian Lee, Kok-Sing Lim, Hang Zhou Yang, Harith Ahmad: Fabrication and Characterization of

- Laser-ablated Cladding Resonances of Two different-diameter Photosensitive Optical Fibers. *Sensors and Actuators A Physical* 03/2016; 243:111-116. DOI: 10.1016/j.sna.2016.03.001
5. Man-Hong Lai, Kok-Sing Lim, **Md. Rajibul Islam**, Dinusha S. Gunawardena, Hang-Zhou Yang, Harith Ahmad: Effect of CO<sub>2</sub> Laser Annealing on Stress Applying Parts Contributing Towards Birefringence Modification in Regenerated Grating in Polarization Maintaining Fiber. *IEEE Photonics Journal* 09/2015; 7(5): Article#7801909. DOI: 10.1109/JPHOT.2015.2477496.
  6. **Md. Rajibul Islam**, Marya Bagherifaez, M. Mahmood Ali, Hwa Kian Chai, Kok-Sing Lim, Harith Ahmad: Tilted Fiber Bragg Grating Sensors for Reinforcement Corrosion Measurement in Marine Concrete Structure. *IEEE Transactions on Instrumentation and Measurement* 08/2015; 64(12): 3510-3516. DOI: 10.1109/TIM.2015.2459511.
  7. Muhammad Mahmood Ali, Yongmin Jung, Kok-Sing Lim, **Md. Rajibul Islam**, Shaif-ul Alam, David J. Richardson, Harith Ahmad: Characterization of mode coupling in few-mode fiber Bragg gratings with selective mode excitation. *IEEE Photonics Technology Letters* 06/2015; 27(16): 1713-1716. DOI: 10.1109/LPT.2015.2438177
  8. Hang Zhou Yang, Muhammad Mahmood Ali, **Md. Rajibul Islam**, Kok-Sing Lim, Dinusha Serandi Gunawardena, Harith Ahmad: Cladless few mode fiber grating sensor for simultaneous refractive index and temperature measurement. *Sensors and Actuators A Physical* 06/2015; 228:62-68. DOI: 10.1016/j.sna.2015.03.001
  9. Kok-Sing Lim, Dinusha Serandi Gunawardena, Man-Hong Lai, **Md. Rajibul Islam**, Hang-Zhou Yang, Xueguang Qiao, Amin Malek Mohammadi, Harith Ahmad: Characterization of phasemask interference visibility and the evolution

- of grating visibility during grating formation. *Measurement* 03/2015; 64:163-167. DOI: 10.1016/j.measurement.2014.12.049
10. Yang Hang Zhou, Qiao Xue Guang, **Md. Rajibul Islam**, Lim Kok-Sing, Harith Ahmad: Simultaneous measurement of aliphatic alcohol concentration and temperature based on etched taper FBG. *Sensors and Actuators B Chemical* 10/2014; 202:959–963. DOI: 10.1016/j.snb.2014.06.058
11. Hang-Zhou Yang, Xue-Guang Qiao, Kok-Sing Lim, S.W. Harun, Wu-Yi Chong, **Md. Rajibul Islam**, Harith Ahmad: Optical Fiber Sensing of Salinity and Liquid Level. *IEEE Photonics Technology Letters* 09/2014; 26(17):1742-1745. DOI: 10.1109/LPT.2014.2330206
12. H.-Z. Yang, W.-Y. Chong, X.-G. Qiao, M.-J. Lim, K.-S. Lim, **Md. Rajibul Islam**, N.M. Ali, Harith Ahmad: 1.3 and 1.55  $\mu\text{m}$  Thermally Regenerated Gratings in Hydrogenated Boron/Germanium Co-Doped Photosensitivity Fiber. *IEEE Sensors Journal* 05/2014; 14(5):1352-1356. DOI: 10.1109/JSEN.2013.2294973
13. Hang-Zhou Yang, Xue-Guang Qiao, M. Mahmood Ali, **Md. Rajibul Islam**, Kok-Sing Lim: Optimized Tapered Optical Fiber for Ethanol ( $\text{C}_2\text{H}_5\text{OH}$ ) Concentration Sensing. *OSA/IEEE Journal of Lightwave Technology* 04/2014; 32(9). DOI: 10.1109/JLT.2014.2311175.

**(e). Candidate's Honors and Awards during Candidature**

1. Selected for **Visiting Ph.D. Research Fellow** at **University of Limerick, Ireland**, under **Erasmus Mundus, INTACT** Programme funded by European Union for **six months** starting from 1<sup>st</sup> October. 2016.

2. Awarded **partial tuition and travel grant** by the **OSA Foundation and IPG Photonics** for attending the Siegman International School on Lasers program and ICFO in **Barcelona, Spain**, 24th – 29th July, 2016. (unused)
3. Won **Bronze Medal** at the **PECIPTA 2015** (International Conference and Exposition on Inventions of Institutions of Higher Learning), 4-6 December 2015, **Kuala Lumpur Convention Centre, Malaysia**.
4. Received **full sponsorship by UNESCO and ICTP** for attending the Advanced School/Workshop on Fibre Optics: Light in action from science to technology program at **University of Fort Hare, Alice, Eastern Cape - South Africa**, 27th Sep – 02nd Oct, 2015.
5. Awarded **partial travel grant** by the **Optics Student Karlsruhe (OSKar)** for attending the IONS International Student Conference 2015 in **Karlsruhe Institute of Technology, Karlsruhe, Germany**, 26<sup>th</sup> – 28<sup>th</sup> June, 2015. (unused)
6. Received **full sponsorship by UNESCO and ICTP** for attending the Winter College on Optics and Light: a Bridge between Earth and Space (preparatory school) program at **The Abdus Salam International Centre for Theoretical Physics (ICTP), Trieste, Italy**, 2<sup>nd</sup> - 20<sup>th</sup> Feb, 2015.
7. Awarded **Postgraduate Research Fund (PPP)** - Cycle 2014A, for Ph.D. Research project from the **Centre for Research Grant Management Unit (PPGP), University of Malaya**.
8. Received **Graduate Research Assistantship Scheme (GRAS)** from the **HIR, University of Malaya** for Ph.D (2014 - 2016).

## APPENDIX A

### MATLAB CODES

This section provides some of the important MATLAB source codes written during the course of this research. Most of the codes written are for the plots and graphs in the result of numerical solutions of the analytical expressions and experimental data in this work.

**Matlab code to show modulated grating period and grating index of FBG by a sinusoidal wave:**

```
clear all
format long
clc;
nef = 1.445;      %effective index
L = 0.01;
dn = 1.4E-06/L;  %index modulation
lg = 1551E-09;   %reflection wavelength
c = 3e5;         % nm/ps;
period = lg/(2*nef);

tic
N_lamb = 201;    % no. of sample for lambda
lamb = linspace(1550.96E-9,1551.4E-09,N_lamb); % wavelength lambda
dl = lamb(2)-lamb(1);
N_disp = 100;
disp = linspace(-L/2,L/2,N_disp); % displacement
mask = ones(1,N_disp);
mask([40 65]) = 0;
dz = disp(2)-disp(1);
FWHM = 0.02;

v = 5760;        % acoustic velocity in silica fiber
f = 3e6;
lambda_a = v/f;
nu = 0.17;
p11 = 0.121;
p12 = 0.27;
E = 70000;      % MPa
dP = 0.1;       % MPa

M = 128;
wt = linspace(0,32*pi, M);
```

```

v = 5760;          % acoustic velocity in silica fiber
p = 1;
freq = linspace(0.1e2,6e6,400);
for f = freq
    lambda_a = v/f;
    m = 1;
    for phase = wt
        l = 1551.051e-9;
        F = [1 0; 0 1];
        %p2 = (gdc.^2)/(kac.^2);
        for z = disp
            deln = nef^3*(1-2*nu)*(2*p12+p11)/(2*E)*dP*sin(2*pi*z/lambda_a+phase);
% core index is modulated by a sinusoidal wave
            del_pitch = period*(1-2*nu)/E*dP*sin(2*pi*z/lambda_a+phase); % grating
period is modulated by a sinusoidal wave
            %dn_z = dn*exp(-4*log(2)*z^2./FWHM^2); %apodised
            dn_z = dn; %uniform
            del = 2*pi*nef*(1/l)- pi./(period+del_pitch);
            sig = 2*pi*(dn_z+deln)/l;
            g = sig + del;

            k = pi*dn_z/l;
            p1 = sqrt(k^2 - g^2);

            A = cosh(p1*dz);
            B = i*(g/p1)*sinh(p1*dz);
            f11 = A - B;
            f12 = -i*(k/p1)*sinh(p1*dz);
            f21 = -f12;
            f22 = A + B;
            ff = [f11 f12; f21 f22];
            F = ff*F;

        end

        r(m) = F(2,1)/F(1,1);
        R(m) = (abs(r(m)))^2;
        m=m+1;
    end
    R_max(p) = max(R);
    fout = abs(fftshift(fft(R-mean(R))));
    MM(p)=max(fout);
    p = p + 1
end
subplot(211)
plot(freq, MM)
ylabel('Sensitivity');
xlabel('Frequency Hz');
subplot(212)
plot(freq, R_max)
data = [freq' MM' R_max'];

```



## APPENDIX B

### Matlab code to show modulated grating period and grating index of FBG based

#### FPR by a sinusoidal wave:

```
clear all
format long
clc;
nef = 1.445;      %effective index
L = 0.005;
dn = 1.4E-06/L;  %index modulation
lg = 1551E-09;   %reflection wavelength
c = 3e5;         % nm/ps;
period = lg/(2*nef);

tic
N_lamb = 201;    % no. of sample for lambda
lamb = linspace(1550.96E-9,1551.4E-09,N_lamb); % wavelength lambda
dl = lamb(2)-lamb(1);
N_disp = 100;
disp = linspace(-L,L,N_disp); % displacement
mask = ones(1,N_disp);
mask([40 65]) = 0;
dz = disp(2)-disp(1);
FWHM = 0.02;

v = 5760;        % acoustic velocity in silica fiber
f = 3e6;
lambda_a = v/f;
nu = 0.17;
p11 = 0.121;
p12 = 0.27;
E = 70000;      % MPa
dP = 0.1;       % MPa

M = 128;
wt = linspace(0,32*pi, M);
v = 5760;       % acoustic velocity in silica fiber
p = 1;
freq = linspace(0.1e2,6e6,400);
for f = freq
    lambda_a = v/f;
    m = 1;
    for phase = wt
        l = 1551.145e-9;
        F = [1 0; 0 1];
        %p2 = (gdc.^2)/(kac.^2);
        for z = disp(1:50)
            deln = nef^3*(1-2*nu)*(2*p12+p11)./(2*E)*dP*sin(2*pi*z/lambda_a+phase);
```

```

del_pitch = period*(1-2*nu)./E*dP*sin(2*pi*z/lambda_a+phase);
%dn_z = dn*exp(-4*log(2)*z^2./FWHM^2); %apodised
dn_z = dn; %uniform
del = 2*pi*nef*(1/l)- pi./(period+del_pitch);
sig = 2*pi*(dn_z+deln)./l;
g = sig + del;

k = pi*dn_z/l;
p1 = sqrt(k^2 - g^2);

A = cosh(p1*dz);
B = i*(g/p1)*sinh(p1*dz);
f11 = A - B;
f12 = -i*(k/p1)*sinh(p1*dz);
f21 = -f12;
f22 = A + B;
ff = [f11 f12; f21 f22];
F = ff*F;

end
PS = [i 0; 0 -i];
F = PS*F;
for z = disp(51:100)
    deln = nef^3*(1-2*nu)*(2*p12+p11)./(2*E)*dP*sin(2*pi*z/lambda_a+phase);
    del_pitch = period*(1-2*nu)./E*dP*sin(2*pi*z/lambda_a+phase);
    %dn_z = dn*exp(-4*log(2)*z^2./FWHM^2); %apodised
    dn_z = dn; %uniform
    del = 2*pi*nef*(1/l)- pi./(period+del_pitch);
    sig = 2*pi*(dn_z+deln)./l;
    g = sig + del;

    k = pi*dn_z/l;
    p1 = sqrt(k^2 - g^2);
    A = cosh(p1*dz);
    B = i*(g/p1)*sinh(p1*dz);
    f11 = A - B;
    f12 = -i*(k/p1)*sinh(p1*dz);
    f21 = -f12;
    f22 = A + B;
    ff = [f11 f12; f21 f22];
    F = ff*F;

end
r(m) = F(2,1)/F(1,1);
R(m) = (abs(r(m)))^2;
m=m+1;
end
R_max(p) = max(R);
fout = abs(fftshift(fft(R-mean(R))));
MM(p)=max(fout);
p = p + 1
end

```

```
subplot(211)
plot(freq, MM)
ylabel('Sensitivity');
xlabel('Frequency Hz');
subplot(212)
plot(freq, R_max)
data = [freq' MM' R_max'];
```

University of Malaya

## APPENDIX C

**Matlab code to show LP<sub>01</sub> and LP<sub>11</sub> mode profile:**

```
clear all
clc
R=62.5;
P=100;
ra = 9.25; %um 2S fiber
l = 1.55; % wavelength
C1=7.42e-6; % photoelastic coefficient
C2=4.102e-5;
k = 2*pi/l;
r = linspace(-ra, ra, 100);
thet = 0;
dr = ra/100;

thet2 = 0;
r2 = linspace(ra,4*ra,300);
r3 = linspace(-4*ra,-ra,300);
%%%%%%%%%%%%%%%%%%%%%%%%%%%%%%%%%%%%%%%%%%%%%%%%%%%%%%%%%%%%%%%%%%%%%%%%
%%%%%%%%%%%%%%%%%%%%%%%%%%%%%%%%%%%%%%%%%%%%%%%%%%%%%%%%%%%%%%%%%%%%%%%%

n01 = 1.4474; %2SF effective index 1.447527732      1.446247196
n11 = 1.4461;
ncore = 1.4483926;
nclad = 1.4433926;
U01 = k*ra*sqrt(ncore^2-n01^2);
W01 = k*ra*sqrt(n01^2-nclad^2);
U11 = k*ra*sqrt(ncore^2-n11^2);
W11 = k*ra*sqrt(n11^2-nclad^2);

E01 = besselj(0,U01*r/ra)./besselj(0,U01);
E11 = besselj(1,U11*r/ra)./besselj(1,U11).*cos(thet);
EE01 =esselk(0,W01*r2/ra)./esselk(0,W01);
EE11 =esselk(1,W11*r2/ra)./esselk(1,W11).*cos(thet2);
EEE01 =esselk(0,W01*r2/ra)./esselk(0,W01);
EEE11 =esselk(1,W11*r2/ra)./esselk(1,W11).*cos(thet2+pi);

e01 = [fliplr(EEE01) E01 EE01];
e11 = [fliplr(EEE11) E11 EE11];
P01 = e01.^2;
P11 = e11.^2;
e01 = e01/sqrt(max(P01));
e11 = e11/sqrt(max(P11));
P01 = e01.^2;
P11 = e11.^2;

subplot(311)
plot([r3 r2], P01, '-')
```

```

xlabel('Radius \mum')
subplot(312)
plot([r3 r r2], P11,'-')
xlabel('Radius \mum')
subplot(313)
hold on
col = 'kbrg';
l = 1;
for rho = linspace(0,0.3,4);
    PU = (rho*e01+(1-rho)*e11).^2
    plot([r3 r r2], PU, [col(l) '-'])
    l = l + 1 ;
end
hold off
legend('1.0 : 0.0', '0.9 : 0.1','0.8 : 0.2','0.7 : 0.3');
xlabel('Radius \mum - LP_1_1:LP_0_1 ratio')

```

University of Malaya

## APPENDIX D

### Matlab code to show line intensity profile of LP<sub>01</sub> and LP<sub>11</sub>:

```
clear all
clc
R=62.5;
P=100;
ra = 9.25; %um
l = 1.53; % wavelength
C1=7.42e-6; % photoelastic coefficient
C2=4.102e-5;
k = 2*pi/l;
[r, thet] = ndgrid(linspace(0,ra,100),linspace(0,2*pi,40));
[x,y] = pol2cart(thet, r);
r = sqrt(x.^2 + y.^2);

dr = ra/100;
[r2,thet2] = ndgrid(linspace(ra,4*ra,300),linspace(0,2*pi,40));
[x2,y2] = pol2cart(thet2, r2);
r2 = sqrt(x2.^2 + y2.^2);

%%%%%%%%%%%%%%%%%%%%%%%%%%%%%%%%%%%%%%%%%%%%%%%%%%%%%%%%%%%%%%%%%%%%%%%%
%%%%%%%%%%%%%%%%%%%%%%%%%%%%%%%%%%%%%%%%%%%%%%%%%%%%%%%%%%%%%%%%%%%%%%%%

n01 = 1.4474; %2SF effective index 1.447527732 1.446247196
n11 = 1.4461;
ncore = 1.4483926;
nclad = 1.4433926;
U01 = k*ra*sqrt(ncore^2-n01^2);
W01 = k*ra*sqrt(n01^2-nclad^2);
U11 = k*ra*sqrt(ncore^2-n11^2);
W11 = k*ra*sqrt(n11^2-nclad^2);

E01 = besselj(0,U01*r/ra)./besselj(0,U01);
E11 = besselj(1,U11*r/ra)./besselj(1,U11).*cos(thet);
EE01 =esselk(0,W01*r2/ra)./esselk(0,W01);
EE11 =esselk(1,W11*r2/ra)./esselk(1,W11).*cos(thet2);

e01 = [E01; EE01];
e11 = [E11; EE11];
P01 = sum(sum(e01.^2));
P11 = sum(sum(e11.^2));
e01 = e01/sqrt(P01);
e11 = e11/sqrt(P11);

figure(1)
surf([x; x2], [y; y2], e01.^2)
```

```
shading interp  
colorbar
```

```
figure(2)  
surf([x; x2], [y; y2], e11.^2)  
shading interp  
colorbar
```

```
figure(3)  
surf([x; x2], [y; y2], (0.5*e01+e11).^2)  
shading interp  
colorbar
```

University of Malaya

## APPENDIX E

### Matlab code to show LP<sub>01</sub>- LP<sub>11</sub> cross mode interference in CG produced in TMF

```
clear all;
close all;
clc;
n01 = 1.448984;      %effective index 1.448984  1.446145
n11 = 1.446145;
%=====
dn = 0.13E-03; % .42E-03      %index modulation
tic
N_lamb = 1201; % no. of sample for lambda
L = 0.010; %L = 0.013;
FWHM = 0.1;
%=====
N_z = 800;
lamb = linspace(1529.5E-9,1561.5E-09,N_lamb); % wavelength lambda
disp = linspace(0,L,N_z); %displacement
alp11 = 0;
dz = disp(2)-disp(1);
dnn = dn*exp(-((disp-L/2)/FWHM).^2/2);
Exp_data = xlsread('Analysis_2G.xlsx',1,'Q3:Q1003');
Experiment=Exp_data(:,1);

%%%%%%%%%%%%%%                               FBG
%%%%%%%%%%%%%%
%=====
period = linspace(530,534.8,N_z)*1e-9;
%period = linspace(530,533.9,N_z)*1e-9;

m = 1;
%=====
a = .95; % 0=LP11/1=LP01 field amplitude
%=====
b = sqrt(1-a^2)*exp(-i*(4.0+0.5*pi)); % LP11 field amplitude with phase difference
for l=lamb;
    G = [1 0 0 0;
          0 1 0 0;
          0 0 1 0;
          0 0 0 1];
    Z = 1;
    for z = disp
        z1_2 = z+dz/2;
        %%%%%%%%%%%%%%%
LP01 %%%%%%%%%%%%%%%
        % dn_01 = dn; %uniform
        dn_01 = dnn(Z); %apodised
        del_01 = 2*pi*n01*(1/l) - pi./period(Z);
        sig_01 = 2*pi*dn_01./l;
```



```

g_01 = sig_01 + del_01;
k_01 = pi*dn_01/l;

```

```

%%%%%%%%%%%%%%%%%%%%%%%%%%%%%%%%%%%%%%%%%%%%%%%%%%%%%%%%%%%%%% LP11
%%%%%%%%%%%%%%%%%%%%%%%%%%%%%%%%%%%%%%%%%%%%%%%%%%%%%%%%%%%%%%
dn_11 = 0.9*dnn(Z); %uniform
del_11 = 2*pi*n11*(1/l) - pi./period(Z);
sig_11 = 2*pi*dn_11./l;
g_11 = sig_11 + del_11;
k_11 = pi*dn_11/l;

```

```

%%%%%%%%%%%%%%%%%%%%%%%%%%%%%%%%%%%%%%%%%%%%%%%%%%%%%%%%%%%%%% LP01-LP11 cross coupling
%%%%%%%%%%%%%%%%%%%%%%%%%%%%%%%%%%%%%%%%%%%%%%%%%%%%%%%%%%%%%%
%=====
dn_c = 0.22*dnn(Z); %uniform
del_c = (del_11 + del_01)/2;
sig_c = 2*pi*dn_c./l;
g_c = sig_c + del_c;
k_c = pi*dn_c/l;

```

```

c11 = i*k_01*exp(-i*(2*del_01*z1_2))*dz;
c12 = i*k_c *exp(-i*(2*del_c *z1_2))*dz;
c21 = i*k_c *exp(-i*(2*del_c *z1_2))*dz;
c22 = i*k_11*exp(-i*(2*del_11*z1_2))*dz;

```

```

d11 = -i*k_01*exp( i*(2*del_01*z1_2))*dz;
d12 = -i*k_c *exp( i*(2*del_c *z1_2))*dz;
d21 = -i*k_c *exp( i*(2*del_c *z1_2))*dz;
d22 = -i*k_11*exp( i*(2*del_11*z1_2))*dz;

```

```

C = [1 0 d11 d12;
     0 1 d21 d22;
     c11 c12 1 0;
     c21 c22 0 1];

```

```

G = C*G;
Z = Z + 1;

```

```
end
```

```

% M = [-1 G(1,2) G(1,3) G(1,4);
%      0 G(2,2) G(2,3) G(2,4);
%      0 G(3,2) G(3,3) G(3,4);
%      0 G(4,2) G(4,3) G(4,4)];

```

```

M = [-1 0 G(1,3) G(1,4);
     0 -1 G(2,3) G(2,4);
     0 0 G(3,3) G(3,4);
     0 0 G(4,3) G(4,4)];

```

```

A = [G(1,1) G(1,2);
     G(2,1) G(2,2);
     G(3,1) G(3,2);

```

```

    G(4,1) G(4,2)]*[a; b];
M = -M^-1*A;
tl01(m) = M(1);
tl11(m) = M(2);
rl01(m) = M(3);
rl11(m) = M(4);

    m=m+1;
end

RL = 0.5*abs(rl01 + rl11).^2;
TL = 0.5*abs(tl01 + tl11).^2;

% RL = abs(rl01).^2+abs(rl11).^2;
% TL = abs(tl01).^2+abs(tl11).^2;
I = RL+TL;
toc

lam = linspace(lamb(1), lamb(end),1001);
figure(1)
plot(lamb*1e9,10*log10(RL),'k', ...
     lamb*1e9,10*log10(TL),'b', ...
     lam*1e9,Experiment,'g')
ylabel('Resultant reflection / transmission(dB)')
xlabel('Wavelength (nm)');
legend('Reflection','Transmission','Experiment');

figure(2)
subplot(211)
plot(lamb*1e9,20*log10(abs(rl01)), 'k',...
     lamb*1e9,20*log10(abs(tl01)), 'b')
ylabel('LP01 - Reflection / Transmission(dB)')
xlabel('Wavelength (nm)');
subplot(212)
plot(lamb*1e9,20*log10(abs(rl11)), 'k',...
     lamb*1e9,20*log10(abs(tl11)), 'b')
ylabel('LP11 - Reflection / Transmission (dB)')
xlabel('Wavelength (nm)');
legend('Reflection','Transmission');
RL = RL';

```

Review

## Chronology of Fabry-Perot Interferometer Fiber-Optic Sensors and Their Applications: A Review

Md. Rajibul Islam, Muhammad Mahmood Ali, Man-Hong Lai, Kok-Sing Lim \* and Harith Ahmad

Photonics Research Centre, University of Malaya, Kuala Lumpur 50603, Malaysia;

E-Mails: md.rajibul.islam@gmail.com (M.R.I.); engrmahmoodnaz@gmail.com (M.M.A.);

a131859.ukm@gmail.com (M.-H.L.); harith@um.edu.my (H.A.)

\* Author to whom correspondence should be addressed; E-Mail: kslim@um.edu.my;  
Tel./Fax: +603-7967-6770.

Received: 30 December 2013; in revised form: 29 March 2014 / Accepted: 18 April 2014 /

Published: 24 April 2014

---

**Abstract:** Optical fibers have been involved in the area of sensing applications for more than four decades. Moreover, interferometric optical fiber sensors have attracted broad interest for their prospective applications in sensing temperature, refractive index, strain measurement, pressure, acoustic wave, vibration, magnetic field, and voltage. During this time, numerous types of interferometers have been developed such as Fabry-Perot, Michelson, Mach-Zehnder, Sagnac Fiber, and Common-path interferometers. Fabry-Perot interferometer (FPI) fiber-optic sensors have been extensively investigated for their exceedingly effective, simple fabrication as well as low cost aspects. In this study, a wide variety of FPI sensors are reviewed in terms of fabrication methods, principle of operation and their sensing applications. The chronology of the development of FPI sensors and their implementation in various applications are discussed.

**Keywords:** interferometer; Fabry-Perot Interferometer (FPI); FPI fabrication techniques; FPI sensing applications

---

### 1. Introduction

The construction of photoinduced gratings in glass optical fibers was first introduced by Hill *et al.* [1] in 1978. A Bragg grating structure is produced in the core of a germanosilicate-made optical fiber by

# Wide-range in-fibre Fabry-Perot resonator for ultrasonic sensing

 ISSN 1751-8768  
 Received on 23rd May 2014  
 Revised on 8th October 2014  
 Accepted on 15th October 2014  
 doi: 10.1049/iet-opt.2014.0056  
 www.ietdl.org

Md. Rajibul Islam<sup>1</sup> ✉, Muhammad Mahmood Ali<sup>1</sup>, Man-Hong Lai<sup>1,2</sup>,  
 Dinusha Serandi Gunawardena<sup>1</sup>, Venkata Rajanikanth Machavaram<sup>3</sup>, Harith Ahmad<sup>1,2</sup>

<sup>1</sup>Photonics Research Centre, University of Malaya, 50603 Kuala Lumpur, Malaysia

<sup>2</sup>Department of Physics, Faculty of Science, University of Malaya, 50603 Kuala Lumpur, Malaysia

<sup>3</sup>School of Electronics Engineering, VIT University, Vellore-632014, Tamilnadu, India

✉ E-mail: md.rajabul.islam@gmail.com

**Abstract:** This study reports on the demonstration and characterisation of a short cavity fibre Fabry-Perot resonator (FPR) for the detection of ultrasonic waves propagating through a solid medium over a frequency range of 1 kHz–10 MHz. The proposed sensing device has some outstanding features in terms of simple fabrication technique, frequency response and high sensitivity over a wide frequency range. The response of the surface-mounted FPR sensor showed good agreement with that of a commercially available piezoelectric transducer during ultrasonic excitation.

## 1 Introduction

Ultrasonic detection is a well-known, safe and non-destructive investigation technique in numerous elementary processes, services, manufacturing industries and also in applications concerning structural metals and aerospace composites [1, 2]. The design of an appropriate ultrasound detection system for any application would generally require flat frequency response over the sensing frequency range; high sensitivity; robustness and ease of deployment. It is widely appreciated that the production and instrumentation costs involved in ultrasound sensors are high compared to other common sensor systems for strain and temperature [1]. Acoustic emission sensing over few tens of kHz to several MHz serves as a means of damage detection in materials where fibre-based sensors are used extensively for a wide variety of applications because of their small size, remote monitoring capability and immunity to electromagnetic interference [2, 3]. Hence, in many structural health monitoring studies [3, 4] based on ultrasound detection, fibre optic sensors (e.g. tapered FBGs; biconical coupler-based fibre sensor; diaphragm-based; and cantilever-based fibre sensors) [5, 6] are increasingly replacing conventional piezoelectric transducers (PZTs). The main drawback for PZT is that it is an electromechanical device whose performance is directly influenced by unwanted surrounding high frequency radiation which can be overcome by optical fibre sensors such as fibre Bragg gratings (FBGs) and Fabry-Perot (FP) sensors [6]. Also because of their light weight, compactness and easy integration, the FBGs are preferable for acousto-ultrasonic damage detection in smart structures, and specifically those materials which have their individual nervous system. A FBG, firstly invented by Hill *et al.* [7] is a very simple in-fibre structure defined as periodic perturbation of the refractive index (RI) along the core of fibre.

As compared to other ultrasound fibre sensors, FBGs [7] can be produced consistently in large numbers. The two main factors that characterise the performance of a FBG ultrasound sensor are its sensitivity and bandwidth. To improve these parameters, various techniques have been utilised for making different types of FBG sensors for detecting ultrasonic waves [8, 9]. Wu and Okabe [8] studied the phase-shifted FBG sensor with balanced photo-detector which exhibits high sensitivity and broad bandwidth with the capability to reduce laser intensity noise. The proposed FP resonator (FPR) design is aimed at improving the sensitivity to ultrasound via the generation of a resonance that is much narrower than a conventional Bragg resonance.

Zhou *et al.* [9] used a modified FBG structure produced by micromachining a channel using a femtosecond laser. In their study, the micro-channel was used to enable dynamic interaction between the liquid under test and light in the fibre where high sensitivity and large dynamic range of RI detection have been demonstrated. In the current work, a short cavity FPR is produced on a FBG to improve the sensitivity of the device. This is achieved by erasing a short length of grating at its centre. This paper describes the short cavity FPR sensor fabrication methodology and characterisation of response of surface-mounted version to ultrasound as compared to a standard PZT.

## 2 Analytical approach

In short cavity FPR, the acoustic pressure wave induces phase change of the light propagating in the sensing region. The phase of light ( $\phi$ ) passing through an optical fibre of  $L$  length, is given by

$$\phi = \beta L \quad (1)$$

Here, a propagation constant  $\beta$ , is given by

$$\beta = n_{\text{eff}} k_0 \quad (2)$$

where  $n_{\text{eff}}$  is the effective RI of the core mode and the wavenumber  $k_0$  is related to wavelength ( $\lambda$ ) of light as  $2\pi/\lambda$ .

The pressure wave-induced phase difference due to the change in grating length and effective modal index can be expressed as [3]

$$\Delta\phi = \beta\Delta L + L\Delta\beta \quad (3)$$

The differential pressure  $\Delta P$  along the length of the sensing region as the wave propagates in a direction parallel to the fibre can be expressed as [4]

$$\Delta P(z, t) = \Delta P_0 \cos\left(\omega t - \frac{2\pi z}{\lambda_S}\right) \quad (4)$$

where  $\Delta P_0$  is the peak pressure,  $\omega$  is the angular frequency and  $\lambda_S$  is the wavelength of the ultrasonic wave;  $z$  is the co-ordinate along the fibre direction; and  $t$  is the time.

# LP<sub>01</sub>–LP<sub>11</sub> Cross-Mode Interference in a Chirped Grating Inscribed in Two-Mode Fiber

Kok-Sing Lim, *Member, IEEE*, Md. Rajibul Islam, Yen-Sian Lee, Hang-Zhou Yang, and Harith Ahmad

**Abstract**—We have demonstrated LP<sub>01</sub>-LP<sub>11</sub> cross-mode interference in a single chirped grating (CG) inscribed in a two-mode fiber (TMF). With the aid of a binary phase plate, LP<sub>01</sub> mode and LP<sub>11</sub> mode can be selectively excited in the CG. By offsetting the position of the phase plate from the center of the input beam, we can simultaneously excite both the spatial modes at different LP<sub>01</sub>:LP<sub>11</sub> intensity ratios in the TMF. The excited modes lead to the formation of different interference patterns in the output spectra. The measured output spectra are found to be in good agreement with the simulation based on a coupled mode theory.

**Index Terms**—Bragg gratings, coupled mode analysis, few-mode fibers.

## I. INTRODUCTION

**C**OUPLED mode theory (CMT) is an important apparatus in describing the wave properties of various gratings imprinted on waveguides and optical fibers. The coupled mode equations (CME) can be derived from the perturbation theory [1] and various approaches based on numerical or analytical methods were proposed to simulate and analyze the spectra and performance of the gratings. Comparison analysis of several employed formulations of CMT in order to simulate fiber Bragg grating in respect of grating phase, pitch and amplitude discontinuities is presented in [2]. In particular, Erdogan [3] presented a comprehensive study on CME and the simulation of the grating spectra mainly focus on single mode fiber (SMF). CME for uniform gratings with constant parameter along the z-axis is simple and they can be analytically solved [4].

However, close form solution is not possible for most non-uniform gratings with varying parameters along the fiber. The problem can be addressed by using the Transfer Matrix Method (TMM), which is a commonly used numerical method for solving the CME of non-uniform grating such as phase-shifted grating, chirped grating (CG), apodized grating, superstructured grating and etc. Apart from the studies in fiber

gratings, CME has also been studied for analysis of mode propagation in uniform and slightly non-uniform cylindrical optical-fiber [5], birefringence in spun 4-lobe stress region fibers [6] and etc.

CME for few mode FBG are more sophisticated due to the additional spatial variables and terms describing the cross mode-coupling between two different spatial modes in the system [7]. Generally, spatial modes in a FMF are orthogonal and they do not couple or interfere with each other except under the condition of inhomogeneous refractive index profile over the cross section of the fiber. For example, optical fiber in curvature may experiences asymmetrical index profile fiber core index due to the bending stress [8], index perturbation in fiber by mechanical stress relaxation using CO<sub>2</sub> laser irradiation [9]–[13] and asymmetrical index change in the fiber core induced by UV laser. UV-induced asymmetrical index change is generally found in fiber Bragg grating written by UV-side illumination [14], in which the side of the fiber core that is nearer to the incoming laser beam receives higher laser intensity and yields greater index change than the far side of the fiber due to the high absorption/attenuation of UV laser in the fiber glass. As the result of inhomogeneous core index profile, the mode profiles deform and the orthogonality between the spatial modes degrades. Subsequently, this leads to the production of non-zero cross-coupling coefficients, enabling the exchange of energy among the spatial modes [15]. For a uniform grating on FMF, multiple resonant wavelengths are observed in the spectrum. Each of them can be associated with the self mode-coupling of a spatial mode or cross mode-coupling between two different spatial modes in the fiber. With the aid of binary phase plates, the associated spatial modes to each resonant wavelength can be identified. In particular, the cross-coupled wavelengths offer an attractive feature of bidirectional conversion between the associated modes [16]. In the excitation of higher order modes in FMFs, there are several available techniques such as core offset technique, binary phase mask, prism mode selector [17] and etc. Among them, core offset technique is the simplest approach for the excitation of multiple higher order modes but it lacks the flexibility in terms of mode selectivity. Binary phase plate is a robust and precise approach for selective mode excitation in FMFs. Despite the high insertion loss and bulky optomechanical setup, phase plates are still the preferred choice for mode conversion and selective mode excitation in various Space-division multiplexing (SDM) applications [18]–[20].

In this work, we have fabricated and investigated the characteristics of CG on TMF. In this grating structure, the lowest two spatial modes, namely LP<sub>01</sub> and LP<sub>11</sub> contribute

Manuscript received March 17, 2016; revised April 29, 2016; accepted May 4, 2016. Date of publication May 6, 2016; date of current version May 16, 2016. This project is supported by the University of Malaya HIR Grant (UM.C/625/1/HIR/MOHE/SCI/01), PPP Grant (PG006-2014A) and FRGS (FP002–2013B). The project is also partly supported by the National Natural Science Foundation of China (No. 61405160).

K.-S. Lim, M. R. Islam, Y.-S. Lee, and H. Ahmad are with the Photonics Research Centre, Physics Department, Science Faculty, University of Malaya, Kuala Lumpur 50603, Malaysia (e-mail: kslim@um.edu.my; md.rajibul.islam@gmail.com; yensian1110@gmail.com; harith@um.edu.my).

H.-Z. Yang is with the School of Physics, Northwest University, Xi'an 710069, China (e-mail: yanghz@nwu.edu.cn).

Color versions of one or more of the figures in this paper are available online at <http://ieeexplore.ieee.org>.

Digital Object Identifier 10.1109/JQE.2016.2564679



# PCF-Cavity FBG Fabry–Perot Resonator for Simultaneous Measurement of Pressure and Temperature

Muhammad Mahmood Ali, *Graduate Student Member, IEEE*, Md. Rajibul Islam, Kok-Sing Lim, *Member, IEEE*, Dinusha Serandi Gunawardena, Hang-Zhou Yang, and Harith Ahmad

**Abstract**—In this paper, we propose a Photonic Crystal Fiber (PCF)-cavity fiber Bragg grating (FBG) Fabry–Perot resonator for simultaneous sensing of temperature and pressure. The proposed device is constructed by splicing a 1.5-mm long PCF segment between two identical saturated FBGs written in SMF-28 forming an FBG-PCF-FBG configuration. As a result, a resonance dip is created within the Bragg reflection curve. Taking advantage of the difference in pressure sensitivities between the two types of fiber, the discriminative measurement of pressure and temperature can be achieved from the shifts of the resonance wavelength and band-edge wavelength. In addition, the same temperature sensitivity of PCF and SMF-28 provides the convenience of eliminating the temperature variable and achieving temperature insensitive pressure measurement.

**Index Terms**—Optical fiber sensors, Fabry-Perot resonator, photonic crystal fiber cavity, pressure sensor, temperature sensor.

## I. INTRODUCTION

IN RECENT years, fiber optic sensor technology has become the leading area of interest to many researchers and industries for several sensing applications due to their potential advantages, such as light weight, low cost, and immunity to electromagnetic interference (EMI). An early fiber based pressure sensor was proposed by Xu et al. [1]. The strain-optic property of FBG was exploited in the detection of hydrostatic pressure. Since then, numerous improved models have been proposed for pressure detection based on FBGs inscribed in specialty fibers [2]–[6]. The use of PCF in pressure sensing is particularly interesting and attractive. Taking advantages of the air-hole and small cross-sectional area of silica region, PCFs show greater pressure sensitivity than most SMFs which are solid fibers. In addition, it is possible to selectively fill

specific air holes in the PCF to achieve desired optical properties such as enhance sensitivity asymmetric coupling [7] and birefringence [8]. Wang et al. proposed the method for selectively filling of PCF using focus ion beam milled microchannel [9]. Furthermore, recent studies have demonstrated high pressure and temperature measurement using PCF along with standard SMF through the construction of a fiber-optic Fabry–Perot interferometer [10]. The proposed structure has a temperature sensitivity of 13.5 pm/°C and pressure sensitivity of  $-5.77$  pm/MPa. A considerable amount of effort has been put into the development of different techniques to distinguish the mechanical and thermal effects [11]–[15]. However, it is necessary to investigate a cost effective single system with ease of characterization and fabrication to fulfill this aspect. Hollow-core fiber based Fabry-Perot interferometers present rather interesting results [5]. Due to the small light-glass interaction, the pressure sensitivity is mainly contributed by the pressure-induced change in fiber cavity length. Yamate et al. [2] measured hydrostatic pressure by monitoring Bragg grating peak splitting caused by transverse strain differences in the core of a side-hole fiber which presents enhanced pressure sensitivity and reduced thermal dependence in comparison with FBG inscribed in solid fiber.

In this work, we proposed a PCF-cavity FBG Fabry-Perot resonator for pressure sensing. The device is assembled from two segments of uniform FBG inscribed in SMF and a short length PCF based on the configuration of FBG-PCF-FBG. In other words, the short PCF cavity in FBG-PCF-FBG structure induces the phase discontinuity between the two FBGs and it presents a similar output spectrum with that of phase shifted FBG [16]. The phase is dependent on the PCF structure and indicates much higher pressure sensitivity compared to the FBG even though both exhibit similar temperature sensitivities. Based on this observation, the proposed device can be used for simultaneous measurement of temperature and pressure including temperature independent pressure measurement. Potential applications of the proposed device include in-situ monitoring of temperature and pressure especially in oil and gas industries as well as down-hole applications in chemical industries.

## II. FABRICATION

A 20 mm long uniform grating is written in a hydrogenated SMF-28 by using KrF excimer laser and a phase mask.

Manuscript received April 5, 2015; revised July 12, 2015; accepted August 11, 2015. Date of publication August 13, 2015; date of current version October 8, 2015. This work was supported in part by the University of Malaya through the High Impact Research (HIR) Project UM.C/625/1/HIR/181 under Grant J-21001-73860, in part by the Postgraduate Research Grant Project under Grant PG006-2014A, in part by the Fundamental Research Grant Scheme Project under Grant FP002-2013B, and in part by the National Natural Science Foundation of China under Grant 61405160. The associate editor coordinating the review of this paper and approving it for publication was Dr. William N. MacPherson.

M. M. Ali, M. R. Islam, K.-S. Lim, D. S. Gunawardena, and H. Ahmad are with the Department of Physics, Faculty of Science, Photonics Research Centre, University of Malaya, Kuala Lumpur 50603, Malaysia (e-mail: kslim@um.edu.my).

H.-Z. Yang is with the School of Physics, Northwest University, Xi'an 710069, China (e-mail: yanghz@nwu.edu.cn).

Color versions of one or more of the figures in this paper are available online at <http://ieeexplore.ieee.org>.

Digital Object Identifier 10.1109/JSEN.2015.2468065



T  
O  
D  
A  
Y  
F  
O  
R  
T  
O  
M  
O  
R  
R  
O  
W

**INNOVATIONS**

**Pecipta'15**  
THE INTERNATIONAL  
CONFERENCE AND EXPOSITION ON INVENTIONS  
by Institutions of Higher Learning

# BRONZE

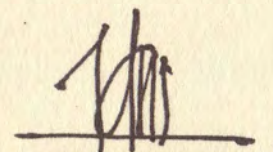
This is certify that

**Few-Mode Fibre Grating Sensor**

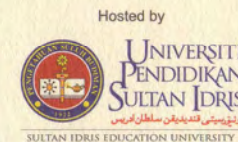
Kok Sing Lim, Muhammad Mahmood Ali, Md. Rajibul Islam, Harith Ahmad,  
Lee Yien Sen

Winner at the International Conference  
and Exposition on Inventions by Institutions  
of Higher Learning

held at  
Kuala Lumpur Convention Centre  
4th - 6th December 2015



**DATO' SERI IDRIS BIN JUSOH**  
Minister of Higher Education  
Ministry of Higher Education





# CERTIFICATE OF PARTICIPATION

This certificate is awarded to

**Few-Mode Fibre Grating Sensor**

Kok Sing Lim, Muhammad Mahmood Ali, Md. Rajibul Islam, Harith Ahmad,  
Lee Yien Sen

who has participated in the **International Conference and Exposition on Inventions by Institutions of Higher Learning**

held at  
**Kuala Lumpur Convention Centre**  
**4th - 6th December 2015**

**Pecipta'15**  
THE INTERNATIONAL  
CONFERENCE AND EXPOSITION ON INVENTIONS  
by Institutions of Higher Learning



**DATO' SERI IDRIS BIN JUSOH**  
Minister of Higher Education  
Ministry of Higher Education

